

**Faculty of Science and Engineering  
Discipline of Medical Radiation Sciences**

**In Vitro and Computational Analyses of Blood Flow at  
Aortoiliac Bifurcation for Patients with Atherosclerotic  
Plaque Treated with Endovascular Procedures**

**Albert Chong**

**This thesis is presented for the degree of  
Doctor of Philosophy  
of  
Curtin University**

**July 2020**

# Declaration

To the best of my knowledge and belief this thesis contains no material previously published by any other person except where due acknowledgment has been made. This thesis contains no material which has been accepted for the award of any other degree or diploma in any university.

A rectangular area filled with a diagonal hatching pattern, used to redact the author's signature. The text "Signature Redacted" is centered within this area.

Signature Redacted

**Albert Chong**

19 July 2020

# Abstract

Covered endovascular reconstruction of aortoiliac bifurcation (CERAB) configuration is a relatively new technique with encouraging results and increasingly being used in favour of the traditional kissing stents technique. When the current gold standard for in-stent restenosis of distal to proximal peak systolic velocity ratio  $> 2.5$  was used, some patients have had computed tomography angiography (CTA) scan performed on them due to false positive results. The additional cost and risk associated with CTA could be avoided if a more robust screening tool was available.

More recently, it was suggested that the use of a unibody stent-graft, designed for aneurysm treatment, could have several advantages for the treatment of Aortoiliac Occlusive Disease (AIOD) over CERAB. It preserves the aortic bifurcation, avoid limb competition in the distal aorta, allow for future endovascular interventions, and protect against potentially fatal aortoiliac rupture in heavily calcified lesions. The benefit of the Anatomical FiXation (AFX) stent-graft is the fact that radial mismatch is totally eliminated because of the one piece bifurcation design. The safety, efficacy, and early patency rates of the AFX unibody stent-graft for treatment of AIOD have been examined extensively by several groups; high primary and secondary patency rates up to three years follow up have been reported.

The objectives of this thesis are:

- (i) to investigate an appropriate approach allowing for accurate assessment of hemodynamic changes following treatment in patients with AIOD
- (ii) to analyse and compare the hemodynamics of CERAB configuration and AFX stent-graft to better understand the flow characteristics of these two endovascular techniques using laser particle image velocimetry (PIV) experiments.
- (iii) to develop a novel roller pump for physiological flow to overcome one of the limitations of the existing flow loop used in laser particle image velocimetry experiment.
- (iv) to validate the computational fluid dynamic method as an viable hemodynamic assessment tool comparable to experimental method

To achieve the first objective, a peak systolic velocity (PSV) predictor was developed as a possible screening tool to supplement the existing re-stenosis guideline. Initial retrospective analysis based on a sample size of 16 patients showed potential of the PSV predictor as a screening tool to avoid CTA for patient with elevated PSV however, when it was tested on a larger sample size of 25 patients, it has an unacceptably low sensitivity value of 42% therefore deemed unsuitable as a clinical screening tool. Manual adjustments to the predictor by considering the vessel compliance based on Ankle Brachial Index (ABI) and iliac artery asymmetry only resulted in marginal improvement. Flute angle and stent height of CERAB configuration when evaluated as independent variables were found to have little influence on PSV predictor statistically and failed to improve the predictor. Further attempts to improve the PSV predictor by adding ABI and iliac asymmetry as independent variables were also not successful. The current PSV predictor is largely based on physiological phenomenon therefore further investigation by taking into account the biological response especially the auto regulation of blood flow by the brain might help to improve the PSV predictor to be a valuable clinical screening tool.

The second objective dealt with the hypothesis that the AFX stent-graft is a better endovascular technique than CERAB configuration in treating AIOD. To test the hypothesis, a hemodynamic comparison between the two techniques was performed using laser PIV experiments. In that experimental study, more disturbed flow was observed in the bifurcation region of AFX stent-graft as compare with CERAB configuration. It was confirmed by the quantified hemodynamic outcomes where the mean time average wall shear stress (TAWSS) of 0.078 Pa (range: 0.009 to 0.242 Pa) for AFX was significantly lower than 0.229 Pa (range: 0.013 to 0.906 Pa) for CERAB,  $p < 0.001$ . Moreover, the mean oscillatory shear index (OSI) of 0.318 (range: 0.123 to 0.496) for AFX was significantly higher than 0.252 (range: 0.055 to 0.472) for CERAB,  $p < 0.001$ . Likewise, the mean relative residence time (RRT) of  $180 \text{ Pa}^{-1}$  (Range: 9 to  $3,603 \text{ Pa}^{-1}$ ) for AFX was significantly longer than  $88 \text{ Pa}^{-1}$  (Range: 2 to  $840 \text{ Pa}^{-1}$ ) for CERAB,  $p = 0.0086$ . These research findings suggest that CERAB configuration is more protective of thrombosis as compared with AFX stent-graft in the experimental setting and further investigation is warranted to confirm whether the undesirable hemodynamic results identified in this study are translated into the clinical setting.

The third objective was to develop a cardiac pump to generate physiological flows for bench top testing.



The fourth objective was to validate a computational fluid dynamics method as a viable hemodynamic assessment tool by comparing its simulation results to that of Laser PIV experiments.

In summary, a PSV prediction tool has been developed as a potential screening tool to improve diagnosis of patients treated with CERAB endovascular procedure but falls short in sensitivity and specificity therefore deemed unsuitable to be used in clinical practice. Further improvement to the predictor are needed to improve its utility for clinical applications.

It was concluded that CERAB is a more superior endovascular technique in treating extensive AIOD based on hemodynamic outcomes comparing AFX stent-graft and CERAB configuration in an experimental setting. Further investigations are warranted to confirm whether the experimental findings are translated into clinical setting.

It was demonstrated that carotid, suprarenal and infrarenal flow profiles were successfully generated by the novel reciprocating roller pump with waveforms conforming to human physiology and closely matched the reference profiles therefore it is deemed suitable for use in experimental studies of vascular blood flow.

A computational fluid dynamics method was partially validated. There were reasonable agreements between PIV and CFD methods for OSI and RRT in the inflow region but poor agreement in the bifurcation region. Further improvements in CFD and PIV models are needed to overcome the inherent limitations in order to fully validate the CFD method for use as a hemodynamic assessment tool.

# Table of Contents

Declaration .....	iii
Abstract .....	v
Table of Contents .....	ix
List of Figures .....	xiii
List of Tables .....	xvii
List of Abbreviations .....	xix
Publications, Conferences and Videos .....	xxi
Statement of Contribution of Others .....	xxiii
Acknowledgements.....	xxv
Dedication .....	xxvii
<b>Chapter One Introduction</b> .....	<b>1</b>
1.1 Clinical Complications .....	2
1.1.1 Background .....	2
1.1.2 Diagnosis .....	4
1.1.2.1 ABI .....	5
1.1.2.2 Doppler Ultrasound (DU) .....	7
1.1.2.3 Computed Tomography Angiography (CTA).....	8
1.1.3 Treatment options.....	10
1.1.3.1 Surgical treatments.....	10
1.1.3.2 Minimally invasive endovascular treatments.....	10
1.2 Hypothesis of the research.....	15
1.3 Objectives.....	15
1.4 Thesis Overview .....	17
<b>Chapter Two Blood Flow Velocity Prediction in Aortoiliac Stent Grafts                   using Computational Fluid Dynamics and Taguchi Method</b> .....	<b>19</b>
Preamble.....	20
2.1 Introduction .....	21
2.2 Methods.....	21
2.2.1 Design of Experiments.....	21
2.2.2 Computational Fluid Dynamics (CFD) .....	22
2.2.3 Acquisition of Patient Specific Data.....	24
2.2.4 Statistical Analysis .....	25
2.3 Results .....	26
2.3.1 CFD Simulation Results .....	26
2.3.1.1 Signal to Noise Ratio Main Effects .....	26
2.3.1.2 Interaction Effects .....	27
2.3.1.3 Analysis of Variance.....	28
2.3.1.4 Predictive Models .....	28

2.3.2	Measurement Results of Patient Data.....	29
2.3.3	Prediction Results from the Predictive Model .....	30
2.4	Discussion .....	32
2.5	Conclusion.....	34
<b>Chapter Three Incorporating Iliac Asymmetry and Ankle Brachial Index Asymmetry into Peak Systolic Velocity Prediction Model</b>		<b>35</b>
	Preamble.....	36
3.1	Introduction .....	36
3.2	Materials and Methods .....	37
3.2.1	Adjustment factor for iliac asymmetry .....	39
3.2.2	Adjustment factor for ABI asymmetry.....	39
3.2.3	Statistical analysis .....	40
3.3	Results .....	40
3.4	Discussion .....	44
3.5	Conclusion.....	46
<b>Chapter Four Influence of Flute Angle, Cuff Length Overlap and Bifurcation Angle on Peak Systolic Velocity</b>		<b>47</b>
	Preamble.....	48
4.1	Introduction .....	48
4.2	Materials and Methods .....	50
4.2.1	3D Model.....	51
4.2.2	Meshing .....	52
4.2.3	CFD Simulations.....	53
4.2.3.1	Inlet Boundary Condition .....	53
4.2.3.2	Outlet Boundary Condition.....	53
4.2.3.3	Periodicity .....	57
4.2.3.4	Parameter of Interest: PSV .....	57
4.3	Results .....	58
4.4	Discussion .....	61
4.5	Conclusion.....	61
<b>Chapter Five Improvement to PSV Predictor by Incorporating Additional Independent Variables in the Prediction Model</b>		<b>63</b>
	Preamble.....	64
5.1	Introduction .....	64
5.2	Materials and Methods .....	65
5.3	Results .....	66
5.4	Discussion .....	72
5.5	Conclusion.....	73

<b>Chapter Six</b>	<b>Hemodynamic Comparison of AFX Stent-Graft and CERAB Configuration for Treatment of Aortoiliac Occlusive Disease</b>	<b>75</b>
	Preamble.....	76
6.1	Introduction.....	76
6.2	Materials and methods.....	77
6.2.1	Model designs and stent deployment.....	77
6.2.2	Experimental flow circuit.....	78
6.2.3	Flow visualization.....	79
6.2.4	Data processing.....	80
6.3	Results.....	83
6.3.1	Inflow pattern.....	83
6.3.2	Bifurcation flow pattern.....	84
6.3.3	Hemodynamic comparison.....	84
6.4	Discussion.....	86
6.5	Conclusion.....	88
<b>Chapter Seven</b>	<b>A Novel Roller Pump for Physiological Flow</b>	<b>89</b>
	Preamble.....	90
7.1	Introduction.....	91
7.2	Materials and Methods.....	92
7.2.1	Experimental Flow Circuit.....	92
7.2.2	Flow Profiles.....	93
7.2.3	Flow Profile Generation.....	95
7.2.4	Flow Profile Measurements.....	95
7.3	Results.....	97
7.3.1	Carotid Flow.....	98
7.3.2	Suprarenal Flow.....	99
7.3.3	Infrarenal Flow.....	99
7.4	Discussion.....	100
7.5	Conclusion.....	101
<b>Chapter Eight</b>	<b>Comparison of Particle Image Velocimetry and Computational Fluid Dynamics Method in an Aortoiliac Model Deployed with AFX Stent-Graft</b>	<b>103</b>
	Preamble.....	104
8.1	Introduction.....	105
8.2	Material and Methods.....	105
8.2.1	PIV Methodology.....	106
8.2.2	CFD Methodology.....	108
8.2.2.1	Struts of AFX stent-graft.....	108
8.2.2.2	Flow phantom.....	109

8.2.2.3	Boundary conditions .....	110
8.2.2.4	Meshing .....	112
8.2.2.5	Grid independence and periodicity convergence tests.....	113
8.3	Results .....	114
8.3.1	Grid-independent convergence .....	114
8.3.2	Inflow pattern .....	117
8.3.3	Bifurcation flow pattern .....	118
8.3.4	Hemodynamic comparison .....	118
8.3.5	Hemodynamic plots .....	120
8.4	Discussion .....	121
8.5	Conclusion.....	123
<b>Chapter Nine</b>	<b>Conclusions and Future Directions</b>	<b>125</b>
9.1	Conclusions .....	126
9.2	Future Directions .....	128
References	.....	129
<hr/>		
APPENDICES		143
<hr/>		
Appendix A	Design of Experiment.....	145
Appendix B	Computational Fluid Dynamics .....	149
Appendix C	AFX Transparent Cover-Making Process.....	153
Appendix D	Hemodynamic Plots.....	155
Appendix E	A Smart-phone Application for PSV Predictor .....	157
Appendix F	Provisional Filing of Novel Cardiac Pump.....	159
Appendix G	Provisional Filing of Cardiac Pump for Surgical Procedures .....	175
Appendix H	Conference Proceedings .....	193
Appendix I	Attribution Statements.....	203
Appendix J	Copyright Permissions.....	206
Appendix K	Published Manuscript Details.....	221

# List of Figures

Figure 1-1	Inter-Society Consensus for the Management of Peripheral Arterial Disease (TASC) classification of aortoiliac lesions.....	4
Figure 1-2	How to measure, calculate and interpret the ABI.....	6
Figure 1-3	Digital ABI Measurement in three simple steps.....	6
Figure 1-4	Velocity Measurement using a DU scanner.....	8
Figure 1-5	CTA technique.....	9
Figure 1-6	Measurement with CTA .....	9
Figure 1-7	Schematic representation of atherosclerotic stenosis.....	11
Figure 1-8	Step-by-step process of the covered endovascular reconstruction of the aortoiliac bifurcation (CERAB) technique .....	13
Figure 1-9	CTA Images .....	14
Figure 2-1	Polyhedral Volume Mesh.....	23
Figure 2-2	Angle and Diameters Measurements .....	24
Figure 2-3	CFD Simulation Results .....	26
Figure 2-4	Interactions between $\alpha$ and $PSV_{in}$ .....	27
Figure 2-5	Interactions between $PSV_{in}$ and R.....	27
Figure 2-6	Interactions between R and $\alpha$ .....	28
Figure 2-7	Predicted vs Doppler Ultrasound measured $PSV_{max}$ Plot.....	32
Figure 3-1	Clinical validation of predictor-CERAB patient selection .....	37
Figure 3-2	Aorta diameter measurement.....	38
Figure 3-3	Iliac diameter measurement.....	38
Figure 3-4	Predicted vs DU measured PSV plot before adjustment .....	43
Figure 3-5	Predicted PSV vs DU-measured PSV adjusted for iliac and ABI asymmetries .....	43
Figure 4-1	Geometrical parameters of a CERAB model.....	49
Figure 4-2	Workflow to assess the effects of independent variables on PSV .....	50
Figure 4-3	Aortoiliac bifurcation model with an aortic stent inserted .....	51
Figure 4-4	Aortoiliac bifurcation model with an aortic stent inserted .....	51
Figure 4-5	Fluent meshing flowchart .....	52
Figure 4-6	Infrarenal triphasic flow profile.....	53
Figure 4-7	Two-element Windkessel model.....	54
Figure 4-8	Three-element Windkessel model.....	55
Figure 4-9	Three-element Windkessel at pressure outlets.....	56
Figure 4-10	Periodicity convergence at the 7 <sup>th</sup> cardiac cycle.....	57
Figure 4-11	Post-processing of CFD simulation showing maximum velocity.....	57
Figure 4-12	PSV vs flute angle plot at 40° bifurcation angle.....	58
Figure 4-13	Average PSV vs flute angle at 40° bifurcation angle .....	59

Figure 4-14	PSV vs flute angle plot at 90° bifurcation angle .....	59
Figure 4-15	Average PSV vs flute angle at 90° d bifurcation angle .....	60
Figure 4-16	Overall PSV vs flute angle.....	60
Figure 4-17	Overall PSV vs cuff-length overlap .....	60
Figure 5-1	Workflow for ideal geometry 3D flow model and CFD simulations.....	65
Figure 5-2	Typical CFD set-up with assigned boundary conditions.....	66
Figure 5-3	Main effects plot .....	68
Figure 5-4	Predicted vs DU measured PSV for improved PSV predictor .....	71
Figure 5-5	Sensitivity vs specificity plot for existing screening tests .....	72
Figure 6-1	Computed Tomography (CT) images of the flow phantoms .....	78
Figure 6-2	Experimental flow circuit and laser particle image velocimetry (PIV) set-up .....	79
Figure 6-3	Images of bifurcation region illuminated by laser during PIV experiment.....	80
Figure 6-4	Flow waveform: Red line represents flow waveform obtained with flow sensor at the inlet of the system.....	82
Figure 6-5	Inflow patterns .....	83
Figure 6-6	Bifurcation flow pattern.....	84
Figure 7-1	Experimental flow circuit.....	93
Figure 7-2	Manual Digitization of Flow Profile .....	94
Figure 7-3	Reference flow profiles .....	95
Figure 7-4	Flow rate measurement by motion analysis.....	96
Figure 7-5	Carotid flow profile .....	98
Figure 7-6	Carotid flow profile measured vs reference.....	98
Figure 7-7	Suprarenal flow profile.....	99
Figure 7-8	Infrarenal flow profile.....	100
Figure 8-1	Flowchart comparing PIV and CFD methodologies .....	106
Figure 8-2.	Laser particle image velocimetry experimental set-up.....	107
Figure 8-3	Reconstructed AFX stent-graft showing four types of linkages used to join the strut wires together. ....	109
Figure 8-4	Laser particle image velocimetry (PIV) and computational fluid dynamics comparison (CFD).....	110
Figure 8-5	Boundary condition set-up for CFD model. ....	111
Figure 8-6	Polyhedral meshes .....	112
Figure 8-7	Region of interest in CFD simulation .....	113
Figure 8-8	Results of TAWSS, OSI and RRT .....	114
Figure 8-9	Results of TAWSS, OSI and RRT from CFD simulations in the AFX bifurcation right edge .....	115
Figure 8-10	Results of TAWSS, OSI and RRT from CFD simulations in the AFX bifurcation left edge.....	116
Figure 8-11	Inflow patterns of laser PIV and CFD.....	117

Figure 8-12	Bifurcation flow patterns.....	118
Figure 8-13	TAWSS, OSI and RRT plots at the inflow region for PIV and CFD methods. ....	120
Figure 8-14	TAWSS, OSI and RRT plots at the bifurcation right edge for PIV and CFD methods. ....	120
Figure 8-15	TAWSS, OSI and RRT plots at the bifurcation left edge for PIV and CFD methods. ....	120

### Figures in Appendices

Figure A.1	A Basic Human Aortoiliac Bifurcation Model.....	145
Figure A.2	$L_8$ Linear Graph.....	148
Figure B.1	Pulsatile inlet velocity profile with a $PSV_{in}$ of 0.7 m/s and the black dot indicates the $PSV_{in}$ at 2.0 second in the third cardiac cycle.....	149
Figure B.2	Velocity Profile Evaluated at 200 mm Entrance Length Intervals from Inlet.....	150
Figure B.3	Instantaneous velocity profiles in the aortoiliac bifurcation model at peak inlet velocity.....	150
Figure D.1	Time averaged wall shear stress (TAWSS), oscillatory shear index (OSI) and relative residence time (RRT) plots at the inflow region of AFX-stent-graft and CERAB configuration. ....	155
Figure D.2	Time averaged wall shear stress (TAWSS), oscillatory shear index (OSI) and relative residence time (RRT) plots at the bifurcation region of AFX-stent-graft and CERAB configuration.....	155
Figure E.1	Smart-phone Application for PSV Predictor.....	157



# List of Tables

Table 2-1	Response table of main effects.....	27
Table 2-2	ANOVA table for S/N ratio of $PSV_{max}$ .....	28
Table 2-3	Patient data.....	30
Table 2-4	Patient Specific Predictions .....	31
Table 3-1	Table parameters of AIOD patients .....	39
Table 3-2	Gold standard re-stenosis screening test .....	40
Table 3-3	Geometric parameters of 25 patients and results of predicted PSV .....	41
Table 3-4	Predicted PSV Results adjusted for iliac symmetry and ABI symmetry....	42
Table 3-5	Status of restenosis according to gold standard before and after adjustments for iliac and ABI asymmetries.....	44
Table 3-6	Sensitivity, specificity, PPV and NPV before and after adjustments for iliac and ABI asymmetries.....	44
Table 4-1	PSV vs flute angle at 40° bifurcation angle and varying cuff length overlap.....	58
Table 4-2	PSV vs Flute Angle at 90° bifurcation angle varying cuff length overlap.....	59
Table 5-1	Data of $PSV_{max}$ from CFD simulations.....	67
Table 5-2	Data of multivariable regression analysis .....	68
Table 5-3	Predicted PSV based on the improved PSV predictor.....	70
Table 5-4	Status of restenosis based on 'gold standard' for improved PSV predictor.....	71
Table 6-1	TAWSS, OSI and RRT results at inflow and bifurcation for AFX stent-graft and CERAB configuration.....	85
Table 7-1	Reference flow rates at PSV, ESV and PDV time-points for carotid, suprarenal and infrarenal flow.....	95
Table 7-2	Test results of comparison between measured and programmed flow profiles .....	97
Table 8-1	P-values for Student's T-test pair-wise comparison of TAWSS, OSI and RRT in the AFX inflow region for coarse, medium and fine meshes .....	114
Table 8-2	P-values for Student's T-test pair-wise comparison of TAWSS, OSI and RRT in the AFX bifurcation right edge for coarse, medium and fine meshes.....	115
Table 8-3	P-values for Student's T-test pair-wise comparison of TAWSS, OSI and RRT in the AFX bifurcation left edge for coarse, medium and fine meshes.....	116
Table 8-4	TAWSS, OSI and RRT data at inflow and bifurcation for PIV and CFD .....	119

**Tables in Appendices**

Table A.1	Aortoiliac bifurcation geometry and physiology from references .....	146
Table A.2	Assignment of 2-level control factors .....	147
Table A.3	L <sub>8</sub> Orthogonal array .....	148
Table B.1	Grid independence test .....	151
Table B.2	Periodicity convergence test.....	152

# List of Abbreviations

<b>ABI</b>	Ankle Brachial Index
<b>AFX</b>	Anatomical FiXation
<b>AIOD</b>	Aortoiliac Occlusive Disease
<b>ANOVA</b>	Analysis of Variance
<b>ANSI</b>	American National Standards Institute
<b>APP</b>	Smart-phone application
<b>BMF</b>	Blood Mimicking Fluid
<b>CAD</b>	Computer Aided Design
<b>CCA</b>	Common Carotid Artery
<b>CERAB</b>	Covered Endovascular Reconstruction of Aortoiliac Bifurcation
<b>CFD</b>	Computational Fluid Dynamics
<b>CIA</b>	Common Iliac Arteries
<b>CLI</b>	Critical Limb Ischemia
<b>CPB</b>	Cardiopulmonary bypass
<b>CT</b>	Computed Tomography
<b>CTA</b>	Computed Tomography Angiography
<b>CVD</b>	Cardiovascular Disease
<b>DSA</b>	Digital Subtraction Angiography
<b>ECMO</b>	Extracorporeal Membrane Oxygenation
<b>ESV</b>	End Systolic Velocity
<b>EVT</b>	Endovascular Treatment
<b>IC</b>	Intermittent Claudication
<b>LDPE</b>	Low Density Polypropylene
<b>LIA</b>	Left Iliac Artery
<b>MLR</b>	Multiple Linear Regression
<b>MS</b>	Mean of Squares
<b>NPV</b>	Negative Predictive Value
<b>OCPC</b>	One Curtin Postgraduate Conference
<b>OSI</b>	Oscillatory Shear Index
<b>PAD</b>	Peripheral Arterial Disease
<b>PDMS</b>	Polydimethylsiloxane
<b>PDV</b>	Peak Diastolic Velocity

## List of Abbreviations

<b>PIV</b>	Particle Image Velocimetry
<b>PPV</b>	Positive Predictive Value
<b>PSV</b>	Peak Systolic Velocity
<b>RIA</b>	Right Iliac Artery
<b>RPM</b>	Rotations Per Minute
<b>RRT</b>	Relative Residence Time
<b>SD</b>	Standard Deviation
<b>SS</b>	Sum of Squares
<b>SVS</b>	Society for Vascular Surgery
<b>TASC</b>	Trans-Atlantic Inter-Society Consensus
<b>TAWSS</b>	Time Averaged Wall Shear Stress
<b>UDF</b>	User Defined Function
<b>WSS</b>	Wall Shear Stress

# Publications, Conferences and Videos

## Publications

- Chong, A.Y., et al., Blood flow velocity prediction in aorto-iliac stent grafts using computational fluid dynamics and Taguchi method. *Computers in Biology and Medicine*, 2017. 84: p. 235-246.
- Chong, A., et al., A novel roller pump for physiological flow. *Artificial Organs*, 2020.
- Chong, A., et al., Hemodynamic comparison of AFX stent-graft and CERAB configuration for treatment of aortoiliac occlusive disease. *Journal of Endovascular Therapy*, submitted on the 23<sup>rd</sup> of June 2020, currently under review.

## Conference Proceedings

- The 9th Congress of Asian Society of Cardiovascular Imaging conference at the Le Meridien, Kuala Lumpur, Malaysia, 11 – 13 June 2015  
*Note: See Appendix H for full transcript.*
- Proceeding of One Curtin International Conference (OCPC) 2017, Miri Sarawak, 10-12 December 2017  
*Note: See Appendix H for full transcript.*

## Videos (On-line only)

- Video 1 shows one cardiac cycle of the flow pattern of AFX stent-graft at the inflow region as derived from laser PIV experiment.  
*URL: <https://vimeo.com/manage/427987384/general>*
- Video 2 shows one cardiac cycle of the flow pattern of CERAB configuration at the inflow region as derived from laser PIV experiment.  
*URL: <https://vimeo.com/manage/427996402/general>*
- Video 3 shows one cardiac cycle of the flow pattern of AFX stent-graft at the bifurcation region as derived from laser PIV experiment.  
*URL: <https://vimeo.com/manage/428009757/general>*
- Video 4 shows one cardiac cycle of the flow pattern of CERAB configuration at the bifurcation region as derived from laser PIV experiment.  
*URL: <https://vimeo.com/manage/428016420/general>*
- Video 5 shows one cardiac cycle of the flow pattern of AFX stent-graft at the inflow region simulated with Ansys CFD Fluent.  
*URL: <https://vimeo.com/manage/429844328/general>*
- Video 6 shows one cardiac cycle of the flow pattern of AFX stent-graft at the bifurcation region simulated with Ansys CFD Fluent.  
*URL: <https://vimeo.com/manage/429849657/general>*

## Statement of Contribution of Others

Albert Chong's input into this research and all journals consisted of the performance of scientific works, and a lead author of research articles to the intellectual property implicated in this thesis. The other specialists who made significant assistance to the research that were sufficient to warrant co-authorship on the appearing journals, are:

- Zhonghua Sun provided overall project supervision and technical advice and manuscript editing.
- Shirley Jansen provided technical support and manuscript editing.
- Barry Doyle provided technical support and manuscript editing.
- Erik Groot Jebbink provided technical support and manuscript editing.
- Hadi Mirgolbabaee provided technical support and manuscript editing.
- Lennart van de Velde provided technical support and manuscript editing.
- Michel Reijnen provided manuscript editing.
- Michel Versluis provided manuscript editing.

Signature Redacted

**Albert Chong**

9 July 2020

Signature Redacted

**Professor Zhonghua Sun**

9 July 2020

# Acknowledgements

This thesis would not have been possible without the help of several people, whose names require particular mention here and to whom I would be indebted throughout my life. First, I would like to take this opportunity to express my sincerest gratitude to my supervisor Professor Zhonghua Sun for his constant encouragement and guidance throughout my PhD experience. I am grateful to Dr. Shirley Jansen MD and Dr. Barry Doyle for their support as co-supervisors and their incommensurable advices. I would also like to take this opportunity to thank our collaborators at the University of Twente, Enschede, the Netherlands for hosting my visit in 2018 to conduct pump comparison study and PIV experiments. I am particularly grateful to Dr. Erik Groot Jebbink for hosting me and coordinating the collaborative research projects. I like to thank Stefan Engelhard, Hadi Mirgolbabaei, Lennart van de Velde, Professor Michel Versluis, Dr. Michel Reijnen MD, Henny Kuipers, Annemiek vos Bevald and Wim Leppink for their friendship and assistance during my visit at University of Twente. I could not have survived my PhD without the support of special people that have characterized the overall experience especially from my wife Mei Li Chong for her support and proof reading this thesis.

# Dedication

*I dedicate this to my wife Mei Li, my sons Shaun and Justin who always  
believed in my ability to earn a doctorate degree*



## Chapter One

# 1

## Introduction

## 1.1 Clinical Complications

Peripheral arterial disease (PAD) was estimated to affect about 200 million people globally in 2010 [1]. Aortoiliac occlusive disease (AIOD) accounted for up to 50% of the PAD patients [2]. If the 23.5% increase from 2000 to 2010 [1] is extrapolated from 2010 to 2020, then more than 123 million people might be affected by AIOD globally by the year 2020. The treatment of AIOD over the past few decades has shifted significantly from open surgery to the less invasive endovascular treatment (EVT) due to its high technical success rate, improved patency, low morbidity rate, and short hospital stay [3-14]. In addition, newer techniques have been successfully introduced to treat complex TransAtlantic Inter-Society Consensus (TASC) type D lesions, especially with covered stents [15-22]. Despite that the blood flow is usually restored by the newer EVT techniques in treating complicated cases of AIOD, its flow pattern and hemodynamic characteristics in the “new normal” are seldom understood and might lead to incorrect diagnosis during follow-up. One such clinical problem is the higher than expected blood flow velocity near the stented region treated with Covered Endovascular Reconstruction of the Aortoiliac Bifurcation (CERAB) configuration. CERAB and AFX stent-graft are two recent EVT techniques that are effective in treating TASC type D lesions. However, clinicians are still posed with the question of which technique offers a better solution from a haemodynamic perspective. This thesis has attempted to address these two clinical issues.

### 1.1.1 Background

AIOD is a subset of PAD and a type of cardiovascular disease (CVD) involving the blockage of the abdominal aorta as it transitions into the left common iliac artery (CIA) and right CIA due to the presence of plaque in the artery wall. This might result in Leriche Syndrome, named after the French surgeon and physiologist René Leriche, who reported a syndrome of thrombotic obliteration of the aortic bifurcation in 1940 [23, 24]. Leriche Syndrome [23] is typically described in male patients with a triad of intermittent claudication in the buttocks and thighs, erectile dysfunction and absent or reduced femoral pulses. Since this report in young male patients, older and females patients have been reported subsequently [25, 26].

Atherosclerosis is a common, degenerative disease with no known single cause [27]. Several factors contribute to the formation of atherosclerotic lesions that are commonly known as plaques in the arteries [28]. It is understood that biological response to arterial injury triggers atherosclerosis. This process and the underlying pathophysiology remains

unclear. However, various studies have suggested that mechanical factors, such as hypertension [4, 29-32] and low wall shear stress (WSS) [31, 33-35], chemical factors, such as hyperlipidaemia [35, 36], hyperglycaemia [32, 37] and homocysteine [38-41,] as well as smoking are known to be injurious to the arterial wall.

Lipid and microphages accumulate in the smooth muscle cells of the arterial wall as an inflammatory response to endothelial injury. Thus, it is hypothesised that low WSS allows the lipids to pass through the injured wall. Atheroma is comprised of cholesterol, cholesterol esters and triglycerides in varying compositions. Some plaques are less stable, and fissures occur on the plaque surface that facilitates the contact of circulating platelets with the internal constituents of the plaque, causing platelet aggregation. This could result in a fresh blood clot or thrombosis, blocking the lumen and causing ischemia to the organ (for example, heart attack or stroke). Blood supply can also be affected by the embolization of plaque debris and clot from atheroma to smaller vessels beyond the plaque location.


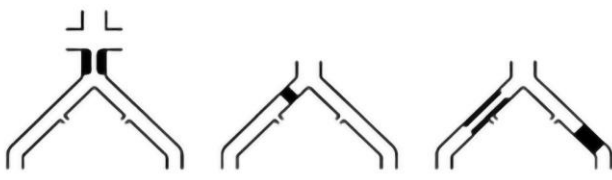
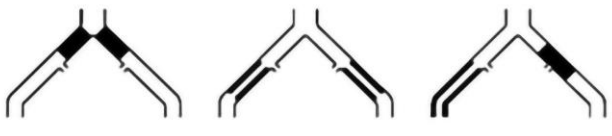
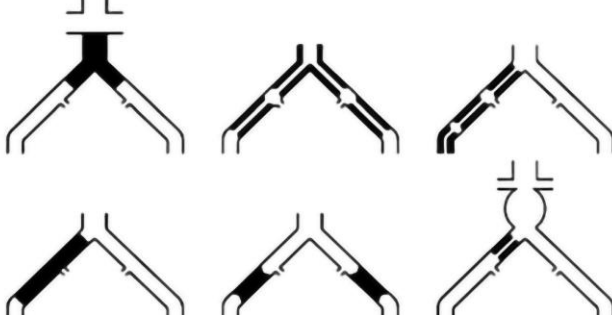
The velocity of the blood flow through stenosis increases significantly if the lumen is compromised by >50%. When this phenomenon occurs in the lower extremities, working muscles are short of oxygen supply, which results in ischemia and subsequent claudication.

In advanced cases, critical tissue ischaemia places the limb at risk, followed by tissue loss. However, critical limb ischemia (CLI) is seldom caused by AIOD alone. Commonly, in patients with CLI, multiple arterial segments are involved in occlusive atherosclerosis.

Three distinct arterial segments distal to the visceral bearing portion of the abdominal aorta may become diseased by atherosclerosis as follows [24]:

- Type I atherosclerosis involves the infrarenal aorta and the common iliac arteries only. The vessels distal to the common iliac arteries are normal or only minimally diseased. This pattern of atherosclerosis is observed in about 5–10% of the PAD patients and is more common in women than men.
- Type II atherosclerosis involves infrarenal aorta and the common and external iliac arteries and may extend into the common femoral arteries. This pattern is observed in 35% of the PAD patients.
- Type III atherosclerosis is the most severe form and the most common type. This pattern of atherosclerosis involves the infrarenal aorta and the iliac, femoral, popliteal and tibial arteries.

PAD is classified according to TASC, including AIOD and its updated version (2015) [42]. According to Figure 1-1, TASC lesion D is the most complicated type and classified as AIOD that is recommended for surgical revascularization according to TASC guidelines [42].

<p><b>TASC A lesions</b></p> <ul style="list-style-type: none"> <li>• Unilateral or bilateral CIA stenoses</li> <li>• Unilateral or bilateral single short (<math>\leq 3</math> cm) EIA stenosis</li> </ul>	
<p><b>TASC B lesions</b></p> <ul style="list-style-type: none"> <li>• Short (<math>\leq 3</math> cm) stenosis of the infrarenal aorta</li> <li>• Unilateral CIA occlusion</li> <li>• Single or multiple stenosis totaling 3 to 10 cm involving the EIA not extending into the CFA</li> <li>• Unilateral EIA occlusion not involving the origins of the internal iliac or CFA</li> </ul>	
<p><b>TASC C lesions</b></p> <ul style="list-style-type: none"> <li>• Bilateral CIA occlusions</li> <li>• Bilateral EIA stenoses 3 to 10 cm long not extending into the CFA</li> <li>• Unilateral EIA stenosis extending into the CFA</li> <li>• Unilateral EIA occlusion involving the origins of the internal iliac and/or CFA</li> <li>• Heavily calcified unilateral EIA occlusion with or without involvement of the origins of the internal iliac and/or CFA</li> </ul>	
<p><b>TASC D lesions</b></p> <ul style="list-style-type: none"> <li>• Infrarenal aortoiliac occlusion</li> <li>• Diffuse disease involving the aorta and both iliac arteries</li> <li>• Diffuse multiple stenoses involving the unilateral CIA, EIA, and CFA</li> <li>• Unilateral occlusions of both CIA and EIA</li> <li>• Bilateral EIA occlusions</li> <li>• Iliac stenoses in patients with AAA not amenable to endograft placement</li> </ul>	

**Figure 1-1** Inter-Society Consensus for the Management of Peripheral Arterial Disease (TASC) classification of aortoiliac lesions. AAA: abdominal aortic aneurysm; CFA: common femoral artery; CIA: common iliac artery; EIA: external iliac artery [42]. Reprinted with permission from Annals of Cardiovascular Disease, Tokyo, Japan.

### 1.1.2 Diagnosis

Physical examination of the patient with AIOD reveals weakened femoral pulses and a reduced ankle-brachial index (ABI). The diagnosis was verified by colour duplex ultrasound scanning, which revealed either a peak systolic velocity (PSV) ratio  $\geq 2.5$  at the site of stenosis and/or a monophasic waveform beyond the site. Multidetector CTA was used to determine the extent and type of occlusion, and valuable information regarding the patency of distal arteries to the lower limbs (e.g. femoral artery) is obtained. The presence of

collateral arteries in the pelvis is critical to maintaining blood flow and lower limb viability<sup>1</sup>. A combination of history, physical examination, duplex ultrasound scanning, and CTA are used to diagnose AIOD.

### 1.1.2.1 ABI

The ABI is the ratio of the systolic blood pressure (SBP) measured at the ankle, followed by that at the brachial artery [43]. The resting ABI is regarded as a reliable, non-invasive measurement to detect the presence and severity of the lower extremity PAD. It also determines the blood flowing by comparing the blood pressure in the legs to that in the arms in the supine position using a hand-held Doppler device [43-48]. Figure 1-2 illustrates the measurement, calculation and interpretation of ABI [45]. The blood pressure in the leg is determined by measuring the systolic pressure of posterior tibial and dorsalis pedis arteries in both ankles. The blood pressure in the arm is determined by measuring the systolic pressure of the brachial artery in both arms.

*ABI calculation:*

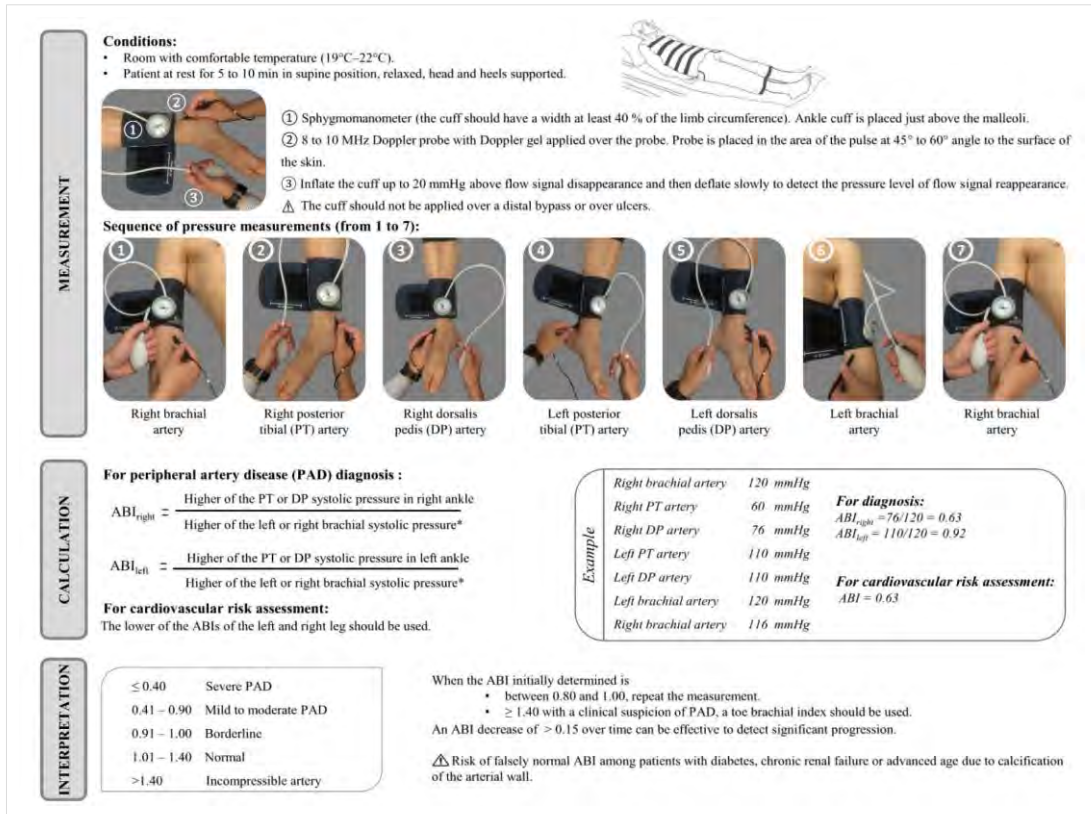
$$\text{Left ABI} = \frac{\text{Higher of the PT or DP systolic pressure in the left ankle}}{\text{Higher of the left or right brachial systolic pressure}} \quad (1.1)$$

$$\text{Right ABI} = \frac{\text{Higher of the PT or DP systolic pressure in the right ankle}}{\text{Higher of the left or right brachial systolic pressure}} \quad (1.2)$$

Although ABI measurement is recommended by AHA guidelines for patients with suspected AIOD and has proven to be a useful and reliable diagnostic tool, drawbacks, such as time-consuming measurement, special training and technical expertise are required for accurate results [49, 50]. An alternative to manual measurement of resting ABI is the recently developed automated, digital ABI based on blood volume plethysmography technology with the advantages of ease of use and speed [51-53]. In order to use this new technique, no special training is required and it can be conducted at a primary healthcare provider's office in three steps, outlined in Figure 1–3.

---

<sup>1</sup> [https://en.wikipedia.org/wiki/Aortoiliac\\_occlusive\\_disease](https://en.wikipedia.org/wiki/Aortoiliac_occlusive_disease) - cite\_note-diagnosis2-2



**Figure 1-2 How to measure, calculate and interpret the ABI.**  
 DP = Dorsalis pedis, PT = Posterior tibia [45]. Reprinted with permission from Elsevier Science and Technologies Journals, Amsterdam, The Netherlands.



**Figure 1-3 Digital ABI Measurement in three simple steps:**  
 (1) Measure both feet; (2) Measure both hands; (3) Print or upload Test Results<sup>2</sup>.  
 Reprinted with permission from Bard Peripheral Vascular, Inc, Tempe, USA

The diagnosis of PAD is confirmed if the traditional resting ABI reading is ≤0.9 or the digital ABI is ≤0.93. Such patients are at risk of early mortality from cardiovascular

<sup>2</sup> Source: <https://www.crbard.com/CRBard/media/ProductAssets/BardPeripheralVascularInc/PF10069/en-US/BPV-FLOC-1215-0007-1-v-1.1-QuantaFlo-Sell-Sheet.pdf>

causes (such as myocardial infarction, stroke and other vascular death). ABI can be used to grade the severity; a low ABI reading suggests severe PAD. However, since ABI is not sensitive to detect low-grade stenosis in the aortoiliac segment, a treadmill exercise test is recommended. Exercising muscles require a greater blood supply than resting ones; nonetheless, which will trigger claudication if the stenosis is severe is yet to be identified.

### 1.1.2.2 Doppler Ultrasound (DU)

Ultrasound is defined by the American National Standards (ANSI) as ‘sound at frequencies > 20,000 Hz (20 KHz)’. Typically, humans can detect and hear sound waves ranging from 20 Hz to 20 KHz. In air at atmospheric pressure of 101,325 N/m<sup>2</sup> (Pascal) or 760 mm Hg, ultrasound waves have a wavelength of ≤ 19 mm. The first use of medical ultrasound was published by Donald et al. in 1958 [54], and all subsequent improvements were enhancements of their groundbreaking work [55]. By the year 2000, colour Doppler was incorporated into medical ultrasound scanners to measure blood flow velocity in blood vessels with enhanced visualization [55]. DU is a non-invasive diagnostic imaging modality that is now routinely used to measure blood flow velocity in the cardiovascular system [56-58]. Usually, a 3–5 MHz B-mode linear or curved-linear probe incorporating a Doppler probe is used to measure the blood flow in vascular anatomy [59].

The Doppler principle states that the frequency of reflected ultrasound is altered by a moving target, in this case, red blood cells. The magnitude of this Doppler shift is related to the velocity of the blood cells, whereas the polarity of the shift reflects the direction of the blood flow towards (positive) or away (negative) from the transducer.

*The Doppler equation [60] is defined as follows:*

$$\Delta F = \frac{V \times 2F_0 \times \cos \theta}{c} \quad (1.3)$$

Where

$\Delta F$  = Doppler shift

$V$  = Velocity of moving target i.e. red blood cells (m/s)

$F_0$  = Transducer frequency (Hz)

$\theta$  = Angle of incidence (when solving Doppler equation,  $\theta$  is assumed 0° or 180° in cardiac application)

$C$  = Speed of sound in tissue, 1540 m/s

The blood flow velocity is derived from the Doppler equation as follows:

$$V = \frac{\Delta F \times c}{2F_0 \times \cos \theta} \quad (1.4)$$

Figure 1-4 shows a typical velocity measurement in the common iliac artery (CIA) post-stenting. The coloured section shows the location and size of the blood vessel being investigated, wherein blue represents one direction of flow and yellow, the opposite direction with respect to the probe. A  $\geq 50\%$  stenosis is defined as a DU peak systolic velocity ratio of  $\geq 2.5$  across the area of narrowing [17, 61-63].

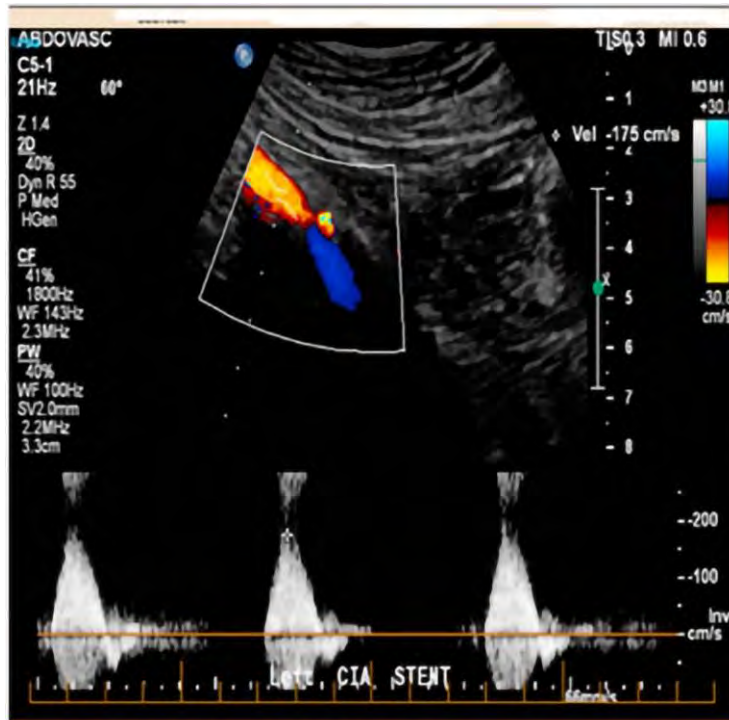
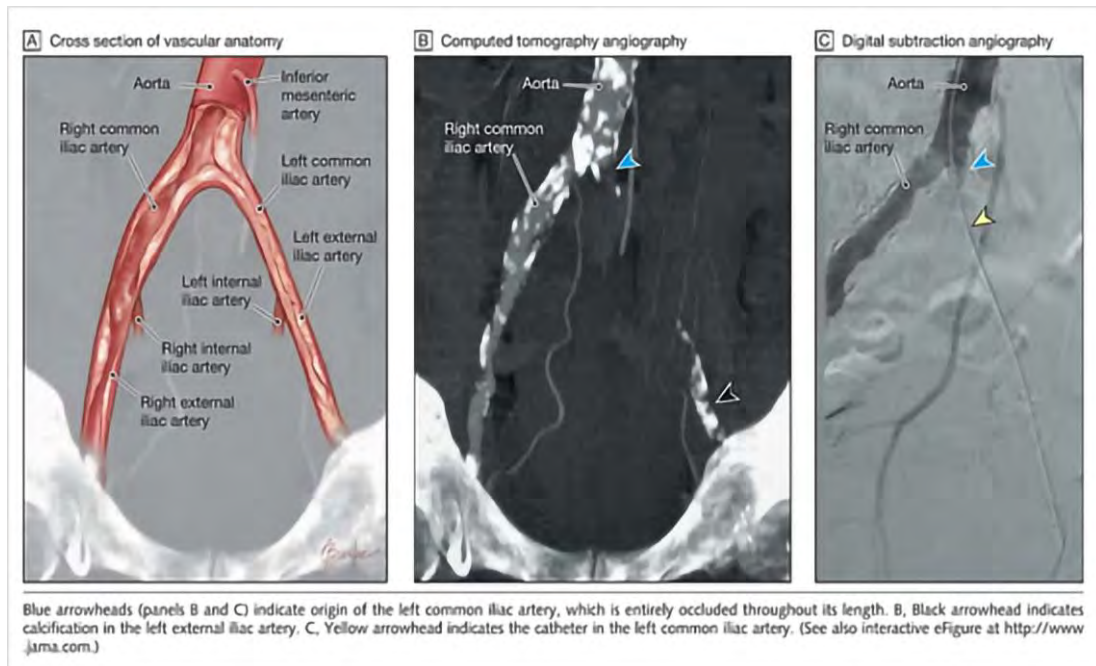


Figure 1-4 Velocity Measurement using a DU scanner [64]. Reprinted with permission from Elsevier Science and Technology Journal, Amsterdam, The Netherlands.

### 1.1.2.3 Computed Tomography Angiography (CTA)

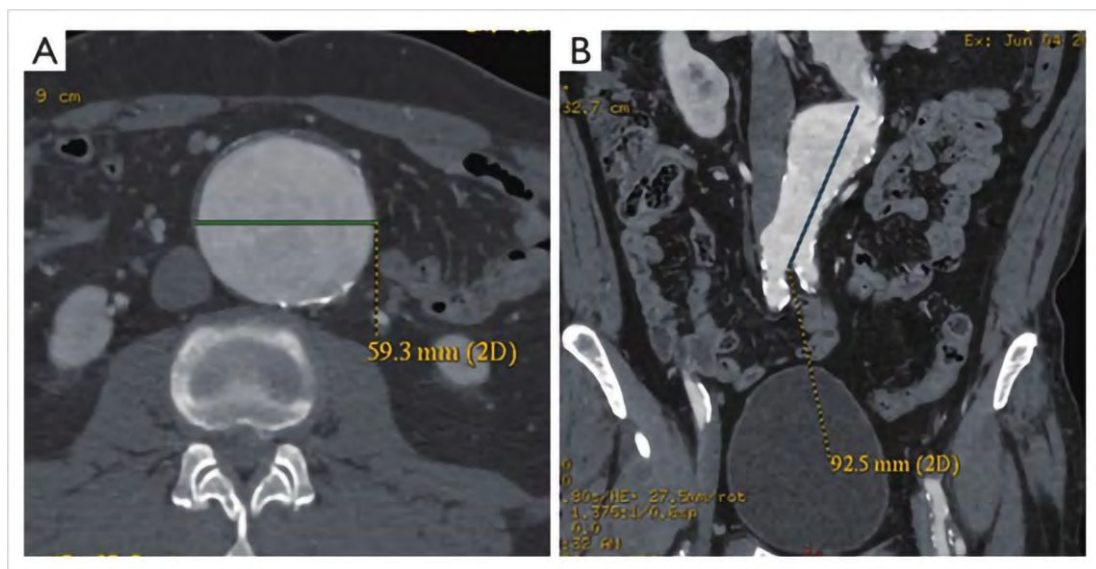
CTA is an imaging technique that uses CT to produce multiple two-dimensional (2D) cross-sectional images of blood vessels. It is an appropriate imaging modality for diagnosis and preoperative planning of EVT or open surgical treatment [65]. The three-dimensional (3D) images of the arterial system can be constructed using the 2D images acquired during CTA for visualization. The accuracy of the resulting 3D images is similar to those achieved from invasive angiography, i.e. digital subtraction angiography (DSA), which is an invasive procedure requiring arterial cannulation. However, with CTA, direct arterial cannulation is not required, thereby reducing the risk of investigation. Figure 1-5 illustrates the detection of severe calcification by CTA and DSA [66].





**Figure 1-5 CTA technique. (A) Cross-section of vascular anatomy. (B) Occlusion of the left common iliac artery (CIA) with severe calcifications detected by CTA and (C) DSA high-lighting the occlusion of left CIA [66]. Reprinted with permission from American Medical Association, Chicago, IL, USA.**

In addition, the CTA images can also be used to measure the regions of interest for preoperative planning purposes [67]. Figure 1-6 illustrates the measurement of the diameter and length in an aortic aneurysm based on 2D CTA images.



**Figure 1-6 Measurement with CTA. (A) Measurement of diameter; (B) Measurement of length [67]. Reprinted with permission from Nancy International Ltd, HK.**

### **1.1.3 Treatment options**

The goal of AIOD treatment is to reduce the severity of symptoms of claudication and prevent amputation in patients diagnosed with critical limb ischaemia (ischemic rest pain with or without tissue loss, such as gangrene or a nonhealing foot ulcer). Such patients require urgent evaluation and revascularisation by minimally invasive endovascular treatment or open surgery to prevent limb loss.

Some patients with AIOD may be asymptomatic. The Practice Guidelines Committee of the Society for Vascular Surgery (SVS) has developed specific practice recommendations for the treatment of asymptomatic AIOD and intermittent claudication (IC) in patients with atherosclerotic disease of the lower extremities. This programme centres on exercise and medical management of vascular disease, including smoking cessation, statin therapy and antiplatelet therapy (aspirin, clopidogrel or aspirin plus clopidogrel) [68]. In the case of AIOD patients with symptoms of IC, surgical treatment, or minimally invasive EVT can be considered depending on the severity of the disease and patient co-morbidities.

#### **1.1.3.1 Surgical treatments**

Surgical options for AIOD include direct aortic reconstruction [aortoiliac bypass, aortofemoral bypass (AFB), aortoiliac endarterectomy), which is the most durable procedure; however, it also presents significant morbidity and mortality. In addition, AIOD patients deemed to be at high risk for aortic surgery or with suitable anatomy or both, extra-anatomical bypasses [iliac-femoral (IFB), axillary-femoral (AxFB), femoral-femoral bypass (FFB)] are suitable alternatives with low morbidity but less durability [68].

#### **1.1.3.2 Minimally invasive endovascular treatments**

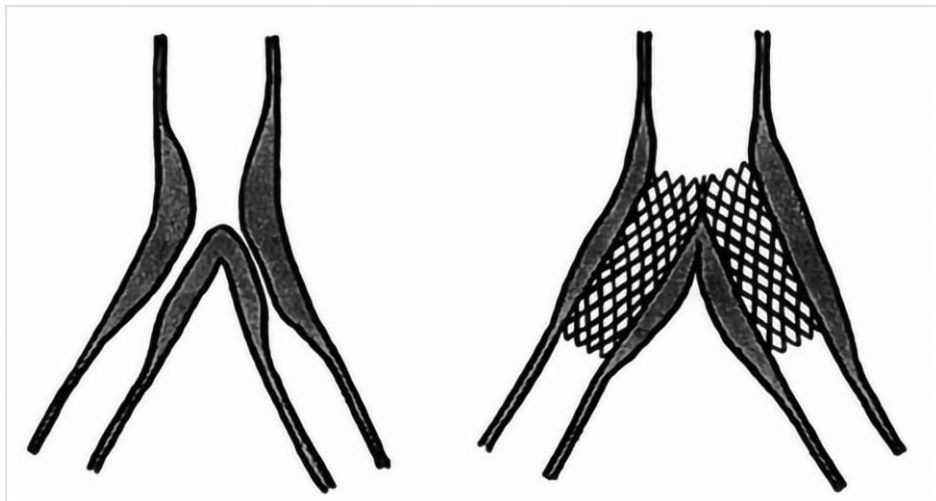
A significant paradigm shift has taken place in the last two decades with respect to the treatment of AIOD [6]. Although TASC guidelines previously recommended endovascular procedures as the primary treatment for focal disease and open surgery for advanced disease [7], improvements in endovascular techniques and novel and advanced technology has replaced open surgical bypass with EVT as the primary treatment for both focal and advanced AIOD in many cases. For minimally invasive EVT of iliac angioplasty using stents, long-term results are favourable with open surgery presenting a significantly low risk profile [7, 8]. Interestingly, new techniques, including covering long segments,

treating total occlusions and using covered stent-grafts [4, 5, 19], are alternatives to surgical reconstruction in patients with suitable anatomy.

Open surgery is now reserved for patients with previously failed endovascular interventions or patients with extensive disease and associated with aortic aneurysms that is deemed impossible to be treated by EVT.

#### **1.1.3.2.1 Kissing stents**

In 1991, the first kissing stent procedure was introduced by Palmaz to improve the treatment outcome of angioplasty of stenosis at aortic bifurcation [69]. This technique uses two stents, typically balloon-expandable, positioned at the two iliac origins distal to the aortic bifurcation and deployed simultaneously to avoid compromise of one or the other lumen (Figure 1-7). High technical success rate, primary patency and secondary patency have been achieved in treating TASC lesions A–D using this technique [3, 10, 70-73].



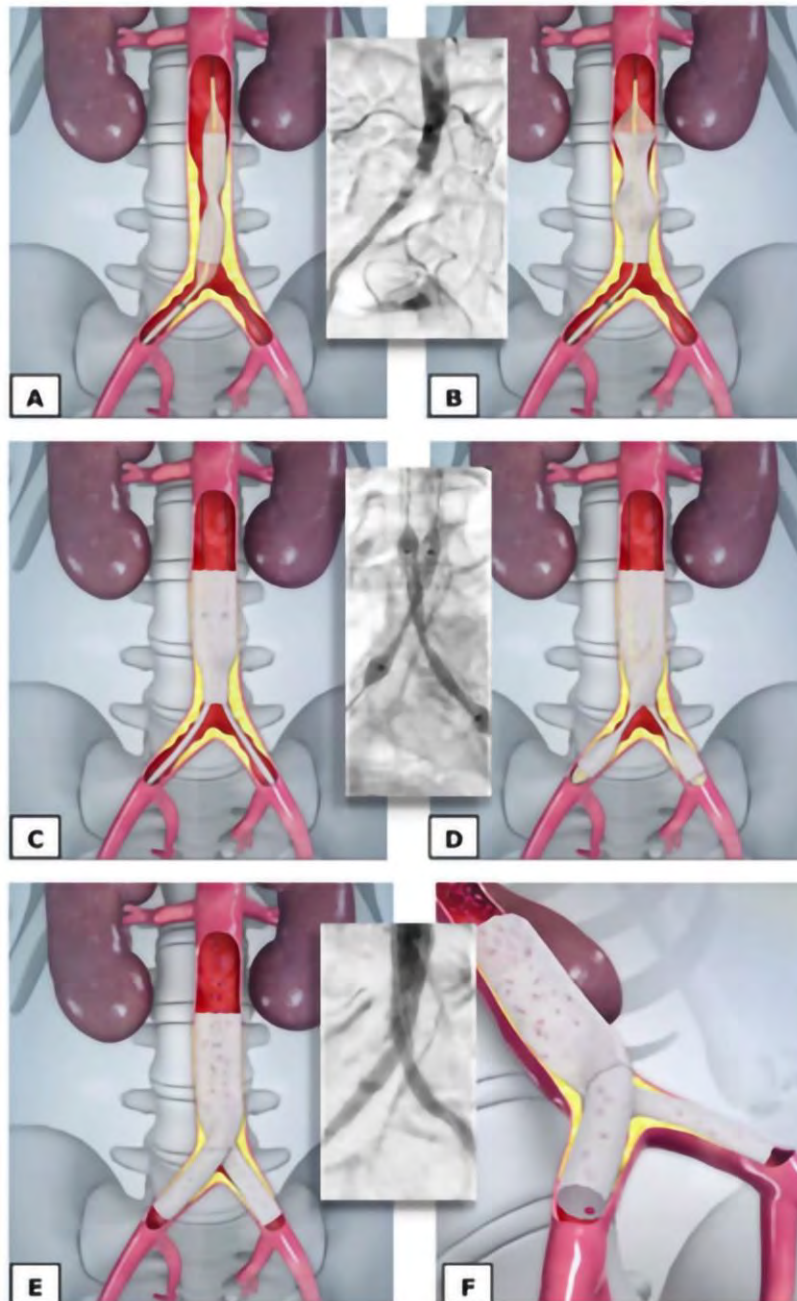
**Figure 1-7** Schematic representation of atherosclerotic stenosis predominantly affecting the aortic bifurcation and origin of the iliac arteries. Bilateral stents placed with the cephalic ends contacting in the midline provide support for the most distal portion of the aortic wall [69]. Reprinted with permission from Elsevier Science and Technology Journal, Amsterdam, the Netherlands.

#### **1.1.3.2.2 Covered endovascular reconstruction of aortoiliac bifurcation (CERAB)**

Groot Jebbink et al evaluated the geometry of kissing stents used to recreate the aortic bifurcation. The study suggested that the patency might be adversely affected by the mismatch between the stented lumen and the aortic lumen [74]. Also, the radial mismatch might give rise to disturbances that might result in the formation of thrombus. Thus, the

findings suggested that a different technique such as CERAB is suitable for recreating the aortic bifurcation.

The CERAB technique is an anatomical approach to reconstruct the aortic bifurcation and reduces the radial mismatch that is inherent with the traditional kissing stent treatment [75]. In the CERAB configuration, three covered stents are used, wherein a covered stent is initially positioned about 15–20 mm above the aortic bifurcation, and a large balloon is used to inflate the stent against the aortic wall. A funnel may be created at the proximal extent by gentle overdilation. Two iliac covered stents are subsequently positioned at the distal end of the aortic funnel and deployed simultaneously. Consequently, a newly formed bifurcation is created with a tight seal between the aortic and iliac stents as shown in Figure 1-8.



**Figure 1-8** Step-by-step process of the covered endovascular reconstruction of the aortoiliac bifurcation (CERAB) technique: A: Placement and expansion of a 12-mm diameter balloon-expandable as V12 covered stent-graft in the distal aorta (through a 9 Fr introducer). B: Post-dilation of the proximal 12-mm V12 stent to the diameter of the native aorta. C: After optimal positioning ( $\pm 20$  mm above the bifurcation) and complete expansion, the distal end of the stent becomes funnel-shaped. Bi-lateral V12 covered stent-grafts are then placed in this conic segment, in a 'kissing-stent' configuration. D: Simultaneous inflation of the bilateral stents. E and F: A tight seal is then formed between the bilateral iliac stents and the aortic stent, simulating a new bifurcation with the hemodynamic aspect of an aortobifemoral prosthesis or 'flow splitter' of an EVAR prosthesis [75]. Reprinted with permission from The Journal of Cardiovascular Surgery, Torino, Italy.



### 1.1.3.2.3 *AFX Unibody stent-graft*

An alternative to CERAB for treating AIOD is to use a single unit or unibody and a low profile covered stent to reconstruct the aortoiliac bifurcation. One such device is manufactured by Endologix and commercially known as the AFX Unibody Stent-graft. It was originally designed for the treatment of aortic aneurysms and has been used in AIOD as it maintains the bifurcation anatomy for future access. Figure 1-9 shows CTA images on the left (A) severe stenosis and CTA image on the right (B) patency after deployment of AFX stent. A recent study by Maldonado et al. described the largest patient cohort of AIOD patients treated with AFX stents [21]. Then, a total of 91 patients were evaluated in the retrospective study. The primary patency rate was > 90%, the primary assisted patency rate was > 98%, and the secondary patency rate at 2 years was > 100%. Notably, 82% of these patients were diagnosed with TASC D lesions, and the remaining 1%, 13% and 4% exhibited type A, B and C lesions, respectively.

One of the limitations of the AFX stent is that adjunctive stent might be required for patients with heavily calcified lesions due to its weak radial force. In this study, 59% of the patients required adjunctive stenting using balloon-expandable stents. Despite this limitation, it appears that AFX is still a reasonable choice, especially for patients who are not suited for open surgery.

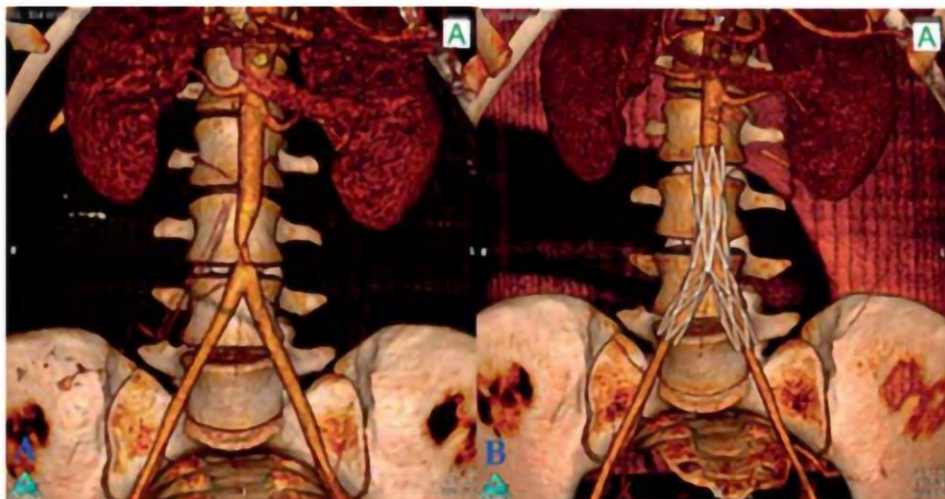


Figure 1-9 CTA Images (A) before and (B) after deployment of AFX stent [20, 21]. Reprinted with permission from ProLitteris, Zurich, Switzerland

## 1.2 Hypothesis of the research

Significant advances were detected in endovascular treatment of aortoiliac occlusive disease since its introduction in the 1990s [69, 76-80], especially in the recent decade when sophisticated techniques [5, 8, 9, 12-15, 17, 19, 21, 22, 72, 75, 81-83] have emerged. The primary issues of endovascular treatment are that vascular surgeons are now inundated with choices of endovascular techniques. In addition, enhanced diagnostic or screening tools are needed to help clinicians improve the monitoring of patients during follow-ups. Since it is impractical to conduct experiments on live patients due to safety concerns; therefore, we aimed to test the hypothesis that computational and in vitro approaches can add new knowledge to this research area. Importantly, these approaches need to be developed for clinical applications, so that patient safety is not compromised.

## 1.3 Objectives

The main objectives of the present work are outlined below:

- to investigate an appropriate approach allowing for accurate assessment of haemodynamic changes following treatment in patients with AIOD.
- to analyse and compare the haemodynamics of CERAB configuration and AFX stent-graft using laser particle image velocimetry (PIV) experiments to understand the flow characteristics of these two endovascular techniques and prove the hypothesis that AFX stent-graft is a superior technique in treating extensive AIOD.
- to develop a novel roller pump for physiological flow to overcome one of the limitations of the existing flow loop used in the laser particle image velocimetry (PIV) experiment.
- to validate the computational fluid dynamic method as a viable haemodynamic assessment tool in comparison to the experimental method.

Stents and stent-grafts alter the haemodynamics according to their size, shape, stiffness, and interaction with the vessel wall. Therefore, interpreting the findings of duplex ultrasound surveillance after the procedure is used by clinicians to assess patency and identify restenosis. The main objective of this thesis is to investigate an appropriate approach allowing for accurate assessment of the haemodynamic changes following treatment in patients with AIOD. Computational fluid dynamics (CFD) allow the investigation of local haemodynamics at a level not that might be inaccessible with experimental techniques or in vivo studies. Velocity flow fields are the main outputs from CFD analysis. In order to

achieve the first objective, a screening tool was developed to supplement the gold standard of restenosis of velocity ratio  $> 2.5$  between proximal and distal velocities of the stented artery. The data obtained from CFD simulations of ideal aortoiliac geometry and design of the experimental method were used to develop a PSV predictor to screen for possible restenosis. The predicted PSV was compared to DU that measured maximum PSV. If accurate, it could be used as a clinical diagnostic tool to help clinicians decide whether CTA is warranted in cases with high PSV detected during the follow-ups.

The second objective of this thesis is to test the hypothesis that AFX stent-graft is a more superior endovascular technique for treating extensive AIOD than the CERAB configuration due to its one-piece design that eliminates the radial mismatch. Maldonado et al. [21] suggested that the unibody and low profile AFX stent-graft has several advantages, such as, preserve the aortic bifurcation, avoid limb competition in the distal aorta, facilitate future endovascular interventions, and protect against potentially fatal aortoiliac rupture in heavily calcified lesions. A haemodynamic comparison would be valuable in identifying the best stent. In order to achieve this objective, laser PIV experiments were performed to obtain the flow pattern, TAWSS, OSI and RRT in aortoiliac flow phantoms deployed with modified transparent AFX stent-graft and CERAB configuration for haemodynamic comparison. WSS measures the blood flow-induced shear stress acting on the arterial wall, whereas OSI measures the degree of disturbed flow along the vessel wall. In addition, relative residence time (RRT) derived from time-averaged WSS (TAWSS), and OSI can be used to identify the putative localization of plaques [84]. Low TAWSS and high OSI have been directly implicated in the pathogenesis of atherosclerosis [27, 31, 85, 86], and therefore, CFD analysis of these parameters will provide clues to the potential site of restenosis.

The third objective was to address one of the limitations of the PIV experimental set-up. The flow phantoms used in the PIV experiments incorporated two renal branches such that physiological infrarenal flow profile could be achieved by applying a suprarenal flow profile at the inlet of the flow phantom by adjusting the flow resistance and compliance at the outlets. However, the unintended consequence was that the laser sheet was partially obscured by the renal branch of the AFX phantom, resulting in partial illumination of the inflow region. A novel roller pump has demonstrated its ability to overcome this limitation.

The fourth objective was to perform a hemodynamic comparison of PIV and CFD methods on a flow phantom deployed with a modified transparent AFX stent-graft in order to validate the CFD model for future clinical applications.



## 1.4 Thesis Overview

Chapter 1 is an introduction to aortoiliac occlusive disease, its background, classification, diagnosis, treatment options with a focus on minimally invasive EVTs, and their benefits and drawbacks are discussed. In this chapter, the objectives of the thesis and the thesis overview are also presented.

In Chapter 2, a blood flow velocity prediction in aortoiliac stent grafts using computational fluid dynamics and Taguchi method is presented. The maximum PSV predictor was developed based on idealized geometries. The predictor was evaluated using 16 patient-specific Perth cohort cases. It was concluded that the predictor used as a screening tool in the retrospective study could avoid some CTAs with the associated cost and risks.

In Chapter 3, the PSV predictor was tested on a larger sample size of 25 patients from the Netherlands collaborators, only 42% of Arnhem cohorts would have avoided CTA even after manual adjustment of iliac asymmetry and flow split based on the ratio of ABIs between left and right limbs.

In Chapter 4, CFD simulations were performed incorporating fluke angle, stent height and anteroposterior angle in the aortoiliac model. The effects of these geometric parameters on PSV were evaluated.

In Chapter 5, details of a large design of experimental study based a 3-level Taguchi orthogonal array L27 are presented. It was used to study the effect of three additional independent variables, i.e. iliac asymmetry, average ABI, ABI ratio and their interactions on PSV. The improved predictor was tested, and the data are presented and discussed.

In Chapter 6, hemodynamic comparisons of AFX stent-graft and CERAB configuration based on the results of laser PIV experiments were used to test the hypothesis that the AFX stent-graft is a more superior endovascular technique in treating extensive AIOD when compared to CERAB configuration. Flow patterns at inflow and bifurcation regions for AFX stent-graft and CERAB configuration were presented and discussed, followed by TAWSS, OSI and RRT comparisons. Student t-tests were used to conclude whether there were any significant differences between the two endovascular techniques. Limitations of the PIV experiments were also discussed, and future investigations recommended.

In Chapter 7, a novel pulsatile pump based on a modified roller pump design is presented. Its ability to generate infrarenal flow profile has the potential to overcome one of the

limitations of the PIV experimental set-up highlighted in Chapter 6. It also has the potential to simplify the PIV flow circuit significantly by eliminating the two renal branches of the aortoiliac model. In addition, the measured flow profiles generated by the novel pump for three types of vascular flows, carotid, suprarenal and infrarenal, matched well with reference flow profiles deemed suitable for benchtop testing of physiological flow. The associated patent filing document for the novel roller pump is described in Appendix F and Appendix G.

In Chapter 8, CFD simulations were performed by modelling the laser PIV experimental set-up of the aortoiliac phantom deployed with a modified transparent AFX stent-graft as outlined in Chapter 6. The haemodynamic parameters, including flow pattern, TAWSS, OSI and RRT, were compared to validate the CFD model for future clinical applications.

Finally, in Chapter 9, the main conclusions were drawn, and future directives were proposed to explore opportunities that would improve clinical outcomes of the endovascular treatment of AOID.



2

Blood Flow Velocity Prediction in  
Aortoiliac Stent Grafts using  
Computational Fluid Dynamics and  
Taguchi Method

## Preamble

One of the challenges with the use of new stent graft is the fact that the hemodynamic changes as a result of the implanted device cannot be evaluated in vivo with the standard protocol. Even though the patency of the stent graft can be assessed real-time during EVT with the aid of X-ray fluoroscopy, it is not possible to obtain flow pattern and other hemodynamic parameters such as WSS or OSI in vivo. Current guidelines to assess restenosis is velocity index greater the 2.5

In the case of CERAB, there is anecdotal evidence in centres here in Australia as well as other centres in Europe including Belgium and the Netherlands that follow up velocity measurements using DU scanner sometimes show high velocity in the stented region but it is not necessarily caused by restenosis. Our aim is to develop a non-invasive PSV prediction tool to supplement the velocity index criterion to better understand the 'new normal' post CERAB procedure.

This published journal paper begins with an abstract that summarizes the research topic, its main objective, methodology, results and conclusions. Outlined in the main section where material and method used to develop the PSV predictor was described in detail. Results section shows the strength of each independent variable and its effect on the dependent variable PSV. The relationship between PSV and the independent variables are expressed in the predictor formula. The predictor was evaluated using sixteen patient data. In the appendices, supplementary materials are provided for Taguchi method, Design of Experiment and Computational Fluid Dynamics.

## 2.1 Introduction

Cardiovascular disease (CVD) is a leading cause of death globally. In Australia, it accounted for 34% of all deaths in 2008[87]. Peripheral arterial disease (PAD) is part of a broad spectrum of atherosclerotic cardiovascular diseases that affect the coronary, cerebrovascular, visceral, aortoiliac, and infrainguinal vascular bed. PAD affects 8 to 10 million people per year in the United States alone [88]. AIOD is a subset of PAD involving an atherosclerotic occlusion of the infra-renal aorta, common iliac arteries, or both. Treatment of AIOD can be performed either via open surgical repair or by minimal invasive endovascular stenting. Most physicians are now using endovascular approaches to treat most levels of AIOD [17, 24] with covered or bare stents. There are several configurations available; some include the newer technique of relining the entire bifurcation with stents (Covered Endovascular Reconstruction of the Aortic Bifurcation (CERAB)). Recent studies indicate good patency and clinical outcome with covered stents [15, 17, 18, 89]. While CERAB has proven to be effective in treating AIOD[17], its hemodynamic effects are not fully understood. There are instances where measurements using ultrasound indicate higher than expected  $PSV_{max}$  usually indicating stenosis, but subsequent CTA reveals excellent patency and absence of restenosis. To address similar concerns, CFD and predictive value of PSV were evaluated and in some cases, treatment plans were proposed for clinical applications [90-93]; and to address our specific issue, a  $PSV_{max}$  predictor was developed using CFD, Taguchi method and Multiple Linear Regression (MLR) with the aim of defining the “new normal” post CERAB and avoiding the requirement for CTA during follow up..

## 2.2 Methods

### 2.2.1 Design of Experiments

Taguchi orthogonal array (OA) takes the form  $L_a(B_c)$ . The ‘a’ subscript of Latin square L represents the number of experimental runs or simulations. B is the number of levels in each column and its c exponent is the number of columns in the array. Design Of Experiments using Taguchi method can help researchers significantly reduce the time required for experimental or simulation investigations.  $L_{16}(2^{15})$  was used by Qi et al [94] to analyse the sensitivity of a middle ear finite-element model from nine parameters whereas  $L_8(2^4)$  was used by Trabelsi et al [95] to study the influence of four control factors and their interactions on Vero cell growth in vaccine production and  $L_{12}(2^{11})$  was applied on a Skin Burn Injury Prediction model from 11 control factors by Autrique and

Lormel [96]. In our studies, L8 ( $2^7$ ) was used to analyse the effects of three control factors namely, infra-renal inlet velocity PSV (PSV<sub>in</sub>), iliac to aortic area ratios (R) and aortoiliac bifurcation angles( $\alpha$ ); and their two-way interactions on PSV<sub>max</sub> in a human aortoiliac bifurcation. Appendix A provides a detailed description of Design Of Experiments planning, OA selection, and design of the simulation studies.

## 2.2.2 Computational Fluid Dynamics (CFD)

Computer Aided Design (CAD) software SolidWorks (Dassault Systems, Velizy, France) and Ansys SpaceClaim (ANSYS, Canonberg, PA, USA) were used to create idealized 3D CAD models to mimic the lumen at the aortic bifurcation treated with CERAB using Atrium V12 stents manufactured by Atrium Medical Corporation (Hudson, New Hampshire, USA). The 3D CAD models were built based on realistic models of still and X-ray images from Groot Jebbink et al [74] and the overall geometrical dimensions were derived from Grimme[17]. Surface meshes were created from 3D CAD models using ANSYS 17.0 Fluent meshing tool and subsequently discretised into polyhedral elements.

The governing equations of the fluid domain were computationally solved using ANSYS Fluent 17.0, a finite volume method CFD solver. Cardiac blood flow was simulated based on the following realistic physiological conditions:

- Blood density of 1060 kg/m<sup>3</sup>
- Blood Flow was considered to be laminar, incompressible and isotropic.
- Blood was assumed to be a Non-Newtonian Fluid, its viscosity was estimated using the Carreau Model[97] where  $\lambda = 3.313$  s,  $n = 0.3568$ ,  $\mu_0 = 0.056$  pa-s,  $\mu_\infty = 0.0035$  pa-s
- Non-slip conditions were applied at the artery walls
- Triphasic pulsatile waveform was applied at the inlet which was obtained from Fraser et al [98] based on 21 subjects via User Define Function(UDF) in ANSYS Fluent.
- An entrance length equal to nine times the inlet diameter of 20mm (9 x 20 mm =180 mm) was introduced to obtain a realistic velocity profile in the infra-renal aortic region[99].
- The exit length was set at 200 mm which is more than 16 times outlet diameter (D)[100] so that the flow can return to a nearly fully developed state and that the outlet boundary does not affect the upstream flow.
- A constant gauge pressure of 100 mmHg (13332 Pa) was applied at the outlets [98]

Based on an average 5L/min cardiac output, 70% of blood flow to the descending aorta resulting in 58 mL/s flow rate, an inlet internal diameter of 2.5 cm, dynamic viscosity of 4.2 mPa.s and density of 1060 kg/m<sup>3</sup> for the blood; Reynold's number of 891 suggests that the vascular blood flow in the region of interest is laminar. CFD simulations were conducted on polyhedral volume mesh as shown in Figure 2-1, generated from idealized geometry according to the parameter setting as outline in Appendix A, Table A.3. Steady state simulation was first performed using laminar model and a semi-implicit SIMPLEC solution method in ANSYS FLUENT 17.0 solver with default solution controls. Under relaxation factors for pressure and momentum were fine-tuned to 0.36 and 0.78 respectively to reduce the number of iterations to reach steady state convergence and were found to be optimal and subsequently used in all simulations. Transient simulation with bounded second order implicit method, 0.01 second fixed time-step were used and a total of three cardiac cycles ( $3 \times 0.93s$ ) = 2.79s or 279 number of time-steps were performed for each simulation.



**Figure 2-1 Polyhedral Volume Mesh**

Appendix B outlines the details of inlet boundary condition, determination of entrance length, grid independence and periodicity convergence tests.

### 2.2.3 Acquisition of Patient Specific Data

All patient data were de-identified in compliance with Human Research Ethics requirements. Retrospective patient spectral Doppler data for infra-renal aortic PSV<sub>in</sub> and intrastent PSV<sub>max</sub> from common iliac arteries were obtained using Philips CX50 Ultrasound Machine (Philips Healthcare, Amsterdam, Netherlands) with a 5-1 MHz curved probe operating in pulsed wave mode. Figure 1-4 shows a typical measurement of CIA velocity.

The associated CTA images for the aortoiliac bifurcation were obtained using GE Medical System LightSpeed VCT CT Scanner (GE Healthcare, Chicago, Illinois, USA) with 512 x 512 resolution and 0.625mm slice thickness. From the CTA images, linear and angular measurement tools in InterViewer software version 4.9.1-P132 (Intelrad Medical Systems, Montreal, Quebec, Canada) were used to determine bifurcation angle ( $\alpha$ ), aortic diameter and left and right iliac diameters as shown in Figure 2-2. The aortic diameter was measured immediately below the two renal arteries whereas the iliac diameters were measured just before they branched into the external and internal iliac arteries. To minimize measurement error, six sets of measurements per patient were taken. The first set of measurements were taken from the front coronal plane and two subsequent sets of measurements from adjacent rotated slices. Likewise three more sets of measurements were taken from the back coronal plane. The iliac to aortic area ratio (R) were then calculated as  $(D_2^2 + D_3^2)/D_1^2$ , as defined in Appendix A, Figure A.1.

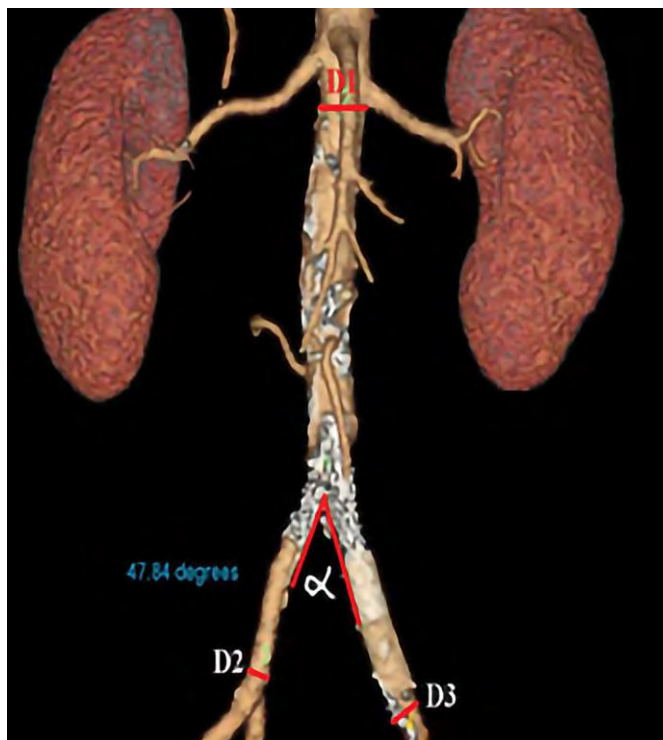


Figure 2-2 Angle and Diameters Measurements



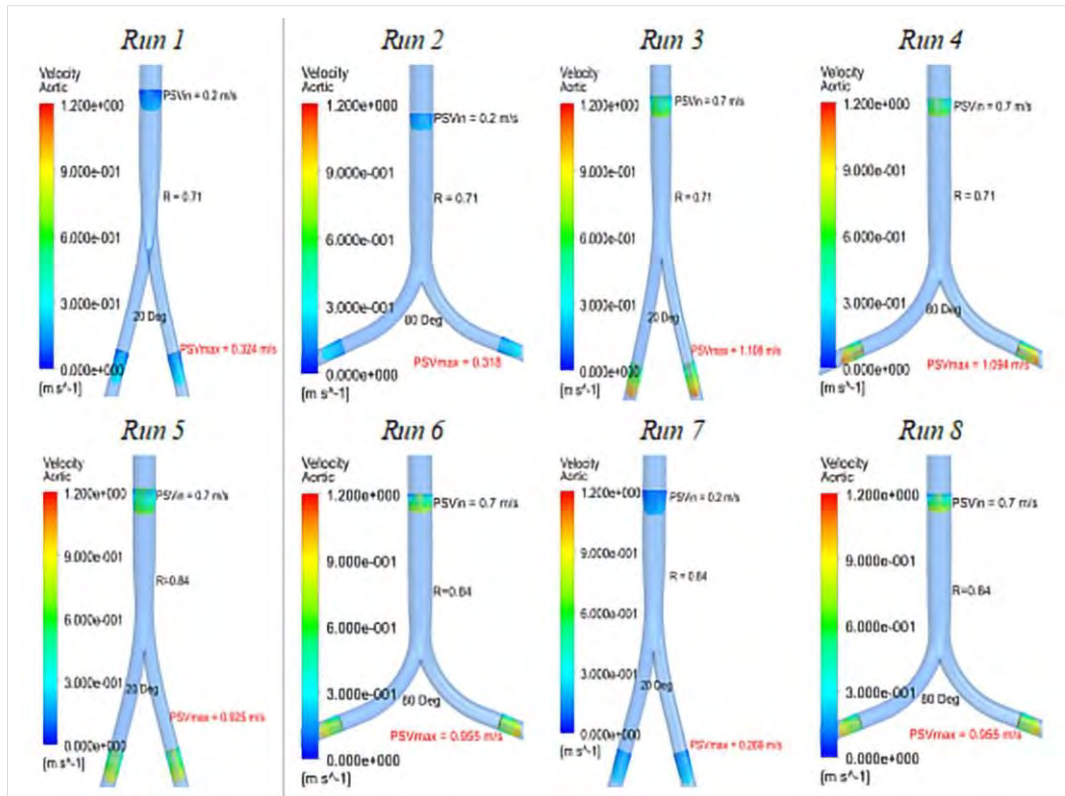
#### 2.2.4 Statistical Analysis

In statistics, multiple linear regression (MLR) is an approach for modelling the relationship between a dependent variable and two or more independent variables. In our studies, SPSS version 23, a statistical analysis software from IBM (Armonk, New York, United States) was used to establish a mathematical function between dependent variable PSVmax and independent variables PSVin, R and  $\alpha$ . A simple linear function MLR model with step-wise elimination method was applied. The constant and coefficients from the MLR output were used to determine the relationship between the dependent variable PSVmax and independent variables PSVin, R and  $\alpha$ . Subsequently, an exponential function was applied. Adjusted R<sup>2</sup>, a measure of Goodness of fit was used to compare how well the independent variables describe the model where 1 is perfect fit. The purpose of the ANOVA is to determine which independent variable, or interactions between independent variables, significantly affect the dependent variable. In addition to Degree Of Freedom, Sum of Squares (SS) and Mean of Squares (MS), F-Ratio, p-value and Contribution (C %) associated with each independent variable was reviewed. The ANOVA was performed for a confidence level of 95%. The p-value for each independent variable was calculated and it must be less than 0.05 to be statistically significant.

## 2.3 Results

### 2.3.1 CFD Simulation Results

Figure 2-3 below shows the results of PSV<sub>max</sub> taken at the peak of the third cardiac cycle at time-step 2.0 second as described in Appendix B.



**Figure 2-3** CFD Simulation Results: Simulation Run 1 to 8 arranged according to L8 Orthogonal Array showing independent variable peak systolic velocity (PSV<sub>max</sub>) by varying independent variables Inlet peak systolic velocity (PSV<sub>in</sub>) 0.2 m/s vs 0.7 m/s, Iliac to Aorta area ratio 0.71 vs 0.84, bifurcation angle 20° vs 80°.

#### 2.3.1.1 Signal to Noise Ratio Main Effects

In Taguchi method, Signal to Noise (S/N) ratio, a measure of robustness, is used to identify control factors that reduce variability in a product or process by minimizing the effects of uncontrollable factors (noise factors). In our current studies, PSV<sub>max</sub> is considered as larger the better attribute and S/N of

$$PSV_{max} = -10 \cdot \log (1/PSV_{max} \cdot PSV_{max}).$$

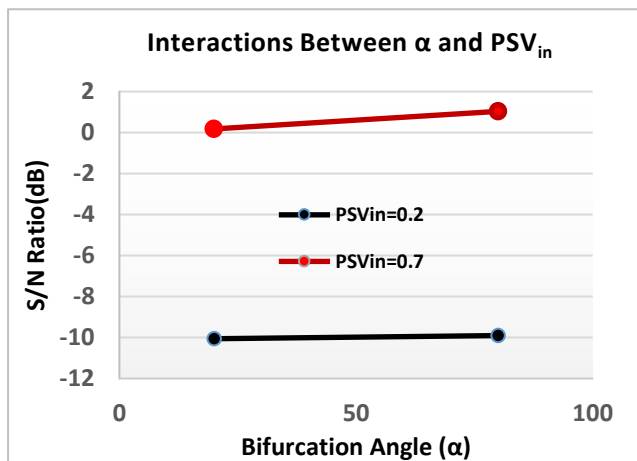
The averages or means of the S/N ratio of PSV<sub>max</sub> for each level of control factor. are shown in Table 2-1 Delta is defined as the difference in responses at level 1 and 2; larger Delta implying greater effect of control factor on PSV<sub>max</sub>. PSV<sub>in</sub> with a Delta of 10.465 ranks the highest followed by R with 1.836 and  $\alpha$ .with 0.593.

**Table 2-1** Response table of main effects

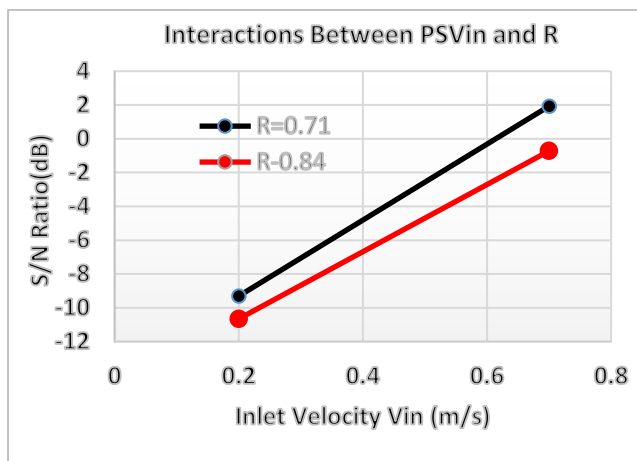
Control Factor	Mean Value		Delta	Rank
	Level 1	Level 2		
A PSV <sub>in</sub> (m/s)	-9.829	0.634	10.465	1
B R	-3.679	-5.515	1.836	2
C $\alpha$ (Degree)	-4.893	-4.300	0.593	3

**2.3.1.2 Interaction Effects**

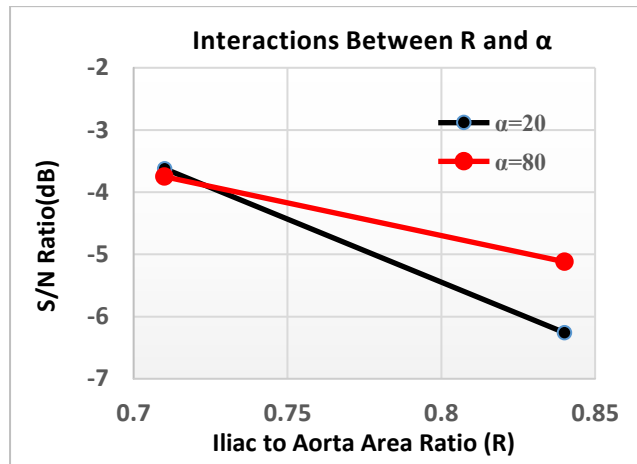
Figure 2-4 to Figure 2-6 show the effects of 2-way interaction between the three control factors. The parallel plot indicates that there is little or no interaction, whereas the size of the angle where the two lines intercept each other indicates the strength of interaction between the two control factors. In our case, there are no interaction effects for 2-way interactions between  $\alpha$  and PSV<sub>in</sub>; and between PSV<sub>in</sub> and R whereas there is a weak interaction effect between R and  $\alpha$ .



**Figure 2-4** Interactions between  $\alpha$  and PSV<sub>in</sub>



**Figure 2-5** Interactions between PSV<sub>in</sub> and R

Figure 2-6 Interactions between R and  $\alpha$ 

### 2.3.1.3 Analysis of Variance

Table 2-2 shows the results of ANOVA for S/N ratio of PSV<sub>max</sub>. Independent variables PSV<sub>in</sub> and R were found to be significant with p-values of 0.000228 and 0.046 respectively. Whereas the p-values of independent variable  $\alpha$ , 2-way and 3-way interactions were found to be greater than 0.05 therefore were deemed to be insignificant. The contributions were in the following order: PSV<sub>in</sub> (94.06%), R (3.36%) and the 3-way interactions among PSV<sub>in</sub>, R and  $\alpha$  (1.57%).

Table 2-2 ANOVA table for S/N ratio of PSV<sub>max</sub>

Factor	Degree Of Freedom	Sum of Square	Mean Square	F	p-value	Contribution (C %)
V <sub>in</sub>	1	224.19	224.19	159.04	0.000228	94.06
R	1	8.0137	8.0137	5.6849	0.045635	3.36
$\alpha$	1	0.5108	0.5108	0.3624	0.579657	0.21
PSV <sub>in</sub> xR	1	0.8479	0.8479	0.6015	0.481310	0.36
Rx $\alpha$	1	0.8038	0.8038	0.5702	0.492208	0.34
$\alpha$ xPSV <sub>in</sub>	1	0.2463	0.2463	0.1747	0.697392	0.10
PSV <sub>in</sub> xRx $\alpha$	1	3.7406	3.7406	2.6536	0.178649	1.57
<b>Error</b>	<b>0</b>	<b>0</b>				
<b>Total</b>	<b>7</b>	<b>238.35</b>				
<b>(Error)</b>	<b>4</b>	<b>5.6386</b>	<b>1.4097</b>	<b>1.0000</b>		<b>2.37</b>

### 2.3.1.4 Predictive Models

Mathematical models are useful tools to determine the relationship between a dependent variable and multiple independent variables and can therefore serve as predictive models. MLR analysis using SPSS was first applied to linear function. From

the output of SPSS MLR analysis, the independent variable  $\alpha$  was ignored after step-wise elimination due to its insignificance. The constant was 0.684 and the coefficients for  $PSV_{in}$  and  $R$  of the predictive model were 1.461 and -0.894 respectively. Its equation was identified as follows:

$$PSV_{max}\text{-hat} = 0.684 + 1.461PSV_{in} - 0.894R \quad (2.1)$$

Where:

"-hat" stands for predicted value. Adjusted  $R^2$  for the linear model was 0.991.

Two way interactions and  $\alpha$  were ignored when investigating exponential function since they were found to be insignificant in section 3.1.3. The exponential equation was postulated as:

$$PSV_{max} = C \cdot PSV_{in}^x \cdot R^y \quad (2.2)$$

$$\ln(PSV_{max}) = \ln(C) + x \cdot \ln(PSV_{in}) + y \cdot \ln(R) \quad (2.3)$$

$\ln(PSV_{max})$  was then considered as the dependent variable whereas  $\ln(PSV_{in})$  and  $\ln(R)$  were considered as independent variables. MLR analysis was then performed and SPSS yielded constant  $\ln(C) = 0.117$ , therefore  $C = e^{0.117} = 1.124$ , whereas coefficients for  $\ln(PSV_{in})$  and  $\ln(R)$  were 0.989 and -0.979 respectively therefore the predictive equation was identified as follows:

$$PSV_{max}\text{-hat} = 1.124 PSV_{in}^{0.989} \cdot R^{-0.979} \quad (2.4)$$

Adjusted  $R^2$  for the exponential function MLR model was found to be 0.999 which was a 0.8% improvement from using linear function.

### 2.3.2 Measurement Results of Patient Data

Sixteen sets of Doppler Ultrasound Scanner and CTA images were provided by collaborating surgeons in Western Australia for retrospective evaluation. All CTA images were with 0.625mm slice resolution suitable for evaluation. Diameter and angle measurements as described in section 2.3.3 were performed on these CTA images. Table 2-3 shows patient data with  $R$  on column 5, bifurcation angle  $\alpha$  on column 6 and  $PSV_{in}$  on column 7.

**Table 2-3 Patient data**

Patient Number	Measurements from CTA Images					Ultrasound Measurements
	Aorta Diameter (Pixels)	Right Iliac Diameter (Pixels)	Left Iliac Diameter (Pixels)	Iliac to Aortic Area Ratio ( $R$ )	Bifurcation Angle $\alpha$ (Degree)	Infra-renal Aortic velocity, $PSV_{in}$ (m/s)
1	24.82	12.27	16.16	0.67	47.27	1.00
2	11.25	7.44	6.18	0.74	47.81	0.89
3	5.73	3.74	3.87	0.88	34.41	1.75
4	12.12	6.12	5.57	0.47	39.78	0.58
5	31.59	18.71	18.12	0.68	37.04	0.77
6	15.95	8.03	7.74	0.49	53.73	0.54
7	11.52	7.51	7.52	0.85	51.81	1.35
8	4.46	2.96	3.10	0.92	44.49	2.01
9	12.54	8.17	7.62	0.79	48.89	0.87
10	19.42	6.48	6.31	0.22	71.30	0.29
11	12.76	8.13	7.29	0.73	45.14	0.86
12	9.69	3.85	3.82	0.31	91.35	0.88
13	18.50	10.33	9.96	0.60	41.09	0.90
14	8.65	4.89	4.73	0.62	34.07	0.91
15	15.69	9.56	7.87	0.62	68.35	0.98
16	13.02	7.49	6.67	0.59	40.02	1.52

### 2.3.3 Prediction Results from the Predictive Model

Using equation (3) and equation (6), predicted  $PSV_{max}$  from linear function analysis and exponential function analysis were compared against Doppler Ultrasound Scanner measured  $PSV_{max}$  as shown in Table 2-4. The mean prediction error and standard deviation reduced from 17.4% and 14.8% in the linear function predictor to 9.9% and 6.4% in the exponential function predictor respectively.

**Table 2-4 Patient Specific Predictions**

<b>Patient Number</b>	<b>Doppler Ultrasound Scanner Measured PSVmax (m/s)</b>	<b>Linear Function MLR</b>		<b>Exponential Function MLR</b>	
		<b>Predicted PSVmax (m/s)</b>	<b>Absolute Actual vs Predicted Error (%)</b>	<b>Predicted PSVmax (m/s)</b>	<b>Absolute Actual vs Predicted Error (%)</b>
1	1.60	1.54	3.7	1.66	4.0
2	1.49	1.33	11.1	1.35	9.7
3	2.27	2.46	8.3	2.22	2.4
4	1.71	1.55	9.3	1.75	2.4
5	1.68	1.10	34.8	1.37	18.2
6	1.53	1.20	21.6	1.27	17.2
7	1.49	1.02	31.5	1.23	17.5
8	1.95	1.90	2.4	1.77	9.1
9	2.87	2.80	2.4	2.43	15.2
10	1.32	1.26	4.9	1.23	6.5
11	1.89	0.88	53.6	1.46	23.0
12	1.39	1.29	7.2	1.32	5.2
13	2.42	1.55	35.8	2.21	8.6
14	1.80	1.45	19.3	1.67	7.2
15	1.77	1.45	18.0	1.64	7.6
16	2.75	2.36	14.2	2.85	3.7
<b>Mean</b>			<b>17.4</b>		<b>9.9</b>
<b>Standard Deviation</b>			<b>14.8</b>		<b>6.4</b>

Figure 2-7 depicts the relationship between Doppler Ultrasound Scanner measured and Predicted PSVmax using exponential function mathematical model as the predictor. If the predicted PSVmax is of the same value as the Doppler Ultrasound Scanner measured PSVmax, then the plotted point will lie on the unity line. Otherwise, the point will either lie above the unity line when the predicted value is higher than Doppler Ultrasound Scanner measured value, or the plotted point will lie below the unity line if the predicted value is lower than the DUS measured value. The +/-15% Prediction Error lines serve as the boundary lines for a prediction error <15%. Blue coloured points are within the 15% prediction error zone whereas red coloured points are outside the 15% prediction error zone therefore CTA is recommended for further investigation for restenosis.

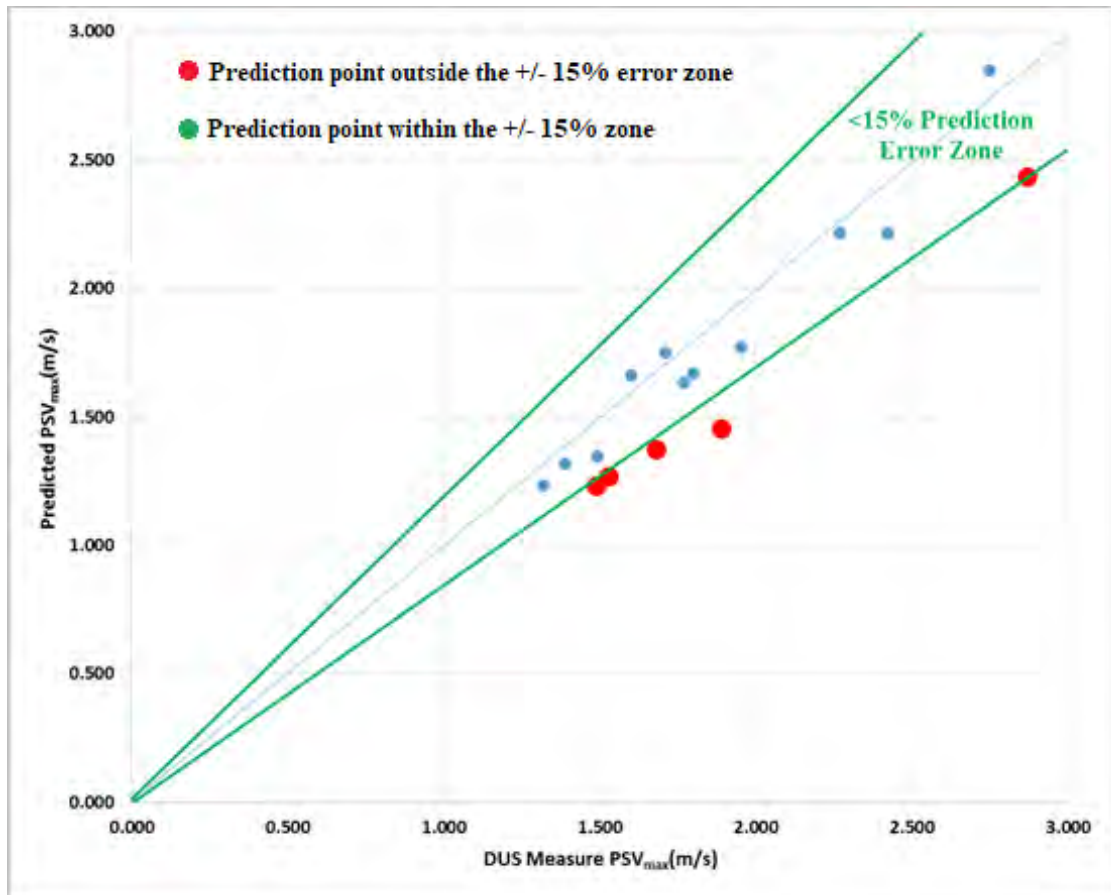


Figure 2-7 Predicted vs Doppler Ultrasound measured  $PSV_{max}$  Plot

## 2.4 Discussion

From Taguchi method's main effect analysis in section 2.3.1.1,  $PSV_{in}$  with a main effect delta of 10.5 was deemed to be six times more significant than  $R$  with a main effect delta of 1.8. However, from ANOVA analysis in section 2.3.1.3,  $PSV_{in}$  and  $R$  were found to contribute 94.06% and 3.36% to  $PSV_{max}$ , respectively. This implies that  $PSV_{in}$  was twenty eight times more significant than  $R$ . There seems to be an over-estimation of the contribution from  $PSV_{in}$  on  $PSV_{max}$  using ANOVA as compared with Taguchi method. Although CERAB will generally use iliac stents which are the same diameter, asymmetry in iliac diameter may result depending how well they expand in the presence of asymmetric iliac disease. This explains the actual iliac measurement results as shown in Table 2-3, showing slight asymmetry. Even though we assumed iliac symmetry in the CFD simulations, the predicted  $PSV_{max}$  matches well with clinical Doppler Ultrasound Scanner measurements with a mean prediction error of 9.9% and a standard deviation of 6.4%. From the plot in Figure 2-7, five out of sixteen (31%) predicted  $PSV_{max}$  were located outside the 15% prediction error zone. It is proposed that for future prospective studies,



patients with predicted  $PSV_{max}$  outside this zone are recommended for CTA scan to investigate possible restenosis. This criterion might be used in conjunction with the restenosis definition of a lesion causing a PSV ratio  $\geq 2.5$  used by Grimme et al[17] and Diehm et al[61]. If this proposed criterion was adapted, 69% or eleven out of sixteen patients from these retrospective studies could have avoided CTA.

Incidentally, the five predicted  $PSV_{max}$  values outside the 15% prediction error zone were all lower than the Doppler Ultrasound Scanner measured values as these data points were below the unity line indicating a possible bias in the predictor based on limited data. A larger population will be required to investigate whether the bias is systematic or random. Shakeri et al [101] found that  $\alpha$  was an independent and significant predictor of aortoiliac atherosclerosis (model  $r^2= 0.662$ ,  $p = 0.027$ ), but both Taguchi method and ANOVA in our current studies revealed that  $\alpha$  does not significantly affect  $PSV_{max}$ . Even though  $\alpha$  does not greatly influence  $PSV_{max}$  in our current studies however, it was reported that low wall shear stress contributes to atherosclerosis[102] .

In our current retrospective studies, infra-renal aortic, and left and right CIA diameters were determined from CTA images because these measurements were not available from Doppler Ultrasound Scanner images. For future prospective studies, a protocol will be established to specify aortic and CIA diameter measurements to be taken in addition to  $PSV_{in}$  and  $PSV_{max}$  measurements during routine post-procedure Doppler Ultrasound Scanner follow-up examinations.

It could be argued that a further limitation of our study was to assume rigid walls in the CFD simulations. Although the in vivo situation is more complex than that, the changes in vessel compliance from increasing disease severity, calcification and placement of balloon expandable stents are to make the vessel more rigid.

It might be interesting to investigate the impact of creating an interface between the end of the rigid stented iliac artery and a more compliant iliac artery beyond it on  $PSV_{max}$  using Fluid Structure Interaction CFD simulations. Since aortoiliac reconstruction procedures are relatively new and only some patients have high  $PSV_{max}$  post procedure, there is a need to collect more patient data for evaluation. Idealized bifurcation models were used in the current CFD simulations studies, further investigations using patient specific bifurcations in CFD simulations are planned to confirm the validity of the predictor. In addition, experimental validation with patient specific flow phantoms will be necessary to validate the accuracy and usefulness of the predictor.

## 2.5 Conclusion

The PSVmax was significantly influenced by PSVin and R. On the other hand,  $\alpha$ , two-way and three-way interactions among the three control factors were found to be insignificant. The combination of CFD simulation, Taguchi Method and MLR modelling is potentially a powerful tool to predict PSVmax in patients treated with an aortoiliac reconstruction procedure; CERAB. The exponential function predictive model with adjusted  $R^2$  of 99.9% was evaluated using sixteen sets of patient specific data with a mean prediction error of 9.9% and standard deviation of 6.4% when compared against Doppler Ultrasound Scanner measured PSVmax. The proposed predictor has a potential to be used as a clinical tool to establish the new normal PSVmax post aortoiliac stenting procedure and can possibly avoid unnecessary CTA investigation with its attendant cost, radiation exposure and contrast risk in cases where Doppler ultrasound measured PSVmax are found to be high.



3

Incorporating Iliac Asymmetry and Ankle  
Brachial Index Asymmetry into Peak  
Systolic Velocity Prediction Model

## Preamble

In this chapter, the peak systolic velocity (PSV) prediction model was tested using large cohort data. Modifications to the PSV prediction model were made by applying adjustment factors for iliac asymmetry and ABI asymmetry. The modified predictor was evaluated with respect to the status of restenosis according to the gold standard. The predictor was found to have 100% sensitivity, 42% specificity, 35% positive predictive value (PPV) and 100% negative predictive value (NPV). However, the predictor was still less than satisfactory and thus deemed unsuitable for clinical application.

### 3.1 Introduction

The gold standard for EVT follow-up is ABI and velocity measurements using ultrasound scanner at 1, 3, 6, 9 and 12 months after the procedure and annually thereafter. Patency is determined at follow-ups, according to Rutherford et al [103]. de Smet et al. investigated the duplex velocity characteristics of aortoiliac stenosis and found that the discriminative value of the PSV ratio was better than that of either the absolute PSV value or the PSV difference. For the detection of  $> 50\%$  aortoiliac stenoses, a PSV ratio  $> 2.8$  provided 86% sensitivity and 84% specificity (PPV: 84%; NPV: 85%). An absolute PSV value of 200 cm/s has a high sensitivity (95%) but a low specificity (55%) in identifying  $> 50\%$  stenoses (PPV: 68%; NPV: 91%) [104]. In addition, Ranke et al. found that a PSV ratio  $\geq 2.4$  indicated a  $> 50\%$  stenosis with a sensitivity of 87% and a specificity of 94% [105]. Plato et al. found that PSV ratio  $\geq 2.25$  could predict  $> 50\%$  stenosis [93], defined as patency, according to Rutherford et al. [103]. In doubtful cases, confirmatory arteriography or CTA is necessary before the intervention. In Chapter 2, 16 patient cases were available for the evaluation of the predictor. In this study, a large sample size of 25 patients was used. The present study aimed to incorporate iliac and ABI asymmetries into the PSV prediction model by manual adjustment. Gold standard based on multi-slice CTA was used as a reference to determine the status of restenosis for the specific case of each patient. Statistical methods were employed with respect to sensitivity, specificity, PPV and NPV for further evaluation.

### 3.2 Materials and Methods

A collaboration was established between Curtin University and the University of Twente, Enschede, The Netherlands, to assess the usefulness of the predictor to detect potential restenosis for patients treated with CERAB. According to the selection criteria, patients who have successfully been treated with CERAB with postoperative CTA and DU present data to facilitate diameter measurement and infrarenal velocity for use as independent variables in the predictor formula. In addition, the ABI data are used to apply an adjustment to the predictor by taking into account the resistance and compliance of downstream arteries in the left and right extremities. Data from 25/44 CERAB patient were selected. Of these, 18 patients were excluded as they did not satisfy the selection criteria outlined in Figure 3-1. The diameter of the aorta and iliac arteries were measured using TeraRecon software (TeraRecon Inc., Foster City, CA, USA), as shown in Figure 3-2 and Figure 3-3.

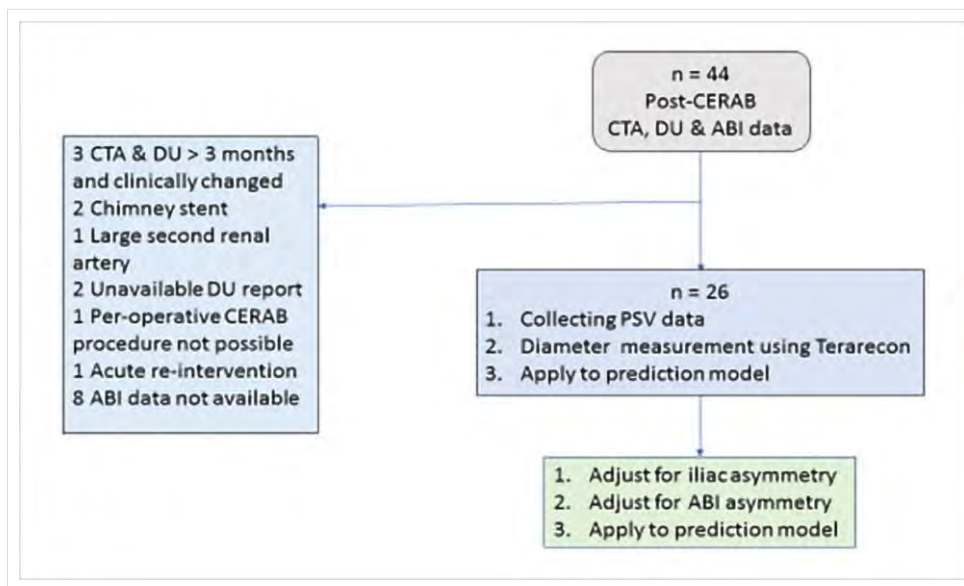
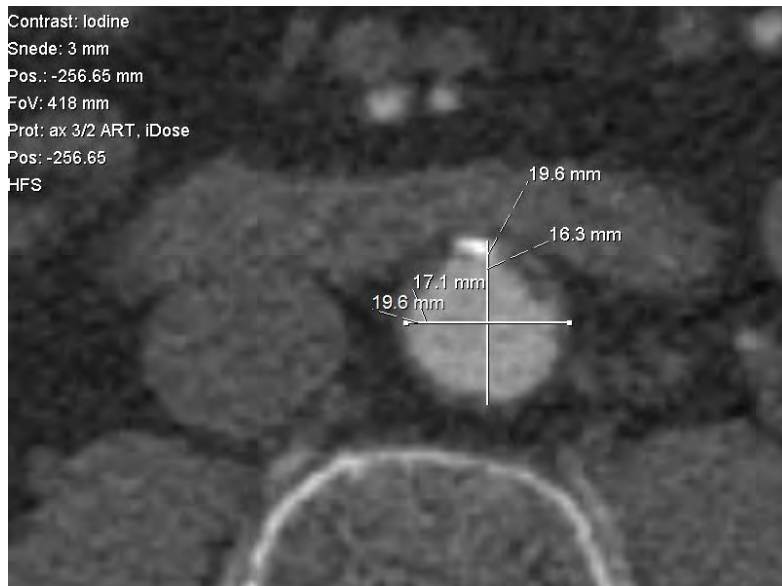
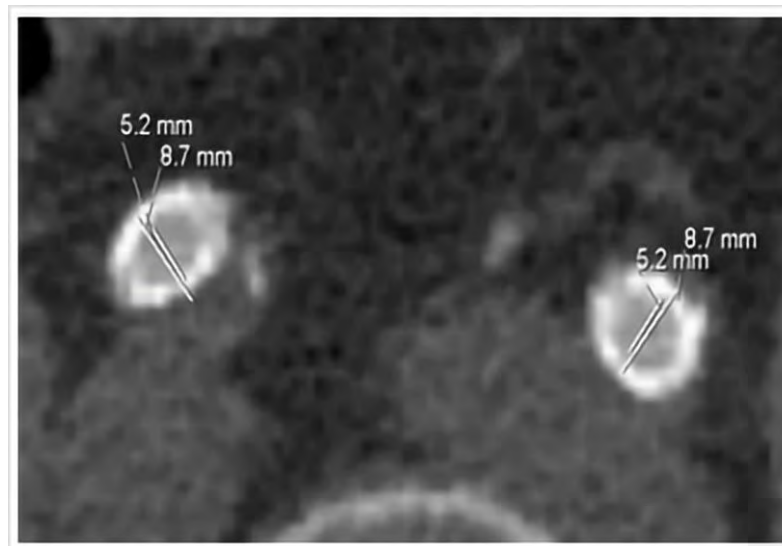


Figure 3-1 Clinical validation of predictor-CERAB patient selection



**Figure 3-2 Aorta diameter measurement**



**Figure 3-3 Iliac diameter measurement**

Table 3-1 summarizes the parameters of 25 AIOD patients in our retrospective study in Rijnstate Hospital. All patients were diagnosed with aortoiliac stenotic lesions that either caused incapacitating claudication symptoms (Fontaine class IIa), pain at rest (fontaine II) or non-healing ulcers on legs (fontaine IV). In terms of stenotic lesions, all patients presented some form of lesions protruding into the aorta, rendering kissing stents less suitable than CERAB. These lesions were relatively complex as compared to that in the other cohorts that received iliac stents, indicating more of TASC C and D type lesions.

**Table 3-1 Table parameters of AIOD patients**

<b>Parameters</b> (Male = 12, Female = 13, Total n= 25)	<b>Mean</b>	<b>Standard deviation</b>
Age (years)	67.90	10.90
Diameter, infrarenal abdominal diameter (mm)	15.31	1.78
Diameter, left common iliac artery (mm)	8.09	1.94
Diameter, right common iliac artery (mm)	7.55	1.51
Velocity, infrarenal (m/s)	0.85	0.32
Ankle Brachial Index, left	0.95	0.18
Ankle Brachial Index, right	0.98	0.19

Adjustments to the PSV predictor were made based on the asymmetries of CIA and ABI as follows:

### 3.2.1 Adjustment factor for iliac asymmetry

The flow rate is proportional to the cross-sectional area or the square of the diameter.

$$\text{Adjustment factor to the left CIA} = D_{\text{right}}^2 / D_{\text{left}}^2 \quad (3.1)$$

$$\text{Adjustment factor to the right CIA} = D_{\text{left}}^2 / D_{\text{right}}^2 \quad (3.2)$$

Where

$D_{\text{right}}$  and  $D_{\text{left}}$  are diameters of right and left CIA, respectively.

The higher of the two iliac asymmetry adjustment factors was applied to the PSV predictor.

### 3.2.2 Adjustment factor for ABI asymmetry

Since ankle systolic pressure is directly proportional to ABI,

$$\text{Adjustment factor to the left ABI} = \text{ABI}_{\text{right}} / \text{ABI}_{\text{left}} \quad (3.3)$$

$$\text{Adjustment factor to the right ABI} = \text{ABI}_{\text{left}} / \text{ABI}_{\text{right}} \quad (3.4)$$

Where

$\text{ABI}_{\text{right}}$  and  $\text{ABI}_{\text{left}}$  indicate the patient's ABI for the right and left ankle/brachial, respectively.

The higher of the two ABI asymmetry adjustment factors was applied to the PSV predictor.

### 3.2.3 Statistical analysis

The statistical analyses were performed based on public health definitions of sensitivity, specificity, PPV and negative predictive value (NPV) (Table 3-2) [106].

**Table 3-2 Gold standard re-stenosis screening test**

		Status of person according to "gold standard"		
		Has the condition	Does not have the condition	
Result from screening test	Positive	a True positive	b False positive	← Row entries for determining <b>positive predictive value</b>
	Negative	c False negative	d True negative	← Row entries for determining <b>negative predictive value</b>
		↑ Column entries for determining <b>sensitivity</b>	↑ Column entries for determining <b>specificity</b>	

$$\text{Sensitivity} = [a/(a+c)] \times 100 \quad (3.5)$$

$$\text{Specificity} = [d/(b+d)] \times 100 \quad (3.6)$$

$$\text{PPV} = [a/(a+b)] \times 100 \quad (3.7)$$

$$\text{NPV} = [d/(c+d)] \times 100 \quad (3.8)$$

### 3.3 Results

Six patients were classified as restenosis cases by a radiologist and vascular surgeon based on the CTA gold standard during the follow-up of each patient. These cases are highlighted in shaded rows in Table 3-3 and Table 3-4 before and after the application of adjustment factors, respectively. The other 19 cases were classified as non-restenosis cases.



**Table 3-3 Geometric parameters of 25 patients and results of predicted PSV**

<b>Patient number</b>	<b>PSV<sub>in</sub> (m/s)</b>	<b>Aorta diameter (mm)</b>	<b>Right CIA dia (mm)</b>	<b>Left CIA dia (mm)</b>	<b>R</b>	<b>Right ABI</b>	<b>Left ABI</b>	<b>Predicted PSV (m/s)</b>
1	0.81	13.60	7.57	6.55	0.54	1.09	1.05	1.38
2	0.94	14.43	7.16	6.73	0.46	1.02	1.08	1.64
3	1.06	15.93	10.87	9.40	0.81	1.10	1.11	1.51
4	0.65	16.30	7.45	7.06	0.40	1.00	1.01	1.28
5	0.88	15.97	9.75	11.50	0.89	1.06	1.08	1.17
6	1.55	18.90	8.17	9.87	0.46	0.70	0.60	2.54
7	0.44	15.67	4.33	6.04	0.22	0.61	0.80	1.13
8	1.41	12.65	6.88	6.81	0.59	1.15	1.09	2.22
9	0.43	16.90	7.09	8.50	0.43	1.08	1.07	0.93
10	0.85	16.00	9.46	7.99	0.60	1.14	1.21	1.39
11	0.55	12.50	8.33	7.07	0.76	1.10	1.02	0.80
12	0.77	14.80	6.44	6.78	0.40	1.10	0.86	1.45
13	1.00	15.27	7.51	7.07	0.46	0.58	1.01	1.74
14	1.11	14.20	6.34	6.85	0.43	1.13	1.15	1.92
15	1.62	13.00	8.32	10.80	1.10	1.07	1.07	2.07
16	0.63	15.47	8.71	10.90	0.81	1.00	0.64	0.88
17	0.62	13.27	4.63	7.58	0.45	0.58	0.55	1.19
18	0.95	17.40	7.85	11.23	0.62	1.25	0.97	1.52
19	0.92	14.17	7.01	7.61	0.53	0.99	1.00	1.55
20	0.70	16.27	8.27	11.70	0.78	0.94	0.98	1.01
21	0.50	17.50	5.27	4.89	0.17	0.73	0.67	1.26
22	0.44	15.60	7.33	7.93	0.48	0.93	0.89	0.90
23	0.64	13.47	8.59	7.49	0.72	1.00	1.00	0.98
24	0.87	14.60	6.52	5.40	0.34	1.07	0.84	1.65
25	0.96	18.90	8.86	8.58	0.43	1.13	1.09	1.71

**Table 3-4 Predicted PSV Results adjusted for iliac symmetry and ABI symmetry**

Patient number	Right CIA dia (mm)	Left CIA dia (mm)	Right CIA dia (mm)	Left CIA dia (mm)	Predicted PSV (m/s)	Iliac adjust factor <sup>1</sup>	ABI adjust factor <sup>2</sup>	Adjusted predicted PSV <sup>3</sup>
1	7.57	6.55	1.09	1.05	1.38	1.34	1.04	1.91
2	7.16	6.73	1.02	1.08	1.64	1.13	1.06	1.97
3	10.87	9.40	1.10	1.11	1.51	1.34	1.01	2.04
4	7.45	7.06	1.00	1.01	1.28	1.11	1.01	1.44
5	9.75	11.50	1.06	1.08	1.17	1.39	1.02	1.66
6	8.17	9.87	0.70	0.60	2.54	1.46	1.17	4.32
7	4.33	6.04	0.61	0.80	1.13	1.95	1.31	2.88
8	6.88	6.81	1.15	1.09	2.22	1.02	1.06	2.39
9	7.09	8.50	1.08	1.07	0.93	1.44	1.01	1.35
10	9.46	7.99	1.14	1.21	1.39	1.40	1.06	2.07
11	8.33	7.07	1.10	1.02	0.80	1.39	1.08	1.20
12	6.44	6.78	1.10	0.86	1.45	1.11	1.28	2.06
13	7.51	7.07	0.58	1.01	1.74	1.13	1.74	3.42
14	6.34	6.85	1.13	1.15	1.92	1.17	1.02	2.28
15	8.32	10.80	1.07	1.07	2.07	1.69	1.00	3.49
16	8.71	10.90	1.00	0.64	0.88	1.57	1.56	2.15
17	4.63	7.58	0.58	0.55	1.19	2.68	1.05	3.36
18	7.85	11.23	1.25	0.97	1.52	2.05	1.29	4.01
19	7.01	7.61	0.99	1.00	1.55	1.18	1.01	1.85
20	8.27	11.70	0.94	0.98	1.01	2.00	1.04	2.11
21	5.27	4.89	0.73	0.67	1.26	1.16	1.09	1.59
22	7.33	7.93	0.93	0.89	0.90	1.17	1.04	1.10
23	8.59	7.49	1.00	1.00	0.98	1.32	1.00	1.29
24	6.52	5.40	1.07	0.84	1.65	1.46	1.27	3.06
25	8.86	8.58	1.13	1.09	1.71	1.07	1.04	1.89

<sup>1</sup> Adjustment factor for iliac asymmetry<sup>2</sup> Adjustment factor for ABI asymmetry<sup>3</sup> Predicted PSV adjusted for iliac asymmetry and ABI asymmetry

The  $\pm 15\%$  tolerance bands, as proposed in Chapter 2, were used as screening tools when the cases falling outside the tolerance bands were restenosis, whereas those falling inside the tolerance bands were deemed as non-restenosis. The data before and after the application of adjustment factors are plotted, as shown in Figure 3-4 and Figure 3-5, respectively.

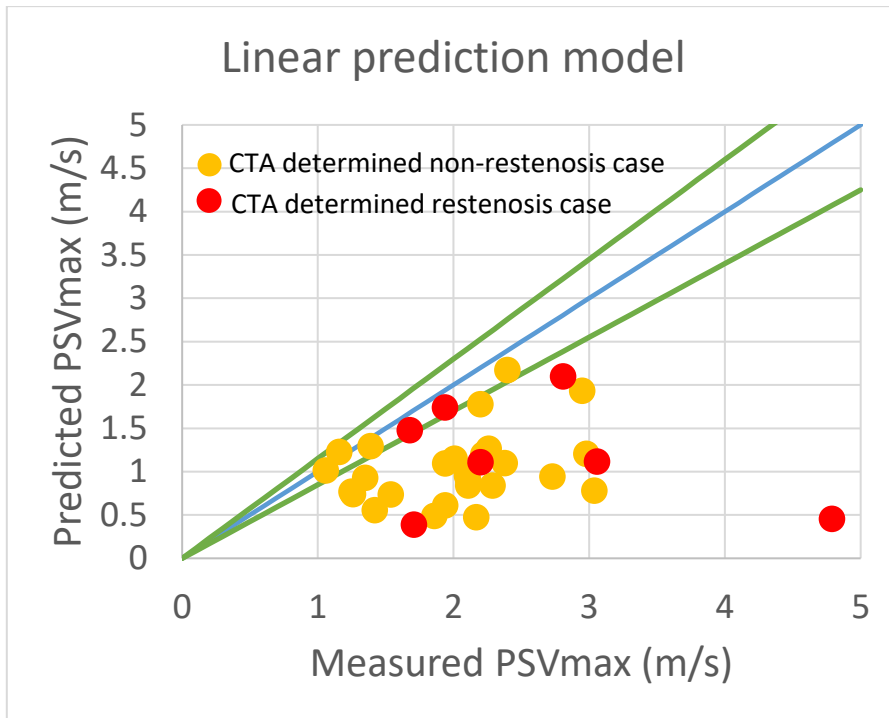


Figure 3-4 Predicted vs DU measured PSV plot before adjustment

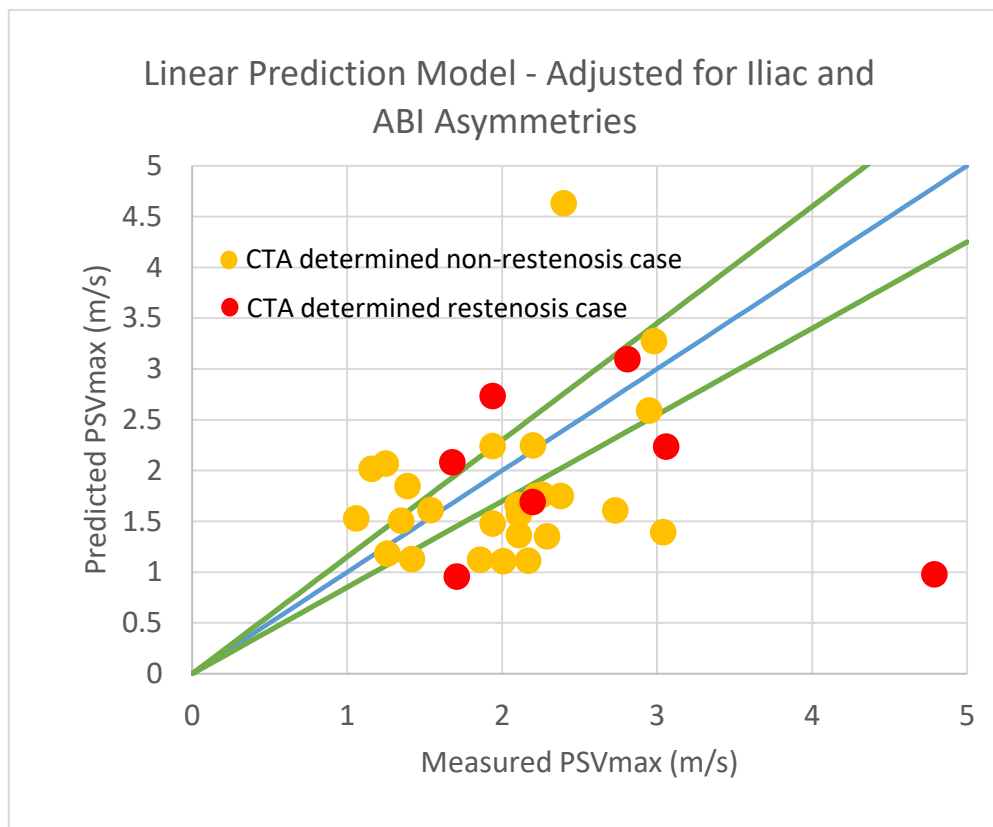


Figure 3-5 Predicted PSV vs DU-measured PSV adjusted for iliac and ABI asymmetries

Table 3-5 shows the statistical data before and after adjustments for iliac and ABI asymmetries. Table 3-6 summarises the sensitivity, specificity, PPV and NPV data: 67%, 11%, 19% and 50% before and 100%, 42%, 35% and 100% after adjustments for iliac and ABI asymmetries.

**Table 3-5 Status of restenosis according to gold standard before and after adjustments for iliac and ABI asymmetries**

Outcome	Before adjustment			After adjustment		
	Has restenosis	Does not have restenosis	Total	Has restenosis	Does not have restenosis	Total
Results from predictor screening						
Positive	4	17	21	6	11	17
Negative	2	2	4	0	8	8
<b>Total</b>	<b>6</b>	<b>19</b>	<b>25</b>	<b>6</b>	<b>19</b>	<b>25</b>

**Table 3-6 Sensitivity, specificity, PPV and NPV before and after adjustments for iliac and ABI asymmetries**

	Before adjustment	After adjustment
Sensitivity	$\frac{4}{4+2} \times 100 = 67\%$	$\frac{6}{6+0} \times 100 = 100\%$
Specificity	$\frac{2}{2+17} \times 100 = 11\%$	$\frac{8}{8+11} \times 100 = 42\%$
PPV	$\frac{4}{4+17} \times 100 = 19\%$	$\frac{6}{6+11} \times 100 = 35\%$
NPV	$\frac{2}{2+2} \times 100 = 50\%$	$\frac{8}{8+0} \times 100 = 100\%$

### 3.4 Discussion

In this study, iliac and ABI asymmetries were incorporated into the peak systolic velocity prediction model and the predictive power was assessed. The adjusted predictor has excellent sensitivity and NPV 100%, which implied that all restenosis cases were identified as true positive and no false negative. Strikingly, the predicted vs DU measured PSV plot before adjustments (Figure 3-4) demonstrated a systematic bias towards the measured PSV values as compared to the predicted PSV as most of the plotted points were located below the unity line. The lower predicted PSV could be attributed to the symmetry of iliac arteries assumed in the development of the predictor. For the predicted vs DU measured PSV plot, when iliac and ABI asymmetries were incorporated in the prediction model, the 25 data points were evenly distributed, approximately 50% each above and

below the unity line. In addition, all six restenosis cases were outside the 'New Normal' zone, with  $\pm 15\%$  from the unity line. Also, the sensitivity improved from 67% to 100%, specificity from 11% to 42%, PPV from 19% to 35% and NPV from 50% to 100%.

A duplex-derived velocity risk prediction model was developed by Hicks et al. [107] to predict the disease progression in patients with moderate asymptomatic carotid artery stenosis with sensitivity, specificity, PPV and NPV of 80.7%, 64.0%, 22.9% and 96.1%, respectively. This predictive model might be useful for identifying high-risk patients who would benefit from routine carotid disease surveillance. Coffi et al. compared the PSV ratio with intra-arterial pressure measurements (IAPM) when assessing the hemodynamic significance of subcritical iliac artery stenosis and found a poor agreement between IAPM and PSV ratios. For the PSV ratio of 2.5, the sensitivity was 37%, specificity was 90%, PPV was 88% and NPV was 43% and 37%, respectively [56]. In comparison, our predictor with 100%, 42%, 35% and 100% sensitivity, specificity, PPV and NPV with similar values might be useful as a clinical screening tool to avoid unnecessary CTA.

One of the limitations of the current study is that the iliac and ABI asymmetries were incorporated in the prediction model by manual adjustment. In addition, the correlation between PSV and iliac artery cross-sectional area was assumed to be linear. The correlation between PSV and ABI was also similar. These correlations might not be perfectly linear in nature. The other limitation is that the vessel is assumed to be perfectly circular when calculating the cross-sectional area of the arteries. Nonetheless, most blood vessels are not perfectly circular.

Although both sensitivity and specificity in this large population cohort study improved significantly from 67% to 100% and 10% to 42.1%, respectively after adjustments. Only 8/19 patients or 42% of the non-stenosis cases in this cohort study would have avoided CTA if this predictor was used as a screening tool to supplement the velocity index criterion of 2.5; therefore, further improvement is required before this tool is useful for clinical applications.

Additional analysis is required to explore the reasons for the unsatisfactory outcome of the predictive model. Future investigations to compare the idealized CFD model and patient-specific model might be useful. In addition, the assumptions of flow condition need further investigation in order to elucidate the underlying cause.

### **3.5 Conclusion**

The incorporation of iliac asymmetry and ABI asymmetry into PSV prediction model resulted in improved sensitivity from 67% to 100%, specificity from 11% to 42%, PPV from 19% to 35% and NPV from 50% to 100%. These data suggested that the PSV predictor has potential for the screening test. In the current retrospective study, 42% of non-restenosis cases avoided unnecessary cost and risk associated with the follow-up CTA. Nonetheless, further improvement is essential for clinical screening applications.



# 4

## Influence of Flute Angle, Cuff Length Overlap and Bifurcation Angle on Peak Systolic Velocity

## Preamble

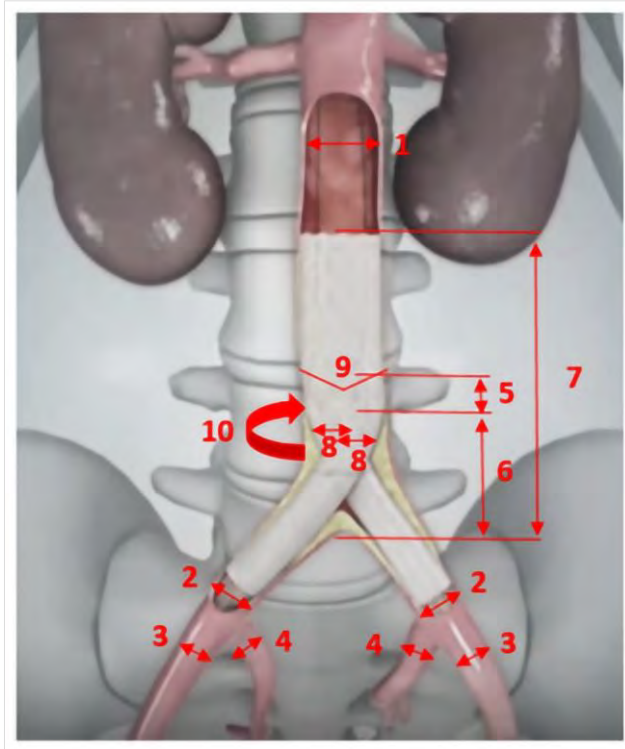
In this chapter, new independent variables are considered. Three-element Windkessel models were coupled to output the idealized flow model. Computational fluid dynamic (CFD) simulations were performed for each combination of variables. Peak systolic velocity (PSV) generated from each combination of variables was analysed statistically to assess the influence of new variables on PSV.

### 4.1 Introduction

The vessel geometry and stent configuration affect arterial blood flow [108-112]. A study by Greiner et al. assessed the influence of stent overlap on the patency rate of 35 AIOD patients treated with aortoiliac kissing stents and found that the primary and assisted primary patency rates at 2 years for the 'non-crossing' group were significantly higher (94.1% and 100%, respectively) compared to 33.2% and 45.3%, respectively, for the 'crossing' group ( $P = 0.01$ ) [113]. Sarafuddin et al. analysed the long-term outcomes following stent reconstruction of the aortic bifurcation and the role of geometric determinants and found that radial mismatch is the only significant determinant of restenosis [114]. Recently, Groot Jebbink et al. analysed the geometrical consequences of kissing stents and CERAB configuration in an in vitro model for the endovascular reconstruction of aortic bifurcation and found that the CERAB configuration is the most anatomical and physiological reconstruction of the aortic bifurcation compared to a bare metal kissing stents and covered kissing stents [74]. Nanto et al. conducted a retrospective study of five-year patency and its predictors after endovascular therapy in 64 AIOD patients and found that a specific stent design E-Luminexx has a high incidence of restenosis (in 29 patients, 48%),  $P = 0.038$  [83]. The current study evaluated the influence of three geometric parameters of CERAB configuration on PSV: flute angle, cuff length overlap and bifurcation angle.

Figure 4-1 shows some of the geometrical parameters of a CERAB model that can be considered for further improvement of the PSV predictor.





**Figure 4-1 Geometrical parameters of a CERAB model**

Geometrical parameters:

1. Aorta diameter (10 mm distal to RA, 10 mm proximal to cuff, middle)
2. CIA diameter (10 mm distal to stent, 10 mm proximal to bifurcation, middle)
3. EIA diameter (10 and 20 mm distal to bifurcation)
4. IIA diameter (10 and 20 mm distal to bifurcation)
5. CIA stent cuff length overlap into aortic stent
6. Stent height: Distance between distal end cuff and native bifurcation
7. Distance between proximal end cuff and native bifurcation
8. CIA stent diameter
9. Flute angle: Angle between proximal and distal ends of CIA stents
10. Rotation of AIC stents

In Chapter 2, parameters 1 and 2 were included in the predictor formula. In this section, the cuff length overlap and flute angle, i.e. items 5 and 9 are investigated using CFD simulation in addition to the bifurcation angle. These parameters were selected due to their correlation with the flow rate. Hence, the velocity stated in Poiseuille's law is described as follows: the flow (Q) of fluid is related to several factors, such as the viscosity ( $\eta$ ) of the fluid, the pressure gradient across the tubing (P) and the length (L) and diameter (r) of the tubing.

## 4.2 Materials and Methods

Three independent variables, namely flute angle, stent height and bifurcation angle, were assessed in this exercise to determine their effects on PSV using CFD simulations. The workflow is outlined in Figure 4-2. The ideal 3D geometry of a flow model with parameters, 20 mm stent height, 90° flute angle and 40° bifurcation angle was created using Ansys SpaceClaim, i.e. a 3D direct modeller computer-aided design (CAD) software. The 3D volume of the fluid model was first created using Ansys Fluent Meshing with minimum mesh size of 1.5 mm, followed by CFD simulation with inlet boundary condition of  $PSV_{in} = 0.7$  m/s using Ansys Fluent 17.2, a finite volume CFD solver. The grid independence was tested by reducing the minimum cell size by 0.25 mm, and the grid refinement was ceased when  $PSV_{max}$  varied by  $< 1\%$  between the two consecutive schemes. In addition, the periodicity could be reached when PSV, end systolic velocity (ESV) and peak diastolic velocity (PDV) of two consecutive periodic cycles varied by  $< 1\%$ .

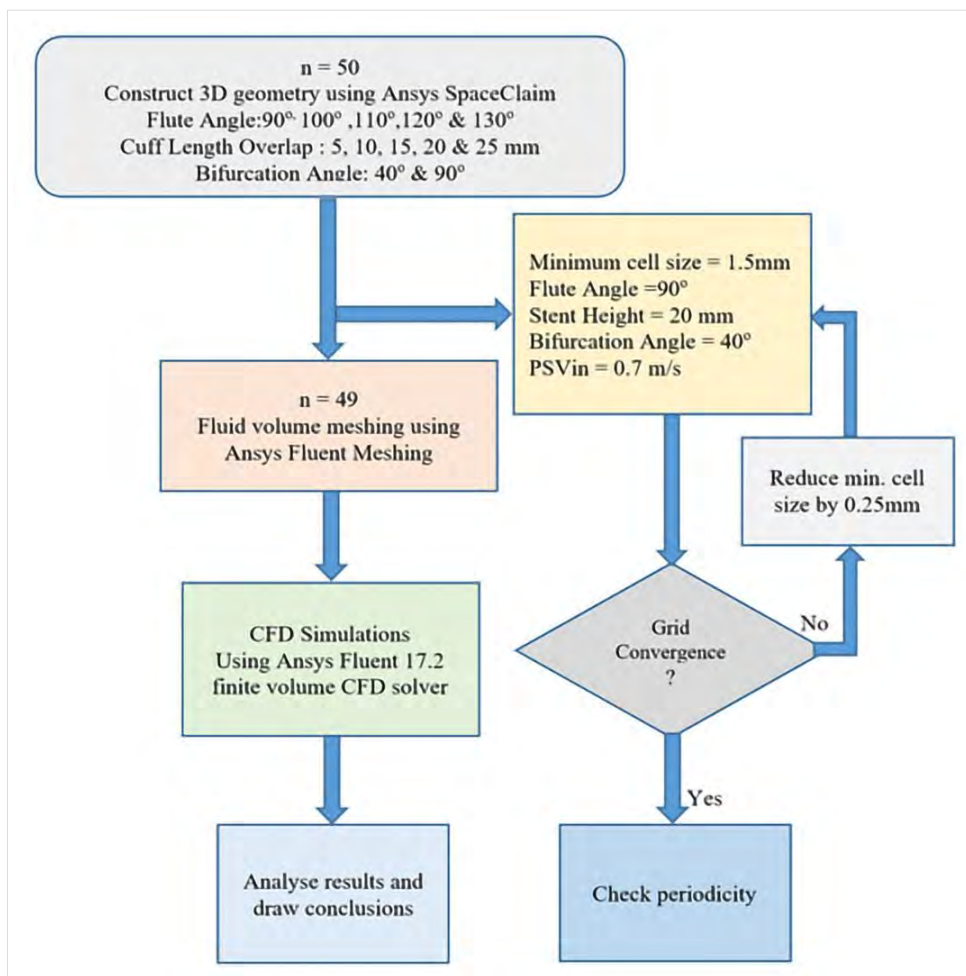


Figure 4-2 Workflow to assess the effects of independent variables on PSV

### 4.2.1 3D Model

Ansys SpaceClaim is a direct modeller CAD software used to create the 3D geometry based on the dimensions from Jebbink et al. [74]: infrarenal proximal diameter = 22 mm, distal aorta diameter = 16 mm, taper =  $2^\circ$  and iliac diameter = 8 mm. A 0.25-mm thick stent graft was inserted, as shown in Figure 4-3.

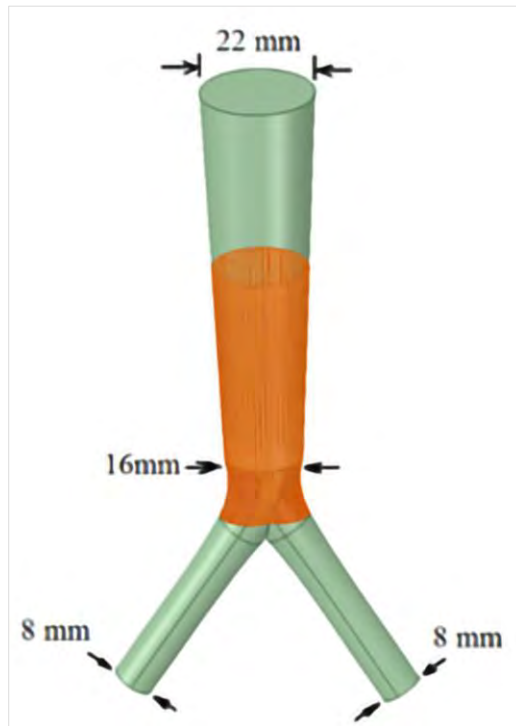


Figure 4-3 Aortoiliac bifurcation model with an aortic stent inserted

Two iliac stents with 0.25 mm thickness and 38 mm length were placed 10 mm above the native bifurcation base, as shown in Figure 4-4.

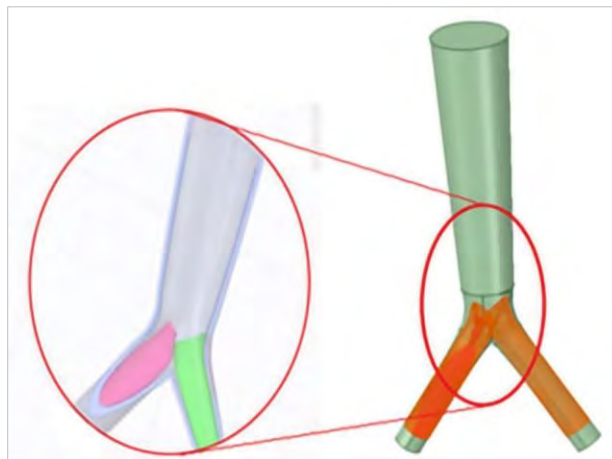


Figure 4-4 Aortoiliac bifurcation model with an aortic stent inserted

## 4.2.2 Meshing

Fluent meshing was used to generate the fluid volume required for CFD simulation. The importation of CAD geometry and the subsequent steps involved in generating the polyhedral mesh elements are depicted in the flowchart in Figure 4-5.

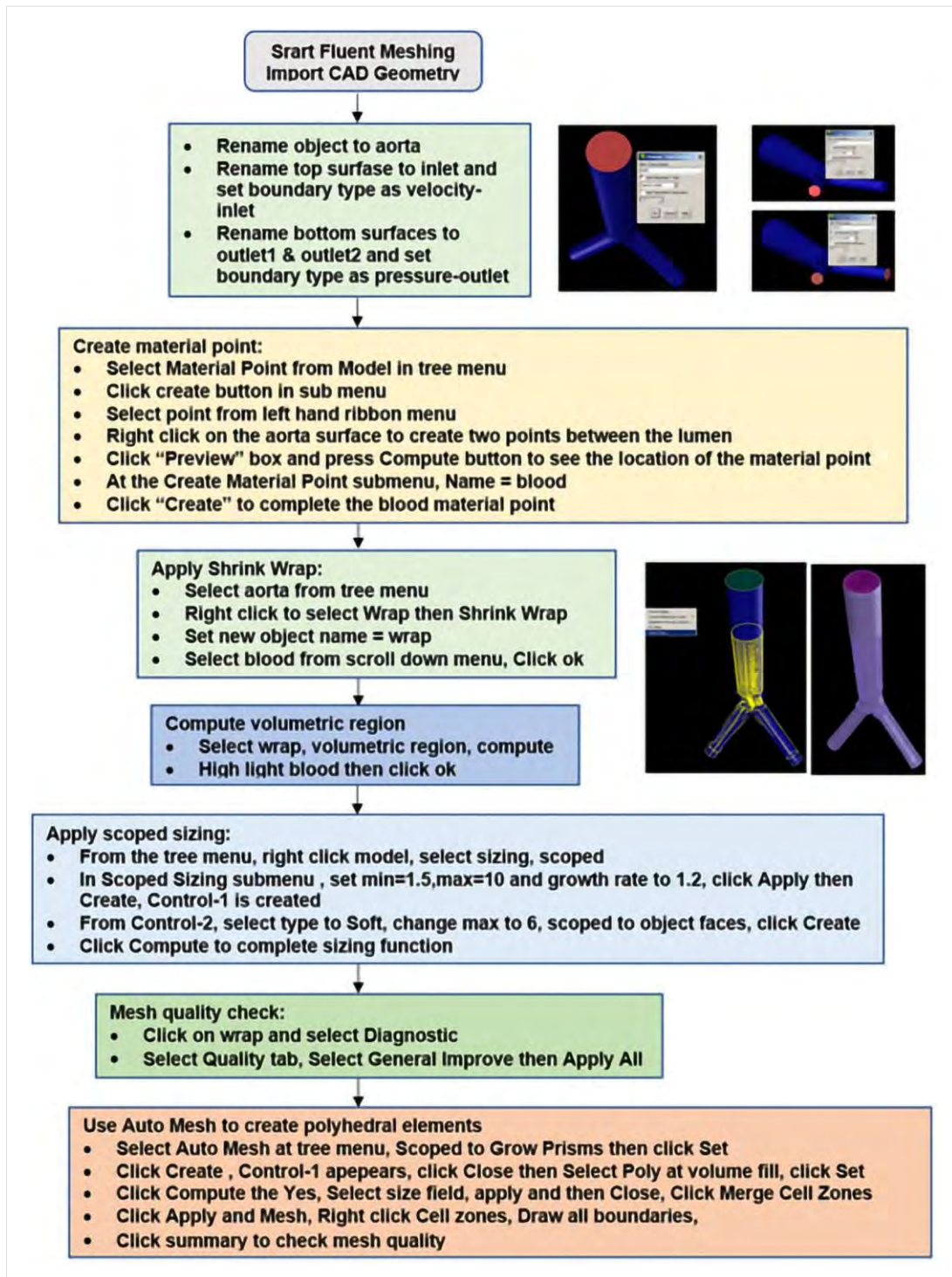


Figure 4-5 Fluent meshing flowchart



### 4.2.3 CFD Simulations

#### 4.2.3.1 Inlet Boundary Condition

An infrarenal triphasic flow profile was prescribed at the inlet with a PSV of 0.7 m/s and 0.93 s period, as shown in Figure 4-6. This inlet boundary condition was implemented in fluent CFD using a user-defined function (UDF) via a Taylor series.

$$\begin{aligned}
 &1.7(0.45e^{-3.47(t-0.14)^2} - 0.134e^{-138.9(t-0.4)^2} + 0.04e^{-3.47(t-0.65)^2} \\
 &+ 0.2e^{346.3(t-0.53)^2} + 0.04e^{868.1(t-0.37)^2} + 0.085e^{74.4(t-0.53)^2} \\
 &+ 0.355e^{114.8(t-0.058)^2} + 0.01e^{78.1(t-0.93)^2})
 \end{aligned} \quad (4.1)$$

Where  
t = time in s

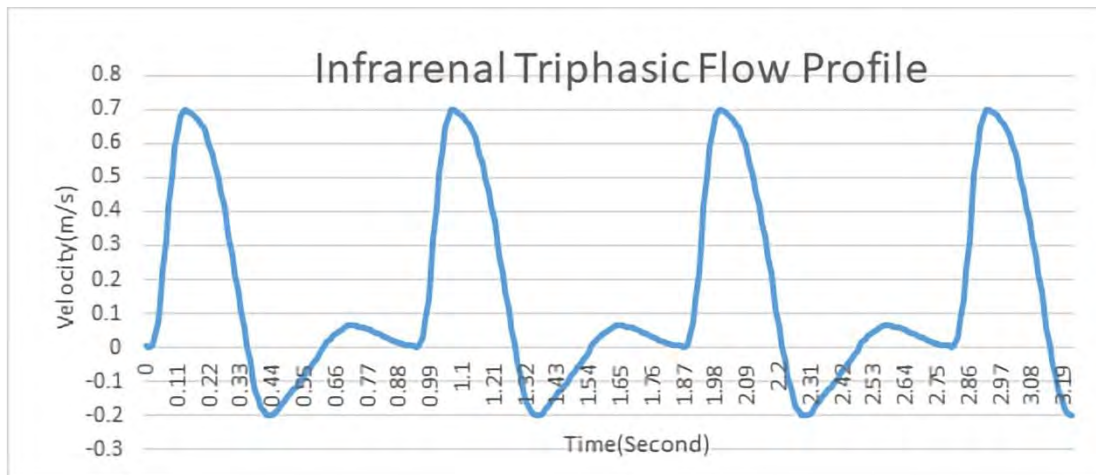


Figure 4-6 Infrarenal triphasic flow profile

#### 4.2.3.2 Outlet Boundary Condition

Windkessel models are frequently used to describe the load faced by the heart in pumping blood through the systemic arterial system. These are also useful in describing the correlation between blood pressure and blood flow in the aorta and peripheral arteries: arterial compliance and peripheral resistance.

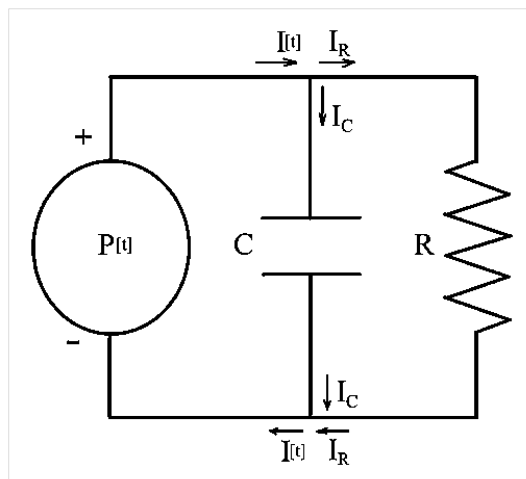
An early Windkessel model was described by the German physiologist Otto Frank in 1899 [115, 116]. The model has been applied recently in the modelling of the cardiovascular system [117, 118] and studies involving carotid [119] and coronary arteries [120]. It likens the heart and systemic arterial system to a closed hydraulic circuit comprised of a water pump connected to a chamber. The circuit is then filled with water except for a pocket of air in the chamber (*Windkessel* is the German word for *air chamber*). As water is pumped into the chamber, the water both compresses the air in the pocket and

pushes the water out of the chamber back to the pump. The compressibility of the air in the pocket simulates the elasticity and extensibility of the major artery, similar to when blood is pumped into it by the heart ventricle. This effect is commonly referred to as arterial compliance. The resistance water encounters while leaving the Windkessel and flowing back to the pump simulates the resistance to the blood flow as it flows through the arterial tree from the major arteries to minor arteries, arterioles and capillaries due to decreasing vessel diameter. This resistance to flow is commonly referred to as peripheral resistance. Assuming the ratio of air pressure to air volume in the chamber is constant and the flow of fluid through the pipes connecting the air chamber to the pump follows Poiseuille's law and is proportional to the fluid pressure, the following differential equation could relate the flow and pressure of the water:

$$I(t) = \frac{P(t)}{R} + C \frac{dP(t)}{dt} \quad (4.2)$$

where  $I(t)$  is the water flow out of the pump as a function of time measured in volume per time unit,  $P(t)$  is the water pressure as a function of time measured in force per area unit,  $C$  is the constant ratio of air pressure to air volume and  $R$  is the flow-pressure proportionality constant.

The same equation describes the correlation between the current,  $I(t)$  and the time-varying electrical potential,  $P(t)$ , in the following electrical circuit:



**Figure 4-7** Two-element Windkessel model

In this circuit,  $I_C$  is the current in the middle branch of the circuit,  $I_R$  is the current in the right branch of the circuit,  $R$  is the resistance of the resistor and  $C$  is the capacitance

of the capacitor. Since there are only two passive elements in this circuit, the resistor and capacitor, this model is commonly referred to as the two-element Windkessel model (WK2) (Figure 4-7). According to Ohm's Law, the decline in the electrical potential across the resistor is  $I_R R$ . The drop in the electrical potential across the capacitor is  $Q/C$ , where  $Q$  is the instantaneous charge on the capacitor and  $[dQ/dt] = I_C$ . According to Kirchhoff's First Law, the net change in the electrical potential around each loop of the circuit is zero; therefore,  $P(t) = I_C R$  and  $P(t) = Q/C$ . According to Kirchhoff's Second Law, the sum of currents into a junction equals the sum of currents out of the same junction:  $I(t) = I_C + I_R$ . Eliminating  $I_C$  and  $I_R$  from the junction equation leads to the differential equation stated above.

During diastole, when there is no blood flow from the heart,  $I(t) = 0$ , and the Windkessel equation can be solved for  $P(t)$ :

$$P(t) = P(t_d) e^{-[(t-t_d)/(RC)]} \quad (4.3)$$

Where:

$t_d$  is the time at the start of diastole and  $P(t_d)$  is the blood pressure in the aorta at the start of diastole.

Another model of the circulatory system is the Broemser model, which was described by the Swiss physiologists, Ph. Broemser and Otto F. Ranke in 1930 [121]. Also known as the 3-element Windkessel (WK3) model, the Broemser model adds a resistive element to the WK2 model between the pump and the air-chamber to simulate resistance to blood flow due to the aortic or pulmonary valve. This model has been recently used to study blood pressure and flow in the human aorta [122].

Figure 4-8 illustrates a schematic of the electrical circuit corresponding to the WK3 model.

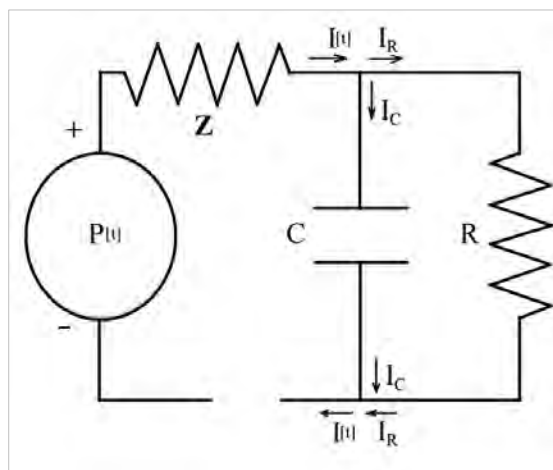


Figure 4-8 Three-element Windkessel model

Using the same circuit analysis technique as for the WK2 model circuit, the differential equation for the WK3 model shown in Figure 4-8 is as follows:

$$\left(1 + \frac{Z}{R}\right) l(t) + C Z \frac{dl(t)}{dt} = \frac{P(t)}{R} + C \frac{dP(t)}{dt} \quad (4.4)$$

Where:

Z represents the characteristic resistance due to the aortic valve, and R represents the peripheral resistance. l(t), P(t) and C indicate the same parameters as in the WK2 equation.

The WK3 was implemented in fluent CFD using a UDF provided by Ansys as an extension function by prescribing it at both the iliac pressure outlets, as shown in Figure 4-9. The values of Z, R and C at the left and right CIA were assigned based on the lumped parameter model of the cardiovascular system developed by Ghasemalizadeh et al. [117], where  $Z = 2.34 \times 10^7 \text{ kg m}^{-4} \text{ s}^{-1}$ ,  $R = 3.94 \times 10^8 \text{ kg m}^{-4} \text{ s}^{-1}$  and  $C = 4.18 \times 10^{-9} \text{ kg}^{-1} \text{ m}^4 \text{ s}^2$

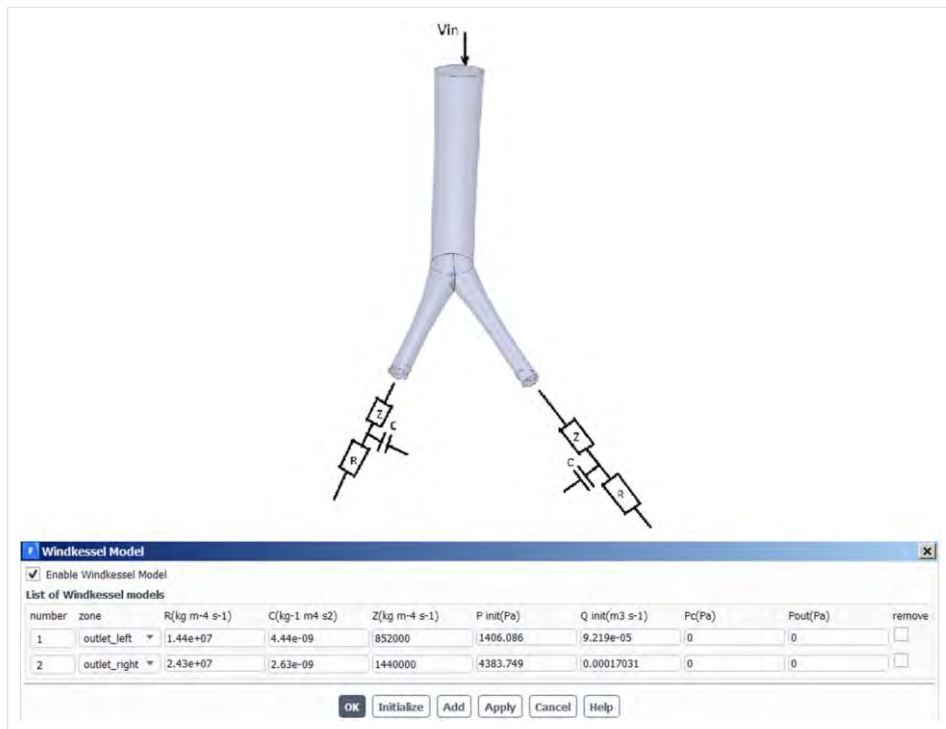


Figure 4-9 Three-element Windkessel at pressure outlets



### 4.2.3.3 Periodicity

The periodicity reached convergence approximately after the 7<sup>th</sup> cardiac cycle, as shown in Figure 4-10. The initial pressure ( $P_{int}$ ) of the WK3 model was set to 3,500 Pa to speed up convergence in the subsequent simulation runs.



Figure 4-10 Periodicity convergence at the 7<sup>th</sup> cardiac cycle

### 4.2.3.4 Parameter of Interest: PSV

For each CFD simulation, maximum PSV was determined by locating the position and magnitude of maximum velocity in the flow domain between the inlet and the outlets. A typical post-processing of the streamline flow showing the maximum velocity is illustrated in Figure 4-11.

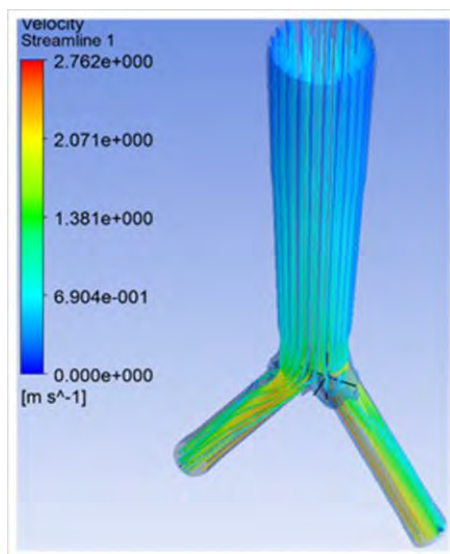


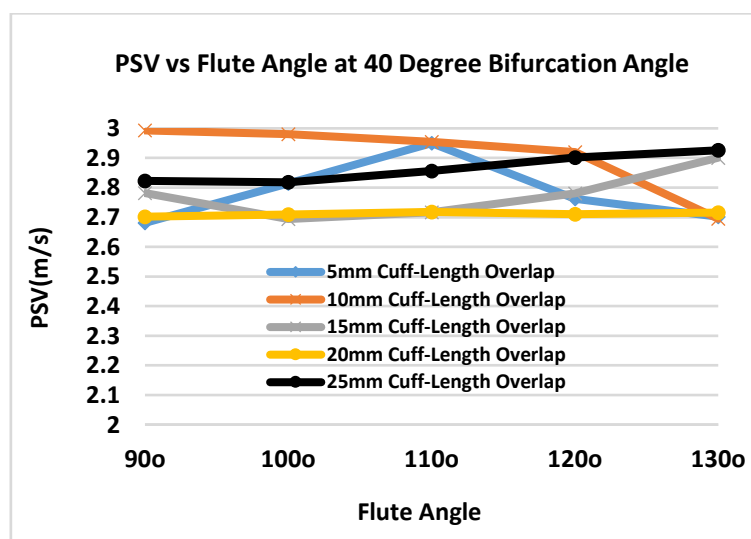
Figure 4-11 Post-processing of CFD simulation showing maximum velocity

### 4.3 Results

The PSV data from CFD simulations are tabulated in Table 4-1 and Table 4-2, and PSV vs flute angle and PSV vs cuff length overlap are plotted as shown in Figure 4-12–Figure 4-17. No significant difference was detected in PSV when comparing the cuff length overlap of 5 mm vs 10 mm, 10 mm vs 15 mm, 15 mm vs 20 mm and 20 mm vs 25 mm ( $P = 0.868, 0.360, 0.843$  and  $0.123$ , respectively). Similarly, no significant difference was detected in PSV when comparing the flute angle:  $90^\circ$  vs  $100^\circ$ ,  $100^\circ$  vs  $110^\circ$ ,  $110^\circ$  vs  $120^\circ$  and  $120^\circ$  vs  $130^\circ$  ( $P = 0.752, 0.667, 0.916$  and  $0.843$ , respectively). Moreover, no significant difference was observed when comparing the bifurcation angle of  $45^\circ$  vs  $90^\circ$  ( $P = 0.993$ ). SPSS was used to analyse the correlation between PSV and flute angle, and it was found that the correlation index (R) was 0.0816, which was insignificant. Also, the R-value for PSV and cuff length overlap was 0.0649, which was insignificant.

**Table 4-1 PSV vs flute angle at  $40^\circ$  bifurcation angle and varying cuff length overlap**

Cuff-length overlap (mm)	Flute angle				
	$90^\circ$	$100^\circ$	$110^\circ$	$120^\circ$	$130^\circ$
5	2.681	2.814	2.95	2.762	2.702
10	2.993	2.98	2.955	2.92	2.695
15	2.782	2.694	2.717	2.781	2.901
20	2.702	2.709	2.718	2.71	2.716
25	2.823	2.818	2.856	2.902	2.926
<b>Average</b>	<b>2.796</b>	<b>2.803</b>	<b>2.839</b>	<b>2.815</b>	<b>2.788</b>



**Figure 4-12 PSV vs flute angle plot at  $40^\circ$  bifurcation angle**

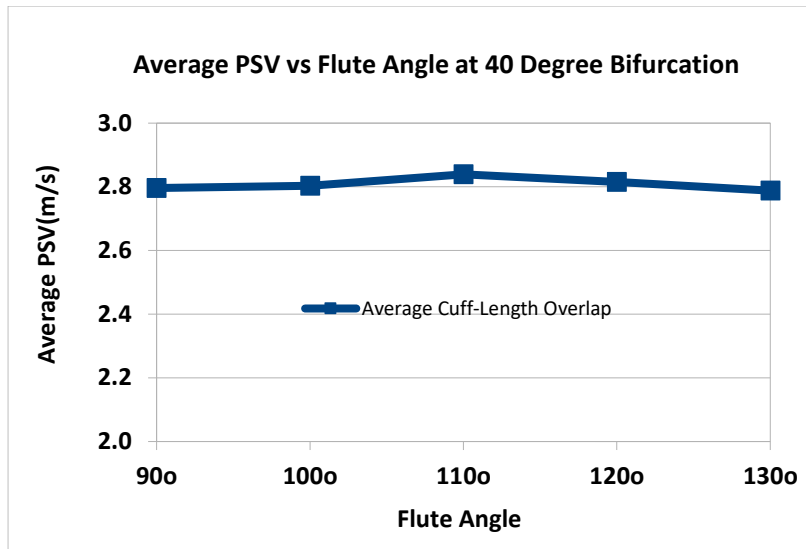


Figure 4-13 Average PSV vs flute angle at 40° bifurcation angle

Table 4-2 PSV vs Flute Angle at 90° bifurcation angle varying cuff length overlap

Cuff-length overlap (mm)	Flute angle				
	90°	100°	110°	120°	130°
5	2.627	2.639	2.693	2.475	2.505
10	2.631	2.535	2.519	2.442	2.329
15	2.436	2.393	2.399	2.502	2.475
20	2.156	2.528	2.588	2.674	2.743
25	2.513	2.528	2.593	2.736	2.743
<b>Average</b>	<b>2.473</b>	<b>2.525</b>	<b>2.558</b>	<b>2.566</b>	<b>2.559</b>

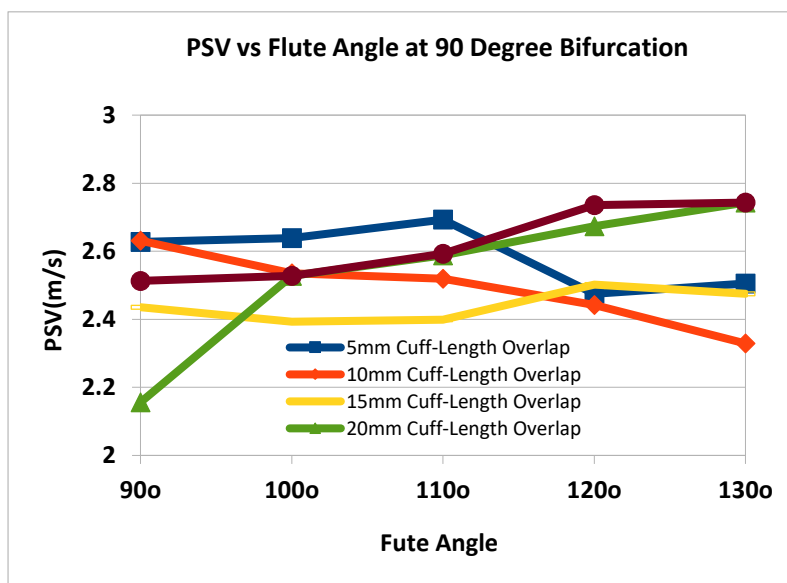


Figure 4-14 PSV vs flute angle plot at 90° bifurcation angle

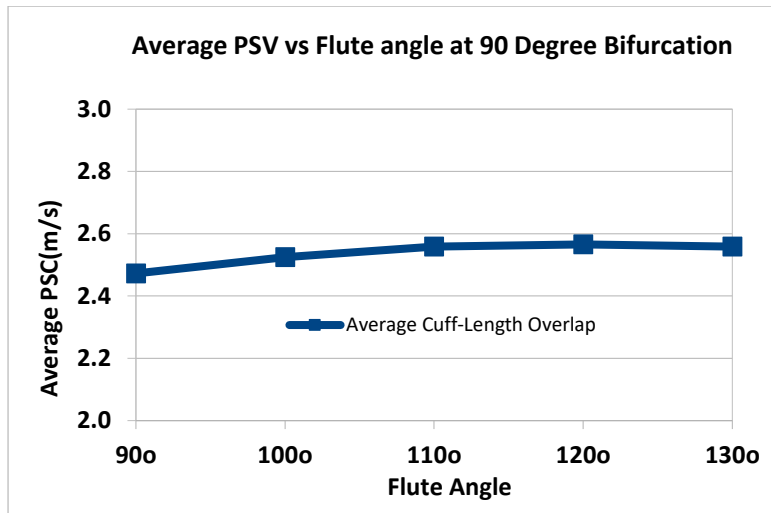


Figure 4-15 Average PSV vs flute angle at 90° d bifurcation angle

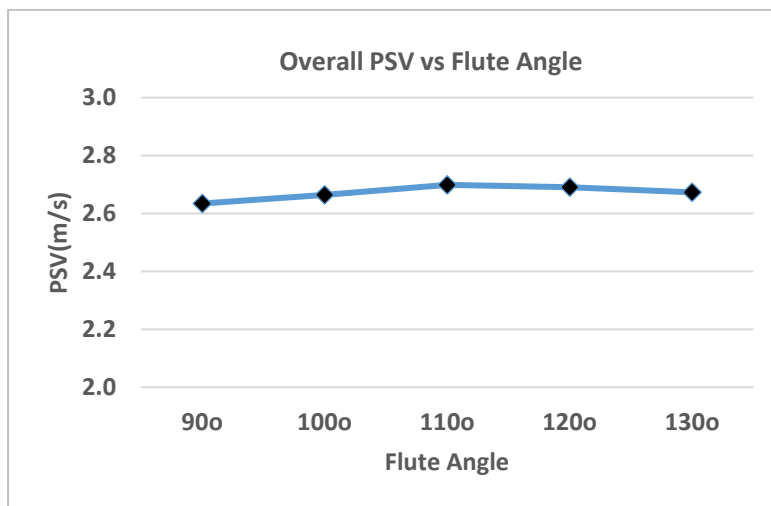


Figure 4-16 Overall PSV vs flute angle

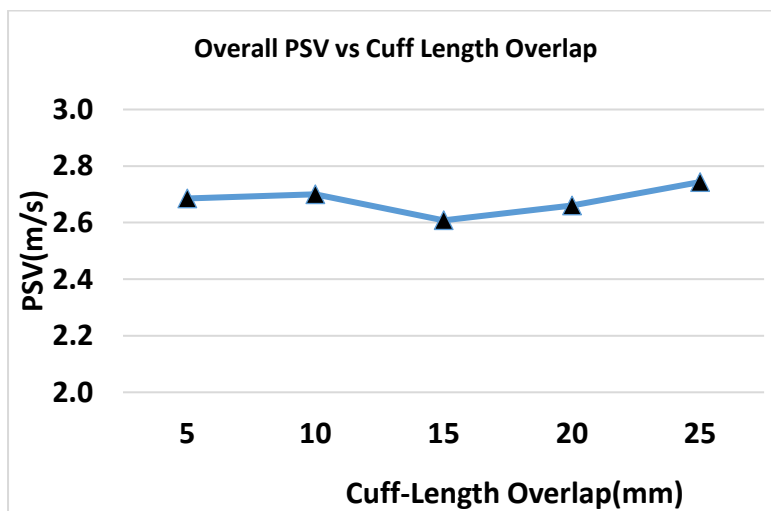


Figure 4-17 Overall PSV vs cuff-length overlap

#### 4.4 Discussion

In this study, 25 CFD simulations were performed on ideal aortoiliac geometry by varying the flute angle ( $90^\circ$  to  $130^\circ$  in  $10^\circ$  increments) and cuff-length overlap (5 mm to 25 mm in 5 mm increments) at the bifurcation angle of  $45^\circ$  and  $90^\circ$ , respectively. Based on the statistical analysis of CFD simulated data for PSV, the cuff-length overlap and flute angle exerted insignificant influence on PSV ( $P > 0.12$  and  $P > 0.67$ , respectively). Rigatelli et al. evaluated the impact of bifurcation angle and different stent configurations on AIOD using CFD [123] and reported that ‘Hi Kissing’ of 20 mm in kissing stents configuration, similar to cuff-length overlap of 20 mm in CERAB configuration in our study, was considered more physiological as compared to ‘Low Kissing’ of 5 mm or the equivalent of 5 mm cuff-length overlap. The result of the previous study was in contradiction to our finding ( $P > 0.12$ ). In addition, the study also reported that the bifurcation angle profoundly impacts the physiology of aortoiliac bifurcations, which contradicts the finding reported previously [64] and also our finding of bifurcation angle having an insignificant impact on PSV ( $P = 0.993$ ). In a retrospective study of 105 AIOD patients treated with kissing stents, Vertes et al. demonstrated that the primary patency was significantly poor ( $P < 0.001$ ) in patients with longer ( $> 20$  mm) aortic stent segments [124]. This finding was opposite to that of Rigatelli et al., thereby rendering that the aortic segment in the kissing stent is an inconclusive predictor. These observations support our finding that cuff-length overlap is insignificant as a predictor of PSV, a surrogate measure for stenosis.

One of the limitations of the current study is that the CFD simulations were based on the artery with a rigid wall; however, human arteries are not totally rigid. In addition, vessel diameters were assumed to be circular, but the actual arterial might not be perfectly circular. Finally, the current study considered the flute angle between  $90^\circ$  and  $130^\circ$ , the cuff-length overlap between 5 mm and 25 mm and bifurcation angle  $45^\circ$  and  $90^\circ$ , and thus, the conclusions drawn in this study are valid within these range of values.

#### 4.5 Conclusion

PSV has a weak correlation with flute angle, cuff length overlap and bifurcation angle, which implied that these three independent variables have a negligible influence on PSV. The current investigation was inconclusive, and no further improvement was added to the PSV predictor. Further investigations are needed to improve the prediction model. The CFD simulation model with fluid-structure interaction accounted for the non-rigid wall of the blood vessels..

## Chapter Five

# 5

### Improvement to PSV Predictor by Incorporating Additional Independent Variables in the Prediction Model

## Preamble

In this chapter, asymmetric iliac branches were introduced in the aortoiliac geometry. In addition, average ABI and ABI ratio was taken into consideration when setting the outlet pressure boundary conditions of CFD simulation based on ideal geometry. With the addition of these three independent variables plus the two independent variables established in Chapter 2, a total of five independent variables were considered in the PSV predictor. A three-level design with five factors orthogonal array was used to reduce the total number of simulations (final number to 27). The new PSV predictor was tested on 25 patients to evaluate its value as a clinical screening tool.

### 5.1 Introduction

In Chapter 3, the PSV predictor was demonstrated to be improved by applying adjustment factors taking into account the iliac and ABI asymmetries that were assumed symmetrical when the predictor was first developed and outlined in Chapter 2.

In this chapter, instead of applying manual adjustments to the PSV predictor, iliac asymmetry, average ABI, and ABI ratio were treated as independent variables in the design of experiments. The correlation between the predicted PSV from CFD simulation and the five independent variables was established based on the coefficients for each of the independent variable derived from the regression analysis, wherein statistically significant variables were incorporated in the prediction model.

The predicted PSV was plotted against that measured by Doppler ultrasound for the 25 clinical cases provided by the clinicians during post-stent implant follow-ups. The graphical plot with  $\pm 15\%$  deviation from the unity line was used as a screening tool wherein cases under the 'new normal' zone are deemed to be non-restenosis cases and those outside the 'new normal' zone are deemed to be restenosis cases. Then, the screening data were compared to the gold standard used by the clinicians in the determination of the status restenosis based on CTA.

Statistical analysis was performed to evaluate the predictive parameters, including sensitivity, specificity, PPV and NPV of the screening tool against the gold standard.

## 5.2 Materials and Methods

Five independent variables, inlet velocity ( $PSV_{in}$ ), iliac to aorta area ratio, iliac asymmetry, average ABI and ABI ratio, were assessed in this exercise to determine their effects on PSV using CFD simulations. The workflow is outlined in Figure 5-1.

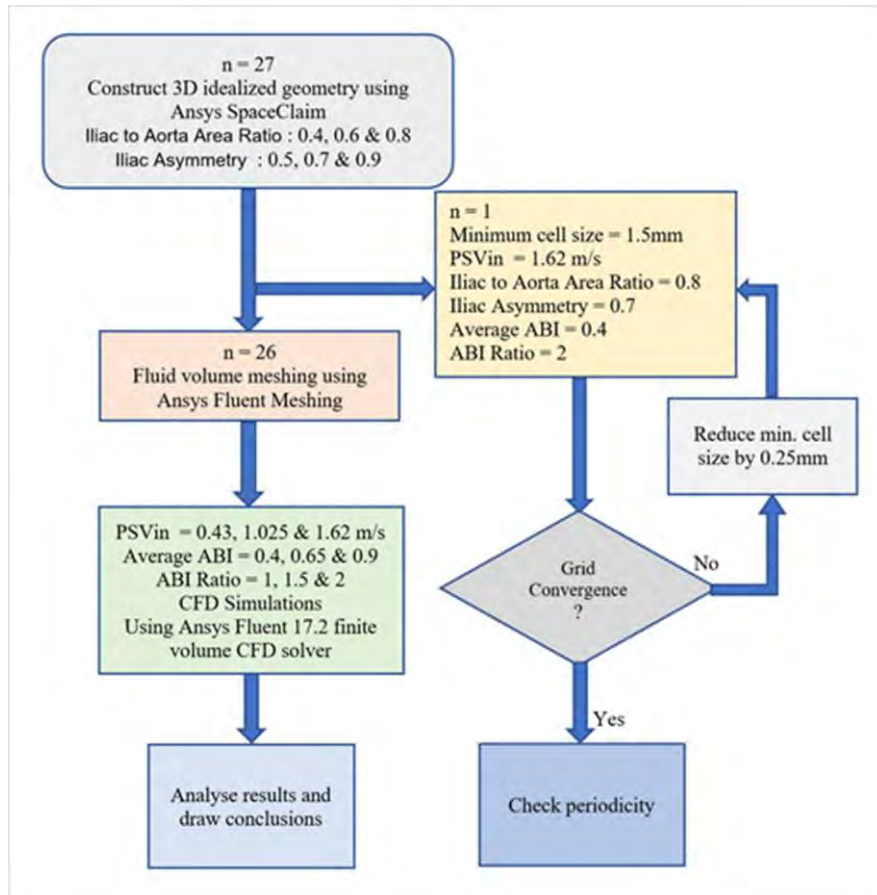


Figure 5-1 Workflow for ideal geometry 3D flow model and CFD simulations

The ideal 3D geometry of an aortoiliac flow model with parameters of 0.8 iliac to aorta area ratio and 0.9 iliac asymmetry was created using Ansys SpaceClaim, a direct modeller CAD software. The 3D volume of the fluid model was first created using Ansys fluent meshing with a minimum mesh size of 1.5 mm, followed by CFD simulation by setting inlet boundary condition of  $PSV_{in}$  to 1.62 m/s and assigning characteristic resistance ( $R_p$ ), distal resistance ( $R_d$ ) and compliance ( $Z$ ) at the two outlets to achieve the desired setting of 0.4 for average ABI and 2 for ABI ratio. Figure 5-2 shows a typical CFD set-up with boundary conditions assigned to inlet and outlets. Ansys Fluent 17.2, a finite volume CFD solver was used for simulation wherein grid independence was tested by reducing the minimum cell size by 0.25 mm, and the grid refinement was ceased when  $PSV_{max}$  varied by  $< 1\%$  between the two consecutive schemes. In addition, it was



speculated that periodicity was reached when PSV, ESV and PDV of two consecutive periodic cycles varied by  $< 1\%$ . 3D model construction, meshing and CFD set-up were implemented as described in Chapter 4, sections 4.2.1 to 4.2.3, and in a total of 27 CFD simulations were performed.

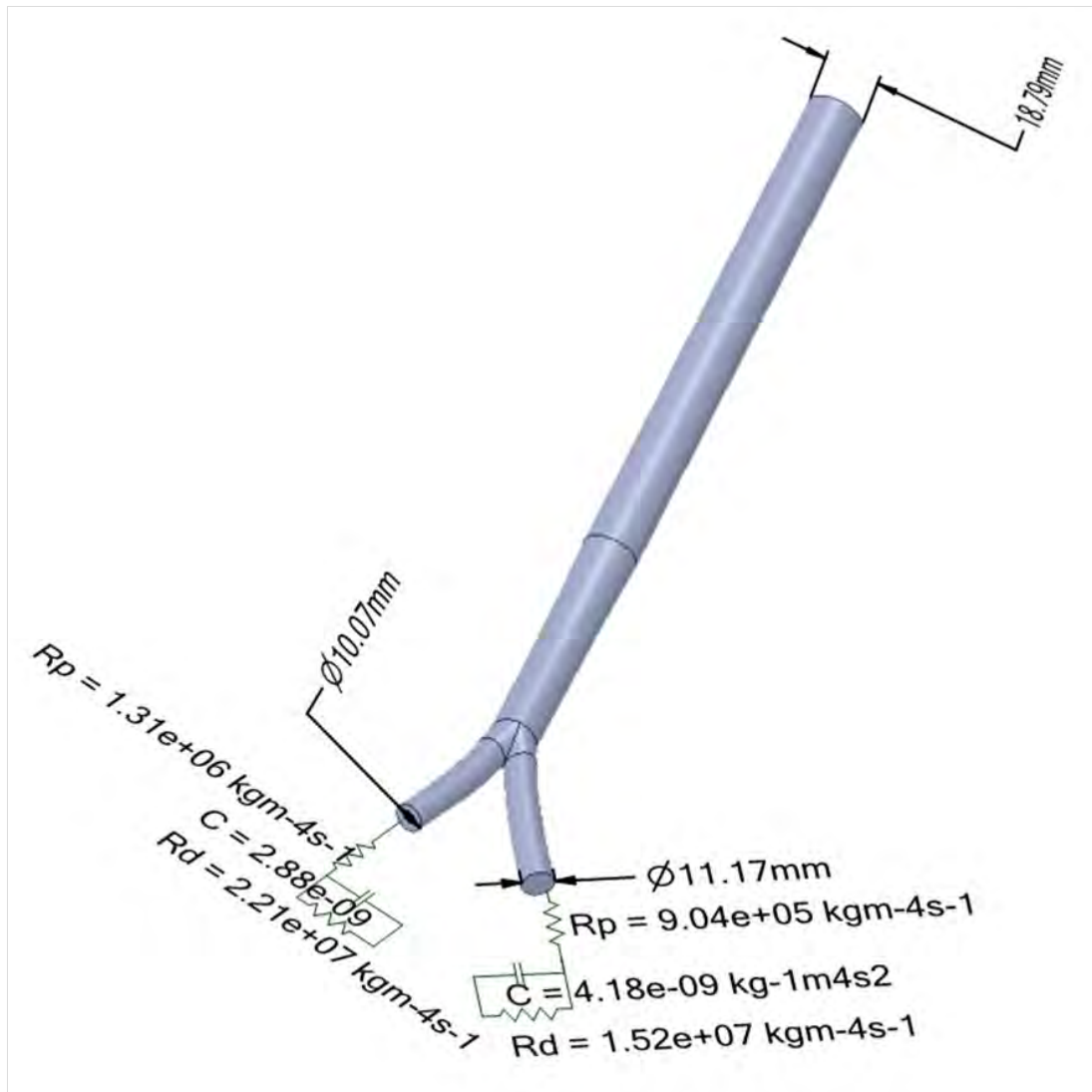


Figure 5-2 Typical CFD set-up with assigned boundary conditions

### 5.3 Results

The five independent variables in L27 Taguchi orthogonal array were organized in such a way that 27 combinations were sufficient to draw a conclusion for the effects of independent variables on the dependent variable. Table 5-1 shows the data of dependent variable  $PSV_{\max}$  from each of the 27 CFD simulations.

**Table 5-1** Data of  $PSV_{max}$  from CFD simulations

Simulation number	$PSV_{in}$	Iliac to aorta area ratio	Iliac asymmetry	Average ABI	ABI ratio ( $ABI_{left}/ABI_{right}$ )	$PSV_{max}$ from CFD Simulation
1	0.43	0.4	0.5	0.4	1	1.384
2	0.43	0.4	0.5	0.4	1.5	1.237
3	0.43	0.4	0.5	0.4	2	1.169
4	0.43	0.6	0.7	0.65	1	0.856
5	0.43	0.6	0.7	0.65	1.5	0.776
6	0.43	0.6	0.7	0.65	2	0.824
7	0.43	0.8	0.9	0.9	1	0.626
8	0.43	0.8	0.9	0.9	1.5	0.686
9	0.43	0.8	0.9	0.9	2	0.737
10	1.025	0.4	0.7	0.9	1	2.619
11	1.025	0.4	0.7	0.9	1.5	2.618
12	1.025	0.4	0.7	0.9	2	2.653
13	1.025	0.6	0.9	0.4	1	1.850
14	1.025	0.6	0.9	0.4	1.5	1.920
15	1.025	0.6	0.9	0.4	2	2.046
16	1.025	0.8	0.5	0.65	1	1.702
17	1.025	0.8	0.5	0.65	1.5	1.796
18	1.025	0.8	0.5	0.65	2	1.890
19	1.62	0.4	0.9	0.65	1	4.021
20	1.62	0.4	0.9	0.65	1.5	4.114
21	1.62	0.4	0.9	0.65	2	4.386
22	1.62	0.6	0.5	0.9	1	3.077
23	1.62	0.6	0.5	0.9	1.5	2.934
24	1.62	0.6	0.5	0.9	2	3.005
25	1.62	0.8	0.7	0.4	1	2.651
26	1.62	0.8	0.7	0.4	1.5	2.635
27	1.62	0.8	0.7	0.4	2	2.682

Based on the main effects plot in Figure 5-3, the mean values of the dependent variable  $PSV_{max}$  were plotted for each level of the dependent variables.  $PSV_{in}$  has the strongest effect on the predicted PSV, followed by iliac to aorta area ratio, iliac asymmetry, average ABI and ABI ratio. The data of multivariable regression analysis are shown in Table 5-2, and the prediction equation was established, as shown in equation (5.1).

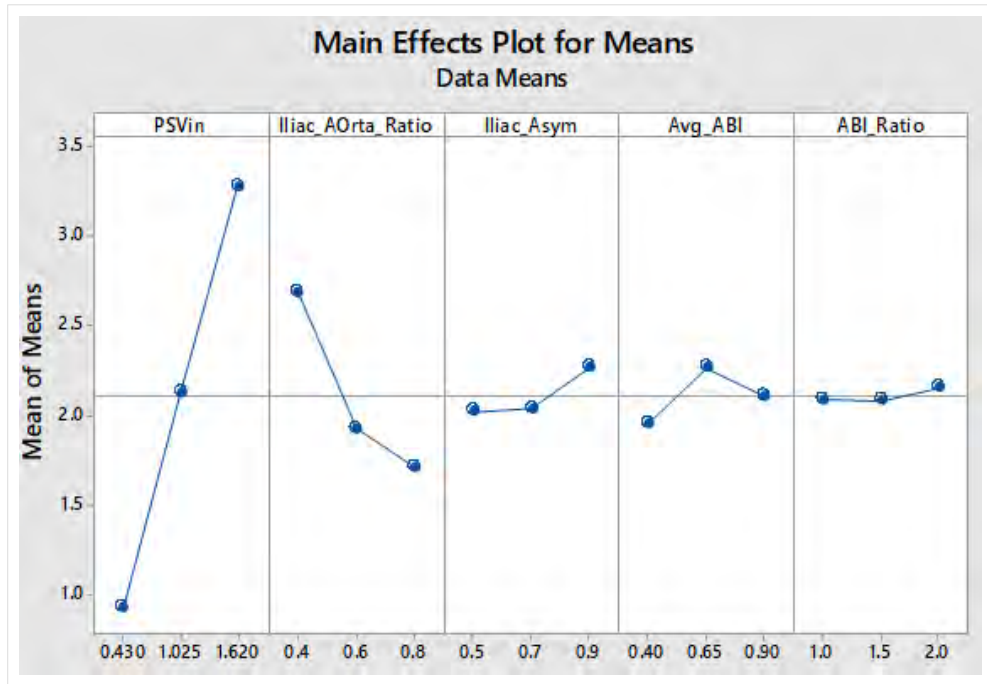


Figure 5-3 Main effects plot

Table 5-2 Data of multivariable regression analysis

SUMMARY OUTPUT						
Multiple R	0.984					
R square	0.967					
Adjusted R square	0.960					
Standard error	0.219					
Observations	27					
ANOVA						
	<i>df</i>	<i>SS</i>	<i>MS</i>	<i>F</i>	<i>F</i>	
Regression	5	29.686	5.937	124.283	0.000	
Residual	21	1.003	0.048			
Total	26	30.689				
	<i>Coefficients</i>	<i>Standard error</i>	<i>t</i>	<i>P-value</i>	<i>Lower 95%</i>	<i>Upper 95%</i>
Intercept	0.817	0.328	2.486	0.021	0.134	1.500
PSV <sub>in</sub>	1.980	0.087	22.873	0.000	1.800	2.160
Iliac to aorta area ratio	-2.444	0.258	-9.488	0.000	-2.980	-1.908
Iliac asymmetry	0.609	0.258	2.365	0.028	0.073	1.145
Average ABI	0.307	0.206	1.489	0.151	-0.122	0.735
ABI ratio (ABI <sub>left</sub> /ABI <sub>right</sub> )	0.068	0.103	0.655	0.519	-0.147	0.282

Predictive equation (5.1) was used to calculate PSV based on each of the 25 patient-specific geometries and ABI measurements.

$$\text{PSV-cap} = 0.817 + 1.98\text{PSV}_{\text{in}} - 2.44\text{R} + 0.609\text{IA} + 0.307\text{AA} + 0.068\text{AR} \quad (5.1)$$

Wherein:

PSV-cap is the predicted PSV

PSV<sub>in</sub> is inlet PSV

R is iliac to aorta area ratio

IA is iliac asymmetry (area ratio of left CIA over right CIA)

AA is average ABI between left and right ankle/brachial

AR is ratio of right ABI over left ABI

Six patients with restenosis of the aortoiliac lesion were identified by clinicians during post-stenting follow-up based on gold standard CTA method in determining restenosis. These six cases are marked with shaded rows in Table 5-3.

The predicted PSV was plotted against measured PSV by Doppler ultrasound measured PSV, as shown in Figure 5-4 Predicted vs DU measured PSV for improved PSV predictor

the six red dots indicate restenosis cases. A screening tool for restenosis was adjusted to  $\pm 15\%$  from the unity line as the upper and lower bounds where points inside the 'new normal' upper and lower bands were deemed to be free from restenosis and points outside the 'new normal' zone were deemed to have the condition of restenosis.

Table 5-4 shows the status of restenosis based on the gold standard as compared to the screening tool. Sensitivity, specificity, PPV and NPV for the improved predictor were found to be 83%, 47%, 33% and 90%, respectively.

**Table 5-3 Predicted PSV based on the improved PSV predictor**

<b>Patient number</b>	<b>PSV<sub>in</sub> (m/s)</b>	<b>Aorta diameter (mm)</b>	<b>Right CIA dia (mm)</b>	<b>Left CIA dia (mm)</b>	<b>R</b>	<b>Right ABI</b>	<b>Left ABI</b>	<b>Predicted PSV (m/s)</b>
1	0.81	13.60	7.57	6.55	0.54	1.09	1.05	2.24
2	0.94	14.43	7.16	6.73	0.46	1.02	1.08	2.56
3	1.06	15.93	10.87	9.40	0.81	1.10	1.11	2.08
4	0.65	16.30	7.45	7.06	0.40	1.00	1.01	2.12
5	0.88	15.97	9.75	11.50	0.89	1.06	1.08	1.56
6	1.55	18.90	8.17	9.87	0.46	0.70	0.60	3.85
7	0.44	15.67	4.33	6.04	0.22	0.61	0.80	2.54
8	1.41	12.65	6.88	6.81	0.59	1.15	1.09	3.15
9	0.43	16.90	7.09	8.50	0.43	1.08	1.07	1.83
10	0.85	16.00	9.46	7.99	0.60	1.14	1.21	2.25
11	0.55	12.50	8.33	7.07	0.76	1.10	1.02	1.21
12	0.77	14.80	6.44	6.78	0.40	1.10	0.86	2.34
13	1.00	15.27	7.51	7.07	0.46	0.58	1.01	2.61
14	1.11	14.20	6.34	6.85	0.43	1.13	1.15	3.02
15	1.62	13.00	8.32	10.80	1.10	1.07	1.07	2.70
16	0.63	15.47	8.71	10.90	0.81	1.00	0.64	1.28
17	0.62	13.27	4.63	7.58	0.45	0.58	0.55	2.75
18	0.95	17.40	7.85	11.23	0.62	1.25	0.97	2.77
19	0.92	14.17	7.01	7.61	0.53	0.99	1.00	2.36
20	0.70	16.27	8.27	11.70	0.78	0.94	0.98	1.82
21	0.50	17.50	5.27	4.89	0.17	0.73	0.67	2.32
22	0.44	15.60	7.33	7.93	0.48	0.93	0.89	1.51
23	0.64	13.47	8.59	7.49	0.72	1.00	1.00	1.45
24	0.87	14.60	6.52	5.40	0.34	1.07	0.84	2.90
25	0.96	18.90	8.86	8.58	0.43	1.13	1.09	2.67

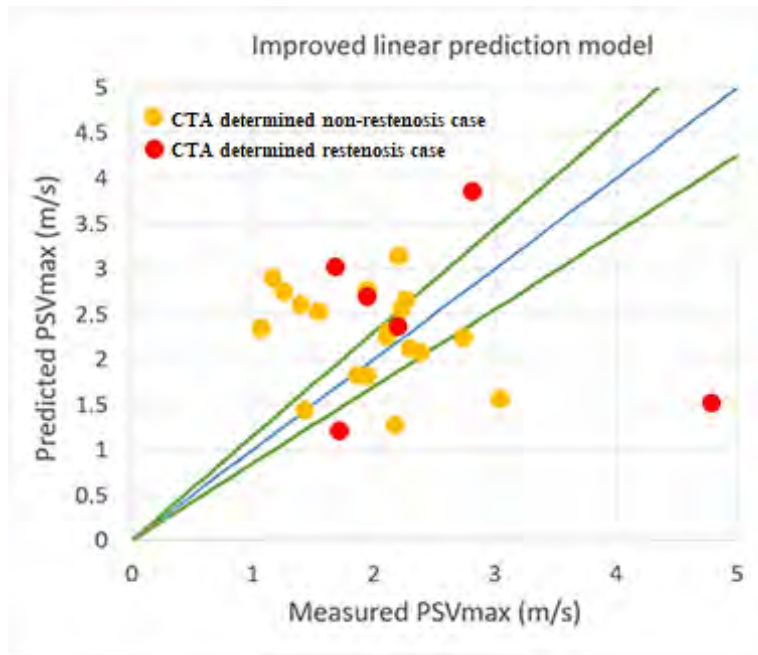


Figure 5-4 Predicted vs DU measured PSV for improved PSV predictor

Table 5-4 Status of restenosis based on 'gold standard' for improved PSV predictor

Outcome	Has restenosis	Does not have restenosis	Total
Results from Predictor Screening			
Positive	5	10	15
Negative	1	9	10
<b>Totals</b>	<b>6</b>	<b>19</b>	<b>25</b>

$$\text{Sensitivity} = \frac{5}{5+1} \times 100 = 83\% \quad (5.2)$$

$$\text{Specificity} = \frac{9}{9+10} \times 100 = 47\% \quad (5.3)$$

$$\text{PPV} = \frac{5}{5+10} \times 100 = 33\% \quad (5.4)$$

$$\text{NPV} = \frac{9}{9+1} \times 100 = 90\% \quad (5.5)$$

## 5.4 Discussion

In the current study, a Taguchi L27 orthogonal array was constructed using five independent variables ( $PSV_{in}$ , iliac to aorta area ratio, iliac asymmetry, average ABI and ABI ratio). The data of PSV obtained from the 27 CFD simulations were compared to the corresponding value measured using duplex ultrasound. Using CTA as reference for restenosis, the sensitivity, specificity, PPV and NPV were assessed for their suitability as a screening tool. The findings were similar to those obtained in Chapter 0 when manual adjustments for the iliac and ABI asymmetries were incorporated into the prediction model: sensitivity was 83% vs 100%, specificity was 47% vs 42%, PPV was 33% vs 35% and NPV was 90% vs 100%. These results are less predictive as compared to the demonstrated sensitivity of 87.6% and specificity of 94.7% for Duplex ultrasound in detecting stenosis, as reported in a meta-analysis by Visser et al. [125]. Based on another meta-analysis of screening tests by Alberg et al. [126], represented by green triangles, and Maxim et al. [127], represented by blue circles, (Figure 5-5), most of the screening tests have coordinates of sensitivity and specificity congregating at the upper right corner of the specificity vs sensitivity plot.

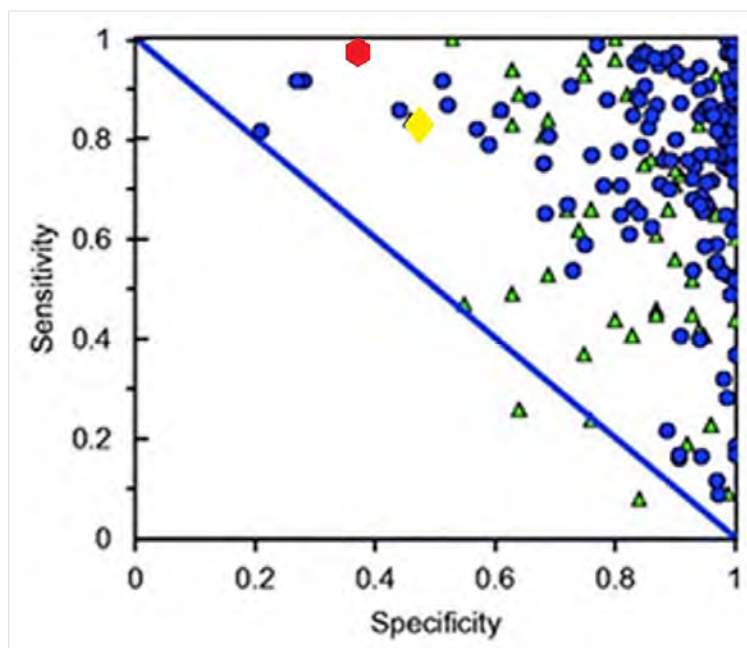


Figure 5-5 Sensitivity vs specificity plot for existing screening tests

The screening test with PSV predictor adjusted for iliac and ABI asymmetries outlined in Chapter 3 is represented by a red hexagon, whereas the PSV predictor modelled on five independent variables outlined in this chapter is represented by a yellow diamond.

Nevertheless, the present study has some limitations. First, it is a retrospective study inherently associated with selection bias and lesser evidence as compared to prospective studies. Second, a small sample size of 25 AIOD patients was available to determine the sensitivity, specificity, PPV and NPV of the predictor. Third, the wall was assumed to be rigid in CFD simulation, but the artery wall is not totally rigid. Finally, the arteries are assumed to be of circular morphology, but human arteries are usually not perfectly circular.

## **5.5 Conclusion**

The improved PSV predictor based on five independent variables has the potential to be used as a screening tool based on high sensitivity. In the current retrospective study of a cohort of 25 patients, 47% of non-restenosis cases would have avoided unnecessary cost and risk associated with follow-up CTA. However, with 83% sensitivity, one of the six restenosis cases would have slipped through the screening test as a false-positive.





6

**Hemodynamic Comparison of AFX Stent-Graft and CERAB Configuration for Treatment of Aortoiliac Occlusive Disease**

## Preamble

Minimally invasive endovascular treatment of complex aortoiliac occlusive disease with stents is now a preferred option as compared with open surgery due to its high technical success, high patency rate and shorter hospital stay. However vascular surgeons are inundated with choices of stents especially treatment strategies using newer and more advanced stent designs. In this chapter, we compared hemodynamic parameters including wall shear stress, oscillatory shear index and relative resident time obtained for CERAB and AFX stents using laser particle image velocimetry experiments.

A manuscript based on the experimental research comparing hemodynamics of CERAB and AFX stents was submitted on the 23<sup>rd</sup> of June, 2020 and it has been accepted for publication by the Journal of Endovascular Therapy on the 29<sup>th</sup> of September, 2020 subject to revisions suggested by the reviewers.

## 6.1 Introduction

The covered endovascular reconstruction of aortic bifurcation (CERAB) technique is a relatively new approach in treating extensive AIOD [75, 128]. One of the advantages of the CERAB configuration is that it reduces radial mismatch defined as the discrepancy between the stented lumen and the vessel lumen after stent placement as compared to the traditional kissing stent procedure [129]. This leads to more favourable flow conditions. Initial clinical data for CERAB are encouraging, with 87.3% and 82.3% primary patency rate at one and two year follow up in a group of 103 patients with 88% TransAtlantic Inter-Society Consensus II D lesions [129] as compared with 91.5% primary patency rate at two year follow up for open surgery [130]. Taeymans et al [131] further updated the CERAB results with a total of 130 patients showing a primary patency of 82.0% was achieved at three year follow up.

More recently, it was suggested that the use of a unibody stent-graft, designed for aneurysm treatment, could have several advantages for the treatment of AIOD over CERAB. It preserves the aortic bifurcation, avoid limb competition in the distal aorta, allow for future endovascular interventions, and protect against potentially fatal aortoiliac rupture in heavily calcified lesions. The AFX stent-graft (Endologix, Inc, Irvine, CA, USA) is a thin-walled expanded polytetrafluoroethylene (ePTFE) sheath with an endoskeleton made of Elgiloy (cobalt-chromium alloy). The benefit of the AFX stent-graft is the fact that radial mismatch is totally eliminated because of the one piece bifurcation design. The safety, efficacy, and early patency rates of the AFX unibody stent-graft for

treatment of AIOD were examined by several groups, totalling 128 patients [20-22, 132]. Primary patency rate for these studies were reported in the range of 80% to 100% at one year follow up. The primary and secondary patency for the largest study with ninety patients were 78.8% and 100% at three years follow up.

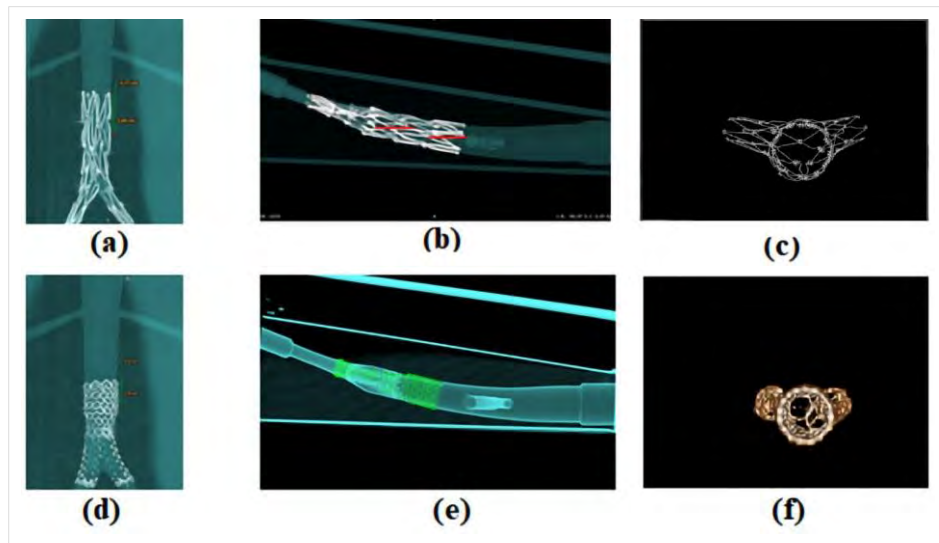
Even though both of these minimally invasive endovascular treatment modalities are effective in treating extensive AIOD, the hemodynamic differences between CERAB and AFX stents are currently unknown therefore a vitro study might provide new and valuable information for existing stent manufacturers and vascular surgeons to make further improvement in treatment of AIOD patients. Particle image velocimetry (PIV) is a powerful experimental method to analyse hemodynamic parameters such as flow pattern, wall shear stress (WSS) and oscillatory flow index (OSI) in an in vitro setting with flow phantoms. Laser PIV is the current gold standard for flow imaging [133-135]. The aim of this study is to test the hypothesis that AFX stent-graft is superior to CERAB in terms of flow pattern and hemodynamic outcomes.

## **6.2 Materials and methods**

### **6.2.1 Model designs and stent deployment**

Two identical aortoiliac bifurcation anatomy mimicking flow models were used in this experimental study [74]. A CERAB configuration with modified covered stents was deployed in one flow model and a modified AFX unibody stent in the other. The detailed production process for making these flow models were previously described [74]. The CERAB model was configured by using three in-house covered stents comprising of two 8-mm and one 12-mm balloon expandable stents. These stents were derived from Advanta V12 stents (Getinge Group, Wayne, MA, USA) where the ePTFE graft covers were manually removed and subsequently individually coated with a transparent polyurethane (Tecoflex TPU clear; The Lubrizol Corporation, Wickliffe, Ohio, United States) cover using a dip coating process which facilitated the visualization of flow patterns inside the flow model [129] and [57]. The polyurethane dipping process was not suitable to replace the ePTFE cover of AFX stent because of the large spaces between unibody struts in its expanded configuration. The AFX ePTFE cover was made of two cylindrical shaped grafts and stitched together to form the unibody. A manual stitching method was used to replicate the ePTFE cover with a low density polyethylene (LDPE) film. The covering material was on the outer layer as with the original stent. Details of AFX transparent cover making process are found in Appendix C. Figure 6-1 shows the computed tomography (CT)

images of the AFX and CERAB flow models. The segmented CT images were used as a guide to determine inflow and bifurcation region of interest.



**Figure 6-1** Computed Tomography (CT) images of the flow phantoms. **A:** Anterior view of AFX. **B:** Lateral view of AFX. **C:** Superior view of AFX. **D:** Anterior view of CERAB. **E:** Lateral view of CERAB. **F:** Superior view of CERAB. The red lines indicate the location of the laser sheet.

## 6.2.2 Experimental flow circuit

An experimental flow circuit as shown in Figure 6-2 was used to study and compare hemodynamics in the AFX and CERAB. The flow loop was driven by a positive displacement pulsatile pump, SuperPump and its accompanying software Vivitest (Vivitro Labs Inc., Victoria, CA). A blood mimicking fluid (BMF) comprising of water (47.4%), glycerol (36.9%) and urea (15.7%) was used to obtain a fluid with refractive index optically matching that of PDMS model and physiologically matching that of human blood (dynamic viscosity 4.3cP, density 1244 kg/m<sup>3</sup>) [136]. The BMF was drawn from the reservoir by Vivitro pump and a suprarenal flow profile mimicking human resting conditions with a mean flow rate of 1.6L/min or a stroke volume of 26.7mL and 60 beats per minute heart rate was generated by the Vivitest software using a custom flow profile. A CORRI\_FLOW M55 Coriolis flow meter (Bronkhorst High-Tech) B.V., AK Ruurlo, the Netherlands) was used to provide real time display of the desired suprarenal flow profile. Three UF8B ultrasound flow sensors (Cynergy3 Components Ltd, Wimborne, Dorset, United Kingdom) and three needle valves were connected to left renal outlet, right renal outlet and the combined iliac outlets. A display unit provided real-time display of flow rates of BMF flowing through the ultrasound flow sensors. The needle valves were manually adjusted to achieve a mean pressure of 100 mmHG and approximately 25% outflow or 0.4L/min at the

left and right renal outlet and approximately 50% or 0.8L/min outflow at the combined iliac outlet. In addition, the two iliac outlets were connected to a single compliance chamber. A DS44 hand held Sphygmomanometer (Welch Allyn, Skaneateles Falls, New York) was used to set the distal peripheral pressure between 80 and 120 mmHg.

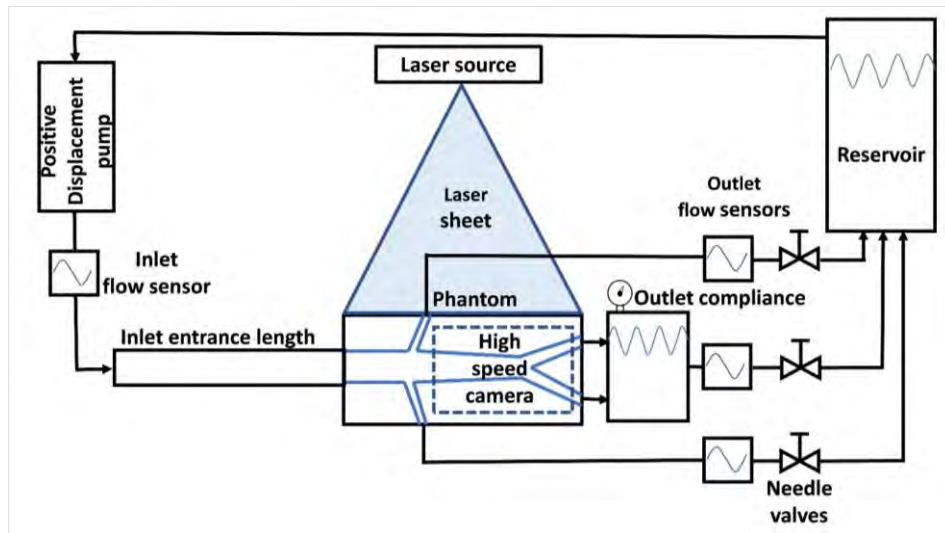
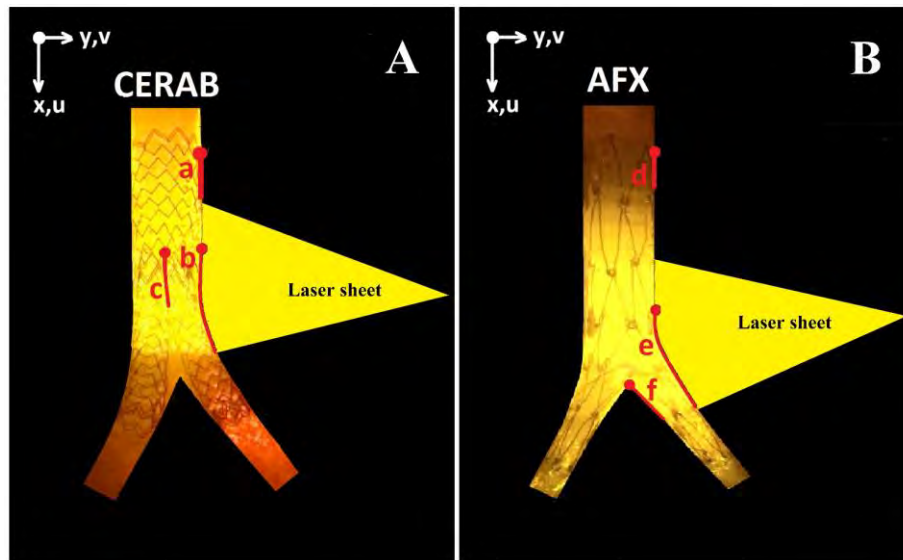


Figure 6-2 Experimental flow circuit and laser particle image velocimetry (PIV) set-up

### 6.2.3 Flow visualization

In order to facilitate the visualization of flow pattern inside the phantom, a continuous laser sheet was projected horizontally into the centre of the stented lumen region of interest. The position of the phantom was manually adjusted in such a way that the laser sheet was projected onto the centre of inflow and bifurcation Regions Of Interest as shown in Figure 6-3. The Regions Of Interests for the AFX and CERAB are not identical due to minor differences in their configurations. The laser sheet was slightly obscured by the renal branch at the inflow proximal section of AFX stent therefore its inflow Region Of Interest was shifted distal slightly as compared with that of CERAB inflow. In addition, the bifurcation Regionb Of Interest for the AFX stent was close to matching the native bifurcation because the configuration of unibody AFX stent was designed to mimic the native bifurcation. However, the bifurcation Regionb Of Interest for the CERAB was shifted proximally about 20 mm towards the renal vessels due to how the CERAB bifurcation was reconstructed using one aortic stent and two iliac stents.



**Figure 6-3** Images of bifurcation region illuminated by laser during PIV experiment. **A:** CERAB configuration, **B:** AFX stent-graft. The red dots are the origins and the red lines are the segment along vessel wall where wall shear data were analysed. (a) CERAB inflow, (b) CERAB bifurcation right edge, (c) CERAB bifurcation left edge, (d) AFX inflow, (e) AFX bifurcation right edge, (f) AFX bifurcation left edge,  $x$ : position in vertical axis,  $y$ : position in horizontal axis,  $u$ : velocity in vertical axis,  $v$ : velocity in horizontal axis.

Rhodamine-coated fluorescent polymethyl methacrylate particles (size, 1-20 $\mu\text{m}$ ; density, 1190  $\text{kg}/\text{m}^3$ ) were suspended in the BMF solution. Digitized photographic images were produced by using a continuous-wave laser (5W DPSS laser, 532 nm; Chlibri, Lightline, Germany) and a high speed camera (FASTCAM SA-Z; Photron Inc, West Wycombe, Buckinghamshire, UK). The images with 1,024 x 1,024 pixels resolution and 8 bit/pixel grey scale intensity were captured at a frequency of 2000 Hz. The camera was mounted with its optical axis perpendicular to the laser sheet. Two sets of images were captured for the CERAB phantom at proximal inflow and aortoiliac bifurcation and then repeated for the AFX phantom.

#### 6.2.4 Data processing

Data processing was described previously [129]. Since there are two regions of interest per stent configuration data processing was performed on a total of four data sets. For each data set, twelve cardiac cycles were obtained and averaged to provide one averaged cycle per data set. Using an in-house developed MATLAB (version 2016ba; The MathWorks Inc, Natick, Mass) script, the following hemodynamic parameters were calculated along the vessel wall. At the inflow, bifurcation right edge and bifurcation left edge were as shown in Figure 6-3. TAWSS, OSI and RRT were computed according to equations (6.1), (6.2) and (6.3).

$$\text{Wall Shear Stress (WSS), } \tau_w = \mu \frac{\partial u}{\partial y},$$

Where:

$\mu$  is dynamic viscosity and  $\frac{\partial u}{\partial y}$  is the rate of change of axial velocity with respect to the distance perpendicular to the direction of blood flow along the vessel wall.

$$\text{Time Averaged Wall Shear Stress (TAWSS)} = \frac{1}{T} \int_0^T |\tau_w| dt \quad (6.1)$$

$$\text{Oscillatory Shear Index (OSI)} = \frac{1}{2} \left( 1 - \frac{\int_0^T \tau_w dt}{\int_0^T |\tau_w| dt} \right) \quad (6.2)$$

$$\text{Relative Residence Time (RRT)} = \left( \frac{1}{(1-2 \cdot \text{OSI}) \cdot \text{TAWSS}} \right) \quad (6.3)$$

TAWSS is computed as the average WSS over a cardiac cycle where only the magnitude of the shear stress is taken into consideration. It is the average shear stress axially exerted on the vessel wall due to the blood flow motion akin to rubbing action along the vessel wall. A value of 0.5 to 1.2 Pa is considered as physiological WSS in human arterial blood flow and values below and above this range are considered low and high WSS, respectively. [137, 138] On the other hand OSI takes into account the WSS direction with respect to the mean blood flow direction during the cardiac cycle. The OSI can vary from 0 to 1, 0 meaning no cyclic variation, 0.5 implying 50% forward flow and 50% reverse flow and 1 a complete 180-degree change in the WSS direction or 100% reverse flow. OSI has been studied as a relevant biomarker, for the assessment of vessel areas that are predisposed to develop atherosclerosis plaque. [139-141] RRT indicates the time of residence the molecules spent at vessel wall and it is an appropriate tools for atherosclerosis localization where high RRT distribution might imply possible regions of atheromatic concentrations [84].

Time points, as indicated in Figure 6-4, for peak systolic velocity (PSV), end-systolic velocity (ESV), and peak diastolic velocity (PDV), were chosen to compare flow patterns between AFX and CERAB models.

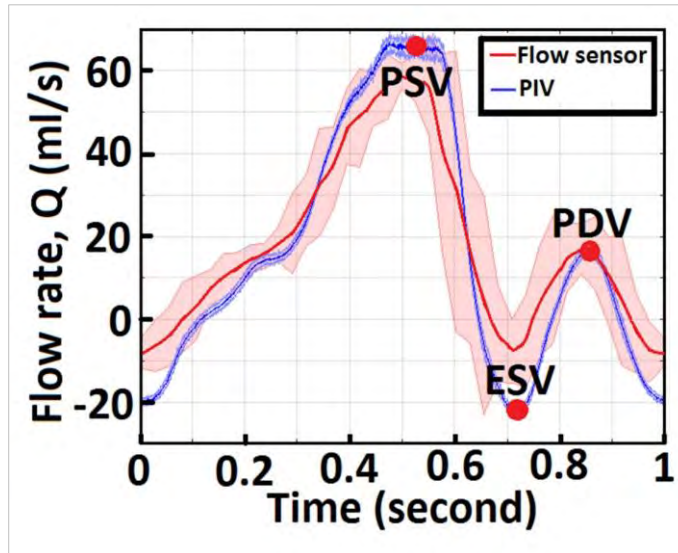


Figure 6-4 Flow waveform: Red line represents flow waveform obtained with flow sensor at the inlet of the system. Blue line represents flow profile in the phantom determined by PIV analysis. The shadow bars represent two standard deviations (SD) over ten cycles. The red dots indicate peak systolic velocity (PSV), end systolic velocity (ESV) and peak diastolic velocity (PDV) time-points used for the hemodynamic analysis



## 6.3 Results

### 6.3.1 Inflow pattern

Figure 6-5 shows the inflow patterns for AFX and CERAB at PSV, ESV and PDV time points. At the PSV time-point, the maximum velocity was achieved as the BMF accelerated into the phantom. A disturbed flow pattern was observed at the AFX inflow especially at the ESV time point as shown in Figure 6-5B. Flow reversal was observed during the end-systolic phase and re-circulation was noticeable in the AFX phantom (Video 1<sup>3</sup>, online only; Figure 5B). In contrast, unidirectional flow was observed in the CERAB inflow without noticeable disturbances (Video 2<sup>4</sup>, online only; Figure 5E). At the PSV time-point, the maximum velocity was achieved as the BMF accelerated into the phantom and achieved a fully developed velocity flow profile in both the AFX and CERAB model. Disturbed flow pattern was observed at AFX inflow especially at the ESV time point as shown in Figure 6-5(B). Flow reversal was observed during the end-systolic phase and re-circulation was noticeable in the AFX phantom (Figure 6-5(B)). In contrast, laminar and streamline flow was observed in the CERAB inflow without noticeable disturbed flow (Figure 6-5(E)).

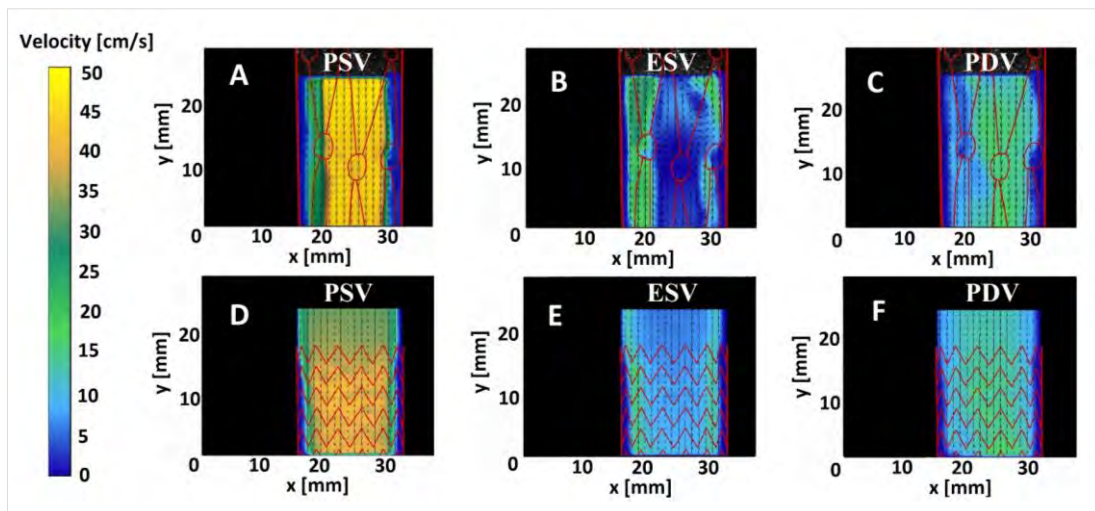


Figure 6-5 Inflow patterns: (A) AFX at PSV time-point, (B) AFX at ESV time-point, (C) AFX at PDV time-point, (D) CERAB at PSV time-point, (E) CERAB at ESV time-point and (F) CERAB at PDV time-point

<sup>3</sup> <https://vimeo.com/manage/427987384/general>

<sup>4</sup> <https://vimeo.com/manage/427996402/general>

### 6.3.2 Bifurcation flow pattern

Bifurcation flow pattern for AFX and CERAB at PSV, ESV and PDV time-points are shown in Figure 6-6. Disturbed flow was observed in the AFX stent in all three phases of the triphasic flow especially more pronounced during the end-systolic phase (Video 3<sup>5</sup>, online only; Figure 6-6(A), (B) and (C)). In contrast, only slightly disturbed flow was observed in the CERAB configuration during the end-systolic phase (Video 4<sup>6</sup>, online only; Figure 6-6(E)).

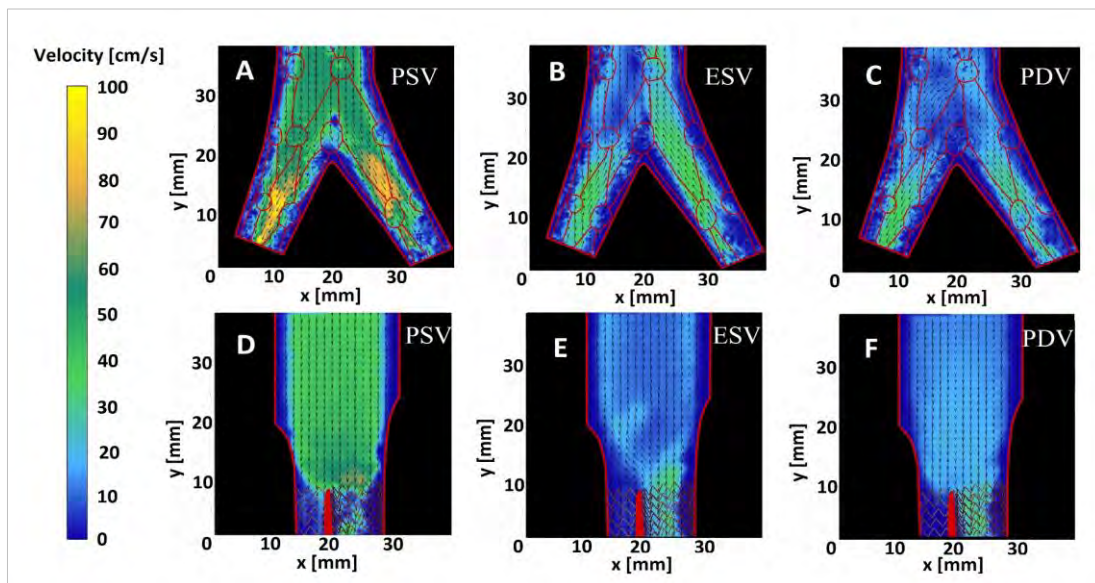


Figure 6-6 Bifurcation flow pattern: (A) AFX at PSV time-point, (B) AFX at ESV time-point, (C) AFX at PDV time-point, (D) CERAB at PSV time-point, (E) CERAB at ESV time-point and (F) CERAB at PDV time-point.

### 6.3.3 Hemodynamic comparison

Table 6-1 summarizes the hemodynamic comparison (TAWSS, OSI and RRT) of AFX and CERAB at the inflow section and the bifurcation. The mean and range for each set of TAWSS, OSI and RRT data were determined and presented in the table. In addition, the p-values for each pairwise Student's t-test between AFX stent-graft and CERAB configuration are also included in the table. The quantified hemodynamic parameters are in agreement with the observation of more disturbed flow in the bifurcation of the AFX stent-graft as compared with CERAB configuration. More details of hemodynamic plots of TAWSS, OSI and RRT along the vessel wall can be found in Appendix B. as compared with  $28.8 \pm 42.1 \text{ Pa}^{-1}$  and  $87.7 \pm 158.2 \text{ Pa}^{-1}$  for CERAB configuration.

<sup>5</sup> <https://vimeo.com/manage/428009757/general>

<sup>6</sup> <https://vimeo.com/manage/428016420/general>

**Table 6-1 TAWSS, OSI and RRT results at inflow and bifurcation for AFX stent-graft and CERAB configuration**

Region of interest	Stent	TAWSS (Pa)			OSI			RRT (Pa <sup>-1</sup> )		
		Mean	Range	P-value	Mean	Range	P-value	Mean	Range	P-value
<b>Inflow</b>										
	AFX (n=20)	0.185	0.036 -0.296	0.0048	0.316	0.207-0.475	0.283	55	8 -342	0.646
	CERAB (n=22)	0.116	0.064-0.175		0.340	0.304-0.428		44	15-158	
<b>Bifurcation</b>										
Right Edge	AFX (n=114)	0.074	0.013-0.186	0.0019	0.307	0.123-0.496	<0.001	134	13-1,744	0.351
	CERAB (n=61)	0.145	0.013-0.654		0.237	0.055-0.472		103	2-840	
Left Edge	AFX (n=57)	0.088	0.009-0.242	<0.001	0.339	0.217-0.482	0.93	273	9-3,603	<0.001
	CERAB (n=12)	0.695	0.448-0.906		0.337	0.250-0.387		5	3-7	
<b>Total</b>	AFX (n=171)	0.078	0.009-0.242	<0.001	0.318	0.123-0.496	<0.001	180	9-3,603	0.0086
	CERAB (n=73)	0.229	0.013-0.906		0.252	0.055-0.472		88	2-840	

## 6.4 Discussion

In the current study, a new method in making transparent cover for AFX stent-graft was introduced. Laser PIV experiments were performed in AFX and CERAB flow phantoms. The images obtained from the experiments were processed and analysed to produce flow patterns, TAWSS, OSI and RRT for comparison. A more disturbed and oscillatory flow was observed in the flow pattern of the bifurcation region in the AFX stent-graft as compared to the CERAB covered stent configuration that showed an undisturbed flow pattern. This result was supported by the quantified hemodynamic parameters where TAWSS was lower in AFX and RRT was higher in AFX stent-graft as compared to the CERAB configuration. This was contrary to the hypothesis of our study. The AFX stent-graft designed for treatment of aneurysmal disease, but used by some surgeons for treatment of occlusive disease, has the advantage over a CERAB configuration because radial mismatch between the stented lumen and vessel lumen is eliminated due to its unibody design. Moreover, the aortic bifurcation is preserved permitting repeated long-term endovascular access. However, from flow pattern and hemodynamic perspective, this study showed that CERAB configuration potentially has the advantage of preventing thrombosis due to less disturbed flow, higher TAWSS, lower OSI and RRT as compared with AFX.

TAWSS and OSI in this study ranged from 0.009 to 0.906 Pa and 0.1 to 0.496, respectively as compared with mean inflow WSS at PSV, ESV and PDV time-points of 1 Pa, -0.3 Pa and 0.4 Pa; and OSI ranged from 0.1 to 0.2 at the bifurcation in the previous similar hemodynamic study [129] which is in line with this current study. In addition, WSS values ranging from 0 to 0.80 Pa and OSI values ranging from 0.01 to 0.49 were obtained in the CERAB results involving WSS study [33] also in agreement with our current study. There was a slightly more disturbed flow at ESV at the CERAB bifurcation in the current study compared with what was observed in the control model of the previous hemodynamic comparison study [129]. The higher WSS values in the CERAB configuration in the bifurcation could also be attributed to the fact that the flow transition from the bifurcation in the distal aorta to the iliac branches is more orderly with higher velocity near the boundary layer along the vessel wall which might provide protection from thrombosis. It is important to note that the TAWSS observed in both the AFX stent-graft and the CERAB configuration at the inflow and at the bifurcation in this in vitro study were lower than the physiological WSS value of 0.5 to 1.2 Pa in human arteries [137-139]. In addition, the maximum value of TAWSS for CERAB at inflow was 0.906

Pa at the bifurcation which was significantly higher than 0.242 Pa for AFX therefore more protective of thrombosis for CERAB in the bifurcation region ( $p = 5.53 \times 10^{-6}$ ). Since blood is not in direct contact with endothelial cells, due to the ePTFE graft material used in the covers of both AFX stent-graft and Atrium V12 stents, the graft material provides protection even though TAWSS might be below physiological values of 0.5 Pa [137].

There are several limitations to our study: firstly, this in vitro study used polyurethane and LDPE for the modified transparent covers with coefficient of friction (0.12 to 0.70) and (0.20 to 2.5) respectively which are slightly higher than that of the original opaque ePTFE covers (0.05 to 0.10) therefore might influence the WSS. Secondly, the PIV method is a two-dimensional analysis of a three-dimensional flow phenomenon therefore only one slice of the 2D-flow pattern centred on the lumen could be recorded for each PIV analysis. Multiple slices would be required to get a more complete picture of 3D flow across the lumen as a whole, which could reveal areas of stagnant flow with low TAWSS in the helical CERAB configuration. Thirdly, the laser sheet was obscured by the renal branch of the AFX phantom therefore unable to capture PIV images upstream of the AFX stent-graft. An alternative approach would be to apply an infrarenal flow profile at the inlet directly using a roller pump [142], or a similar pump, in order to eliminate the renal branches in the flow model as to allow an unobstructed laser sheet entry into the model to produce complete AFX inflow. Finally, the proximity of the AFX to the renal arteries could explain part of the re-circulations in the inflow [33] which could generate strong flow disturbances that are less normalized at the AFX relative to the CERAB. However, clinically AFX is likely to be deployed nearer to the renal arteries than CERAB which remains low.

The disturbed and oscillatory flow might have been caused by the inner skeleton of the AFX stent-graft, protruding into the vessel lumen. In addition, the infolding of the graft material could also be a factor as the stent-graft was slightly oversized. In the current study a transparent AFX device was designed, in order to enable laser-PIV, considered the gold standard of flow imaging. Future studies using the original AFX, in combination with ultrasound-PIV might confirm whether infolding of LDPE graft material contributed to the disturbed flow. Another future study using computational fluid dynamics (CFD) methods to simulate the experimental set-up can be performed to predict the hemodynamics of the 3D flow model. When the results of this study are combined with previous literature [129] the hemodynamic consequences of bare metal stent, covered kissing stents, CERAB configuration and the AFX stent-graft for treating AIOD can be compared. From a hemodynamic perspective, CERAB seems to have a slightly better performance compared with the other three types of stents. The AFX stent-graft has the

geometric advantage of eliminating radial mismatch but this is counteracted by disturbed flow in the bifurcation region. Therefore, it might be beneficial to investigate design improvement such as an inner ePTFE graft to smoothen the protruding strut links. This approach potentially reduces disturbed flow if it is to be considered a definitive treatment for occlusive disease rather than aneurysm for which it was designed.

## **6.5 Conclusion**

In this in vitro study, it was found that the flow pattern of a modified AFX stent-graft was more disturbed in the bifurcation region and the associated low TAWSS and high OSI and RRT may predispose to thrombosis and are, thus, less desirable as compared to a CERAB configuration. Further investigations are warranted to confirm whether the in vitro hemodynamic results identified in this study are translated into the clinical setting and correlate with an increased incidence of thrombosis.

## Chapter Seven

# 7

## A Novel Roller Pump for Physiological Flow

## Preamble

One of the limitations of the laser particle image velocimetry experimental set-up is that a complicated flow loop is required in order to obtain physiological flow in the aortoiliac bifurcation with a suprarenal flow profile as input. Two renal arterials with needle valves located in each renal artery plus two needle valves located at the iliac arteries and a compliance chamber located at the combined output of the iliac arteries are included in the flow loop in order to obtain the desired triphasic flow profile at the aortoiliac bifurcation. It is achieved by adjusting the resistances of the needle valves and the pressure of the compliance chamber to match the physiological velocity and pressure profiles at infrarenal inlet and iliac outlets.

A novel roller pump was developed to mimic physiological flow profile based on the principle of reciprocating actuators. It was demonstrated that the novel pump is capable of generating carotid, suprarenal and infrarenal flow profiles matching those of human physiological flow profiles. The results of this innovation was published in the *Artificial Organs* journal on the 17<sup>th</sup> of February, 2020 in electronic format and print version was published on the 1<sup>st</sup> of August, 2020. <https://doi.org/10.1111/aor.13670>

This published journal paper begins with an abstract that summarizes the research topic, its main objective, methodology, results and conclusions. Outlined in the main section where material and method used to develop the novel roller pump was described in detail. Results section shows that the novel roller pump is capable of mimicking flow profiles at carotid, suprarenal and infrarenal arteries with similarity index ranging from 0.96 to 0.99. The novel roller pump is deemed suitable for bench top testing. Computational Fluid Dynamics.



## 7.1 Introduction

Experimental flow phantoms for blood flow simulation are used by researchers to carry out experiments without subjecting living subjects to potential risk of injuries or damage to living organs. It is an indispensable tool for *in vitro* studies, especially in relation to the study of stenosis, aneurysms and failing heart valves. Furthermore, it has been successfully used by researchers to study and validate new treatment methods such as minimally invasive endovascular stent treatments [33, 129]. In addition, computational fluid dynamics (CFD) numerical method was validated by running particle imaging velocimetry (PIV) experiments with flow phantoms [133, 143, 144]. The requirements of flow setups to reproduce realistic arterial flow waveforms were reviewed extensively by Law et al. [145, 146], Holdsworth et al [146] and Hoskins et al. [147]. The basic requirement is that it must be capable of reproducing pulsatile flow mimicking human arterial flow physiology and that it is easy to program.

These authors have also provided thorough reviews of previous work. Previous devices can be classified according to the type of pumps used in the setup i.e. gear, piston or roller/peristaltic. Gear pumps have been used by Groot Jebbink et al. [129], Boersen et al. [33] and Hoskins [147] to generate pulsatile waveforms. However, the disadvantage of gear pump is that suspended particles are easily damaged and it is sensitive to cavitation produced by the hydrodynamic action of the gears. Holdsworth, [146], Rudenick et al [148] and Poot et al. [149] simulated peripheral arterial flow with piston pumps. This class of pumps shares the general disadvantage of difficulty in programming. Standard peristaltic pumps were modified by Law et al. [145] and Douville et al. [150] to generate physiological flow waveforms based on mechanical manipulation of the actuating back plate and computer control of the roller. This technique allows the generation of a limited number of waveforms however, it is difficult to program new waveforms and even harder to produce reverse flow which is physiological relevant to simulate.

More recently Shkolnikov et al. [151] and Neto et al. [152] developed a roller-free peristaltic pump using actuators to produce pulsatile waveforms. However, these pumps were developed for use in microfluidic applications at low flow rates and are not suitable for larger arteries. The main limitation of the standard roller pump is that it generates approximately a sinusoidal waveform at low speed in rotations per minute (RPM) and approaches continuous flow at higher RPM to generate higher stroke volume which do not conform to human blood flow physiology. The reciprocating roller pump proposed here is an improved version, which circumvents the limitation of the standard roller pump with a

unique mechanical design, combined with precision digital motion control technology. Three types of vascular flow namely carotid, suprarenal and infrarenal flows were generated from a proof of concept prototype and the measured flow profiles were compared against reference flow profiles.

## **7.2 Materials and Methods**

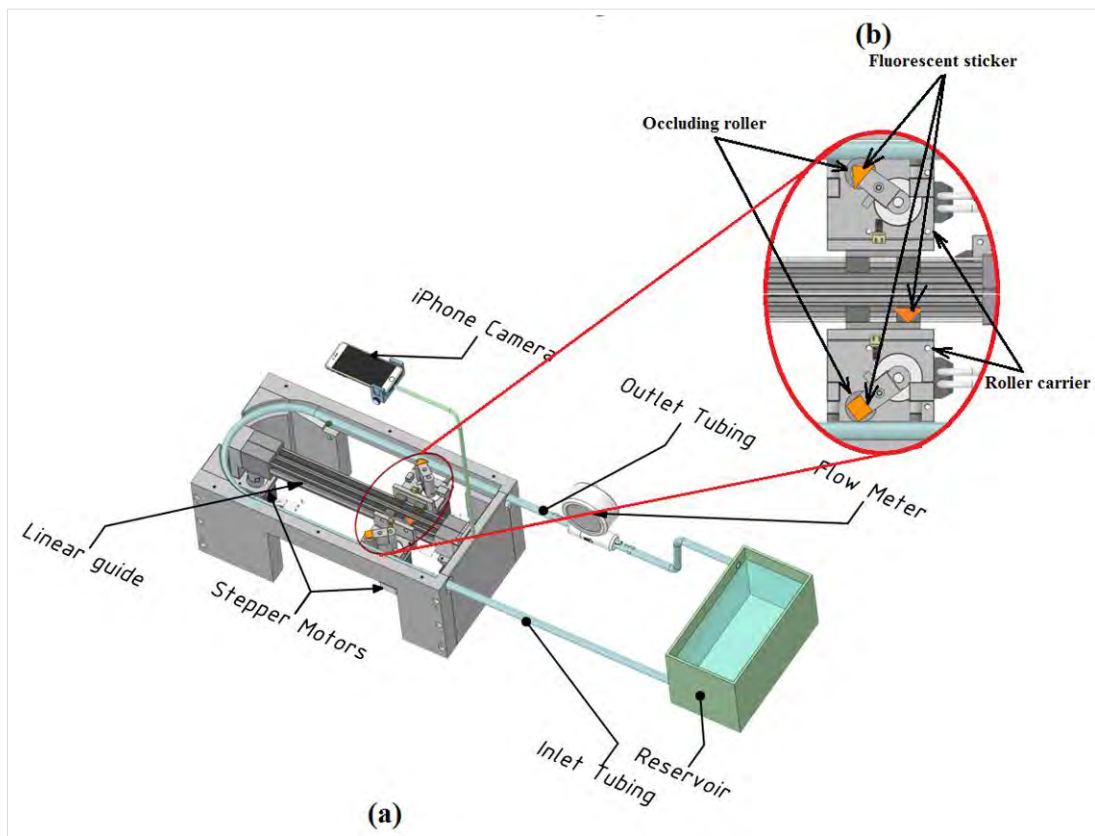
### **7.2.1 Experimental Flow Circuit**

A novel, reciprocating roller pump was developed based on the principle of reciprocating peristaltic movements on two parallel straight tracks as outlined in Figure 7-1. The main pumping chamber consisted of two occluding rollers driven by two sets of 2 Nm hybrid servo stepper motors (NEMA23, model number 57J1880EC-1000) and closed loop hybrid servo drives (2HSS57, Just Motion Control, Shenzhen, China) and two roller carriers driven by a further two sets of stepper motors and drives. Each occluding roller was mounted offset from the shaft of the stepper motor whereby the tubing can be occluded by rotating the shaft in one direction and released by rotating the shaft in the opposite direction. Each roller carrier was mounted on a linear guide and attached to a toothed belt (ZLW-0630 drylin linear guide, Igus, Cologne, Germany) driven by a stepper motor. An Arduino compatible, high speed microcontroller Teensy 4.0 (PJRC.com, LLC 14723, SE Brooke, CT Sherwood, OR 97140 USA) with a 600MHz processor was used to generate control signals that drive the movement of the stepper motors.

Smooth motion and low noise were achieved by means of micro stepping. Masterflex platinum-cured silicone tubing I/P82 (Cole-Parmer, Vernon Hills, Illinois, USA) with tubing internal diameter of 12.5 mm was used to contain carotid, suprarenal and infrarenal flows in this study. The tubing connected to a port located at the lower section of the reservoir to the pumping chamber is the inlet tubing whereas the tubing connected to the pumping chamber to a high precision ultrasound flow meter ES-Flow 1131 (Bronkhorst High-Tech B.V. Nijverheidsstraat 1A, NL-7261 AK Ruurlo, The Netherlands) is the outlet tubing. A blood mimicking fluid (BMF) comprising of 40% by volume of Glycerine (Sanofi Consumer Healthcare, 87 Yarraman Place, Virginia QLD 4014, Australia) and 60% water by volume was used as a working fluid in the flow circuit as its density and viscosity approximates that of human blood.

A flow loop was created by circulating the BMF from the reservoir to the pumping chamber via the inlet tubing and then to the flow meter via the outlet tubing and finally

discharging the BMF back into the reservoir to complete the flow circuit. The circulation was achieved by occluding the roller located near the inlet tubing in the initial position as shown in Figure 7-1 but not the roller located near the outlet tubing then moving the roller carriers away from the reservoir hence creating the first cardiac cycle. The next cardiac cycle is achieved by occluding the roller near the outlet tubing but not the roller near the inlet tubing and subsequently moving the roller carriers toward the reservoir. A continuous cycle is then created by alternating movement of the roller carrier between the two tracks of the pumping chamber.

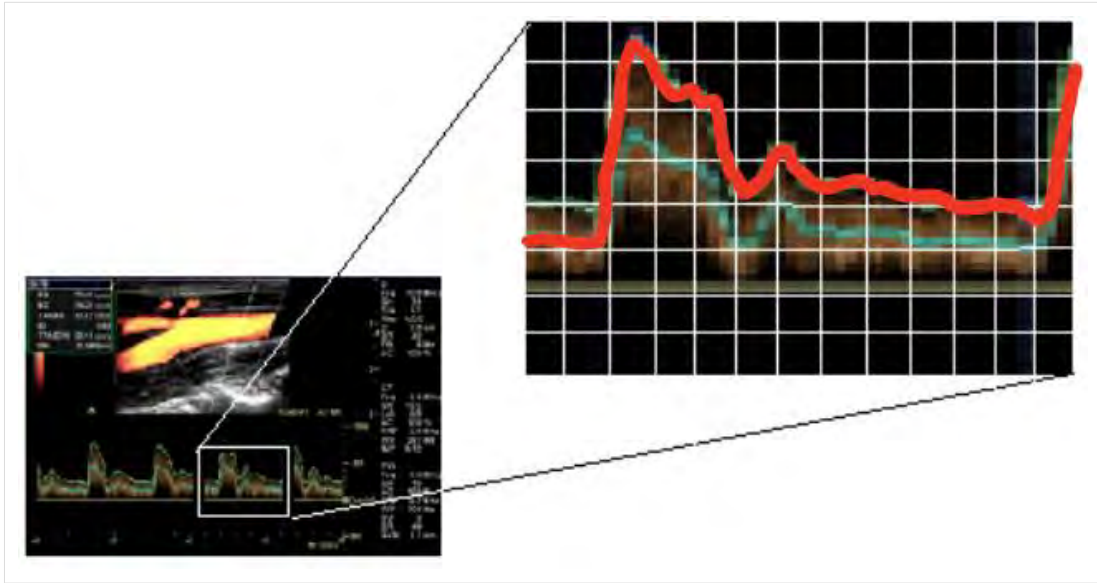


**Figure 7-1** Experimental flow circuit. (a) Experimental flow circuit with ultrasonic flow meter and camera motion analysis set-up (b) Details of tubing occlusion mechanism and locations of fluorescent stickers

## 7.2.2 Flow Profiles

The flow rates at 10 ms intervals of a carotid flow profile based on Sousa et al. were digitized manually by placing a tracing graph paper on top of an enlarged copy of a periodic cycle obtained from a clinical Doppler ultrasound scanner as shown in Figure 7-2 [153]. The flow rate at each time-point was calculated by multiplying the cross-sectional

area of the common carotid artery (CCA) by the average velocity. Assuming fully developed flow in CCA therefore average velocity is half of centre line velocity. Based on CCA diameter of 0.7cm and PSV of 76.43 cm/s [153], the flow rate at PSV time-point was determined to be 0.88L/min. A look-up table with 100 pairs of flow rate vs time values was then created for use by the in-house developed motion control software to drive the reciprocating roller pump.



**Figure 7-2 Manual Digitization of Flow Profile**

The suprarenal flow profile used in this study was based on Lee et al. [154] where the flow rate  $Q$  in L/min was represented by a trigonometric formula as shown in Equation (7.1)

$$Q = C_1 + C_2 \cos(2\pi t/T) + C_3 \cos(4\pi t/T) + C_4 \sin(2\pi t/T) + C_5 \sin(4\pi t/T) \quad (7.1)$$

Where:

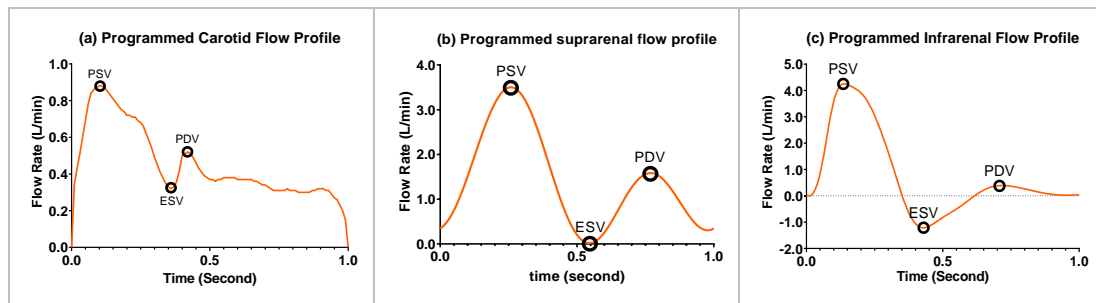
$C_1=1.281$ ,  $C_2=0.064$ ,  $C_3=-1.03$ ,  $C_4=0.885$ ,  $C_5=-0.166$ , and  $t$  is the time in second.

The period  $T$  and coefficient  $C_1$  were modified from 0.83 and 2.891 to produce zero End Systolic Velocity (ESV) and 60 beats per minute or 1 Hz ( $T=1$  s), resting heart rate to match the suprarenal profile used by Groot Jebbink et al. [129][1]. Infrarenal flow profile based on Fraser et al. [98][16] was digitized manually with 100 time points at 10 ms intervals. The effective flow rate was adjusted from 13.3 to 12.5 mL and heart rate adjusted from 64.5 to 60 beats/minute. Table 7-1 shows the flow rate values at Peak Systolic Velocity (PSV), End Systolic Velocity (ESV) and Peak Diastolic Velocity (PDV) time-points for carotid, suprarenal and infrarenal flows. The flow profiles as shown in

Figure 7-3 were loaded into the roller pump Arduino sketch (Arduino IDE, Arduino Holdings, Somerville, MA, USA).

**Table 7-1 Reference flow rates at PSV, ESV and PDV time-points for carotid, suprarenal and infrarenal flow**

Flow Type	Programmed flow rate at specific time-point (L/min)		
	PSV	ESV	PDV
Carotid	0.880	0.319	0.520
Suprarenal	3.500	0	1.453
Infrarenal	4.250	-1.213	0.391



**Figure 7-3 Reference flow profiles (a) carotid (b) suprarenal and (c) infrarenal flow**

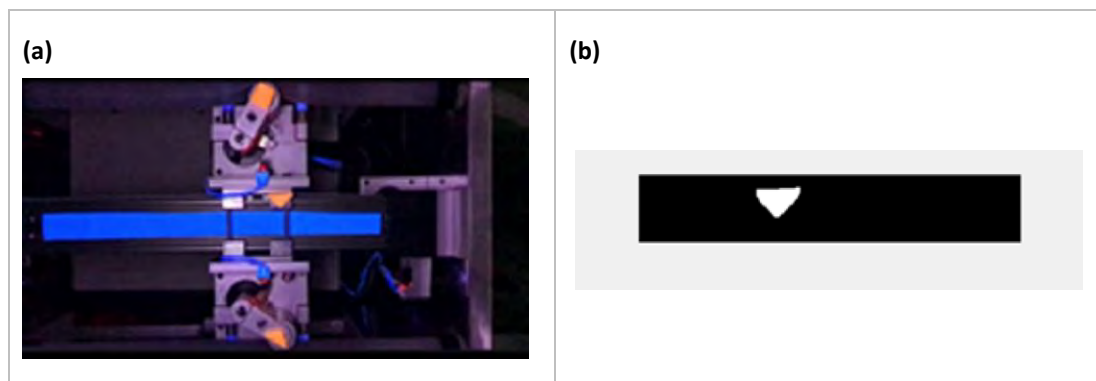
### 7.2.3 Flow Profile Generation

Flow profiles were generated based on human physiological resting conditions with effective volumetric flow rates of 0.36, 1.5 and 0.75 L/min or stroke volumes of 6, 25 and 12.5 mL for carotid, suprarenal and infrarenal flows respectively. A stop watch was used to count the number of strokes per minute and the desired 60 beats/minute heart rate was achieved by adjusting the Heart Beat control knob on the user interface panel. The volume of BMF from ten strokes was collected into a 400mL graduated glass beaker (Pyrex No.1000, Corning Inc., NY, USA) from the outlet tubing and the stroke volume was then calculated by dividing the content in the beaker by ten. The desired stroke volume was achieved by adjusting the Stroke Volume control knob on the user interface panel.

### 7.2.4 Flow Profile Measurements

An ultrasonic flow meter (Bronkhorst ES-Flow 1131) with a minimum polling time of 10 ms was used to provide fast response and a real time display of the flow profile. In addition, twelve periodic cycles of a carotid flow profile were captured, stored and later retrieved for further analysis. Since the maximum flow rate for the Bronkhorst ES-Flow

1131 was 1.5 L/min, it was only suitable for carotid flow profile with a PSV flow rate of 0.88 L/min. For flows with a PSV flow rate higher than 1.5 L/min, an indirect method based on motion analysis was developed to determine its suitability. A Cynergy3 ultrasonic flow sensor (Type UF8B; Cynergy3 Components Ltd, Wimborne, Dorset, United Kingdom) was used to guide the set-up of the desired flow rate for suprarenal and infrarenal flows as it is able to measure flow rates up to 10 L/min with a 100 ms response time. An Apple iPhone 7 (Apple Computer Inc., 1 Apple Park Way, Cupertino, California, USA) mounted on top of the roller pump as shown in Figure 7-4(a) was used to capture images with 1280 x 720 pixel resolution at 240 frames per second and an in-house developed Matlab (MathWorks, Natick, Massachusetts, USA) script was used to analyse the movement of fluorescent stickers. The clarity of the fluorescent stickers was enhanced by illuminating ultraviolet light in a dark room during the recording as shown in Figure 7-4(a). Segmentation of the images to extract the centroid position of the fluorescent sticker was achieved based on thresholding of the image as shown in Figure 7-4(b). A 200 mm x 10 mm reflective tape (Scotchlite, 3M Company, Maplewood, Minnesota, USA) was used to calibrate the camera pixel dimensions in the captured image. The velocity of the centroid was calculated based on displacement of the centroid between two successive frames. Smoothing was applied by averaging five adjacent displacements to remove vibrations and lighting artefacts. The volumetric flow was determined by multiplying velocity and internal cross-sectional area of the tubing. For each flow type, twelve profiles were averaged for statistical and similarity analyses.



**Figure 7-4** Flow rate measurement by motion analysis. (a) Recording of fluorescent stickers with ultraviolet light and (b) Segmentation of a fluorescent sticker recording.

Specific time points at Peak Systolic Velocity (PSV), End Systolic Velocity (ESV) and Peak Diastolic Velocity (PDV) in each flow profile as described were used to compare how well a flow profile generated by the reciprocating roller pump matched the reference profile that was programmed into the machine. In addition, cosine similarity was used to

compare measured versus programmed profile, where the similarity index is defined as given in Equation (7.2).

$$\text{similarity index} = \cos(\theta) = \frac{A \cdot B}{\|A\| \|B\|} = \frac{\sum_{i=1}^n A_i B_i}{\sqrt{\sum_{i=1}^n A_i^2} \sqrt{\sum_{i=1}^n B_i^2}} \quad (7.2)$$

Where:

$A \cdot B$  is the dot product of two vectors: vector A contains the programmed values and vector B contains the measured values of the flow profiles.  $\|A\|$  and  $\|B\|$  are the magnitudes of the vectors A and B respectively.

The resulting similarity index ranges from zero to one.

### 7.3 Results

Table 7-2 summarizes the test results comparing measured versus programmed flow profiles. Flow profiles measured directly from the ultrasonic flow meter and indirectly through motion analysis of the fluorescent stickers attached to pump roller matched well for the carotid profile with similarity indices of 0.97 and 0.99. Therefore, the motion analysis was deemed as a quantitative measurement method. In addition, similarity indices between measured and programmed profiles based on the motion analysis method for suprarenal and infrarenal flow profiles were 0.99 and 0.96, respectively.

**Table 7-2 Test results of comparison between measured and programmed flow profiles**

Flow Type (Measurement Method)	Programmed PSV (L/min)	Measured Flow Rate at PSV time- point (L/min)		Programmed ESV (L/min)	Measured Flow Rate at ESV time- point (L/min)		Programmed PDV (L/min)	Measured Flow Rate at PDV time- point (L/min)		Similarity Index
		Mean	Std Dev		Mean	Std Dev		Mean	Std Dev	
Carotid (Ultrasound Flow Meter)	0.880	0.894	0.021	0.319	0.333	0.016	0.520	0.514	0.013	0.97
Carotid (Motion Analysis)	0.880	0.883	0.016	0.319	0.342	0.007	0.520	0.485	0.009	0.99
Suprarenal (Motion Analysis)	3.500	3.497	0.014	0	0.004	0.003	1.453	1.656	0.073	0.99
Infrarenal (Motion Analysis)	4.250	4.179	0.024	-1.213	-1.147	0.015	0.391	0.339	0.017	0.96

### 7.3.1 Carotid Flow

Twelve cycles of carotid flow profile measured with ultrasonic flow meter method and motion analysis method are as shown in Figure 7-5(a) and Figure 7-5 (b). There was a small difference for flow rates at PSV time-point between even and odd cycles indicating a slight systematic difference between the two tracks of the pumping chamber. Figure 7-6 shows the plots of mean flow rate with  $\pm$  one standard deviation (SD) for measured flow profile against the programmed profile. The measured carotid flow profiles for direct and indirect methods matched well with reference profile except, the PSV time-point for measured profile occurred about 0.1 and 0.05 second later as compared with programmed profile for direct and indirect method respectively. Measured mean flow rate and SD vs programmed flow rate at PSV, ESV and PDV time-points were: 0.894/0.021 and 0.883/0.016 vs 0.880; 0.333/0.016 and 0.342/0.007 vs 0.319; 0.514/0.013 and 0.485/0.009 vs 0-.520 L/min for ultrasonic flow meter and motion analysis method respectively.

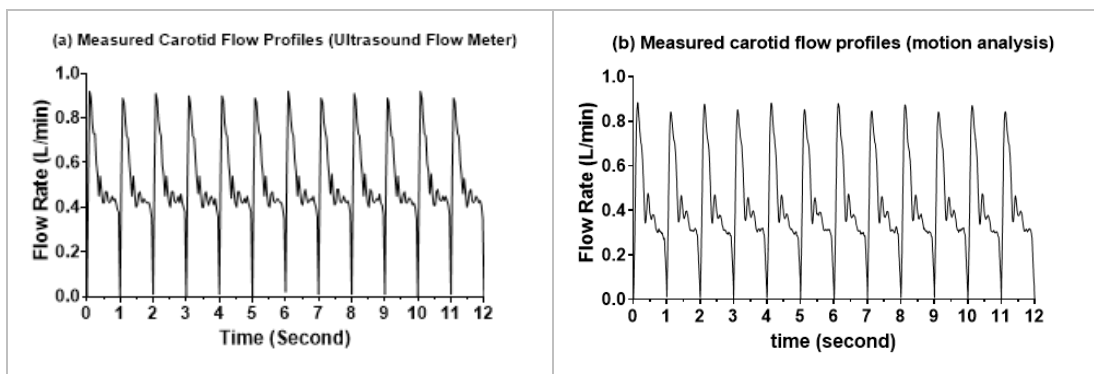


Figure 7-5 Carotid flow profile measured with (a) ultrasonic flow meter and (b) motion analysis method.

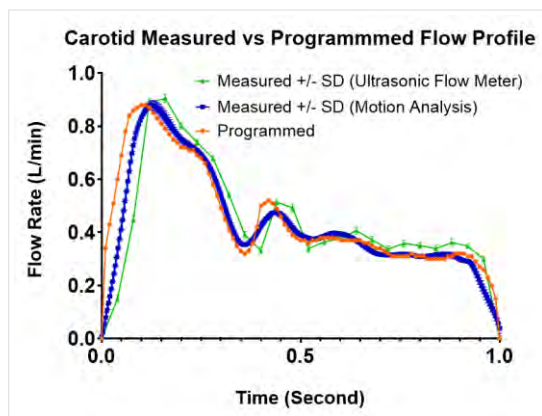
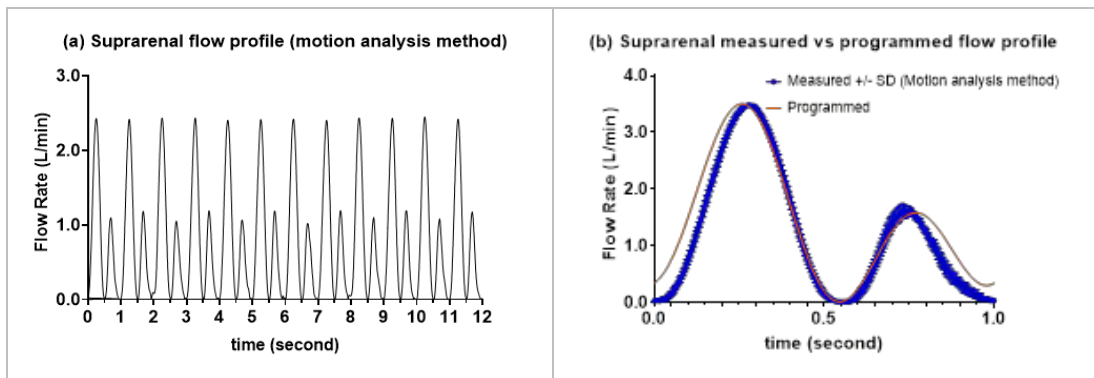


Figure 7-6 Carotid flow profile measured vs reference



### 7.3.2 Suprarenal Flow

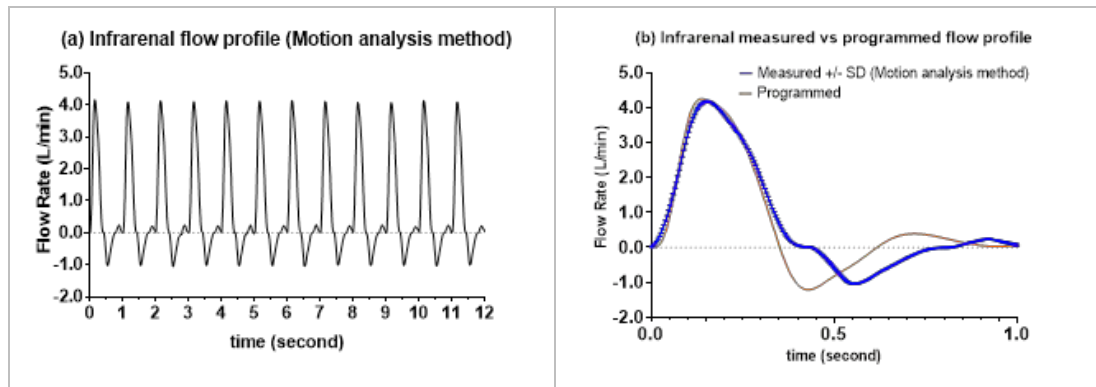
From Figure 7-7(a), flow rate at PSV time-point was consistent from cycle to cycle, however at PDV time-point, the flow rate from odd cycles were slightly lower than those from even cycles indicating a slight systematic difference between the alternating tracks. Figure 7-7(b) shows the plot of mean with  $\pm$  one SD for the measured flow profile based on motion analysis method against the programmed profile. Measured suprarenal mean and SD vs programmed flow rate at PSV, ESV, and PDV time-points were: 3.497/0.014 vs 3.500, 0.004/0.003 vs 0 and 1.656/0.073 vs 1.453 L/min respectively. In addition, PSV time-point from motion analysis method was about 0.05 second sooner than reference whereas PDV time-point was about 0.05 second later than reference.



**Figure 7-7** Suprarenal flow profile. (a) Measured suprarenal flow profile (twelve cycle) (b) Measured vs programmed suprarenal flow profile.

### 7.3.3 Infrarenal Flow

Figure 7-8(a) shows a plot of twelve cycles when the pump was selected to generate infrarenal flow. The measured flow rate at PSV time-point based on the motion analysis method matched well with reference. In contrast, the measured flow rates at ESV and PDV time-points were slightly lower as compared with reference. In addition, these time-points also occurred about 150 ms later in the cycle compared with the programmed ESV and PDV time-points. The delay might be caused by backlash when the roller carrier was changing direction. Measured infrarenal mean and SD vs programmed flow rate at PSV, ESV, and PDV time-points were: 4.179/0.024 vs 4.250, -1.147/0.015 vs -1.213 and 0.339/0.017 vs 0.391 L/min respectively.



**Figure 7-8 Infrarenal flow profile. (a) Measured infrarenal flow profile (twelve cycles) (b) Measured vs programmed infrarenal flow profile.**

## 7.4 Discussion

In this study, it was demonstrated that the flow profile generated by the reciprocating roller pump and measured with a high precision ultrasound flow meter matched well with programmed profile with a similarity index of 0.98. In addition, the magnitude of the measured flow rates at PSV, ESV and PDV time-points also matched well against reference. Moreover, it was also demonstrated that the indirect method based on motion analysis produced good results with a similarity index of 0.99 and well matched flow rates at PSV, ESV and PDV time-points therefore suitable as a surrogate flow measurement method. The main advantage of this novel pump compared with other commercially available pumps is its simplicity in generating peripheral flow profiles.

Traditionally, two needle valves located at renal artery outlets, an air chamber and a needle valve in series located at the combined common iliac artery outlets representing a two-element Windkessel were used [33, 129, 155, 156] to simulate vessel resistance and peripheral compliance in order to generate flow profile with reverse flow in the early diastolic phase. With the reciprocating roller pump design, it can produce back flow in the peripheral artery without the use of renal artery flow in the circuit, therefore it simplifies the flow circuit for in vitro studies involving infrarenal aorta, iliac, femoral and other peripheral arteries.

In this study only flow profiles were measured and no resistance was applied at the outflow apart from the resistance created by the inline ultrasonic flow meter. Future work to accurately simulate in vivo blood pressure is required. In a real-time programmable pulsatile flow pump for in vitro cardiovascular experimentation, Mechoor et al. [157] reported that a feedback algorithm could reduce normalized RMS error by 5.5% in six iteration. A similar algorithm is being considered for the reciprocating roller pump where it might improve the accuracy of the desired flow rates at each time point.

Tubing material used in the roller pump was found to have different performance and durability, as investigated by G.J. Peek et al. [158], therefore it might be beneficial to conduct future studies to compare performance and durability of various biocompatible tubings and to identify an optimum tubing for the reciprocating roller pump. Another issue that may be of interest is to study the flow patterns after the pump. A non-invasive occluding roller may be added at either the inlet or the outlet of the roller pump to act as a pressure regulating or one-way check valve. In particular when looking at the valve at the inlet, this may be interesting to investigate swirling flow in the aortic arch.

One of the limitations of the current study is that two ultrasonic flow meters were used. The high precision, fast response Bronkhorst ES1311 was used to guide set-up as well as measure flow profile with a flow rate of less than 1.5 L/min and to validate the indirect motion analysis method. The slower response Cynergy3 UF8B with a maximum sampling rate of 10 Hz was used to guide the flow set-up with flow rates up to 10 L/min. A fast response ultrasonic flow meter with sampling rate higher than 25 Hz, accuracy better than +/-1% and maximum flow rate >5 L/min or a Coriolis flow meter such as Bronkhorst M55 can be useful to validate the suprarenal and infrarenal flow profiles.

The roller pump is a proven technology which has been widely used in cardiopulmonary bypass (CPB) and extracorporeal membrane oxygenation (ECMO) procedures [159, 160]. Its main advantage is the fact that there is no contact between the pump driving components and the liquid. In addition, the pumping chamber, i.e. the tubing is disposable [161], which ensures the sterility and avoids cross-contamination [162, 163]. The reciprocating roller pump can be programmed to ensure non-total occlusion of tubing therefore it has the potential to reduce damage to blood cells in these procedures.

A cardiac pump patent based on the reciprocating roller design was submitted to Australian Patent Office on July 2018. Details of the patent can be found in Appendix E.

## **7.5 Conclusion**

The reciprocating roller pump was capable of generating waveforms conforming to human physiology and closely matched the reference profiles therefore it is deemed suitable for use in experimental studies of vascular blood flow. It might also have the potential to be used in CPB and ECMO procedures due to its simplicity in design and low cost of disposable tubing.



Comparison of Particle Image Velocimetry  
and Computational Fluid Dynamics  
Method in an Aortoiliac Model Deployed  
with AFX Stent-Graft

## Preamble

CFD method is a special area of mathematics and a branch of fluid mechanics. It is applied routinely in a diverse range of safety-critical engineering systems, which is increasingly applied to the cardiovascular system. It has revolutionised the research and development of devices, such as stents, mechanical valves and ventricular assist devices. Combined with cardiovascular imaging, CFD simulation enables detailed characterisation of complex physiological pressure and flow fields and the computation of metrics that cannot be measured directly; for example, wall shear stress, oscillatory shear index and relative residence time. CFD models are also being translated into clinical tools so that the physicians could use them across the spectrum of coronary, valvular, congenital, myocardial and peripheral vascular diseases as they effectuate minimally-invasive patient assessment. Patient-specific modelling enables individualised risk prediction and virtual treatment planning. This represents a significant departure from traditional dependence upon ideal geometry, registry-based or population-averaged data. Model integration is progressively moving towards ‘digital patient’ or ‘virtual physiological human’ representation. When combined with population-scale numerical models, these models have the potential to reduce the cost, time and risk associated with clinical trials. The adoption of CFD modelling signals a new era in cardiovascular medicine. However, these computational methods are validated against the experimental data to assess their agreement with the actual measured physical quantities. Previous experimental validations of CFD have investigated anatomy including, carotid bifurcation [164-167], cerebral aneurysm [133, 168] and abdominal aortic aneurysm [169, 170] but none of the studies has investigated aortoiliac anatomy.

This chapter compares the flow patterns and haemodynamic parameters including wall shear stress, oscillatory shear index and relative residence time between laser particle image velocimetry (PIV) in vitro method and CFD method in order to validate the CFD model at the aortoiliac bifurcation.

## 8.1 Introduction

In Chapter 6, particle image velocimetry (PIV) method using the gold standard in flow imaging was applied to compare the flow patterns and haemodynamics between the two endovascular techniques, AFX stent-graft and CERAB configuration for the treatment of advanced aortoiliac occlusive disease (AIOD). In that study, the hypothesis that AFX stent-graft is a more superior technique in treating AIOD compared to CERAB configuration, due to its one-piece design eliminating radial mismatch and preserving the aortic bifurcation for possible future endovascular intervention, was proven. However, the experimental data revealed that low time-averaged wall shear stress (TAWSS), high oscillatory shear index (OSI) and prolonged relative residence time (RRT) in the bifurcation region and disturbed flow associated with AFX stent-graft contradicted the hypothesis that AFX stent-graft is a better technique than CERAB configuration. An in vivo study in either animal or human subjects should be able to confirm whether the experimental data can be translated to real-life clinical situations. In order to conduct a clinical study comparing the two endovascular techniques, two live subjects with identical anatomy are required, which is impractical to find in real life. In addition, the costs and risks associated with such in vivo experiments are high and difficult to justify. Thus, an alternative approach is to perform a CFD simulation, and the data have been validated with respect to cerebral aneurysm [133], thoracic aorta [134], intracranial aneurysm [135] and stenosed carotid bifurcation [171] using PIV method by researchers. The current study aimed to use haemodynamic results obtained from PIV experiments to validate the CFD simulation replicating the experimental set-up of the AFX stent-graft model.

## 8.2 Material and Methods

Haemodynamic parameters determined from PIV experimental method, as described in Chapter 6, were used as a reference to compare to the parameters obtained from CFD simulation method based on the same anatomically realistic aortoiliac model deployed with a modified transparent AFX stent-graft. The parallels between the two methodologies are as depicted in the flowchart, as shown in Figure 8-1.

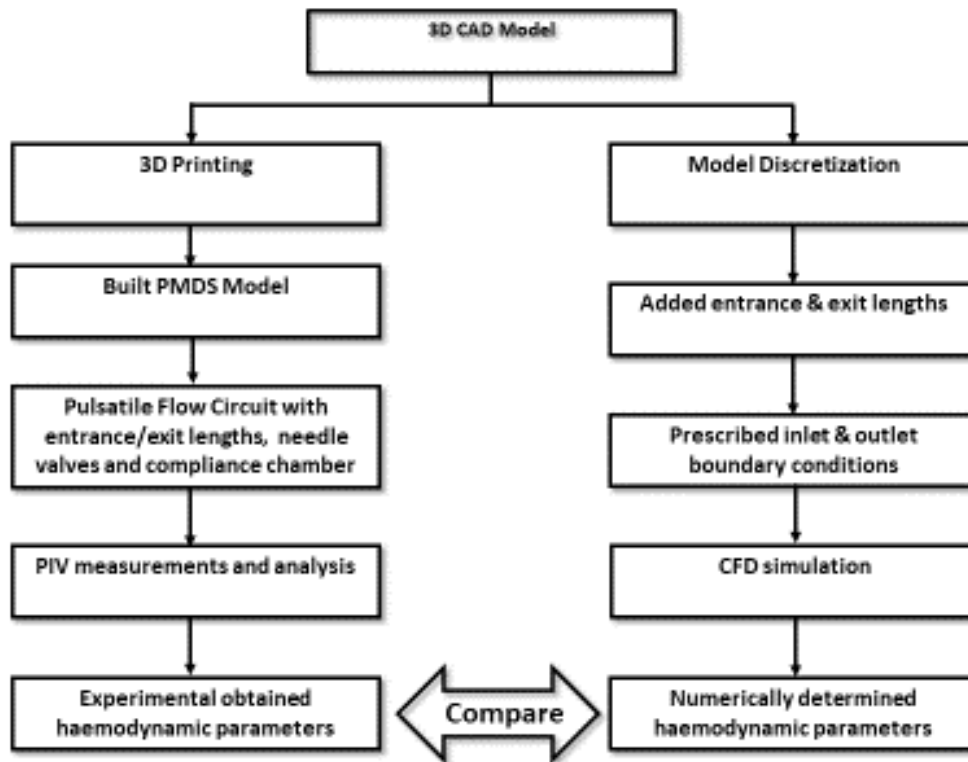


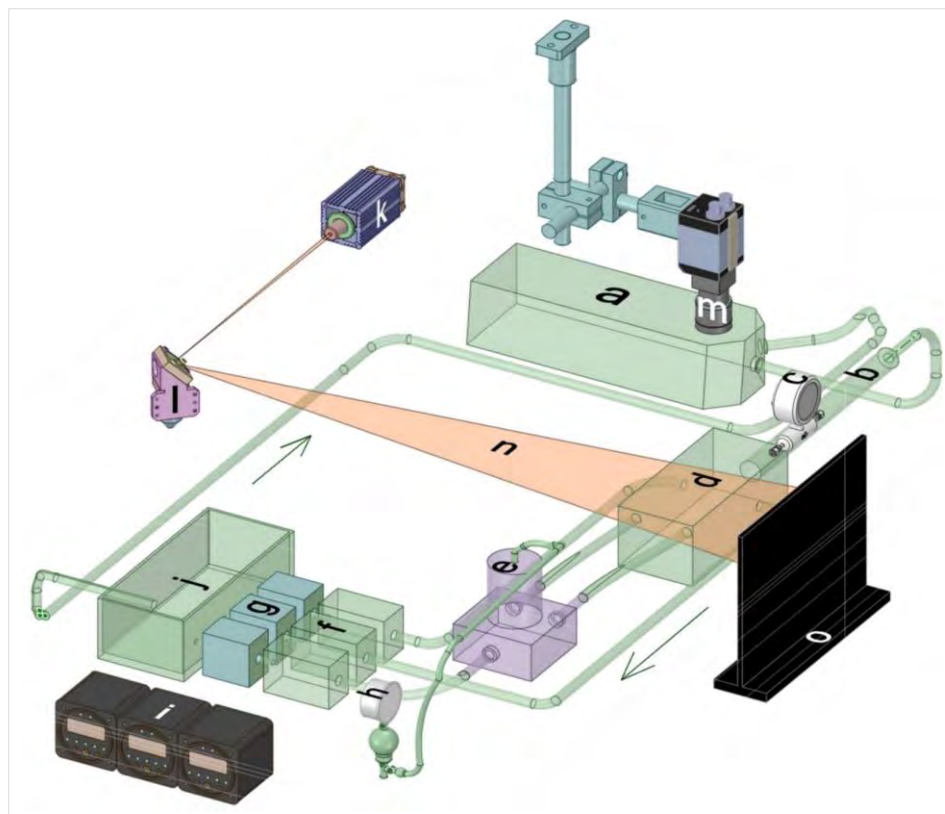
Figure 8-1 Flowchart comparing PIV and CFD methodologies

### 8.2.1 PIV Methodology

The laser PIV experimental set-up (Figure 8-2) consists of two sub-systems. The first sub-system is the fluid circulation loop driven by a programmable hydraulic piston-driven pump (SuperPump) and the corresponding software Vivitest (Vivitro Labs Inc., Victoria, CA, USA). The reference is blood-mimicking fluid (BMF) comprising of water (44.1%), glycerol (34.5%) and urea (21.4%) with a refractive index optically matched to that of PDMS model and physiologically matched to that of human blood (dynamic viscosity 4.2 mPa.s and density 1114 kg/m<sup>3</sup>) [172]. The pump draws the BMF from the reservoir, generates a physiological suprarenal flow profile with a mean flow rate of 1.6L/min, 60 beats per minute (bpm) heart rate and circulates it through a CORRI-FLOW M55 Coriolis flowmeter (Bronkhorst High-Tech B.V., Ruurlo, The Netherlands) with an extended entrance length (20 x inlet diameter), a flow phantom, a compliance chamber, three units of UF8B ultrasound flow sensors (Cynergy3 Components Ltd, Wimborne, Dorset, UK), three units of needle valves and completed flow loop by returning the BMF to the reservoir. The needle valves were manually adjusted to achieve a mean pressure of 100 mmHg and approximately 25% outflow or 0.4 L/min each at renal outlets and approximately 50% outflow or 0.8 L/min at the combined iliac outlet. In addition, the two iliac outlets were connected to a single compliance chamber. A DS44 hand-held

sphygmomanometer (Welch Allyn, Skaneateles Falls, NY, USA) was used to set the distal peripheral pressure between 80 and 120 mmHg.

The second sub-system comprises of a continuous-wave laser (5 W DPPS laser, 532 nm; Cohlibri, Lightline, Germany) projecting the laser sheet through a deflector to illuminate the flow phantom. Rhodamine-coated fluorescent polymethyl methacrylate particles (size 1–2  $\mu\text{m}$ ; density,  $1190 \text{ kg/m}^3$ ) were suspended in the BMF solution enabling the visualization of the flow images. A high-speed charge-coupled device (CCD) camera (FASTCAM SA-Z; Photron Inc., West Wycombe, Buckinghamshire, UK) was used to capture the images at  $1,024 \times 1,024$  pixels resolution and 8 bit/pixel greyscale intensity at a frequency of 2000 Hz. The camera was mounted with its optical axis perpendicular to the laser sheet. Two sets of images were captured for the AFX flow phantom at proximal inflow and bifurcation regions for ten cardiac cycles. Data were processed as described in section 6.2.4 to generate a flow pattern and haemodynamic parameters, including TAWSS, OSI and RRT. These PIV data were used to validate the corresponding results predicted with CFD simulation.



**Figure 8-2.** Laser particle image velocimetry experimental set-up comprises (a) Vivitro pump, (b) extended entrance length, (c) Bronkhorst M55 Coriolis flow meter, (d) flow phantom, (e) compliance chamber, (f) Cynergy3 UF8B ultrasound flow sensor x 3, (g) needle valve x 3, (h) manometer, (i) flow meter display x 3, (j) reservoir, (k) laser source, (l) deflector, (m) high speed CCD camera, (n) laser sheet and (o) laser shield.



## 8.2.2 CFD Methodology

In order to compare the PIV and CFD methods, the discretised models utilized to perform CFD simulation were matched to the physical models used in the PIV measurement. These include stent struts, PDMS Sylgard-184 model, exit lengths of iliac outlets and the associated resistance, compliance elements represented by needle valves and compliance chamber in the experimental flow circuit. Non-Newtonian fluid models were adopted by some researchers to study blood flow [173-176], while Newtonian fluid models were used by others to characterize blood flow in human arteries [177-179]. In the case of PIV experiment, the fluid flow is incompressible, isothermal, steady and Newtonian. Compatible to the experiment, the wall boundaries of the CFD model are assumed to be rigid and impermeable. Based on the maximum inlet volumetric flow rate of 68 mL/s, an inlet internal diameter of 2.5 cm, dynamic viscosity of 4.2 mPa.s and density of 1114 kg/m<sup>3</sup> for the BMF; Reynold's number of 1045 suggests laminar fluid flow. A generic finite volume laminar flow CFD code ANSYS-FLUENT 19.2 was utilized to solve the Navier–Stokes equations. Numerical solutions were obtained through the iterative algebraic multi-grid solver with the advection terms approximated via the second-order upwind differencing scheme. Ansys Windkessel extension module<sup>7</sup> was adopted in the CFD simulation to account for the Windkessel effects at the iliac outlets. In the present study, steady-state simulation was performed and convergence was achieved within 120 iterations with 10<sup>-6</sup> residual criteria. A fixed time step of 0.0005 s was adopted for transient simulations for three periodic cycles. Periodicity was observed at the third cardiac cycle with < 0.2% maximum iliac outlet pressure at the PSV time-point. The data from the first two cardiac cycles were discarded and only those of the third cardiac cycle were used in the subsequent analyses.

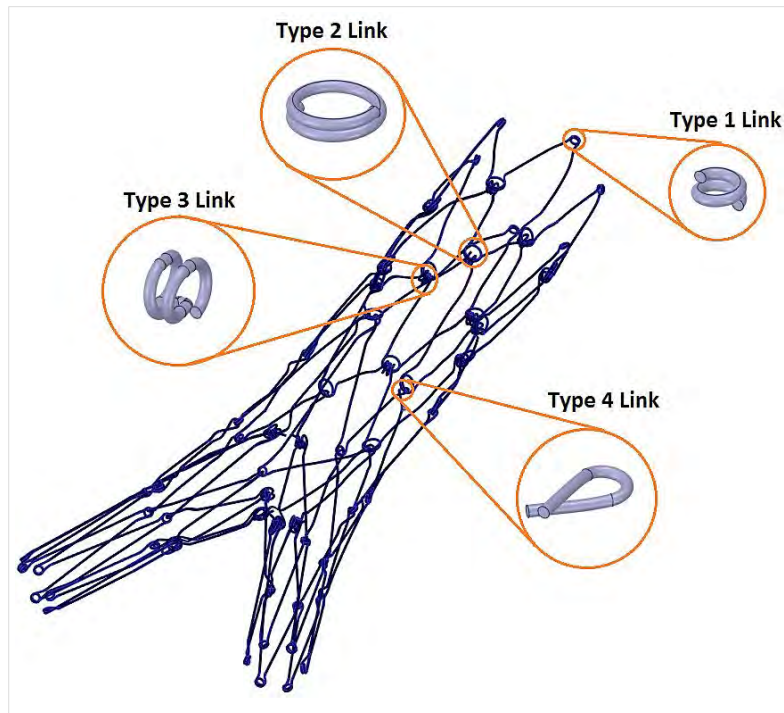
### 8.2.2.1 Struts of AFX stent-graft

The struts of the AFX stent-graft were physically measured using an Absolute Digimatic 0–200 mm #500-172-30 digital Vernier calliper (Mitutoyo Corporation, Sakado, Takatsu-ku, Kawasaki, Kanagawa, Japan). The diameter of the strut wire was 0.3 mm, whereas the length of each individual strut varies from 15–25 mm. Four types of distinct linkages were identified in the AFX Stent-graft where the strut wires were joined to form a self-expandable stent as shown in Figure 8-3. The entire stent was reconstructed

---

<sup>7</sup> Source: <https://catalog.ansys.com/product/5b3bc6857a2f9a5c90d32ee8/windkessel>

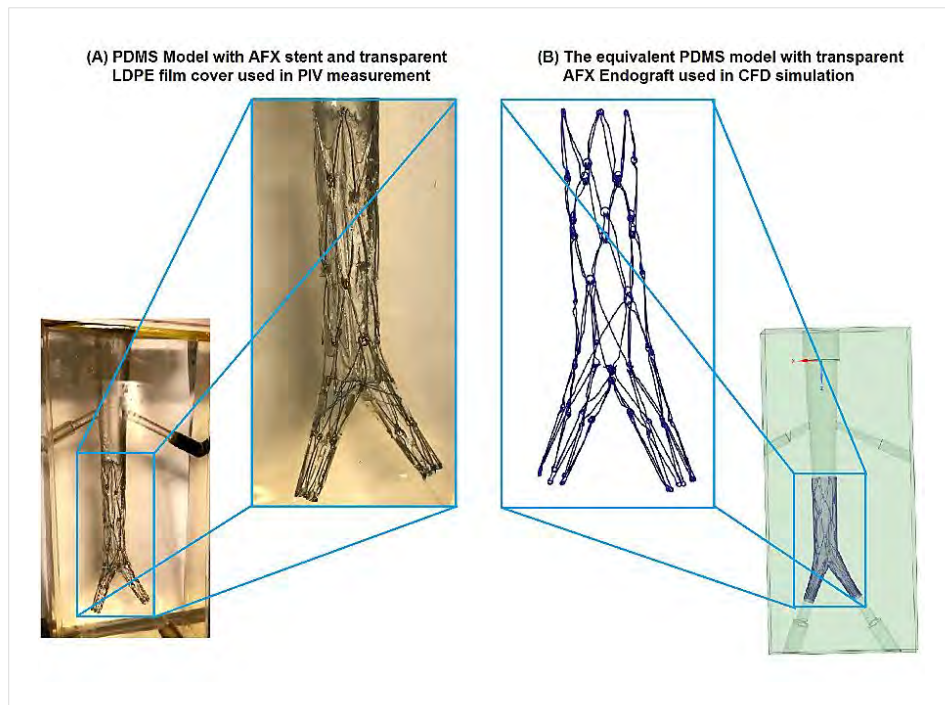
using Ansys SpaceClaim Release 19.2, a 3D direct modelling CAD software (Ansys Inc. Canonsburg, PA, USA).



**Figure 8-3** Reconstructed AFX stent-graft showing four types of linkages used to join the strut wires together.

### 8.2.2.2 Flow phantom

The 3D CAD drawing generated by SolidWorks 2018 (Dassault Systems Concord, MA, USA) used to fabricate the PDMS model was first imported into Ansys SpaceClaim Release 19.2 software. A 40-micron thick LDPE film replicating the modified transparent cover of AFX stent-graft was then added to the inside wall of the PDMS model. Lastly, the struts of the AFX stent-graft created in section 8.2.2.1 were then inserted into the PDMS model to replicate the physical phantom shown in Figure 8-4.



**Figure 8-4** Laser particle image velocimetry (PIV) and computational fluid dynamics comparison (CFD). **A:** Physical PDMS model used in PIV measurement; **B:** Equivalent digitized model used in CFD simulation.

### 8.2.2.3 Boundary conditions

In order to minimize the simulation time, a fully developed pulsatile flow profile was prescribed at the infrarenal aorta inlet. The extended exit lengths were added to the left iliac artery (LIA) and the right iliac artery (RIA) to minimize the end effects of the openings (Figure 8-5). Since an average flow rate of 1.6 L/min was generated by the positive displacement pump at the suprarenal aorta and equally distributed to the renal and iliac arteries in the flow phantom, a flow rate of 0.8 L/min was prescribed at the infrarenal aorta in the CFD simulation. Three-element Windkessel models were prescribed at LIA and RIA. The initial values of total resistance ( $R_T$ ) and compliance ( $C$ ) at the iliac outlets were adopted from a previous study [117]. The 5.6% ratio of proximal resistance ( $Z$ ) to  $R_T$  and 94.4% of distal resistance ( $R$ ) to  $R_T$  was adopted from another study [122]. Subsequently,  $R$ ,  $Z$  and  $C$  were fine-tuned to produce an outflow of 0.4 L/min at LIA and RIA and a cardiac pressure of 80–120 mmHg.

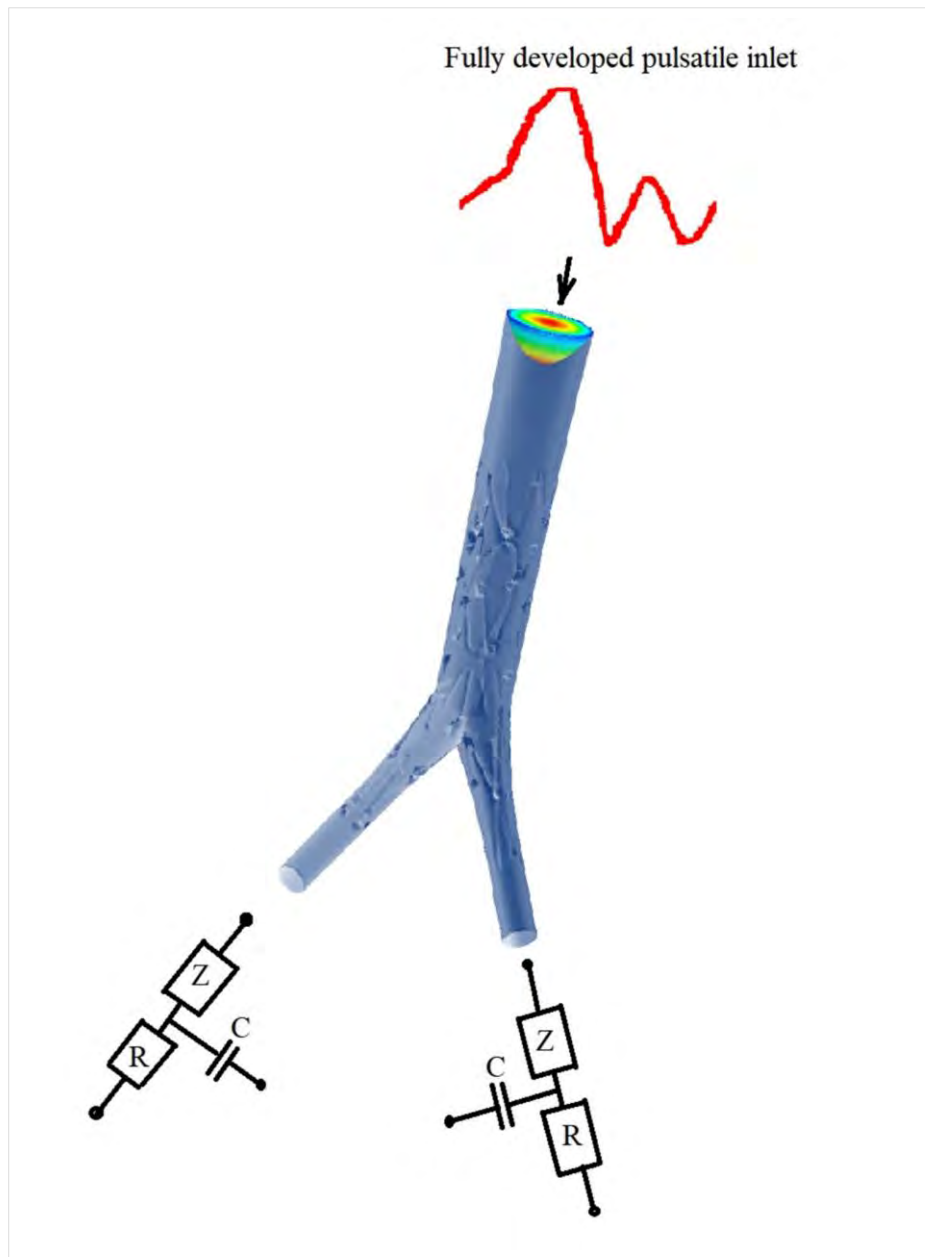


Figure 8-5 Boundary condition set-up for CFD model.

#### 8.2.2.4 Meshing

Fluent meshing was used to generate polyhedral meshes. The three meshes were created for grid independence and periodicity convergence analyses. The coarse, medium and fine meshes with 51,564, 160,744 and 478,338 cells, respectively, were used in the CFD simulations as shown in Figure 8-6.

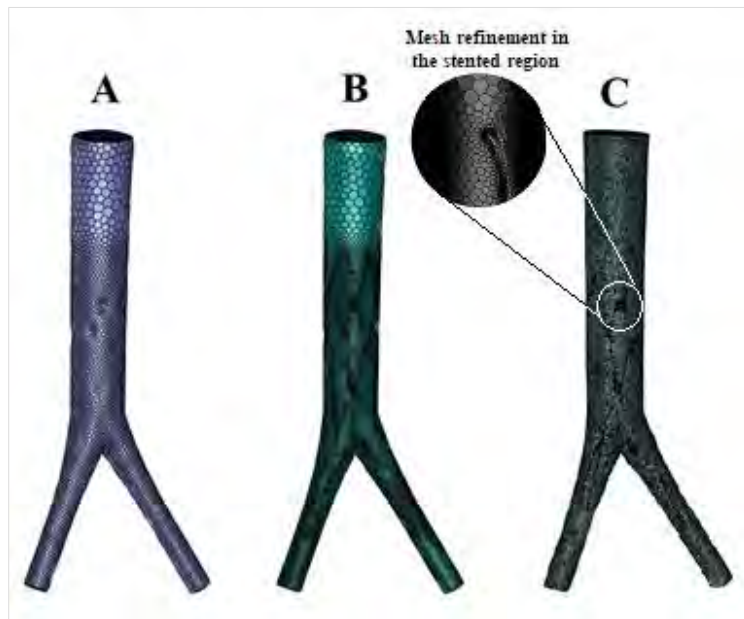


Figure 8-6 Polyhedral meshes A: 46,806 cells coarse mesh, B: 160,132 cells medium mesh, C: 470,857 cells fine mesh.

### 8.2.2.5 Grid independence and periodicity convergence tests

The hemodynamic parameters for inflow and bifurcation regions were determined based on the distance from the origin matching that of PIV analyses (Figure 8-7). The predicted maximum outlet pressure at the iliac arteries between the medium and fine meshes was at a discrepancy of 0.2%. Pair-wise Student's T-test confirmed no significant difference between medium and fine meshes ( $P > 0.05$ ).

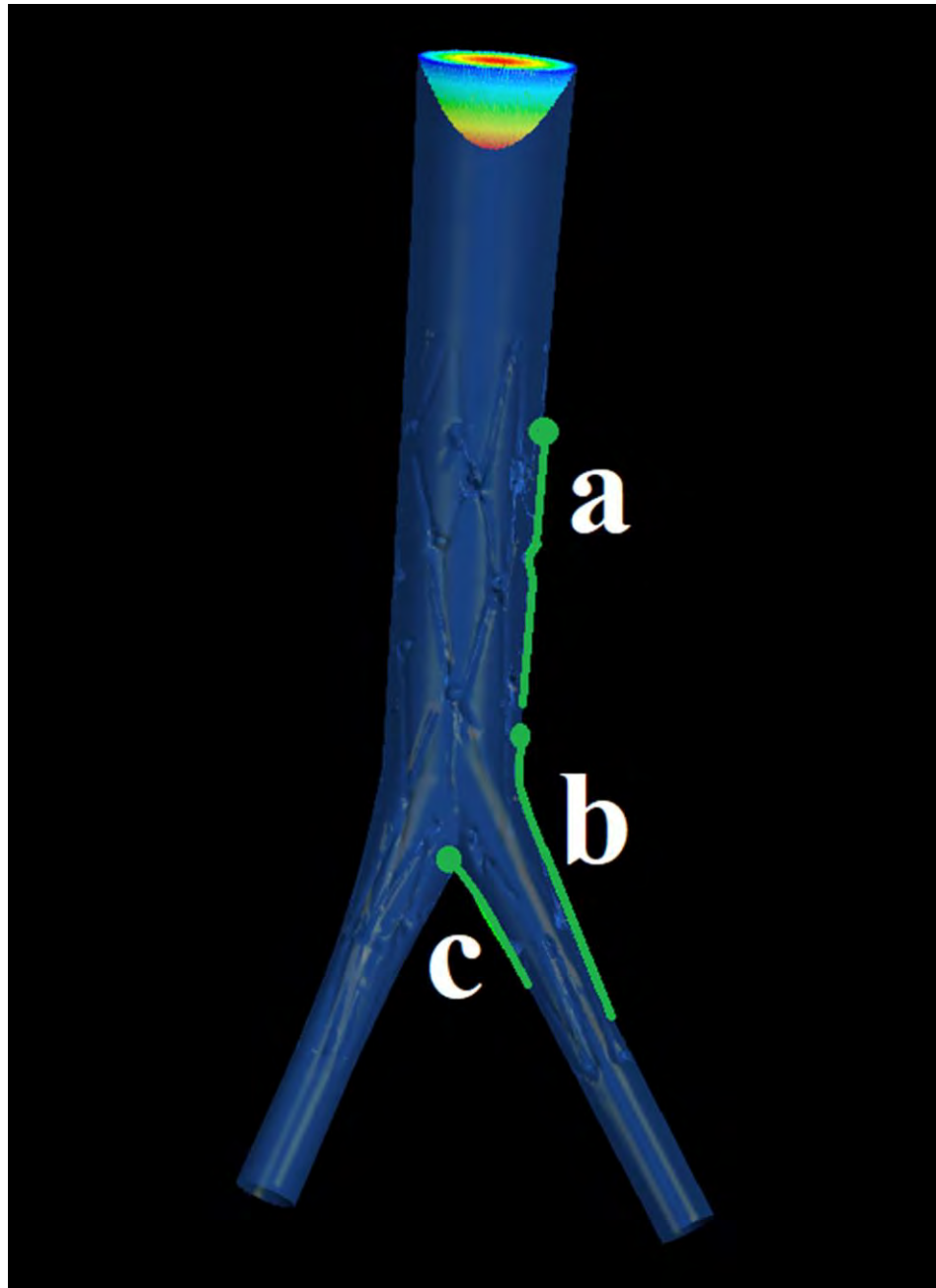


Figure 8-7 Region of interest in CFD simulation, (a) Inflow region, (b) bifurcation right edge and (c) bifurcation left edge.

### 8.3 Results

#### 8.3.1 Grid-independent convergence

Figure 8-8–Figure 8-10 show the plots of TAWSS, OSI and RRT for coarse, medium and fine meshes, respectively, indicating little difference between medium and fine meshes. Students’ T-tests were used to compare the predicted TAWSS, OSI and RRT at the inflow and bifurcation regions ( $P > 0.05$ ; Table 8-1 – Table 8-3). The values obtained led to the conclusion that the fine mesh could be employed in obtaining grid-independent solutions. Hereafter, the prediction results in the subsequent sections are based on fine mesh.

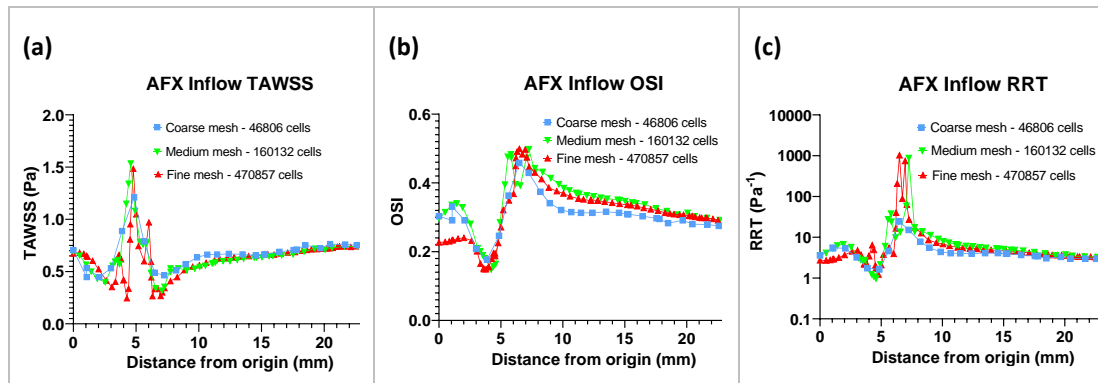


Figure 8-8 Results of TAWSS, OSI and RRT from CFD simulations in the inflow region for (a) coarse, (b) medium and (c) fine meshes.

Table 8-1 P-values for Student’s T-test pair-wise comparison of TAWSS, OSI and RRT in the AFX inflow region for coarse, medium and fine meshes

Mesh (elements)	TAWSS (Pa)			OSI			RRT (Pa <sup>-1</sup> )		
	Mean	Range	P-value	Mean	Range	P-value	Mean	Range	P-value
46806	0.669	0.447 - 1.209	0.720	0.308	0.177 - 0.458	0.049	5	1.6 - 24	0.241
160132	0.653	0.689 - 1.535		0.340	0.148 - 0.498		26	1 - 877	
470857	0.617	0.244 - 1.484	0.376	0.310	0.149 - 0.499	0.070	37	1.2 - 1028	0.681

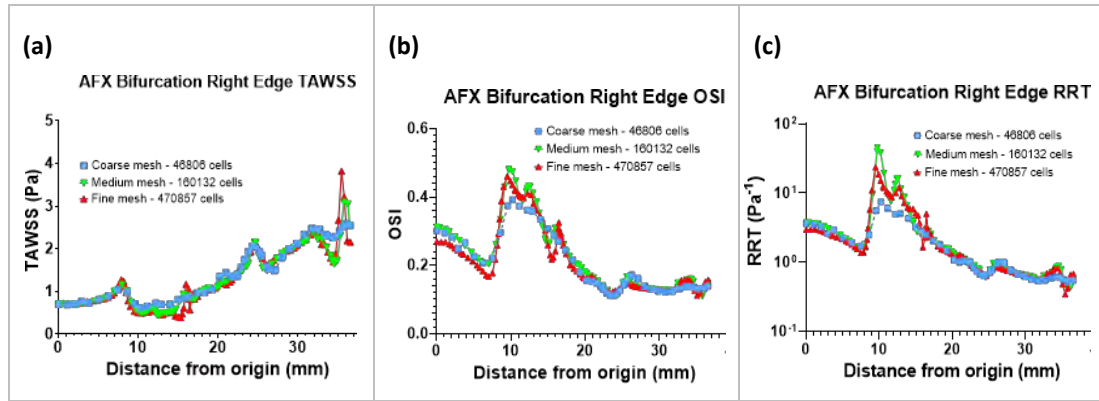


Figure 8-9 Results of TAWSS, OSI and RRT from CFD simulations in the AFX bifurcation right edge for (a) coarse, (b) medium and (c) fine meshes.

Table 8-2 P-values for Student’s T-test pair-wise comparison of TAWSS, OSI and RRT in the AFX bifurcation right edge for coarse, medium and fine meshes

Mesh (elements)	TAWSS (Pa)			OSI			RRT (Pa <sup>-1</sup> )		
	Mean	Range	P-value	Mean	Range	P-value	Mean	Range	P-value
46806	1.554	0.621–2.595	0.021	0.191	0.111–0.392	0.016	1.7	0.5–7.5	0.004
160132	1.290	0.446–3.089		0.312	0.110–0.481		4.3	0.4–45.3	
470857	1.256	0.391–3.818		0.221	0.112–0.460		3.1	0.3–23.5	



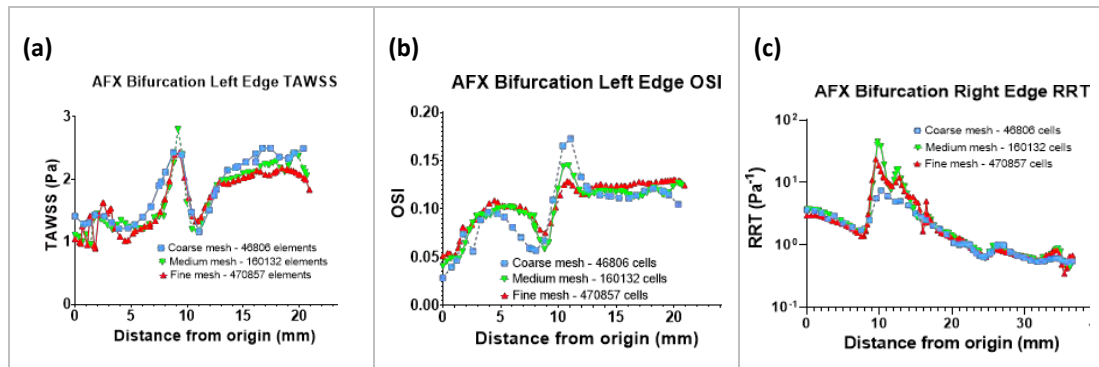


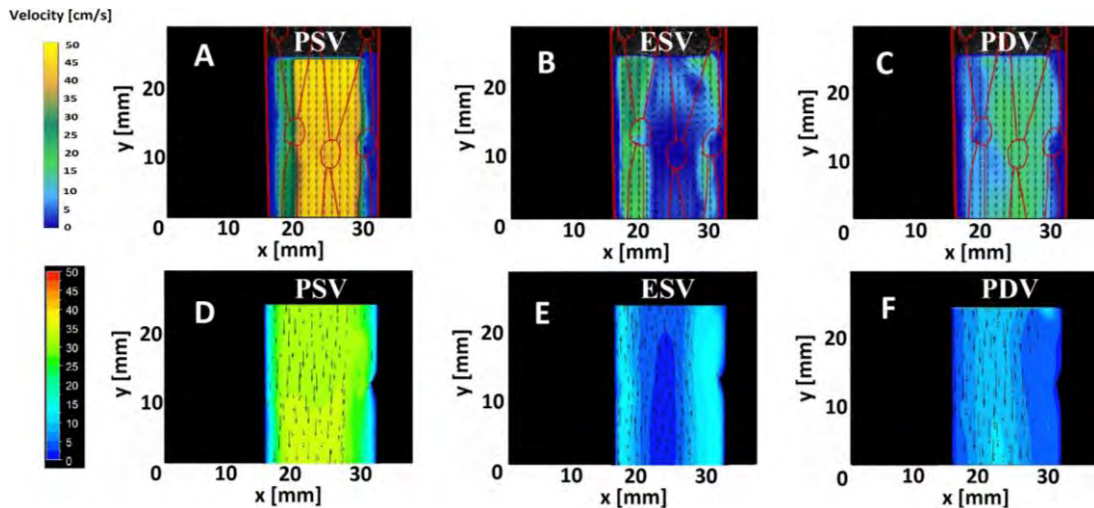
Figure 8-10 Results of TAWSS, OSI and RRT from CFD simulations in the AFX bifurcation left edge for (a) coarse, (b) medium and (c) fine meshes.

Table 8-3 P-values for Student’s T-test pair-wise comparison of TAWSS, OSI and RRT in the AFX bifurcation left edge for coarse, medium and fine meshes

Mesh (elements)	TAWSS (Pa)			OSI			RRT (Pa <sup>-1</sup> )		
	Mean	Range	P-value	Mean	Range	P-value	Mean	Range	P-value
46806	1.878	1.412–2.502	0.145	0.098	0.029–0.173	0.590	0.7	0.5–1.4	0.124
160132	1.730	0.962–2.802		0.101	0.041–0.145		0.7	0.4–1.3	
470857	1.665	0.901–2.435		0.106	0.051–0.130		0.8	0.5–1.3	

### 8.3.2 Inflow pattern

At the PSV time-point, the maximum velocity was achieved as the BMF accelerated into the phantom in both PIV and CFD methods. A disrupted flow pattern was observed at the left side of the aorta for both PIV and CFD, especially at the ESV phase (Figure 8-11(B); Video 1<sup>8</sup>, online only and Figure 8-11(E); Video 5<sup>9</sup>, online only). The data obtained using PIV and CFD methods were consistent.



**Figure 8-11** Inflow patterns of laser PIV and CFD. A: PIV at PSV time-point, B: PIV at ESV time-point, C: PIV at PDV time-point, D: CFD at PSV time-point, E: CFD at ESV end-point and F: CFD at PDV time-point

<sup>8</sup> <https://vimeo.com/manage/427987384/general>

<sup>9</sup> <https://vimeo.com/manage/429844328/general>

### 8.3.3 Bifurcation flow pattern

The flow pattern at the bifurcation at PSV, ESV and PDV time-points for PIV and CFD methods is shown in Figure 8-12. The recirculation was distinctly observed, especially at the ESV phase in the PIV method (Figure 8-12(B); Video 2<sup>10</sup>, online only), as compared to that in the CFD method (Figure 8-12(E); Video 6<sup>11</sup>, online only).

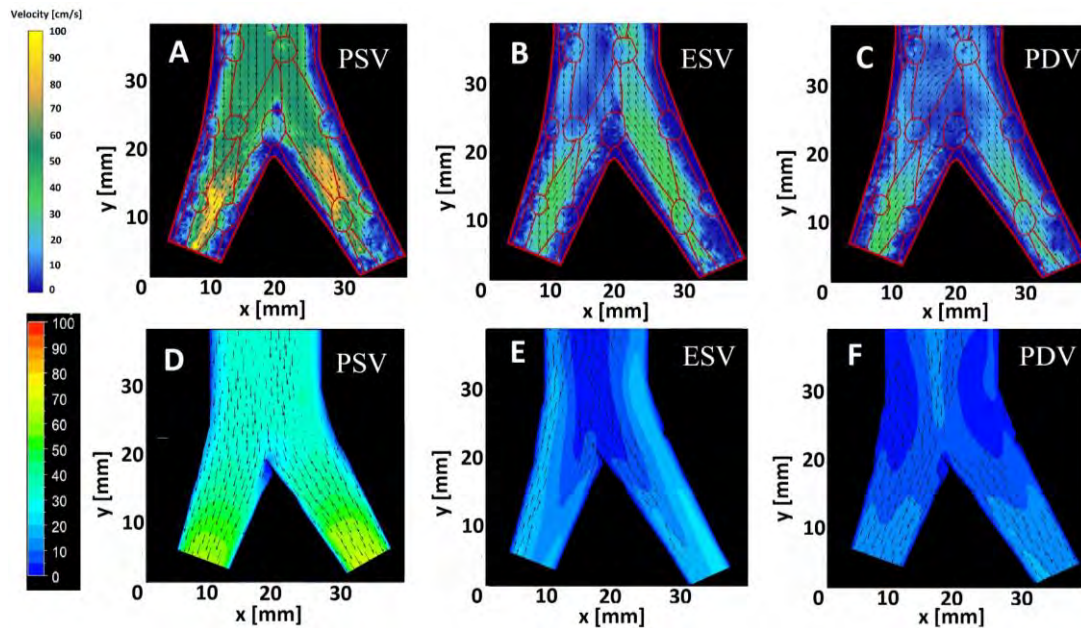


Figure 8-12 Bifurcation flow patterns. A: PIV at PSV, B: PIV at ESV, C: PIV at PDV, D: CFD at PSV, E: CFD at ESV, and F: CFD at PDV.

### 8.3.4 Hemodynamic comparison

Table 8-4 summarizes the results of haemodynamic comparison (TAWSS, OSI and RRT) between the PIV and CFD methods at the inflow and bifurcation regions. The mean and range for each hemodynamic parameter were calculated from the raw data, and P-value of pair-wise Student's T-test was included in the table;  $P > 0.05$  indicated an agreement between the two methods, while  $P < 0.05$  implied a disagreement between the two methods.

<sup>10</sup> <https://vimeo.com/manage/427996402/general>

<sup>11</sup> <https://vimeo.com/manage/429849657/general>

**Table 8-4 TAWSS, OSI and RRT data at inflow and bifurcation for PIV and CFD**

Region of interest	Stent	TAWSS (Pa)			OSI			RRT (Pa <sup>-1</sup> )		
		Mean	Range	P-value	Mean	Range	P-value	Mean	Range	P-value
<b>Inflow</b>										
	PIV (n=39)	0.185	0.036–0.296	<0.001	0.316	0.207–0.475	0.068	55	8–342	0.304
	CFD (n=67)	0.617	0.244–1.484		0.310	0.149–0.499		37	1–1028	
<b>Bifurcation</b>										
Right Edge	PIV (n=114)	0.074	0.013–0.186	<0.001	0.307	0.123–0.496	<0.001	134	13–1,744	<0.001
	CFD (n=105)	1.264	0.391–3.818		0.221	0.112–0.460		3	0.3–24	
Left Edge	PIV (n=57)	0.088	0.009–0.242	<0.001	0.339	0.217–0.482	<0.001	273	9–3,603	<0.001
	CFD (n=72)	1.665	0.901–2.435		0.108	0.053–0.138		0.8	0.5–1.3	
<b>Total</b>	PIV (n=171)	0.078	0.009–0.242	<0.001	0.318	0.123–0.496	<0.001	180	9–3,603	<0.001
	CFD (n=177)	1.406	0.391–3.818		0.177	0.053–0.460		2.3	0.3–24	

### 8.3.5 Hemodynamic plots

Figure 8-13 to Figure 8-15 show the plots of TAWSS, OSI and RRT along the vessel wall at the inflow, bifurcation right edge and bifurcation left edge, respectively.

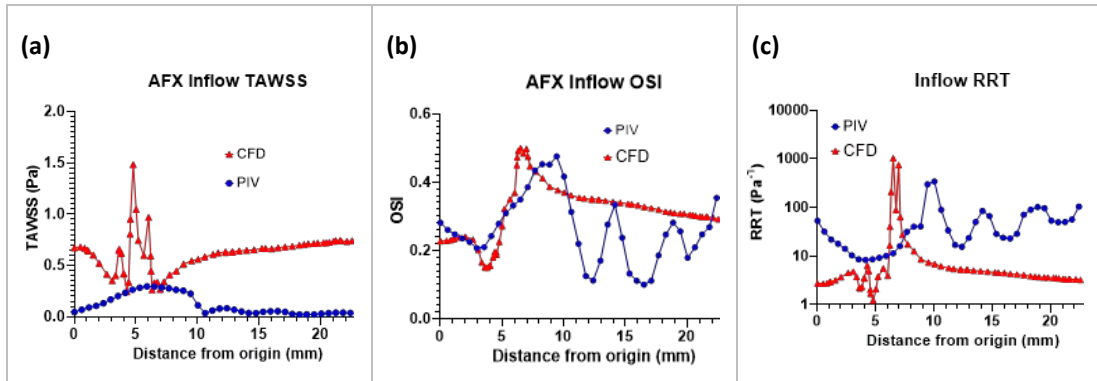


Figure 8-13 TAWSS, OSI and RRT plots at the inflow region for PIV and CFD methods.

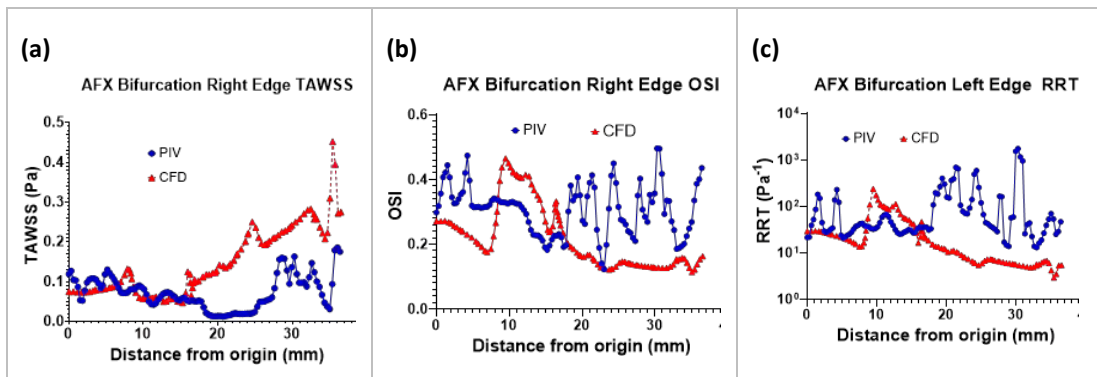


Figure 8-14 TAWSS, OSI and RRT plots at the bifurcation right edge for PIV and CFD methods.

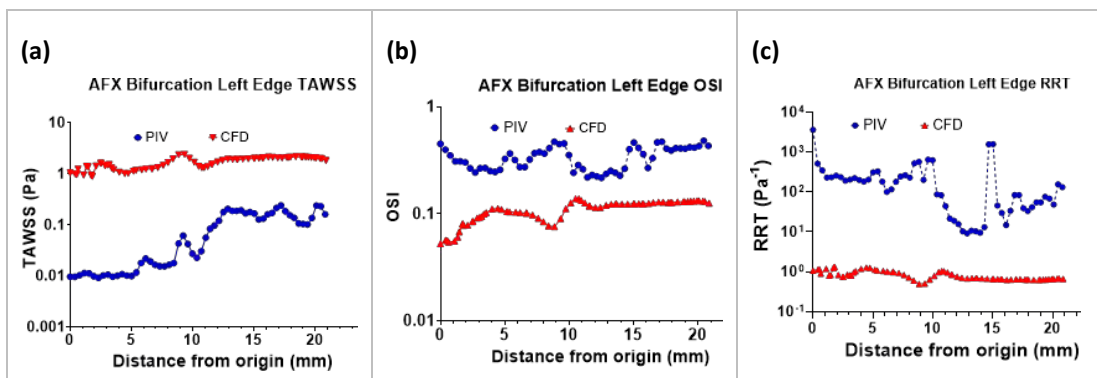


Figure 8-15. TAWSS, OSI and RRT plots at the bifurcation left edge for PIV and CFD methods.

## 8.4 Discussion

In the current study, a new method to reconstruct the AFX stent-graft was introduced. CFD simulations were performed using a fluid flow model that replicated the PIV experimental set-up. The CFD results of TAWSS, OSI and RRT were compared to those of the PIV method using pair-wise Student's T-tests. A poor agreement was observed between the two methods for TAWSS in the inflow region as the mean TAWSS of 0.617 Pa predicted by CFD was significantly higher than 0.185 Pa measured with PIV method ( $P < 0.001$ ). However, reasonable agreements were noted for OSI and RRT in the inflow region ( $P = 0.068$  and  $0.304$ , respectively). These values indicated no significant differences were detected between the OSI and RRT predicted by CFD and those measured with PIV method in the inflow region. Furthermore, the strongest agreement was for RRT in the inflow region, wherein the P-value was more than six-fold of the significant value 0.05. In contrast, a poor agreement was detected in the bifurcation region with  $P < 0.001$  for TAWSS, OSI and RRT. Intriguingly, CFD over-estimated TAWSS and underestimated OSI and RRT in the bifurcation region. The mean TAWSS of 1.406 Pa predicted by CFD was significantly higher than 0.078 Pa measured by PIV method ( $P < 0.001$ ). The mean OSI of 0.177 predicted by CFD was significantly  $< 0.318$ , determined by the PIV experiment. Similarly, the mean RRT of 2.3 predicted by CFD was significantly lower than 180 by the PIV method. This was in agreement with the overestimated velocity in the CFD method as compared to PIV or ultrasound measurement methods, as reported previously [168, 171].

The current study was in agreement with a previous study by Gallo et al. to validate CFD results with respect to PIV findings of pulsatile blood flow [134]. Also, the findings were consistent between PIV and CFD methods near the inlet section of the flow as compared to a weaker agreement close to the outlet section of the flow. In the study, the velocity magnitude in the downstream region of aortic flow showed a poor agreement with the experimentally measured counterpart. However, in the current study, a reasonable agreement of OSI and RRT between PIV and CFD methods was established with  $P = 0.068$  and  $0.304$  in the inflow region, respectively, as opposed to a poor agreement with  $P < 0.001$  in the downstream bifurcation region. Raschi et al. [135] reported marked differences between PIV and CFD in regions close to the wall, in regions of slow flow and during the diastolic phase. This phenomenon could be ascribed to the poor agreement in the bifurcation region in the current study.

As pointed out by Bordone et al. [180], spatial velocity resolution might contribute to the discrepancies observed in the shear stresses between PIV and CFD methods because it is limited by seeding density of the 10-micron fluorescent rhodamine-B particles. Thus, it was speculated that the seeding density of the particles affected the spatial resolution of the PIV measurements, specifically those close to the flow boundaries. This phenomenon was evident when the overestimation of WSS by the CFD method was similar to that in the bifurcation region.

The rigid wall was assumed in our CFD simulation; however, the PDMS phantom presented a Young modulus of 0.5–2 MPa [181]. Moreover, the silicone tubes used in the flow loop are also not rigid. When a compliant carotid model was compared to a rigid wall model, the peak WSS was reported to be 40% higher and TAWSS 19% higher in the rigid wall than in the compliant wall [182]. Although a wall-less PDMS was used in our PIV experiment, the dispensability of the PDMS phantom and silicone tubing could have contributed to the overestimation of TAWSS in our study.

One of the limitations of our CFD model is that the struts of the AFX stent-graft reconstructed using 3D CAD software might not be the replica of the actual stent-graft and its position in the 3D model might not match perfectly with the model used in the PIV experiment. Scanning and reconstructing the phantom using a micro-CT scanner [133, 168, 183, 184] might improve the accuracy of the CFD model. Secondly, the selection of the region of interest in the PIV method, as described in section 6.2.3, and the CFD method, as described in section 8.2.2.5, does not allow for a precise superimposition between the experimental and CFD geometries. This drawback could be overcome to improve alignment by embedding the ROI markers in the flow phantom such that the laser sheet can be aimed precisely in the PIV experiments, and the corresponding region of interest locations can be determined accurately when scanning the phantom with micro-CT scanner for 3D reconstruction in the CFD method. Thirdly, the CFD scheme is a well-validated laminar scheme for blood flow analysis based on the Reynold number  $< 2300$ ; therefore, any transition from a steady flow to disturbed flow in the reverse flow phase is not accounted for in the CFD.

## **8.5 Conclusion**

In this comparison study, a disrupted flow was observed in the inflow and bifurcation regions, especially at the end-systolic phase in the PIV experiments in comparison to corresponding results from CFD simulations. The CFD predictions overestimated TAWSS in inflow and bifurcation regions resulting in poor agreement between the two methods. However, a reasonable agreement was established between PIV and CFD methods for OSI and RRT in the inflow region but a poor consistency in the bifurcation region. Thus, further improvements in CFD and PIV models are needed to overcome the inherent limitations in order to substantiate the use of CFD method as a clinical tool for diagnosis and provide an in-depth insight into the haemodynamic behaviour in vascular flow.



## Chapter Nine

# 9

## Conclusions and Future Directions

This thesis describes several chapters on AIOD. AIOD results from stenotic lesions present at the distal aorta, and the proximal iliac arteries are the most difficult stenoses to treat due to their complexity and location. The treatment using CERAB configuration and AFX stent-graft are addressed extensively. These chapters also address topics that combine biofluidics, medical insights and their clinical implications. The ultimate goal is to make an evidence-based decision to justify the choices in the treatment of AIOD to improve the long-term outcomes.

## 9.1 Conclusions

Regarding the first research objective, we combined the ideas of CFD simulations, design of experiment and multivariate regression tool and established a PSV predictor as a potential screening tool to supplement the current restenosis gold standard of a lesion with a PSV value ratio  $> 2.5$  [158]. However, with 47% specificity and 83% sensitivity based on the retrospective studies, the PSV predictor is deemed unsuitable as a clinical screening tool.

In the second research objective, we sought to test the hypothesis that AFX stent-graft is a more effective endovascular treatment of AIOD compared to CERAB configuration due to its one-piece design, eliminating radial mismatch and restoring the native bifurcation for possible future endovascular interventions. The results of the haemodynamic comparison between the two endovascular techniques demonstrated a disturbed flow in the bifurcation region of AFX stent-graft as compared to CERAB configuration. Subsequently, the quantified hemodynamic outcomes showed a significantly lower mean TAWSS of 0.078 (range: 0.009–0.242) Pa, a significantly higher mean OSI of 0.318 (range: 0.123–0.496) and a significantly prolonged mean RRT of 180 (range: 9–3,603)  $\text{Pa}^{-1}$  by PIV analysis in the bifurcation region of the AFX stent-graft as compared to a mean TAWSS of 0.229 (range: 0.013–0.906) Pa, a mean OSI of 0.252 (range: 0.055–0.472) and a mean RRT of 88 (range: 2–840)  $\text{Pa}^{-1}$  in the bifurcation region of the CERAB configuration ( $P < 0.001$ ). Thus, we could conclude that CERAB configuration is more protective of thrombosis and therefore, more effective in treating AIOD as compared to the AFX stent-graft in an experimental setting.

Furthermore, a novel roller pump has been developed to resolve one of the limitations of the PIV experimental set-up that applied the suprarenal flow profile at the inlet of the phantom eliminating the renal branches and allowing a laser sheet to illuminate the inflow region of the AFX flow phantom. The measured flow profiles for the three types of

vascular flows, carotid, suprarenal and infrarenal, generated by the novel pump matched well with reference flow profiles. Thus, it could be concluded that the novel roller pump is suitable for benchtop testing of physiological flow.

In addition, the study comparing the haemodynamics of laser PIV experiments and CFD simulations on the flow phantom deployed with a modified transparent AFX stent-graft concluded that reasonable agreements were found between CFD and PIV methods for OSI and RRT in the inflow region. However, a poor agreement was established for TAWSS in the inflow region. Also, a poor agreement was noted for TAWSS, OSI and RRT in the bifurcation region, ( $P < 0.001$ ). Further improvements to overcome the limitations inherent to PIV and CFD models are needed for better haemodynamic agreements between the two methods in order to validate the CFD model for clinical applications.

Our data were validated by a well-developed method based on the parameters described in the literature. CFD is a well-established technique for the investigation of haemodynamics in cardiovascular disease. We also used laser PIV because it is the gold standard for in vitro flow studies of the cardiovascular system. Thus, AIOD researchers will gain a better understanding of flow pattern, velocity and haemodynamic parameters post-stenting. Clinicians might use our findings to select the appropriate type of stent for their patients to improve the diagnosis and monitor the patients following endovascular treatments.

The de facto standard non-invasive flow measurement techniques in research laboratories are based on optical principles; the most prominent current method is laser PIV. One of the limitations of this method is that it is a 2D technique, thereby necessitating multiple experiments on a pseudo-3D flow field in the region of interest. However, the PVI method would not be able to measure components along the z-axis (towards/away from the camera). These components might also introduce interference in the data for the x/y-components caused by parallax. These issues do not exist in stereoscopic PIV, which uses two cameras to measure all the three velocity components. A stereoscopic PIV will be expensive, and its data acquisition complex. In addition, the accuracy of the experimental results is dependent on the spatial resolution, and hence, a high-resolution camera, a small region of interest and thick laser sheet would produce better results but at a high cost. Another limitation is the use of class IV laser, a safety constraint. An alternative echo-PIV method is the emerging ultrasound PIV, but it is not yet widely available.

In summary, a PSV prediction tool has been developed as a potential screening tool to improve the diagnosis of patients treated with CERAB endovascular procedure; however,

the sensitivity and specificity are inadequate, thereby deeming the tool unsuitable for clinical practice.

Herein, we concluded that CERAB is a more superior endovascular technique in treating extensive AIOD based on haemodynamic outcomes in comparison to AFX stent-graft and CERAB configuration.

## 9.2 Future Directions

CFD simulations and laser PIV experiments avoid the use of live subjects and facilitate the investigation of the haemodynamics of human anatomy using an in vivo method. Our study improves the understanding of biofluidics of human aortoiliac bifurcation. These research findings would assist in the diagnosis and improve long-term treatment outcomes. However, a few suggestions for further research are outlined as follows:

- Future study to improve the predictive and CFD models.
- Prospective studies to evaluate the sensitivity and specificity of the PSV predictor using a smart-phone application, as described in Appendix E.
- Re-evaluate the PSV predictor with CFD simulations incorporating fluid-structure interaction to account for the non-rigid blood vessel.
- In vivo study of the haemodynamics of AFX stent-graft and CERAB configuration using ultrasound image velocimetry (UIV) and compare with the laser PIV findings.
- Perform laser PIV experiments using flow phantom embedded with markers and 3D reconstruction with micro-CT scanning for alignment of regions of interest between PIV and CFD methods and validate the CFD simulation.
- Study the effect of various pulsatile flow profiles on the surplus haemodynamic energy (SHE), a surrogate measure of microcirculation during cardiopulmonary bypass procedure using a novel pump based on the design outlined in Appendix G.

The computational resource will be a critical element of future research, especially supercomputer, might be required to carry out computational simulations involving resources that demand fluid-structure interactions.

## References

1. Fowkes, F.G.R., et al., Comparison of global estimates of prevalence and risk factors for peripheral artery disease in 2000 and 2010: a systematic review and analysis. *The Lancet*, 2013. **382**(9901): p. 1329-1340.
2. Lakhter, V. and V. Aggarwal, Current Status and Outcomes of Iliac Artery Endovascular Intervention. *Interventional Cardiology Clinics*, 2017. **6**(2): p. 167-180.
3. Mouanoutoua, M., et al., Endovascular treatment of aortoiliac occlusive disease using kissing stents in high-risk patients: Procedural results and long-term follow-up. *Journal of the American College of Cardiology*, 2003. **41**(6, Supplement 1): p. 76-77.
4. Rzucidlo, E.M., et al., Early results of stent-grafting to treat diffuse aortoiliac occlusive disease. *Journal of Vascular Surgery*, 2003. **37**(6): p. 1175-1180.
5. Carnevale, F.C., Percutaneous Endovascular Treatment of Chronic Iliac Artery Occlusion. *Cardiovascular and Interventional Radiology*, 2004. **27**(5).
6. Upchurch, G.R., et al., Diffusion of new technology in health care: The case of aorto-iliac occlusive disease. *Surgery*, 2004. **136**(4): p. 812-818.
7. Galaria, I.I. and M.G. Davies, Percutaneous Transluminal Revascularization for Iliac Occlusive Disease: Long-term Outcomes in TransAtlantic Inter-Society Consensus A and B Lesions. *ACC Current Journal Review*, 2005. **14**(9): p. 56-56.
8. Simons, P.C.G., et al., Long-term results of primary stent placement to treat infrarenal aortic stenosis. *European journal of vascular and endovascular surgery : the official journal of the European Society for Vascular Surgery*, 2006. **32**(6): p. 627-633.
9. Chang, R.W., et al., Long-term results of combined common femoral endarterectomy and iliac stenting/stent grafting for occlusive disease. *Journal of Vascular Surgery*, 2008. **48**(2): p. 362-367.
10. van't Riet, M., et al., Endovascular treatment of atherosclerosis at the aortoiliac bifurcation with kissing stents or distal aortic stents: A temporary solution or durable improvement? *Journal of Vascular Nursing*, 2008. **26**(3): p. 82-85.
11. Moise, M.A., et al., Endovascular management of chronic infrarenal aortic occlusion. *J Endovasc Ther*, 2009. **16**(1): p. 84-92.
12. Jongkind, V., et al., A systematic review of endovascular treatment of extensive aortoiliac occlusive disease. *Journal of Vascular Surgery*, 2010. **52**(5): p. 1376-1383.
13. Dosluoglu, H.H., Endovascular Therapy Should Be the First Line of Treatment in Patients With Severe (TASC II C or D) Aortoiliac Occlusive Disease. *Journal of Endovascular Therapy*, 2013. **20**(1): p. 74-79.

14. Sixt, S., et al., Endovascular Treatment for Extensive Aortoiliac Artery Reconstruction: A Single-Center Experience Based on 1712 Interventions. *Journal of Endovascular Therapy*, 2013. **20**(1): p. 64-73.
15. Tewksbury, R., et al., Outcomes of covered expandable stents for the treatment of TASC D aorto-iliac occlusive lesions. *Vascular*, 2015. **23**(6): p. 630-636.
16. Grimme, F.A.B., et al., Endovascular Treatment of Occlusive Lesions in the Aortic Bifurcation with Kissing Polytetrafluoroethylene-Covered Stents. *Journal of Vascular and Interventional Radiology*, 2015. **26**(9): p. 1277-1284.
17. Grimme, F.A.B., et al., First Results of the Covered Endovascular Reconstruction of the Aortic Bifurcation (CERAB) Technique for Aortoiliac Occlusive Disease. *European Journal of Vascular and Endovascular Surgery*, 2015. **50**(5): p. 638-647.
18. Grimme, F.A.B., et al., Midterm Outcome of Balloon-Expandable Polytetrafluoroethylene-Covered Stents in the Treatment of Iliac Artery Chronic Occlusive Disease. *Journal of Endovascular Therapy*, 2012. **19**(6): p. 797-804.
19. Mwipatayi, B.P., et al., A comparison of covered vs bare expandable stents for the treatment of aortoiliac occlusive disease. *Journal of Vascular Surgery*, 2011. **54**(6): p. 1561-1570.e1.
20. Cury, M.V.M., T.O. Rodrigues, and A.A.T. Issa, Percutaneous implantation of a unibody endograft to treat non-aneurysmal aortoiliac disease. *Vasa*, 2017. **46**(2): p. 138-141.
21. Maldonado, T.S., et al., Treatment of Aortoiliac Occlusive Disease with the Endologix AFX Unibody Endograft. *Eur J Vasc Endovasc Surg*, 2016. **52**(1): p. 64-74.
22. Sirignano, P., et al., Results of AFX Unibody Stent-Graft Implantation in Patients With TASC D Aortoiliac Lesions and Coexistent Abdominal Aortic Aneurysms. *J Endovasc Ther*, 2017. **24**(6): p. 846-851.
23. Leriche, R. and A. Morel, The Syndrome of Thrombotic Obliteration of the Aortic Bifurcation. *Annals of surgery*, 1948. **127**(2): p. 193-206.
24. Wooten, C., et al., Anatomical significance in aortoiliac occlusive disease. *Clinical Anatomy*, 2014. **27**(8): p. 1264-1274.
25. Zankl, A.R., et al., Neurological symptoms in acute Leriche's syndrome. *Clinical Research in Cardiology*, 2010. **99**(7): p. 459-462.
26. Günaydin, Z.Y., et al., Juxtarenal leriche syndrome. *Turk Kardiyoloji Dernegi Arsivi*, 2015. **43**(2): p. 212.
27. Shaaban, A.M. and A.J. Duerinckx, Wall Shear Stress and Early Atherosclerosis. *American Journal of Roentgenology*, 2000. **174**(6): p. 1657-1665.

28. Stary, C.H., et al., A Definition of the Intima of Human Arteries and of Its Atherosclerosis-Prone Regions: A Report From the Committee on Vascular Lesions of the Council on Arteriosclerosis, American Heart Association. *Circulation*, 1992. **85**(1): p. 391-405.
29. Bae, M., et al., Risk factors associated with postoperative prosthetic graft patency in Leriche syndrome. *Asian Journal of Surgery*, 2019. **42**(1): p. 235-239.
30. Aboyans, V., et al., The General Prognosis of Patients With Peripheral Arterial Disease Differs According to the Disease Localization. *Journal of the American College of Cardiology*, 2010. **55**(9): p. 898-903.
31. Hiwada, K., Y. Jiang, and K. Kohara, Low wall shear stress in carotid arteries in subjects with left ventricular hypertrophy\*. *American Journal of Hypertension*, 2000. **13**(8): p. 892-898.
32. Wild, S.H., et al., Metabolic syndrome, haemostatic and inflammatory markers, cerebrovascular and peripheral arterial disease: The Edinburgh Artery Study. *Atherosclerosis*, 2009. **203**(2): p. 604-609.
33. Boersen, J.T., et al., Flow and wall shear stress characterization after endovascular aneurysm repair and endovascular aneurysm sealing in an infrarenal aneurysm model. *Journal of Vascular Surgery*, 2017: p. 1844-1853.
34. Wang, H.Y., et al., Hemodynamics in Transplant Renal Artery Stenosis and its Alteration after Stent Implantation Based on a Patient-specific Computational Fluid Dynamics Model. *Chin Med J (Engl)*, 2017. **130**(1): p. 23-31.
35. Malek, A.M., S.L. Alper, and S. Izumo, Hemodynamic Shear Stress and Its Role in Atherosclerosis. *JAMA*, 1999. **282**(21): p. 2035-2042.
36. Indes, J.E., et al., Endovascular procedures for aorto-iliac occlusive disease are associated with superior short-term clinical and economic outcomes compared with open surgery in the inpatient population. *Journal of Vascular Surgery*, 2010. **52**(5): p. 1173-1179.e1.
37. Bornfeldt, Karin E. and I. Tabas, Insulin Resistance, Hyperglycemia, and Atherosclerosis. *Cell Metabolism*, 2011. **14**(5): p. 575-585.
38. Bertoia, M.L., et al., Plasma homocysteine, dietary B vitamins, betaine, and choline and risk of peripheral artery disease. *Atherosclerosis*, 2014. **235**(1): p. 94-101.
39. Tsigkou, V., et al., Peripheral artery disease and antiplatelet treatment. *Current Opinion in Pharmacology*, 2018. **39**: p. 43-52.
40. Conte, S.M. and P.R. Vale, Peripheral Arterial Disease. *Heart, Lung and Circulation*, 2018. **27**(4): p. 427-432.
41. Criqui, M.H., et al., Peripheral Artery Disease and Aortic Disease. *Global Heart*, 2016. **11**(3): p. 313-326.

42. Jaff, M.R., et al., An Update on Methods for Revascularization and Expansion of the TASC Lesion Classification to Include Below-the-Knee Arteries: A Supplement to the Inter-Society Consensus for the Management of Peripheral Arterial Disease (TASC II): The TASC Steering Committee(.). *Annals of vascular diseases*, 2015. **8**(4): p. 343-357.
43. McDermott, M.M., et al., Lower ankle/brachial index, as calculated by averaging the dorsalis pedis and posterior tibial arterial pressures, and association with leg functioning in peripheral arterial disease. *Journal of vascular surgery*, 2000. **32**(6): p. 1164-1171.
44. Khan, T.H., F.A. Farooqui, and K. Niazi, Critical review of the ankle brachial index. *Current cardiology reviews*, 2008. **4**(2): p. 101-106.
45. Chaudru, S., et al., Training to Perform Ankle-Brachial Index: Systematic Review and Perspectives to Improve Teaching and Learning. *European Journal of Vascular and Endovascular Surgery*, 2016. **51**(2): p. 240-247.
46. Chaudru, S., et al., Ankle brachial index teaching: A call for an international action. *International Journal of Cardiology*, 2015. **184**: p. 489-491.
47. Ghannam, M., et al., Ankle-brachial Index as a Clinical Tool. *The American Journal of Medicine*, 2012. **125**(12): p. 1171-1172.
48. Carbayo, J.A., et al., Using ankle-brachial index to detect peripheral arterial disease: Prevalence and associated risk factors in a random population sample. *Nutrition, Metabolism and Cardiovascular Diseases*, 2007. **17**(1): p. 41-49.
49. Premanath, M. and M. Raghunath, Ankle-Brachial index by oscillometry: A very useful method to assess peripheral arterial disease in diabetes. *International journal of diabetes in developing countries*, 2010. **30**(2): p. 97-101.
50. Nelson, M.R., et al., Ankle-Brachial Index determination and peripheral arterial disease diagnosis by an oscillometric blood pressure device in primary care: validation and diagnostic accuracy study. *BMJ Open*, 2012. **2**(5): p. e001689.
51. Beasley, R.E., Digital ankle brachial index— a valuable tool for Office evaluation of PAD? *Cardiovascular Revascularization Medicine*, 2019. **20**(3): p. 266.
52. Gajanana, D., et al., Validation of digital ankle-brachial index as a screening tool in symptomatic patients with peripheral arterial disease. *Cardiovasc Revasc Med*, 2019. **20**(3): p. 207-209.
53. Diage, T.R., G. Johnson, and G. Ravipati, Digital ankle-brachial index technology used in primary care settings to detect flow obstruction: a population based registry study. *BMC Research Notes*, 2013. **6**(1): p. 404.
54. Donald, I., J. Macvicar, and T.G. Brown, Investigation of abdominal masses by pulsed ultrasound. *Lancet*, 1958. **1**(7032): p. 1188-95.



55. Campbell, S., A short history of sonography in obstetrics and gynaecology. Facts, views & vision in ObGyn, 2013. **5**(3): p. 213-229.
56. Coffi, S.B., et al., The Value of the Peak Systolic Velocity Ratio in the Assessment of the Haemodynamic Significance of Subcritical Iliac Artery Stenoses. European Journal of Vascular and Endovascular Surgery, 2001. **22**(5): p. 424-428.
57. Hughes, P. and T. How, PULSATILE VELOCITY DISTRIBUTION AND WALL SHEAR RATE MEASUREMENT USING PULSED DOPPLER ULTRASOUND. J. Biomech., 1994. **27**(1): p. 103-110.
58. Keller, M.H., et al., Noninvasive Measurement of Velocity Profiles and Blood Flow in the Common Carotid Artery by Pulsed Doppler Ultrasound. Stroke, 1976. **7**(4): p. 370-377.
59. Cantisani, V., et al., Prospective Comparative Analysis of Colour-Doppler Ultrasound, Contrast-enhanced Ultrasound, Computed Tomography and Magnetic Resonance in Detecting Endoleak after Endovascular Abdominal Aortic Aneurysm Repair. European Journal of Vascular and Endovascular Surgery, 2011. **41**(2): p. 186-192.
60. Zoghbi, W.A., et al., American Society of Echocardiography: recommendations for evaluation of the severity of native valvular regurgitation with two-dimensional and Doppler echocardiography. A report from the American Society of Echocardiography's Nomenclature and Standards Committee and The Task Force on Valvular Regurgitation, developed in conjunction with the American College of Cardiology Echocardiography Committee, The Cardiac Imaging Committee, Council on Clinical Cardiology, The American Heart Association, and the European Society of Cardiology Working Group on Echocardiography, represented by:, 2003. **4**(4): p. 237-261.
61. Diehm, N., et al., Clinical Endpoints in Peripheral Endovascular Revascularization Trials: a Case for Standardized Definitions. European Journal of Vascular and Endovascular Surgery, 2008. **36**(4): p. 409-419.
62. Ranke, C., et al., Color and conventional image-directed Doppler ultrasonography: Accuracy and sources of error in quantitative blood flow measurements. Journal of Clinical Ultrasound, 1992. **20**(3): p. 187-193.
63. Mintz, G.S., et al., Intravascular ultrasound predictors of restenosis after percutaneous transcatheter coronary revascularization. Journal of the American College of Cardiology, 1996. **27**(7): p. 1678-1687.
64. Chong, A.Y., et al., Blood flow velocity prediction in aorto-iliac stent grafts using computational fluid dynamics and Taguchi method. Computers in Biology and Medicine, 2017. **84**: p. 235-246.
65. S, A.S., R.S.P. SP, and F.E.K. EK, CT angiography and 3D imaging in aortoiliac occlusive disease: collateral pathways in Leriche syndrome. Vol. 42. 2017: Abdominal Radiology. 2346-2357.

66. Met, R., et al., Diagnostic performance of computed tomography angiography in peripheral arterial disease: A systematic review and meta-analysis. *JAMA*, 2009. **301**(4): p. 415-424.
67. Sun, Z., M. Almoudi, and Y. Cao, CT angiography in the diagnosis of cardiovascular disease: A transformation in cardiovascular CT practice. 2014.
68. Conte, M.S., et al., Society for Vascular Surgery practice guidelines for atherosclerotic occlusive disease of the lower extremities: Management of asymptomatic disease and claudication. *Journal of Vascular Surgery*, 2015. **61**(3): p. 2S-41S.e1.
69. Palmaz, J.C., et al., Aortic Bifurcation Stenosis: Treatment with Intravascular Stents. *Journal of Vascular and Interventional Radiology*, 1991. **2**(3): p. 319-323.
70. Björses, K., et al., Kissing stents in the Aortic Bifurcation – a Valid Reconstruction for Aorto-iliac Occlusive Disease. *European Journal of Vascular and Endovascular Surgery*, 2008. **36**(4): p. 424-431.
71. Brittenden, J., G. Beattie, and A.W. Bradbury, Outcome of Iliac Kissing Stents. *European Journal of Vascular and Endovascular Surgery*, 2001. **22**(5): p. 466-468.
72. Greiner, A., et al., Kissing stents for treatment of complex aortoiliac disease. *European Journal of Vascular and Endovascular Surgery*, 2003. **26**(2): p. 161-165.
73. Sabri, S.S., et al., Outcomes of Covered Kissing Stent Placement Compared with Bare Metal Stent Placement in the Treatment of Atherosclerotic Occlusive Disease at the Aortic Bifurcation. *Journal of Vascular and Interventional Radiology*, 2010. **21**(7): p. 995-1003.
74. Groot Jebbink, E., et al., Geometrical consequences of kissing stents and the Covered Endovascular Reconstruction of the Aortic Bifurcation configuration in an in vitro model for endovascular reconstruction of aortic bifurcation. *J Vasc Surg*, 2015. **61**(5): p. 1306-11.
75. Goverde, P.C., et al., Covered endovascular reconstruction of aortic bifurcation (CERAB) technique: a new approach in treating extensive aortoiliac occlusive disease. *J Cardiovasc Surg (Torino)*, 2013. **54**(3): p. 383-7.
76. Parodi, J.C., et al., Endovascular Stent-Graft Treatment of Traumatic Arterial Lesions. *Annals of Vascular Surgery*, 1999. **13**(2): p. 121-129.
77. Küffer, G., F. Spengel, and B. Steckmeier, Percutaneous reconstruction of the aortic bifurcation with plamaz stents: Case report. *CardioVascular and Interventional Radiology*, 1991. **14**(3): p. 170-172.
78. Marin, M.L. and F.J. Veith, Clinical application of endovascular grafts in aortoiliac occlusive disease and vascular trauma. *Cardiovascular Surgery*, 1995. **3**(2): p. 115-120.

79. Mendelsohn, F.O., et al., Kissing stents in the aortic bifurcation. *Am Heart J*, 1998. **136**(4 Pt 1): p. 600-5.
80. Ramaswami, G. and M.L. Marin, STENT GRAFTS IN OCCLUSIVE ARTERIAL DISEASE. *Surgical Clinics of North America*, 1999. **79**(3): p. 597-609.
81. Parodi, J.C., et al., Use of covered stents and endograft as a rescue treatment in a patient with a complex form of recurrent aortic coarctation. *Journal of Vascular Surgery*, 2007. **45**(6): p. 1263-1267.
82. Rouwet, E.V., et al., Final Results of the Prospective European Trial of the Endurant Stent Graft for Endovascular Abdominal Aortic Aneurysm Repair. *European Journal of Vascular and Endovascular Surgery*, 2011. **42**(4): p. 489-497.
83. Nanto, K., et al., Five-year patency and its predictors after endovascular therapy for aortoiliac occlusive disease. *Journal of atherosclerosis and thrombosis*, 2019: p. 45617.
84. Soulis, J.V., et al. Relative residence time and oscillatory shear index of non-Newtonian flow models in aorta. In 2011 10th International Workshop on Biomedical Engineering. 2011.
85. Numata, S., et al., Blood flow analysis of the aortic arch using computational fluid dynamics. *European Journal of Cardio-Thoracic Surgery*, 2016. **49**(6): p. 1578-1585.
86. He, X. and D.N. Ku, Pulsatile flow in the human left coronary artery bifurcation: average conditions. *J Biomech Eng*, 1996. **118**(1): p. 74-82.
87. AIHW, Cardiovascular disease mortality: trends at different ages. *Cardiovascular disease*, 2010. **Series no. 31**(Cat. no. CVD 47): p. 1-93.
88. Lars, N. and R.H. William, INTER-SOCIETY CONSENSUS FOR THE MANAGEMENT OF PERIPHERAL ARTERIAL DISEASE. *International Angiology*, 2007. **26**(2): p. 81-157.
89. Liu, M. and F. Zhang, Endovascular Management of Aorta-Iliac Stenosis and Occlusive Disease by Kissing-Stent Technique. *Stem Cells International*, 2016.
90. Goubergrits, L., et al., MRI-based computational fluid dynamics for diagnosis and treatment prediction: clinical validation study in patients with coarctation of aorta. *Journal of magnetic resonance imaging : JMRI*, 2015. **41**(4): p. 909-916.
91. Tokunaga, K., et al., Optimal Peak Systolic Velocity Thresholds for Predicting Internal Carotid Artery Stenosis Greater than or Equal to 50%, 60%, 70%, and 80%. *Journal of Stroke and Cerebrovascular Diseases*, 2016. **25**(4): p. 921-926.
92. Karthikesalingam, A., et al., Predictive Value of Peak Systolic Velocity for the Development of Graft Limb Complications After Endovascular Aneurysm Repair. *Journal of Endovascular Therapy*, 2012. **19**(3): p. 428-433.

93. Plato Ii, S.A., et al., Elevated Peak Systolic Velocity and Velocity Ratio from Duplex Ultrasound are Associated with Hemodynamically Significant Lesions in Arteriovenous Access. *Annals of Vascular Surgery*, 2016. **35**: p. 68-74.
94. Qi, L., C.S. Mikhael, and W.R.J. Funnell. Application of the Taguchi method to sensitivity analysis of a middle-ear finite-element model. in *Proc. 28th Ann. Conf. Can. Med. Biol. Eng. Soc.* 2004.
95. Trabelsi, K., et al., Optimization of virus yield as a strategy to improve rabies vaccine production by Vero cells in a bioreactor. *J Biotechnol*, 2006. **121**(2): p. 261-71.
96. Autrique, L. and C. Lormel, Numerical Design of Experiment for Sensitivity Analysis : Application to Skin Burn Injury Prediction. *Biomedical Engineering, IEEE Transactions on*, 2008. **55**(4): p. 1279-1290.
97. Yilmaz, F. and M.Y. Gundogdu, A critical review on blood flow in large arteries relevance to blood rheology, viscosity models, and physiologic conditions. *Korea Australia Rheology Journal*, 2008. **20**(4): p. 197-211.
98. Fraser, K.H., et al., Characterization of an Abdominal Aortic Velocity Waveform in Patients with Abdominal Aortic Aneurysm. *Ultrasound in Medicine & Biology*, 2008. **34**(1): p. 73-80.
99. Wood, N., Aspects of fluid dynamics applied to the larger arteries. *J. Theor. Biol.*, 1999. **199**(2): p. 137-161.
100. Straatman, A.G. and D.A. Steinman, Low Reynolds number modeling of pulsatile flow in a moderately constricted geometry. Eleventh annual conference of the CFD Society of Canada (CFD 2003) Proceedings. 2003, Canada.
101. Shakeri Babil, A., et al., AORTIC BIFURCATION ANGLE AS AN INDEPENDENT RISK FACTOR FOR AORTOILIAC OCCLUSIVE DISEASE. *Folia Morphologica*, 2007. **66**(3): p. 181-184.
102. Jiang, Y., K. Kohara, and K. Hiwada, Low wall shear stress contributes to atherosclerosis of the carotid artery in hypertensive patients. *Hypertens Res*, 1999. **22**(3): p. 203-7.
103. Rutherford, R.B., et al., Recommended standards for reports dealing with lower extremity ischemia: Revised version. *Journal of Vascular Surgery*, 1997. **26**(3): p. 517-538.
104. de Smet, A.A., E.J. Ermers, and P.J. Kitslaar, Duplex velocity characteristics of aortoiliac stenoses. *Journal of vascular surgery*, 1996. **23**(4): p. 628-636.
105. Ranke, C., A. Creutzig, and K. Alexander, Duplex scanning of the peripheral arteries: correlation of the peak velocity ratio with angiographic diameter reduction. *Ultrasound in Medicine and Biology*, 1992. **18**(5): p. 433-440.

106. Trevethan, R., Sensitivity, Specificity, and Predictive Values: Foundations, Pliabilities, and Pitfalls in Research and Practice. *Frontiers in public health*, 2017. **5**: p. 307-307.
107. Hicks, C.W., et al., Development of a duplex-derived velocity risk prediction model of disease progression in patients with moderate asymptomatic carotid artery stenosis. *Journal of Vascular Surgery*, 2014. **60**(6): p. 1585-1592.
108. Alkhalili, K., et al., The Effect of Stents in Cerebral Aneurysms: A Review. *Asian journal of neurosurgery*, 2018. **13**(2): p. 201-211.
109. Sundell, P.M. and M.R. Roach, The role of taper on the distribution of atherosclerosis in the human infra-renal aorta. *Atherosclerosis*, 1998. **139**(1): p. 123-129.
110. O'Flynn, P., G. O'Sullivan, and A. Pandit, Geometric Variability of the Abdominal Aorta and Its Major Peripheral Branches. *The Journal of the Biomedical Engineering Society*, 2010. **38**(3): p. 824-840.
111. Balossino, R., et al., Effects of different stent designs on local hemodynamics in stented arteries. *Journal of Biomechanics*, 2008. **41**(5): p. 1053-1061.
112. Paisal, M.S.A., et al., Flow Characteristics Near to Stent Strut Configurations on Femoropopliteal Artery. *IOP Conference Series: Materials Science and Engineering*, 2017. **226**: p. 012147.
113. Greiner, A., et al., Does stent overlap influence the patency rate of aortoiliac kissing stents? *Journal of Endovascular Therapy*, 2005. **12**(6): p. 696-703.
114. Sharafuddin, M.J., et al., Long-term outcome following stent reconstruction of the aortic bifurcation and the role of geometric determinants. *Ann Vasc Surg*, 2008. **22**(3): p. 346-57.
115. Otto, F., Die grundform des arteriellen pulses. *Zeitung fur Biologie*, 1899. **37**: p. 483-586.
116. Sagawa, K., R.K. Lie, and J. Schaefer, Translation of Otto Frank's paper "Die Grundform des Arteriellen Pulses" *Zeitschrift fur Biologie* 37: 483-526 (1899). *J Mol Cell Cardiol*, 1990. **22**(3): p. 253-4.
117. Ghasemalizadeh, O., et al., Exact Modeling of Cardiovascular System Using Lumped Method. *BIOCOMP*, pp. 408-417. 2008, 2014: p. pp.408-417. 2008.
118. Westerhof, N., J.-W. Lankhaar, and B.E. Westerhof, The arterial Windkessel. *Medical & Biological Engineering & Computing*, 2009. **47**(2): p. 131-141.
119. Malvè, M., et al., Impedance-based outflow boundary conditions for human carotid haemodynamics. *Computer Methods in Biomechanics and Biomedical Engineering*, 2014. **17**(11): p. 1248-1260.
120. Chiastra, C., et al., Computational fluid dynamic simulations of image-based stented coronary bifurcation models. *J R Soc Interface*, 2013. **10**(84): p. 20130193.

121. Broemser, P. and O.F. Ranke, Ueber die Messung des Schlagvolumens des Herzens auf unblutigem Weg. 1930: Lehmann.
122. Les, A., et al., Quantification of Hemodynamics in Abdominal Aortic Aneurysms During Rest and Exercise Using Magnetic Resonance Imaging and Computational Fluid Dynamics. *The Journal of the Biomedical Engineering Society*, 2010. **38**(4): p. 1288-1313.
123. Rigatelli, G., et al., Non-invasive Evaluation of Fluid Dynamic of Aortoiliac Atherosclerotic Disease: Impact of Bifurcation Angle and Different Stent Configurations. *Journal of translational internal medicine*, 2018. **6**(3): p. 138-145.
124. Vértes, M., et al., Stent Protrusion >20 mm Into the Aorta: A New Predictor for Restenosis After Kissing Stent Reconstruction of the Aortoiliac Bifurcation. *J Endovasc Ther*, 2018. **25**(5): p. 632-639.
125. Visser, K. and M.G.M. Hunink, Peripheral Arterial Disease: Gadolinium-enhanced MR Angiography versus Color-guided Duplex US—A Meta-analysis. *Radiology*, 2000. **216**(1): p. 67-77.
126. Alberg, A.J., et al., The use of "overall accuracy" to evaluate the validity of screening or diagnostic tests. *J Gen Intern Med*, 2004. **19**(5 Pt 1): p. 460-5.
127. Maxim, L.D., R. Niebo, and M.J. Utell, Screening tests: a review with examples. *Inhal Toxicol*, 2014. **26**(13): p. 811-28.
128. Reijnen, M.M., Update on covered endovascular reconstruction of the aortic bifurcation. *Vascular*, 2020: p. 1708538119896197.
129. Groot Jebbink, E., et al., Hemodynamic comparison of stent configurations used for aortoiliac occlusive disease. *Journal of Vascular Surgery*, 2017. **66**(1): p. 251-260.e1.
130. Chiu, K.W.H., et al., Review of Direct Anatomical Open Surgical Management of Atherosclerotic Aorto-Iliac Occlusive Disease. *European Journal of Vascular & Endovascular Surgery*, 2010. **39**(4): p. 460-471.
131. Taeymans, K., et al., Three-year outcome of the covered endovascular reconstruction of the aortic bifurcation technique for aortoiliac occlusive disease. *J Vasc Surg*, 2018. **67**(5): p. 1438-1447.
132. Van Haren, R.M., et al., Endovascular treatment of TransAtlantic Inter-Society Consensus D aortoiliac occlusive disease using unibody bifurcated endografts. *Journal of vascular surgery*, 2017. **65**(2): p. 398-405.
133. Ford, M.D., et al., PIV-measured versus CFD-predicted flow dynamics in anatomically realistic cerebral aneurysm models. *Journal of Biomechanical Engineering*, 2008. **130**(2): p. <xocs:firstpage xmlns:xocs=&#034;&#034;/&gt;.

134. Gallo, D., et al., Analysis of thoracic aorta hemodynamics using 3D particle tracking velocimetry and computational fluid dynamics. *Journal of Biomechanics*, 2014. **47**(12): p. 3149-3155.
135. Raschi, M., et al., CFD and PIV analysis of hemodynamics in a growing intracranial aneurysm. *International journal for numerical methods in biomedical engineering*, 2012. **28**(2): p. 214-228.
136. Brindise, M.C., M.M. Busse, and P.P. Vlachos, Density- and viscosity-matched Newtonian and non-Newtonian blood-analog solutions with PDMS refractive index. *Experiments in Fluids*, 2018. **59**(11): p. 173.
137. Dhawan, S.S., et al., Shear stress and plaque development. Expert review of cardiovascular therapy, 2010. **8**(4): p. 545-556.
138. Zarins, C.K., et al., Carotid bifurcation atherosclerosis. Quantitative correlation of plaque localization with flow velocity profiles and wall shear stress. *Circulation research*, 1983. **53**(4): p. 502-514.
139. Sotelo, J., et al., 3D Quantification of Wall Shear Stress and Oscillatory Shear Index Using a Finite-Element Method in 3D CINE PC-MRI Data of the Thoracic Aorta. *IEEE Transactions on Medical Imaging*, 2016. **35**(6): p. 1475-1487.
140. Moore, J.E., et al., Fluid wall shear stress measurements in a model of the human abdominal aorta: oscillatory behavior and relationship to atherosclerosis. *Atherosclerosis*, 1994. **110**(2): p. 225-240.
141. De Keulenaer, G.W., et al., Oscillatory and steady laminar shear stress differentially affect human endothelial redox state: role of a superoxide-producing NADH oxidase. *Circulation research*, 1998. **82**(10): p. 1094-1101.
142. Chong, A., et al., A novel roller pump for physiological flow. *Artificial organs*, 2020.
143. Soudah, E., et al., Validation of numerical flow simulations against in vitro phantom measurements in different type B aortic dissection scenarios. *Computer Methods in Biomechanics and Biomedical Engineering*, 2013: p. 1-11.
144. Hariharan, P., et al., Multilaboratory Particle Image Velocimetry Analysis of the FDA Benchmark Nozzle Model to Support Validation of Computational Fluid Dynamics Simulations. *J. Biomech. Eng.-Trans. ASME*, 2011. **133**(4).
145. Law, Y.F., et al., Computer-controlled pulsatile pump system for physiological flow simulation. *Medical and Biological Engineering and Computing*, 1987. **25**(5): p. 590-595.
146. Holdsworth, D., et al., COMPUTER-CONTROLLED POSITIVE DISPLACEMENT PUMP FOR PHYSIOLOGICAL FLOW SIMULATION. *Med. Biol. Eng. Comput.*, 1991. **29**(6): p. 565-570.
147. Hoskins, P.R., Simulation and Validation of Arterial Ultrasound Imaging and Blood Flow. *Ultrasound in Medicine & Biology*, 2008. **34**(5): p. 693-717.

148. Rudenick, P.A., et al., An in vitro phantom study on the influence of tear size and configuration on the hemodynamics of the lumina in chronic type B aortic dissections. *Journal of Vascular Surgery*, 2013. **57**(2): p. 464-474.e5.
149. Poots, K., et al., A new pulsatile flow visualization method using a photochromic dye with application to Doppler ultrasound. *Annals of Biomedical Engineering*, 1986. **14**(3): p. 203-218.
150. Douville, Y., et al., An in vitro model and its application for the study of carotid doppler spectral broadening. *Ultrasound in Medicine & Biology*, 1983. **9**(4): p. 347-356.
151. Shkolnikov, V., J. Ramunas, and J.G. Santiago, A self-priming, roller-free, miniature, peristaltic pump operable with a single, reciprocating actuator. *Sensors and actuators. A, Physical*, 2010. **160**(1-2): p. 141-146.
152. Neto, A.G.S.B., et al., Linear peristaltic pump driven by three magnetic actuators: Simulation and experimental results. 2011. p. 1-6.
153. Sousa, L.C., et al., Toward hemodynamic diagnosis of carotid artery stenosis based on ultrasound image data and computational modeling. *Medical and Biological Engineering and Computing*, 2014. **52**(11).
154. LEE, D. and J.Y. CHEN, PULSATILE FLOW FIELDS IN A MODEL OF ABDOMINAL AORTA WITH ITS PERIPHERAL BRANCHES. *Biomedical Engineering: Applications, Basis and Communications*, 2003. **15**(05): p. 170-178.
155. Boersen, J.T., et al., Benchtop quantification of gutter formation and compression of chimney stent grafts in relation to renal flow in chimney endovascular aneurysm repair and endovascular aneurysm sealing configurations. *Journal of Vascular Surgery*, 2016. **66**(5): p. 1565-1573.
156. Boersen, J.T., et al., The Influence of Positioning of the Nellix Endovascular Aneurysm Sealing System on Suprarenal and Renal Flow: An In Vitro Study. *J Endovasc Ther*, 2017: p. 1526602817719465.
157. Mechoor, R.R., T. Schmidt, and E. Kung, A Real-Time Programmable Pulsatile Flow Pump for In Vitro Cardiovascular Experimentation. *Journal of Biomechanical Engineering*, 2016. **138**(11).
158. Peek, G.J., et al., Tubing failure during prolonged roller pump use: a laboratory study. *Perfusion*, 1999. **14**(6): p. 443-452.
159. Passaroni, A.C., M.A. Silva, and W.B. Yoshida, Cardiopulmonary bypass: development of John Gibbon's heart-lung machine. *Rev Bras Cir Cardiovasc*, 2015. **30**(2): p. 235-45.
160. Sievert, A.N., A.G. Shackelford, and M.M. McCall, Trends and emerging technologies in extracorporeal life support: results of the 2006 ECLS survey. *The journal of extra-corporeal technology*, 2009. **41**(2): p. 73-78.



161. Graf, N.J. and M.T. Bowser, A soft-polymer piezoelectric bimorph cantilever-actuated peristaltic micropump. *Lab on a Chip*, 2008. **8**(10): p. 1664-1670.
162. Laser, D.J., A review of micropumps. 2004. p. R35-R64.
163. Iverson, B. and S. Garimella, Recent advances in microscale pumping technologies: a review and evaluation. *Microfluidics and Nanofluidics*, 2008. **5**(2): p. 145-174.
164. Botnar, R., et al., Hemodynamics in the carotid artery bifurcation: a comparison between numerical simulations and in vitro MRI measurements. *J Biomech*, 2000. **33**(2): p. 137-44.
165. Marshall, I., et al., MRI and CFD studies of pulsatile flow in healthy and stenosed carotid bifurcation models. *J Biomech*, 2004. **37**(5): p. 679-87.
166. Papathanasopoulou, P., et al., MRI measurement of time-resolved wall shear stress vectors in a carotid bifurcation model, and comparison with CFD predictions. *J Magn Reson Imaging*, 2003. **17**(2): p. 153-62.
167. Zhao, S.Z., et al., Comparative Study of Magnetic Resonance Imaging and Image-Based Computational Fluid Dynamics for Quantification of Pulsatile Flow in a Carotid Bifurcation Phantom. *Annals of Biomedical Engineering*, 2003. **31**(8): p. 962-971.
168. Hoi, Y., et al., Validation of CFD simulations of cerebral aneurysms with implication of geometric variations. 2006.
169. Frauenfelder, T., et al., Computational fluid dynamics: hemodynamic changes in abdominal aortic aneurysm after stent-graft implantation. *Cardiovasc Intervent Radiol*, 2006. **29**(4): p. 613-23.
170. Kung, E.O., et al., In vitro validation of finite-element model of AAA hemodynamics incorporating realistic outlet boundary conditions. *J Biomech Eng*, 2011. **133**(4): p. 041003.
171. Cheung, S.C.P., et al., Experimental and numerical study on the hemodynamics of stenosed carotid bifurcation. *Australasian Physical & Engineering Sciences in Medicine*, 2010. **33**(4): p. 319-328.
172. Brewster, D.C., et al., Initial experience with endovascular aneurysm repair: Comparison of early results with outcome of conventional open repair. *Journal of Vascular Surgery*, 1998. **27**(6): p. 992-1005.
173. Manimaran, R., CFD simulation of non-Newtonian fluid flow in arterial stenoses with surface irregularities. *World Academy of Science, Engineering and Technology*, 2011. **73**(5): p. 804-809.
174. Castro, M.A., et al. Realistic comparison between aneurysmal wall shear stress vector and blood rheology in patient-specific computational hemodynamic models. in *Medical Imaging 2013: Biomedical Applications in Molecular, Structural, and Functional Imaging*. 2013. International Society for Optics and Photonics.

175. Huang, C., Z. Chai, and B. Shi, Non-newtonian effect on hemodynamic characteristics of blood flow in stented cerebral aneurysm. *Communications in Computational Physics*, 2013. **13**(3): p. 916-928.
176. Apostolidis, A.J., A.P. Moyer, and A.N. Beris, Non-Newtonian effects in simulations of coronary arterial blood flow. *Journal of Non-Newtonian Fluid Mechanics*, 2016. **233**: p. 155-165.
177. Midulla, M., et al., Haemodynamic imaging of thoracic stent-grafts by computational fluid dynamics (CFD): presentation of a patient-specific method combining magnetic resonance imaging and numerical simulations. *European radiology*, 2012. **22**(10): p. 2094-2102.
178. Neofytou, P., A 3rd order upwind finite volume method for generalised Newtonian fluid flows. *Advances in Engineering Software*, 2005. **36**(10): p. 664-680.
179. Shishir, S.S., et al., Blood Flow Dynamics in Cerebral Aneurysm-A CFD Simulation. *Procedia Engineering*, 2015. **105**: p. 919-927.
180. Bordones, A.D., et al., Computational fluid dynamics modeling of the human pulmonary arteries with experimental validation. *Annals of biomedical engineering*, 2018. **46**(9): p. 1309-1324.
181. Rubino, E. and T. Ioppolo, Young's modulus and loss tangent measurement of polydimethylsiloxane using an optical lever. *Journal of Polymer Science Part B: Polymer Physics*, 2016. **54**(7): p. 747-751.
182. Geoghegan, P.H., M.C. Jermy, and D.S. Nobes, A PIV comparison of the flow field and wall shear stress in rigid and compliant models of healthy carotid arteries. *Journal of Mechanics in Medicine and Biology*, 2017. **17**(03): p. 1750041.
183. Rudin, S., et al., High-resolution vascular radiological imaging. *Medical Physics*, 2004. **31**(6): p. 1826-1827.
184. Ohta, M., et al., Three-Dimensional Reconstruction of a Cerebral Stent using Micro-CT for Computational Simulation. *Journal of Intelligent Material Systems and Structures*, 2008. **19**(3): p. 313-318.
185. Smedby, Ö., Geometric risk factors for atherosclerosis in the aortic bifurcation: A digitized angiography study. *Annals of Biomedical Engineering*, 1996. **24**(4): p. 481-488.

*Every reasonable attempt has been made to acknowledge the owners of copyright material. I would be pleased to hear from any copyright owner who has been omitted or incorrectly acknowledged.*

---

## APPENDICES

---

# Appendix A Design of Experiment

## Planning

The region of interest in our study is the shaded section of aortoiliac bifurcation as outlined in Figure A.1. Based on literature review, Smedby[185] and Shakeri et al[101] found that iliac to aortic area ratio  $R = (D2^2 + D3^2)/D1^2$  and bifurcation angle ( $\alpha$ ) are potential risk factors for the formation of atherosclerotic plaque in the aortoiliac bifurcation. In addition, Fraser et al[98] have characterized the abdominal aortic velocity or infra-renal Peak Systolic Velocity ( $PSV_{in}$ ) for in vitro and in silico investigations.

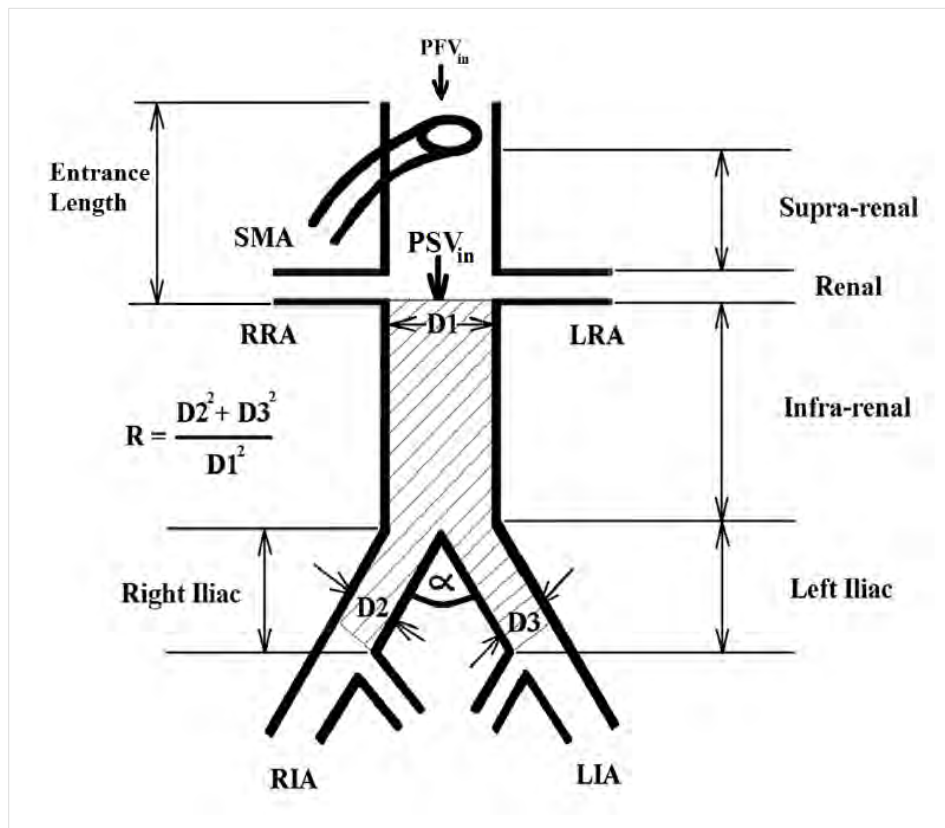


Figure A.1 A Basic Human Aortoiliac Bifurcation Model

Table A.1 shows the range of these three parameter values obtained in literature [98, 101, 185] describing the aortoiliac geometry and physiology.

**Table A.1 Aortoiliac bifurcation geometry and physiology from references**

Parameter/ Control Factor	Symbol	Unit	Authors	Mean	Std Dev	Upper Limit*	Lower Limit*
Infra-Renal PSV	$PSV_{in}$	m/s	Fraser et al	0.454	0.128	0.2	0.7
Iliac to Aortic Area Ratio	R	<i>Dimensionless</i>	Smedby	0.78	0.038	0.71	0.84
Bifurcation Angle	A	Degree	Shakeri et al	51	14	20	80

\* $p=0.05$

CFD solver was used to solve the fluid flow problem governed by Navier –Stokes equations and to determine  $PSV_{max}$  for each combination of  $PSV_{in}$ , R and  $\alpha$ . Since there was no prior knowledge of the potential interaction effects between these three control factors on  $PSV_{max}$ , their two-way interactions were included in our investigations. To reduce the number of simulations, two levels for each of the control factors were used.

## Design

The outputs from the planning were used as inputs to the design namely,

- Number of control factors to be investigated
- Number of levels for each control factor
- Specific 2-way and 3-way interactions to be investigated

Orthogonal Array is a partial factorial design used in the design of experiments to minimize the number of experiments or simulations, and yet be able to draw similar conclusions as compared to full factorial experiments. In order to choose a suitable Orthogonal Array, firstly the total Degrees Of Freedom need to be counted which dictates the minimum number of simulation runs. One Degree Of Freedom is associated with overall mean regardless of the number of control factors being investigated. As a general principle, the number of Degree Of Freedoms associated with a control factor is equal to one less than the number of levels being investigated. The Degree Of Freedom associated with interactions between two control factors is the product of the Degree Of Freedom for

each control factor. A suitable Orthogonal Array was selected based on the total Degree Of Freedom. In our case,

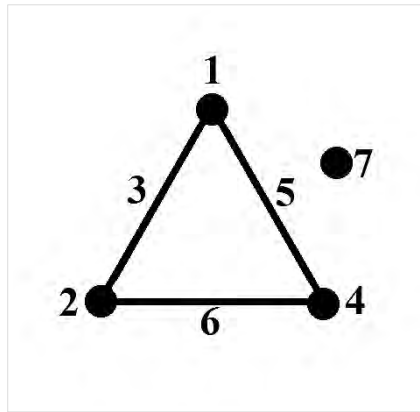
- Number of control factors = 3
- Number of levels per control factor = 2
- Total Degree Of Freedom for 3 control factors =  $3 \times (2-1) = 3$
- Number of Interactions considered = 3
- Degree Of Freedom for interaction =  $3 \times 1 \times 1 = 3$
- Minimum no. of simulations = Total Degree Of Freedom  $(3+3)+1=7$

The Latin Square with symbol  $L_n(m^f)$  is used as an Orthogonal Array representation where L stands for Latin Square and n is the total number of experimental or simulation runs, m represents the number of levels per factor and f is the number of factors. The Taguchi  $L_8(2^7)$  Orthogonal Array satisfies the minimum required number of simulations based on the Degree Of Freedom criterion [24]. The assignment of two levels for each of the three control factors based on references [14,17,23] and are as summarized in Table A.2.

**Table A.2 Assignment of 2-level control factors**

Control Factor	Level	
	1	2
A PSVin(m/s)	0.2	0.7
B R	0.71	0.84
C $\alpha$ (Degree)	20	80

A total of 7 control factors with two levels each can be assigned to the  $L_8(2^7)$  Orthogonal Array. The  $L_8$  linear graph as shown in Figure A.2 was used as a guide to assign each control factor to a column in the Orthogonal Array layout. The dots represent control factors and the line connecting the two dots represents the interaction between the two associated control factors. Since there are three control factors under our investigation, only three columns will be assigned i.e. columns 1, 2 and 4 whereas column 3, 5, 6 and 7 were left empty so that their two-way interactions can be assessed. The interactions between columns 1 and 2, 1 and 4 and 2 and 4 appear in column 3, 5 and 6 respectively. Column 7 is not connected to any control factor and therefore considered as an independent point or it can be used to estimate three-way interactions.

Figure A.2  $L_8$  Linear Graph

In our studies, interactions between  $V_{in}$  and  $R$ ,  $R$  and  $\alpha$ ; and between  $\alpha$  and  $V_{in}$  appear in column 3, 5 and 6 respectively as shown in Table A.3

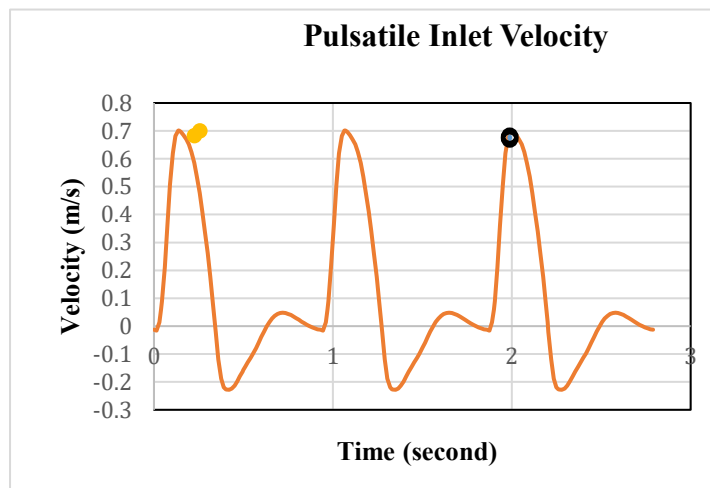
Table A.3  $L_8$  Orthogonal array

Stimulus Number	Column						
	Iliac to Aortic Area Ratio ( $R$ )	$V_{in}$ (m/s)	3	Bifurcation Angle $\alpha$ (Degree)	5	6	7
1	0.71	0.2	A1B1	20	B1C1	A1C1	A1B1C1
2	0.71	0.2	A1B1	80	B1C2	A1C2	A1B1C2
3	0.71	0.7	A2B1	20	B1C1	A2C1	A2B1C1
4	0.71	0.7	A2B1	80	B1C2	A2C2	A2B1C2
5	0.84	0.7	A2B2	20	B2C1	A2C1	A2B2C1
6	0.84	0.7	A2B2	80	B2C2	A2C2	A2B2C2
7	0.84	0.2	A1B2	20	B2C1	A1C1	A1B2C1
8	0.84	0.2	A1B2	80	B2C2	A1C2	A1B2C2
<b>Factor Assignment</b>							
	<b>B</b>	<b>A</b>	<b>AxB</b>	<b>C</b>	<b>BXC</b>	<b>AXC</b>	<b>AXBXC</b>

## Appendix B Computational Fluid Dynamics

### Inlet Boundary Condition

A pulsatile boundary condition was prescribed as the inlet velocity. Its profile was derived from [17] with a cardiac cycle of 0.93 second and PSV of 0.45 m/s at 0.14 second. The cardiac cycle of 0.93 second was kept however  $PSV_{in}$  of 0.2 m/s and 0.7 m/s were used in these studies therefore the profile in the vertical axis was scaled proportionally. Figure B.1 shows the pulsatile inlet velocity profile with a  $PSV_{in}$  of 0.7 m/s and the black dot indicates the  $PSV_{in}$  at 2.0 second in the third cardiac cycle.



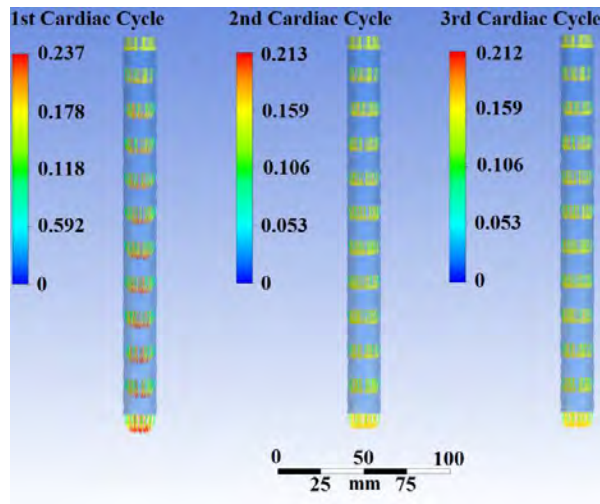
**Figure B.1** Pulsatile inlet velocity profile with a  $PSV_{in}$  of 0.7 m/s and the black dot indicates the  $PSV_{in}$  at 2.0 second in the third cardiac cycle

### Entrance length to Evaluate Velocity Profile

A 220mm long cylinder with 20mm diameter was used to evaluate entrance length required to establish fully developed velocity profile. The cylinder was created by SolidWorks CAD software and meshed with Fluent Meshing tools and then CFD simulation was performed by ANSYS Fluent 17.0 software using 0.2m/s as Plug Flow Velocity ( $PFV_{in}$ ) at the inlet, as shown in Figure B.2. Velocity profiles at 20mm intervals from the inlet were evaluated and it took about 120mm for the velocity profile to fully develop in the first cardiac cycle. However, the second and subsequent cardiac cycles did not fully develop into parabolic profile up to 220mm at the end of the cardiac cycle due to pulsatile nature of  $PFV_{in}$ . In all subsequent transient CFD simulations, entrance length of 180mm was introduced to obtain a realistic velocity profile in the infra-renal aortic region. PSV at 180 mm from the inlet was then defined as the infra-renal PSV or  $PSV_{in}$  as defined



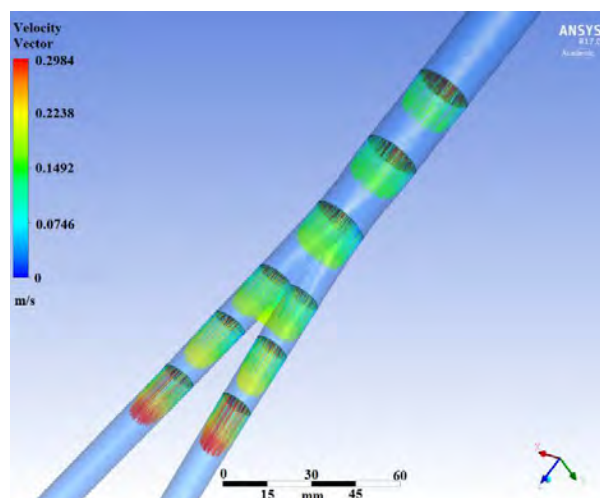
in Appendix A, Figure A.1. The ratio of  $PFV_{in}/PSV_{in}$  for the 3<sup>rd</sup> cardiac cycle was found to be 0.927 in the cylinder model. For example, by applying a 0.927 m/s  $PFV_{in}$  at the Inlet,  $PSV_{in}$  of 1 m/s can be expected at 180 mm from the Inlet.



**Figure B.2** Velocity Profile Evaluated at 200 mm Entrance Length Intervals from Inlet

### Reading $PSV_{max}$ in the Stented Segment

$PSV_{max}$  was obtained from CFD simulation by examining the velocity vectors in Common Iliac Arteries (CIA) in the stented segment 50 mm downstream from the bifurcation as shown in Figure B.3. After each CFD simulation,  $PSV_{in}$  was checked to see if the desired value was achieved. Minor adjustment to inlet Plug Flow Velocity ( $PFV_{in}$ ) was made where necessary to achieve the desired  $PSV_{in}$  and CFD simulation was repeated accordingly.



**Figure B.3** Instantaneous velocity profiles in the aortoiliac bifurcation model at peak inlet velocity

### Grid Independence Tests.

Polyhedral elements with boundary layers were meshed using unstructured Fluent meshing due to improved computational convergence and reduced computation time as compared with tetrahedral elements proposed by Spiegel et al [25]. Four types of meshes coarse, medium, fine and finer were used to test grid convergence mas shown in Table B.1. The CFD simulation was assumed to have achieved grid independence when further refinement of cells resulted in less than 1% change in the parameter of interest, in our case,  $PSV_{max}$ . Fine mesh with minimum 0.5 mm cells and about 100,000 elements were used in all the CFD simulations performed on a Dell Precision T1700 desktop computer (Dell Computer, Round Rock, Texas, U.S.A.), with a typical 1 hour computation time running 8-cores in parallel.

**Table B.1** Grid independence test

<b>Mesh Type</b>	<b>Min. Cell (mm)</b>	<b>Cell Count</b>	<b>PSVmax (m/s)</b>	<b>Change* (%)</b>
Coarse	1.5	65,245	0.893	2.54
Medium	1.0	73,861	0.915	1.30
Fine	0.5	96,677	0.927	0.82
Finer	0.25	124,982	0.920	

\*from previous period

### Periodicity Convergence Test

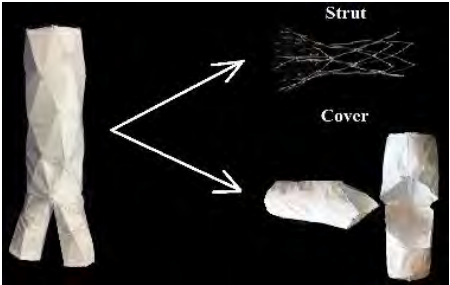

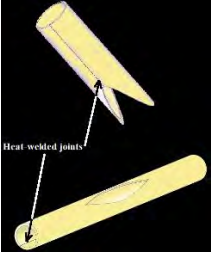
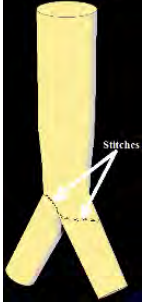
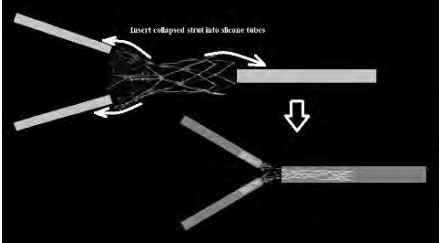
The simulation was assumed to have achieved its periodicity when the changes in  $PSV_{max}$  at various time-steps are less than 1% from the previous cardiac cycle. Table B.2 shows periodicity reached in the third cardiac cycle.

**Table B.2** Periodicity convergence test

<b>Cardiac Cycle</b> <i>(0.93s Period)</i>	<b>Time Step (s)</b>	<b>PSVmax (m/s)</b>	<b>Change* (%)</b>
First	0.14	0.998	
	0.15	1.002	
	0.40	0.463	
Second	1.07	0.903	9.52
	1.08	0.911	9.08
	1.33	0.420	9.29
Third	2.00	0.898	0.55
	2.01	0.908	0.33
	2.26	0.419	0.24
Fourth	2.93	0.898	0
	2.94	0.908	0
	3.19	0.419	0

\*from previous period

## Appendix C AFX Transparent Cover-Making Process

Step	Description	Process
1	Remove ePTFE cover from the original AFX stent-graft	
2	Cut LDPE film to the desired shape	
3	Heat-weld the LDPE films to form cylindrical shape	
4	Stitch the two parts with sutures to form the LDPE cover	
5	Insert the collapsed stents into silicone tubes.	

Step	Description	Process
6	Insert collapsed stent strut into LDPE cover	
7	Pull silicone tube out of stent strut, it will self-expand in the LDPE cover. Stitch the three openings with suture.	
8	Insert collapsed LDPE cover into silicone tubes.	
9	Insert collapsed stent with LDPE cover into flow phantom	
10	Pull out silicone tubes, the AFX stent with LDPE cover will expand inside the flow phantom	

## Appendix D Hemodynamic Plots

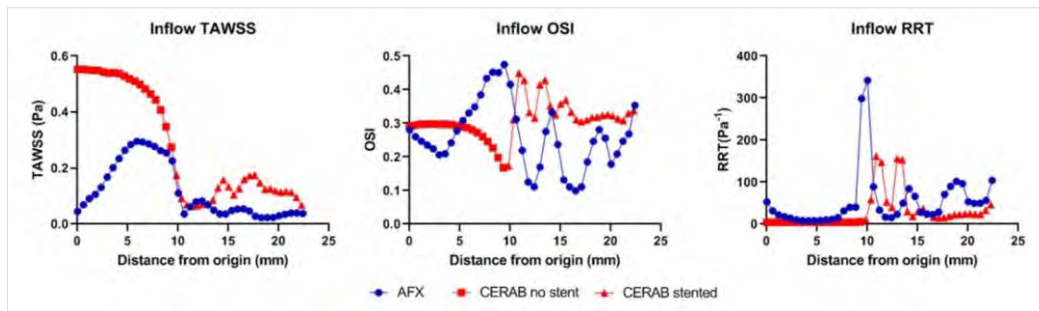


Figure D.1 Time averaged wall shear stress (TAWSS), oscillatory shear index (OSI) and relative residence time (RRT) plots at the inflow region of AFX-stent-graft and CERAB configuration.

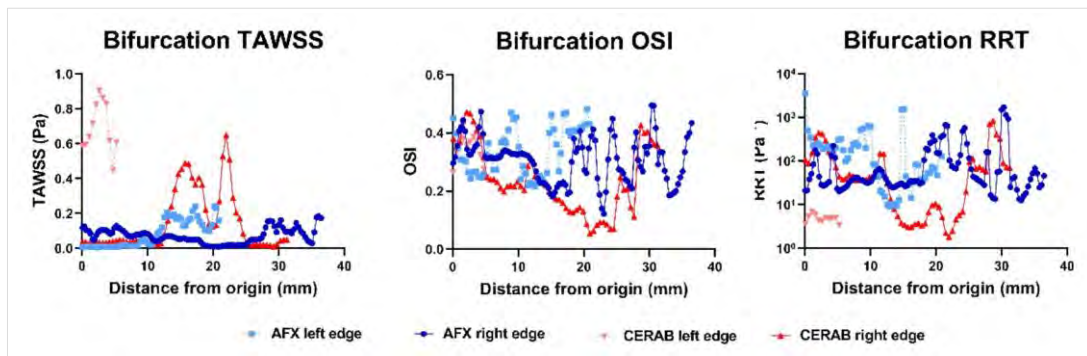
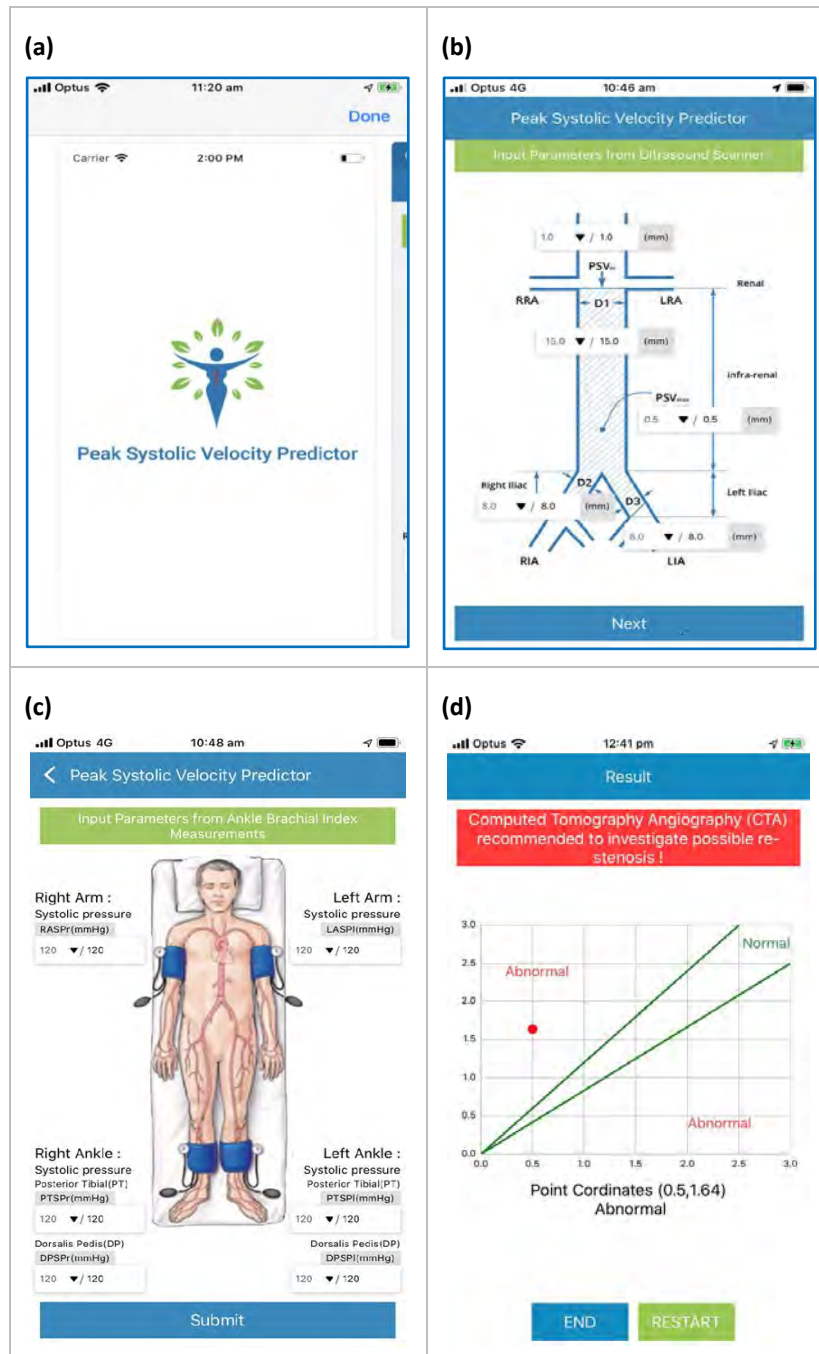


Figure D.2 Time averaged wall shear stress (TAWSS), oscillatory shear index (OSI) and relative residence time (RRT) plots at the bifurcation region of AFX-stent-graft and CERAB configuration.

# Appendix E A Smart-phone Application for PSV Predictor



**Figure E.1** Smart-phone Application for PSV Predictor. (a) the PSV Predictor welcome screen, (b) user is prompted to enter geometric details of the aortoiliac bifurcation; these data were determined from routine follow-up using duplex ultrasound scanning, (c) user is prompted to enter details of cardiac pressures from ABI measurements, (d) upon entry of the requested data, the Predictor Application will perform prediction calculation and determine whether the predicted PSV fall within an acceptable range and display the outcome accordingly.

# Appendix F Provisional Filing of Novel Cardiac Pump

**AUSTRALIA**

*Patents Act 1990*

## **PROVISIONAL SPECIFICATION**

**Invention title:**

**“PUMP FOR MIMICKING  
PHYSIOLOGICAL FLOW IN A PATIENT”**

**Applicant:**

**TRIPHASIC CARDIAC PUMP PTY LTD**

**The invention is described in the following statement:**



## **“PUMP FOR MIMICKING PHYSIOLOGICAL FLOW IN A PATIENT”**

### **Field of the Invention**

[0001] The present invention relates to a pump, primarily arranged for medical use to provide physiological flow for use as part of a cardiopulmonary bypass perfusion system or an extracorporeal membrane oxygenation system, or for use in therapeutic treatment of oxygen insufficiency in critical organs. Additionally it can be arranged to function as an artificial heart. The pump is considered to have wider application, for instance in industrial applications where it can be programmed to dose a predetermined amount of fluid or semisolid material into a container at a desired filling profile.

### **Background to the Invention**

[0002] Cardiac pumps used in surgery traditionally fall into two types: peristaltic and centrifugal. Both types of pump can be arranged to provide a consistent flow of blood at an appropriate pressure, with the pumps being adjustable to compensate for changes in flow rate or pressure requirements.

[0003] Traditional peristaltic and centrifugal pumps provide a pulsatile or continuous flow of blood. These have proved to be sufficient to maintain a patient through surgery.

[0004] It is notable, however, that the flow of blood provided by such cardiac pumps is notably different to the physiological flow provided by a beating heart. Natural aortic flow is triphasic in nature: through systolic, early diastolic and late diastolic phases. Traditional cardiac pumps do not replicate this flow.

[0005] The effects of pulsatile or steady pumping of blood rather than physiological flow during surgery are not well understood. It is at least possible that using a pump which more closely replicates patient physiology will lead to improved patient outcomes. A further disadvantage of centrifugal cardiac pumps used in surgery is that pump heads are generally single-use

items, as it is impractical to completely clean all blood residue from a pump. This represents a significant expense in cardiac surgery.

[0006] The present invention seeks to provide a cardiac pump which mimics a physiological flow, and is able to be safely reused.

[0007] The inventor of this application is also the inventor of the International Patent Application published under number WO2019/163520, the contents of which are incorporated herein by reference.

### **Summary of the Invention**

[0008] According to one aspect of the present invention there is provided a pump having a fluid line formed from flexible tubing, the pump having a reciprocating actuator, the actuator having an actuating member arranged to move between a first orientation and a second orientation such that the actuating member at least partially occludes the fluid line when in its second orientation; the actuator being arranged to move in a direction generally perpendicular to the fluid line, the pump being operable such that when the actuator moves from the first orientation to the second orientation it acts to peristaltically force fluid in the fluid line towards a fluid outlet.

[0009] The pump can be programmed to match the physiological flow profile of a human patient or an animal, with typical stroke volume between 5ml and 100ml, and typical heart rate between 60 and 120 beats per minute.

[0010] The first orientation may be free of the fluid line, such that the fluid line is not occluded. In a preferred embodiment, the first orientation represents a partial occlusion of the fluid line, with the second orientation representing a greater occlusion.

[0011] The pump preferably includes a check valve located at an inlet end of the fluid line. The check valve prevents backflow, ensuring that fluid flows in the desired direction along the fluid line.

[0012] Although the pump was developed for use as a cardiac pump during bypass procedures, it is considered to have other applications, both medical and industrial. In addition to cardiopulmonary bypass and extracorporeal membrane oxygenation procedures, the following treatments are made possible by use of the present invention to supplement the perfusion of a human patient's or an animal's organ, mimicking the physiological flow profile of the artery that supplies oxygenated blood to the affected organ. This is done by diverting part of the oxygenated blood from the lower extremities to the intended organ.

[0013] According to one such aspect of the present invention there is provided a method for treating brain injury, dementia or stroke in a subject in need thereof, by diverting part of the oxygenated blood from lower extremities to provide more perfusion to brain cells using a programmable pump to synchronize the pulses with the patient's physiological blood flow in order to assist with healing of injured brain cells or a treatment option for vertebrobasilar insufficiency.

[0014] According to another such aspect of the present invention there is provided a method for treating cancer patients by diverting oxygenated blood from lower extremities such as femoral arteries to arteries of injured organs that have undergone cancer treatment/chemotherapy by using a programmable pump to synchronize the pulses with the patient's physiological blood flow in order to assist with healing of injured organs. Possible organs which can be treated include the kidneys, lungs, pancreas, stomach and liver.

[0015] According to yet another aspect of the present there is provided a method for treating chronic wounds by using a programmable pump synchronised with the patient's ECG pulse to supply adequate physiological flow of oxygenated blood to wound tissues near the wound site. It is anticipated that this method may be efficacious in assisting healing, particularly in diabetic patients.

**Brief Description of the Drawings**

[0016] It will be convenient to further describe the invention with reference to preferred embodiments of the present invention. Other embodiments are possible, and consequently the particularity of the following discussion is not to be understood as superseding the generality of the preceding description of the invention. In the drawings:

[0017] Figure 1 is a photograph of a prototype cardiac pump in accordance with the present invention;

[0018] Figure 2 is a schematic representation of the operation of an actuator within the pump of Figure 1;

[0019] Figure 3 is a graph showing anticipated discharged volume per stroke of the pump of Figure 1;

[0020] Figure 4 is an image of an ECG showing a cardiac rhythm able to be mimicked by the pump of Figure 1;

[0021] Figure 5 is a schematic of an artificial heart in accordance with the present invention;

[0022] Figure 6 is diagram showing distributed perfusion as proposed by the present invention.

**Detailed Description of Preferred Embodiments**

[0023] Referring to the Figures, there is shown a pump 10. The pump 10 is arranged to force fluid (notionally blood) through a tube 12. In this embodiment the tube 12 is formed from platinum coated silicone tubing having an internal diameter of 19mm. It is considered that bio-compatible tubing having an internal diameter between 6mm and 25mm may be suitable for this purpose.

[0024] The tube 12 has an inlet 14 associated with a check valve 16. The tube has an outlet 18. In between the tube inlet 14 and outlet 18 is an operating portion 20.

[0025] The operating portion 20 is arranged to rest atop a rigid base plate 22. A generally L-shaped actuator 24 is positioned above the operating portion 20.

[0026] The actuator 24 has an actuating member being a compressing plate 26 which is generally horizontal, and parallel with the base plate 22. The actuator 24 has a generally vertical supporting plate 28. The supporting plate 28 is coupled to a linear slide 30 on a servo motor 32. The servo motor 32 is driven by a belt 34, and provides reciprocal linear motion to the linear slide 30 and thus to the actuator 24.

[0027] The servo motor 32 and actuator 24 may be calibrated such that the actuator reciprocates between a first position wherein the compressing plate 26 sits immediately above the operating portion 20 of the tube 12, and a second position wherein the compressing plate 26 is moved towards the base plate 22, thus compressing the operating portion 20 between the compressing plate 26 and base plate 22. This is shown schematically in Figure 2. It will be understood that this substantially occludes the tube 12, forcing fluid to flow towards the outlet 18. This generally mimics the systolic phase of a heart's action.

[0028] Return of the actuator 24 to its first position allows the tube 12 to elastically return to a generally cylindrical shape. This removes the forcing action of the pump, creating a relative pressure drop which encourages the flow of fluid from the inlet. This generally mimics the diastolic phase of a heart's action.

[0029] It will be appreciated that the stroke length of the servo motor 32 and the frequency of strokes can be calibrated to closely mimic a patient's own blood flow.

[0030] It is anticipated that the closest alignment of pump performance with human physiology will have the actuator 24 partially occluding the tube 12 in its first position, and more fully occluding the tube 12 in its second position.

[0031] In use, a patient's actual echocardiology will be measured as shown in Figure 4; digitized; and entered into operating software for the pump 10.

[0032] It is anticipated that the pump may be used to mimic arterial flow in any artery, and potentially in multiple arteries simultaneously. It is proposed that a number of pumps may be used, with each pump providing physiological-style flow to particular arteries, rather than through a single access point. The anticipated advantages of this approach include:

a) The PSV and pressure of physiological flow at a cannula will be reduced significantly relative to a single access point, making it possible to implement true physiological flow.

b) More oxygenated blood can be directed to the brain and organs within the chest cavity to ensure adequate supply of oxygenated blood to the critical organs during open heart surgery, thus potentially preventing injuries and organ failures.

c) A longer period of surgery might be possible which will enable surgeons to fix more complicated clinical disease due to safer perfusion with distributed perfusion.

[0033] It is further proposed that an artificial heart 50 can be made from this new invention as shown in Figure 5. First tubes 52 represents a Left Ventricle where oxygenated blood will be drawn from left and right pulmonary veins 54 combined inside a manifold 56 and passing through a check valve during diastole. The actuator 24 pushes the first tubes 52 against the base plate 22 to pump oxygenated blood to the rest of the body through the ascending aorta during systole. Likewise second tubes 62 represent a Right Ventricle where de-oxygenated blood will be drawn from superior and inferior vena cava 64; combined inside the manifold 56; and passes through a check valve during diastole. The actuator 24 pushes the

second tubes 62 against the base plate 22 to pump the de-oxygenated blood to the lung through pulmonary artery during systole.

[0034] Modifications and variations as would be apparent to a skilled addressee are deemed to be within the scope of the present invention.

**Claims**

1. A pump having a fluid line formed from flexible tubing, the pump having a reciprocating actuator, the actuator having an actuating member arranged to move between a first orientation and a second orientation such that the actuating member at least partially occludes the fluid line when in its second orientation; the actuator being arranged to move in a direction generally perpendicular to the fluid line, the pump being operable such that when the actuator moves from the first orientation to the second orientation it acts to peristaltically force fluid in the fluid line towards a fluid outlet.
2. A pump as claimed in claim 1, wherein the first orientation is free of the fluid line, such that the fluid line is not occluded.
3. A pump as claimed in claim 1, wherein the first orientation represents a partial occlusion of the fluid line, with the second orientation representing a greater occlusion.
4. A pump as claimed in any preceding claim, wherein the pump includes a check valve located at an inlet end of the fluid line.
5. A method for treating brain injury, dementia or stroke in a subject in need thereof, by diverting part of the oxygenated blood from lower extremities to provide more perfusion to brain cells using a programmable pump to synchronize the pulses with the patient's physiological blood flow in order to assist with healing of injured brain cells or a treatment option for vertebrobasilar insufficiency.
6. A method for treating cancer patients by diverting oxygenated blood from lower extremities such as femoral arteries to arteries of injured organs that have undergone cancer treatment/chemotherapy by using a programmable pump to synchronize the pulses with the patient's physiological blood flow in order to assist with healing of injured organs.



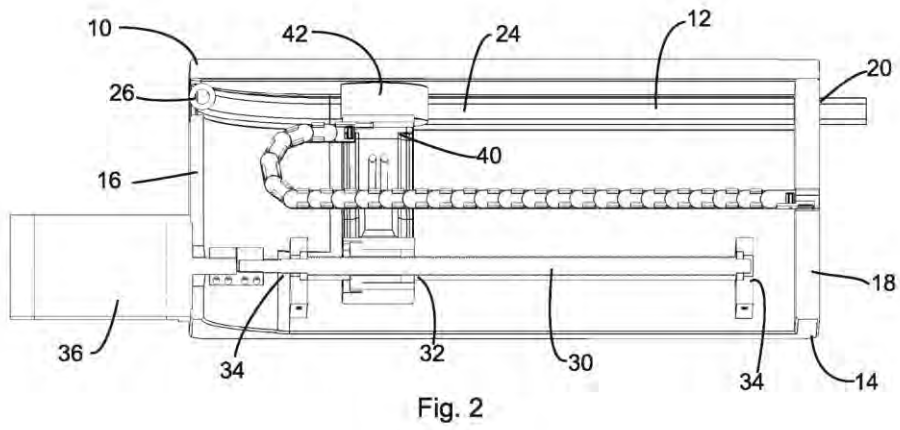
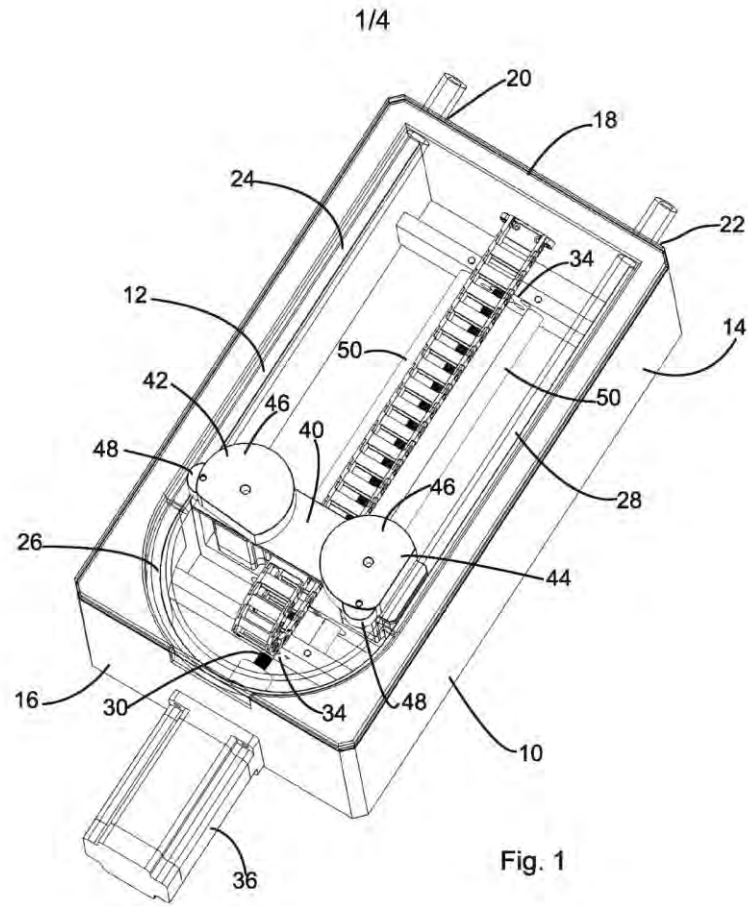
7. A method for treating chronic wounds by using a programmable pump synchronised with the patient's ECG pulse to supply adequate physiological flow of oxygenated blood to wound tissues near the wound site.
8. A method for physiological perfusion of an adult patient in CPB procedure whereby a typical 12 to 15 French cannula is inserted into left and right carotid artery each and arterial cross clamps are located proximal away from the cannula so that desired blood flow to the left and right brain can be delivered by two programmable pumps.
9. A method for physiological perfusion as claimed in claim 8, whereby a third programmable pump is connected to a femoral artery to provide abdominal perfusion and to fourth and fifth pumps to provide perfusion to the lower extremities.
10. A method for a programmable pump to mimic the left and right ventricle of a human heart and function as an artificial heart, wherein the artificial left ventricle draws oxygenated blood from the lungs through the left and right pulmonary veins and delivers to the rest of the body via the ascending aorta, and the artificial right ventricle draws de-oxygenated blood from the venous system via the inferior and superior vena cavae and deliver to the lungs.
11. A pump as claimed in any one of claims 1 to 4 when used to provide physiological perfusion in veterinary and animal experimentation.
12. A pump as claimed in any one of claims 1 to 4 when used to provide physiological perfusion in artificial organs, tissue cultured organs or 3D printed organs.
13. A pump as claimed in any one of claims 1 to 4 when used to provide physiological perfusion of a human patient or and animal as an arterial pump in a CPB or an ECMO procedure.

**TRIPHASIC CARDIAC PUMP PTY LTD**

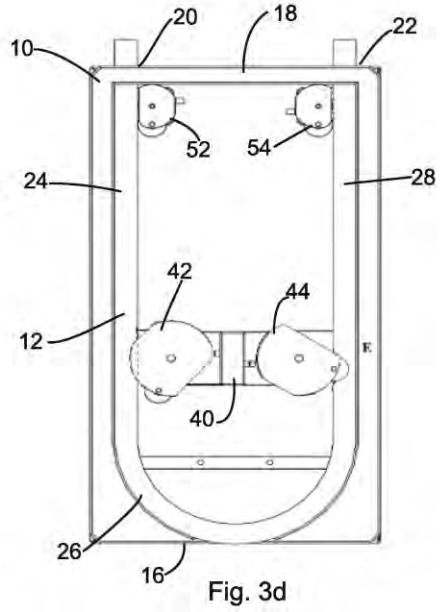
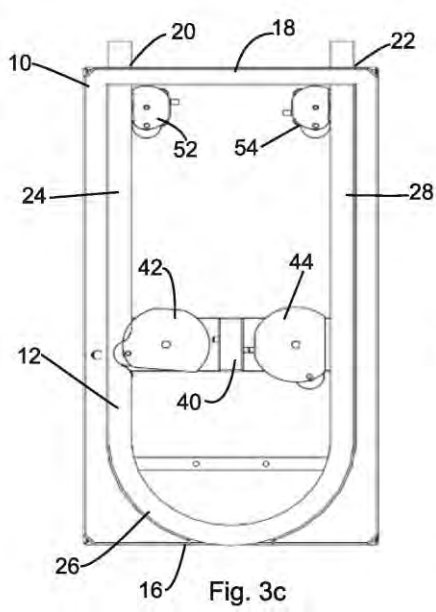
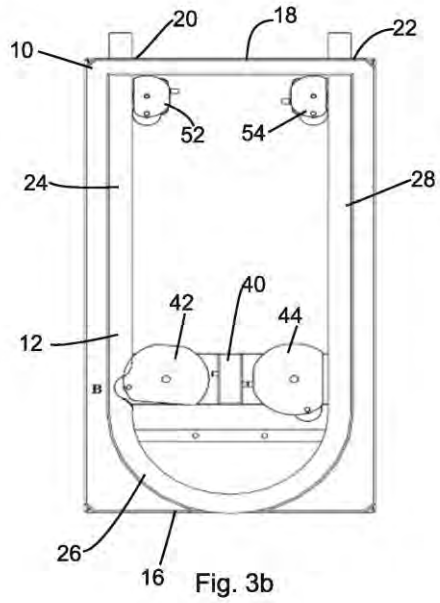
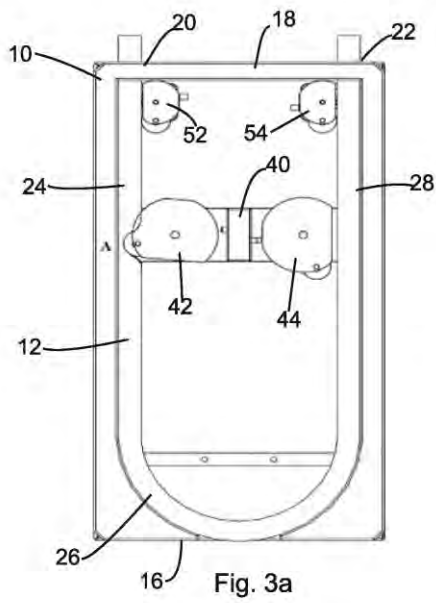
By its Patent Attorneys

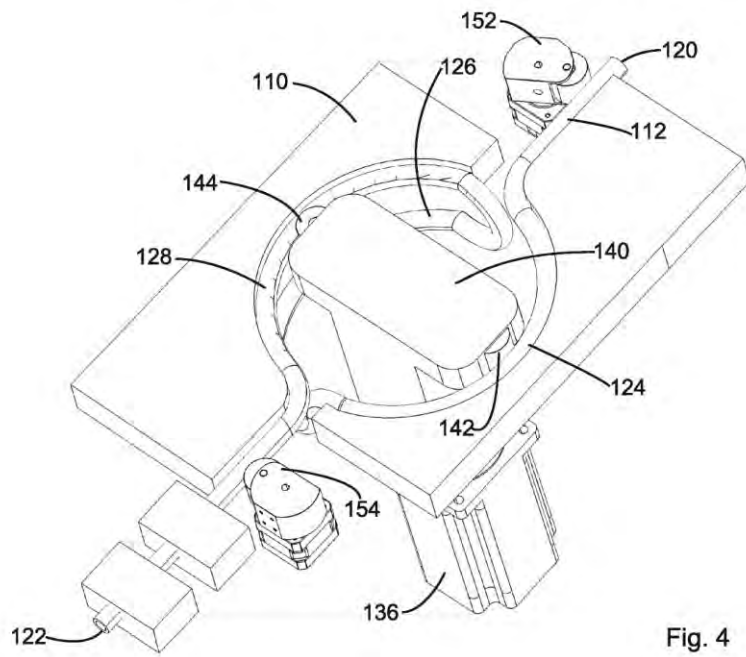
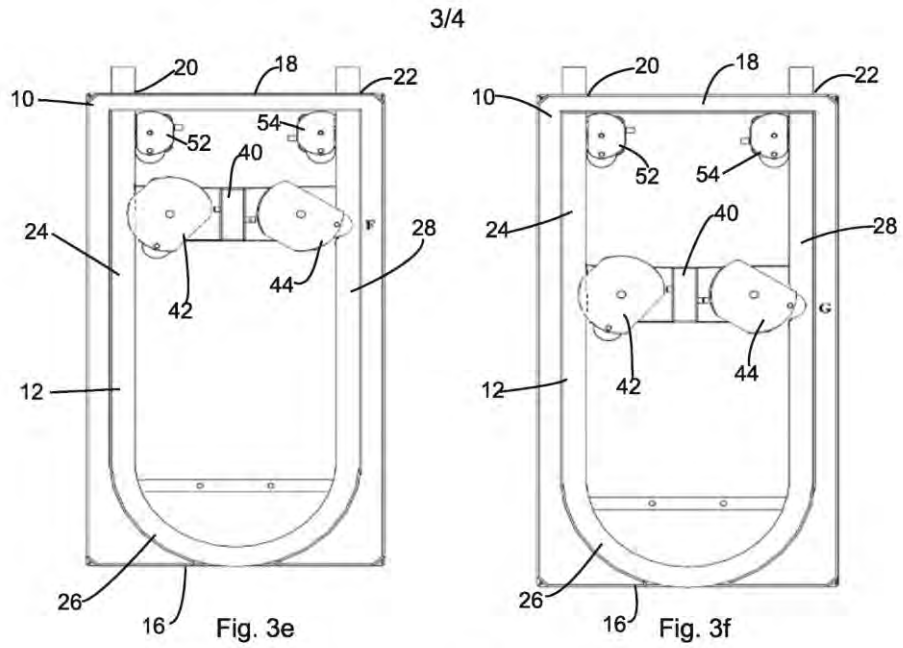
**ARMOUR IP**

P2325AU00



2/4





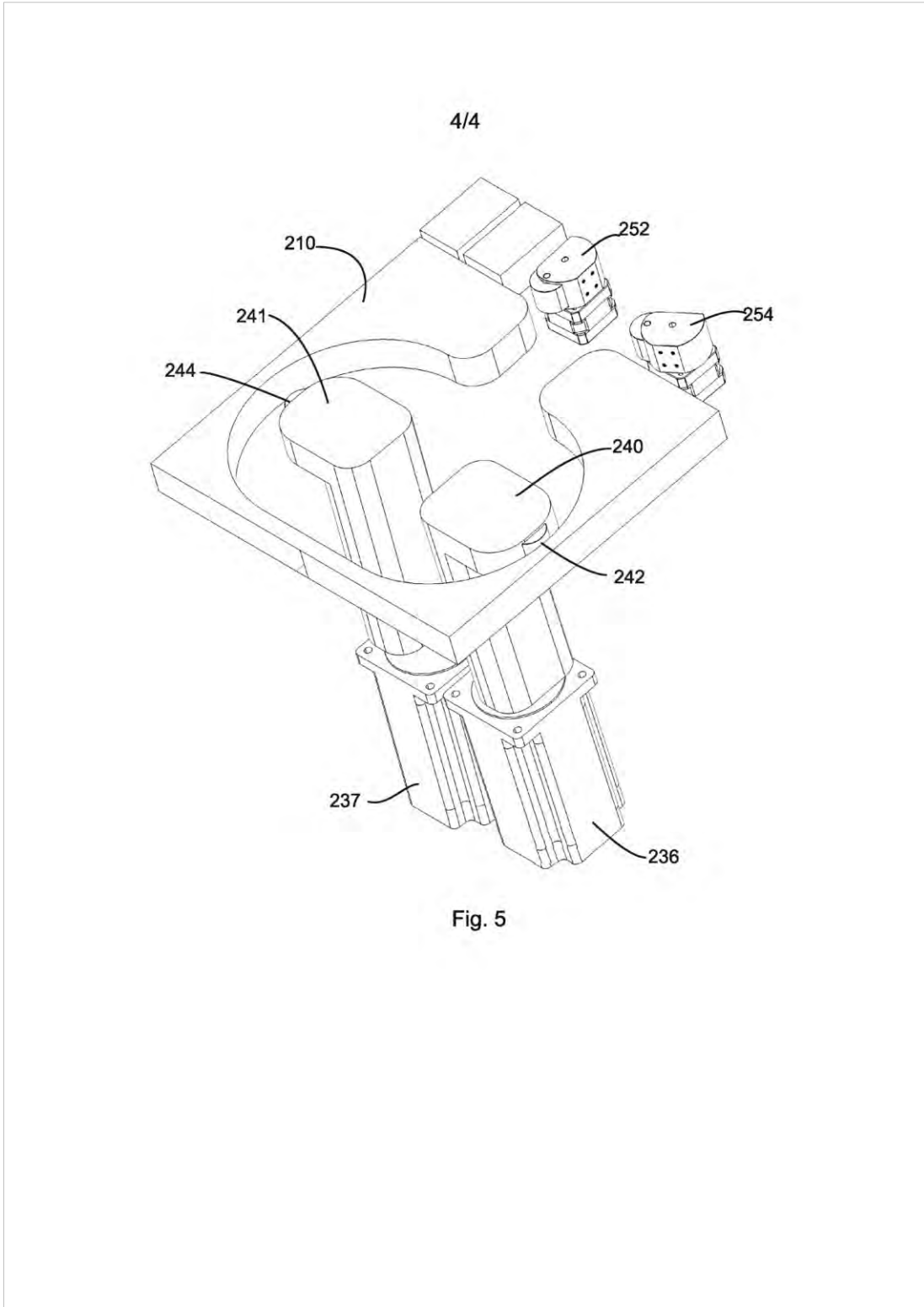


Fig. 5

# Appendix G Provisional Filing of Cardiac Pump for Surgical Procedures

## “CARDIAC PUMP”

### **Field of the Invention**

[0001] The present invention relates to a cardiac pump, primarily arranged for use as part of a cardiopulmonary bypass perfusion system or an extracorporeal membrane oxygenation system.

### **Background to the Invention**

[0002] Cardiac pumps used in surgery traditionally fall into two types: peristaltic and centrifugal. Both types of pump can be arranged to provide a consistent flow of blood at an appropriate pressure, with the pumps being adjustable to compensate for changes in flow rate or pressure requirements.

[0003] Traditional peristaltic pumps provide a pulsatile flow of blood. Traditional centrifugal pumps provide a steady flow of blood. These have proved to be sufficient to maintain a patient through surgery.

[0004] It is notable, however, that the flow of blood provided by such cardiac pumps is notably different to the aortic flow provided by a beating heart. Natural aortic flow is triphasic in nature: through systolic, early diastolic and late diastolic phases. Traditional cardiac pumps do not replicate this flow.

[0005] The effects of pulsatile or steady pumping of blood rather than triphasic flow during open heart surgery are not well understood. It is at least possible that using a pump which more closely replicates patient physiology will lead to improved patient outcomes. It is also considered valuable to provide such a pump for use within a laboratory setting, to enable further testing to be done.

[0006] The present invention seeks to provide a cardiac pump which mimics a natural triphasic aortic flow.

[0007] A further disadvantage of cardiac pumps used in surgery is that pump heads are generally single-use items, as it is impractical to completely clean all blood residue from a pump. This represents a significant expense in cardiac surgery.

#### **Summary of the Invention**

[0008] According to one aspect of the present invention there is provided a cardiac pump having a fluid line formed from flexible tubing, the fluid line having a first portion which acts as an inlet line, a second connecting portion, and a third portion which acts as a return line, the cardiac pump having a reciprocating actuator, the actuator having a first actuating member arranged to move between a free orientation and an occluding orientation such that the first actuating member at least partially occludes the fluid line when in its occluding orientation; the cardiac pump being operable such that when the actuator moves away from an inlet the first actuating member may be in its occluding orientation so as to peristaltically force fluid towards a fluid outlet.

[0009] According to a second aspect of the present invention there is provided a cardiac pump having a fluid line formed from flexible tubing, the fluid line having a first portion which acts as an inlet line, a second connecting portion, and a third portion which acts as a return line, the cardiac pump having a reciprocating actuator, the actuator having a first actuating member arranged to move between a free orientation and an occluding orientation such that the first actuating member at least partially occludes the first portion of the fluid line when in its occluding orientation; the actuator having a second actuating member arranged to move between a free orientation and an occluding orientation such that the second actuating member at least partially occludes the third portion of the fluid line when in its occluding orientation; the cardiac pump being operable such that when the actuator moves away from an inlet the first actuating member may be in its occluding orientation so as to peristaltically force fluid towards a fluid outlet, and when the actuator moves towards the inlet the second



member may be in its occluding orientation so as to peristaltically force fluid towards the fluid outlet.

[0010] The first portion and the third portion may each be generally linear and parallel to each other, with the actuator being moveable in a linear manner.

[0011] Alternatively, the first portion and the third portion may be arcuate, with the actuator being movable in a rotational manner.

[0012] The actuator may be a single moving body on which both the first actuating member and the second actuating member are mounted. Alternatively, the actuator may have two independently moving bodies, with the first actuating member mounted on a first actuator body and the second actuating member mounted on a second actuator body.

[0013] It is preferred that the actuator is arranged to have a long stroke and at least one short stroke. In a preferred embodiment, the long stroke corresponds to close to the length of the first and third portions of the inlet line, and the short stroke represents about 5% to 25% of the length of the long stroke (adjustable based on patient physiology). The arrangement is such that the actuator moves in a forward direction through a long stroke; in a reverse direction through a first short stroke (typically about 20% of the length of the long stroke); in the forward direction through a second short stroke shorter than the first short stroke (typically about 5% of the length of the long stroke); in the reverse direction through a long stroke; in the forward direction through a first short stroke; and in the reverse direction through a second short stroke to return to the starting position. It will be appreciated that this 'long, short, shorter' pattern represents a triphasic operation.

[0014] In a preferred mode of operation the actuator has its first member in the occluding orientation and its second member in the free orientation during a long stroke away from the pump inlet and the immediately following two short strokes; and then has the orientations of the first and second

members reversed for the long stroke towards the pump inlet and the immediately following two short strokes.

[0015] The cardiac pump may include a check valve associated with the pump inlet. The check valve may be moveable between a first orientation in which it acts as a one-way valve and a second orientation in which it acts as a two-way valve. The arrangement is such that the check valve is in its first orientation during a long stroke of the actuator and during a second short stroke of the actuator, and is in its second orientation during a first short stroke of the actuator. The cardiac pump may include a similar check valve associated with the pump outlet.

[0016] It is preferred that the actuator is mounted on a linear screw drive. Alternatively, a belt-driven linear drive or a rack-and-pinion linear slide can be used.

[0017] Each of the first and second members of the actuator may be rollers mounted on cams. In a preferred embodiment of the invention, each cam is controlled by a stepper motor.

#### **Brief Description of the Drawings**

[0018] It will be convenient to further describe the invention with reference to preferred embodiments of the present invention. Other embodiments are possible, and consequently the particularity of the following discussion is not to be understood as superseding the generality of the preceding description of the invention. In the drawings:

[0019] Figure 1 is a perspective of a cardiac pump in accordance with the present invention;

[0020] Figure 2 is a cross-section through the cardiac pump of Figure 1;

[0021] Figures 3a to 3f are a sequential series of plan views showing the operation of the cardiac pump of Figure 1.

[0022] Figure 4 is an indicative perspective of a second embodiment of a cardiac pump in accordance with the present invention;

[0023] Figure 5 is an indicative perspective of a third embodiment of a cardiac pump in accordance with the present invention; and

[0024] Figures 6a to 6d are a sequential series of plan views showing the operation of a cardiac pump in accordance with a further embodiment of the present invention.

#### **Detailed Description of Preferred Embodiments**

[0025] Referring to Figures 1 to 3, there is shown a pump 10. The pump 10 is arranged to force fluid (notionally blood) through a tube 12. In this embodiment the tube 12 is formed from platinum coated silicone tubing having an internal diameter of 19mm. It is considered that bio-compatible tubing having an internal diameter between 6mm and 25mm may be suitable for this purpose.

[0026] The pump 10 has a generally rectangular outer housing 14, having a front wall 16 and a rear wall 18. The pump 10 has a fluid entry 20 and a fluid exit 22 both located near the top of the rear wall 18.

[0027] The tube 12 has a straight first tube portion 24 which extends from the fluid entry 20 along an internal side wall of the housing 14; a U-shaped second tube portion 26 which bends through 180° internally of the front wall 16; and a straight third tube portion 28 which extends along an internal side wall of the housing 14 to the fluid exit 22. The first tube portion 24 and the third tube portion 28 are parallel to each other, and are spaced across the housing 14.

[0028] A linear drive system is located along the base of the housing 14. The drive system is a ball screw drive system, including a driving screw 30 on which is located a ball nut 32. The driving screw 30 is parallel to the first and third tube portions 24, 28 of the tube 12, and is mounted in bearings 34

located respectively near the front wall 16 and the rear wall 18. The driving screw 30 is driven by a stepper motor 36 located outside the front wall 16. The arrangement is such that driving of the driving screw 30 by the motor 36 causes linear movement of the ball nut 32.

[0029] An actuator 40 is mounted atop the ball nut 32. The actuator 40 has a first actuating member 42 located towards the first tube portion 24 and a second actuating member 44 located towards the third tube portion 28.

[0030] The actuating members 42, 44 each include a roller 46 mounted on a cam member 48. The actuating members 42, 44 are controllable such that the cam members 48 can each be independently rotated between a free orientation in which the cam member 48 and roller 46 are clear of the respective tube portion 24, 28, and an occluding orientation in which the roller 46 impinges against the respective tube portion 24, 28. It is preferred that the roller 46 has a total travel distance of 19mm and thus acts to fully occlude the tube 12. In Figure 1, the first actuating member 42 is shown in its occluding orientation occluding the first tube portion 24 and the second actuating member 44 is shown in its free orientation clear of the third tube portion 28.

[0031] Two guide rods 50 are associated with the actuator 40 and are arranged to constrain movement of the actuator 40 in the linear direction.

[0032] Operation of the pump 10 will now be described with reference to Figures 3a to 3f.

[0033] The pump 10 generally operates to pump fluid such as blood in a peristaltic fashion from the fluid entry 20 to the fluid exit 22. It does this in one of two ways: by moving the actuator from near the rear wall 18 in the direction of the front wall 16 with the first actuating member 42 in its occluding orientation and the second actuating member 44 in its free orientation; and by moving the actuator from near the front wall 16 in the

direction of the rear wall 18 with the first actuating member 42 in its free orientation and the second actuating member 44 in its occluding orientation.

[0034] It will be appreciated that the pump 10 can be continuously operated in such a fashion, providing a continuous (monophasic) pumping operation.

[0035] It is preferred that the pump 10 be operated in a triphasic manner, replicating the action of the human heart.

[0036] In such a mode the pump 10 operates in a six-step cycle, beginning in the position where the actuator 40 is close to the rear wall 18. In steps one to three (drawings 3a to 3c), the first actuating member 42 is in its occluding orientation and the second actuating member 44 is in its free orientation. In steps four to six (drawings 3d to 3f), the first actuating member 42 is in its free orientation and the second actuating member 44 is in its occluding orientation.

[0037] In step one as shown in Figure 3a, the actuator 40 is driven in a long stroke the full length of travel towards the front wall 16. This mimics the systolic phase of normal cardiac function.

[0038] In step two, shown in Figure 3b, the actuator 40 is driven in a short stroke (about 20% of the full length of travel) back towards the rear wall 18. This mimics the early diastolic phase of cardiac function. The actual length of this short stroke can be chosen to reflect an individual patient's physiology.

[0039] In step three, shown in Figure 3c, the actuator 40 is driven in a still shorter stroke (about 5% of the full length of travel) back towards the front wall 16. This mimics the late diastolic phase of cardiac function, and is also adjustable for an individual patient.

[0040] In step four, shown in Figure 3d, the actuator 40 is driven in a long stroke the full length of travel towards the rear wall 18. This mimics the next systolic phase of normal cardiac function.

[0041] In step five, shown in Figure 3e, the actuator 40 is driven in a short stroke (about 20% of the full length of travel) back towards the front wall 16. This mimics the early diastolic phase of cardiac function.

[0042] In step six, shown in Figure 3f, the actuator 40 is driven in a shorter stroke back towards the rear wall 18. This mimics the late diastolic phase of cardiac function.

[0043] The cycle then repeats.

[0044] In order for correct flow rates and pressures to be maintained, a first valve 52 is associated with both the fluid entry 20 and a second valve 54 is associated with the fluid exit 22. The valves 52, 54 are structured so as to operate as one-way valves during the long strokes (i.e. the systolic phase) and the shortest strokes (i.e. the late diastolic phase), but to permit reverse flow (i.e. negative pressure) during the early diastolic phase.

[0045] It will be appreciated that actual reverse flow may not be useful in all settings. Although it may be valuable in a laboratory setting, reverse flow may not be prudent in a clinical environment. It is anticipated that the pump 10 may be operated in 'long stroke – rest – short stroke' mode to simulate triphasic flow without a negative pressure stage.

[0046] Figure 4 shows an alternative cardiac pump 110. The cardiac pump 110 operates in a similar fashion to the cardiac pump 10, however the first tube portion 124 and the third tube portion 128 are both circular, with the second tube portion 126 extending through a 180° arc to connect the first tube portion 124 and the third tube portion 128.

[0047] The actuator 140 is driven by a rotational motor 136. The first actuating member 142 and the second actuating member 144 work in similar fashion to the actuating members 42, 44 of the linear embodiment.

[0048] The operation of the pump 110 is broadly similar to that of the pump 10. Rather than each of the steps being measured as a linear stroke, the steps are measured as a rotation of the actuator 140. The first step is a clockwise rotation of about 100°; the second step a counter-clockwise rotation of about 20°; the third step a clockwise rotation of about 5°; fourth step a counter-clockwise rotation of about 100° (the drawing shows the position halfway through the fourth step); the fifth step a clockwise rotation of about 20°; and the sixth step a counter-clockwise rotation of about 5°. The first and second actuating members 142, 144 move between free and occluding orientations accordingly.

[0049] Figure 5 shows another alternative cardiac pump 210. This pump is similar to the pump 110, however the actuator 140 has been replaced with a first actuator body 240 powered by a first actuator motor 136 and a second actuator body 241 powered by a second actuator motor 137. This arrangement allows the first and second actuating members 242, 244 to be operated independently; that is, when the first actuating member 242 is in its occluding position (and working through steps 1-3 of the operation), the second actuating member 244 in its free position can be rotated into the correct 'start' position for step 4.

[0050] In this way the operation of the first and second actuating members 242, 244 can be in the same angular direction, simplifying the arrangement of the tubing (not shown).

[0051] Figure 6a shows yet another alternative cardiac pump 310. This pump is similar to the pump 110, with an actuator 340 operating against second tube portion 326, the pump 310 having an inlet portion being a first tube portion 324 and an outlet being a third tube portion 328.

[0052] The actuator 340 has a single actuating member 342, moveable between a free orientation as shown in Figures 6a and 6d, and an occluding orientation as shown in Figures 6b and 6c. The arrangement is such that the actuator 340 moves through close to 180° with the actuating member 342 in its occluded orientation, and then is arranged to rapidly rotate through the remaining 180° (or slightly more) whilst the actuating member 342 is in its free orientation.

[0053] Modifications and variations as would be apparent to a skilled addressee are deemed to be within the scope of the present invention.



### Claims

1. A cardiac pump having a fluid line formed from flexible tubing, the fluid line having a first portion which acts as an inlet line, a second connecting portion, and a third portion which acts as a return line, the cardiac pump having a reciprocating actuator, the actuator having a first actuating member arranged to move between a free orientation and an occluding orientation such that the first actuating member at least partially occludes the first portion of the fluid line when in its occluding orientation; the actuator having a second actuating member arranged to move between a free orientation and an occluding orientation such that the second actuating member at least partially occludes the third portion of the fluid line when in its occluding orientation; the cardiac pump being operable such that when the actuator moves away from an inlet the first actuating member may be in its occluding orientation so as to peristaltically force fluid towards a fluid outlet, and when the actuator moves towards the inlet the second member may be in its occluding orientation so as to peristaltically force fluid towards the fluid outlet.
2. A cardiac pump as claimed in claim 1, wherein the first portion and the third portion are be generally linear and parallel to each other, with the actuator being moveable in a linear manner.
3. A cardiac pump as claimed in claim 1, wherein the first portion and the third portion are arcuate, with the actuator being movable in a rotational manner.
4. A cardiac pump as claimed in any one of claims 1 to 3, wherein the actuator is a single moving body on which both the first actuating member and the second actuating member are mounted.
5. A cardiac pump as claimed in any one of claims 1 to 3, wherein the actuator has two independently moving bodies, with the first actuating member mounted on a first actuator body and the second actuating member mounted on a second actuator body.

6. A cardiac pump as claimed in any preceding claim, wherein the actuator is arranged to have a long stroke and at least one short stroke.
7. A cardiac pump as claimed in claim 6, wherein the long stroke corresponds to the length of the first and third portions of the inlet line, and the short stroke represents between 5% and 25% of the length of the long stroke.
8. A cardiac pump as claimed in claim 6 or claim 7, wherein the actuator is arranged to have a first short stroke and a second short stroke, the second short stroke being shorter than the first short stroke.
9. A cardiac pump as claimed in claim 8, wherein the actuator moves in a forward direction through a long stroke; in a reverse direction through a first short stroke; in the forward direction through a second short stroke; in the reverse direction through a long stroke; in the forward direction through a first short stroke; and in the reverse direction through a second short stroke to return to the starting position.
10. A cardiac pump as claimed in claim 9, wherein the actuator has its first member in the occluding orientation and its second member in the free orientation during a long stroke away from the pump inlet and the immediately following two short strokes; and then has the orientations of the first and second members reversed for the long stroke towards the pump inlet and the immediately following two short strokes.
11. A cardiac pump as claimed in any preceding claim, wherein the cardiac pump includes an inlet check valve associated with the pump inlet.
12. A cardiac pump as claimed in claim 11, wherein the inlet check valve is moveable between a first orientation in which it acts as a one-way valve and a second orientation in which it acts as a two-way valve.

13. A cardiac pump as claimed in any preceding claim, wherein the cardiac pump includes an outlet check valve associated with the pump outlet.
14. A cardiac pump as claimed in claim 13, wherein the outlet check valve is moveable between a first orientation in which it acts as a one-way valve and a second orientation in which it acts as a two-way valve.
15. A cardiac pump as claimed in claim 2, wherein the actuator is mounted on a linear screw drive.
16. A cardiac pump as claimed in any preceding claim, wherein each of the first and second members of the actuator is a roller.
17. A cardiac pump as claimed in claim 16, wherein each roller is controlled by a cam.
18. A cardiac pump having a fluid line formed from flexible tubing, the fluid line having a first portion which acts as an inlet line, a second connecting portion, and a third portion which acts as a return line, the cardiac pump having a reciprocating actuator, the actuator having a first actuating member arranged to move between a free orientation and an occluding orientation such that the first actuating member at least partially occludes the fluid line when in its occluding orientation; the cardiac pump being operable such that when the actuator moves away from an inlet the first actuating member may be in its occluding orientation so as to peristaltically force fluid towards a fluid outlet.

**Abstract**

A cardiac pump is arranged to mimic triphasic operation. The pump uses a fluid line formed from flexible tubing, along with a reciprocating actuator arranged to move between a free orientation and an occluding orientation. This allows a portion of the fluid line to be selectively occluded during movement of the actuator, enabling blood or other fluids to be peristaltically forced fluid towards a fluid outlet. The direction of operation of the actuator, and the selection of appropriate occluding or free orientations, allows the pump to be operated in a triphasic manner.

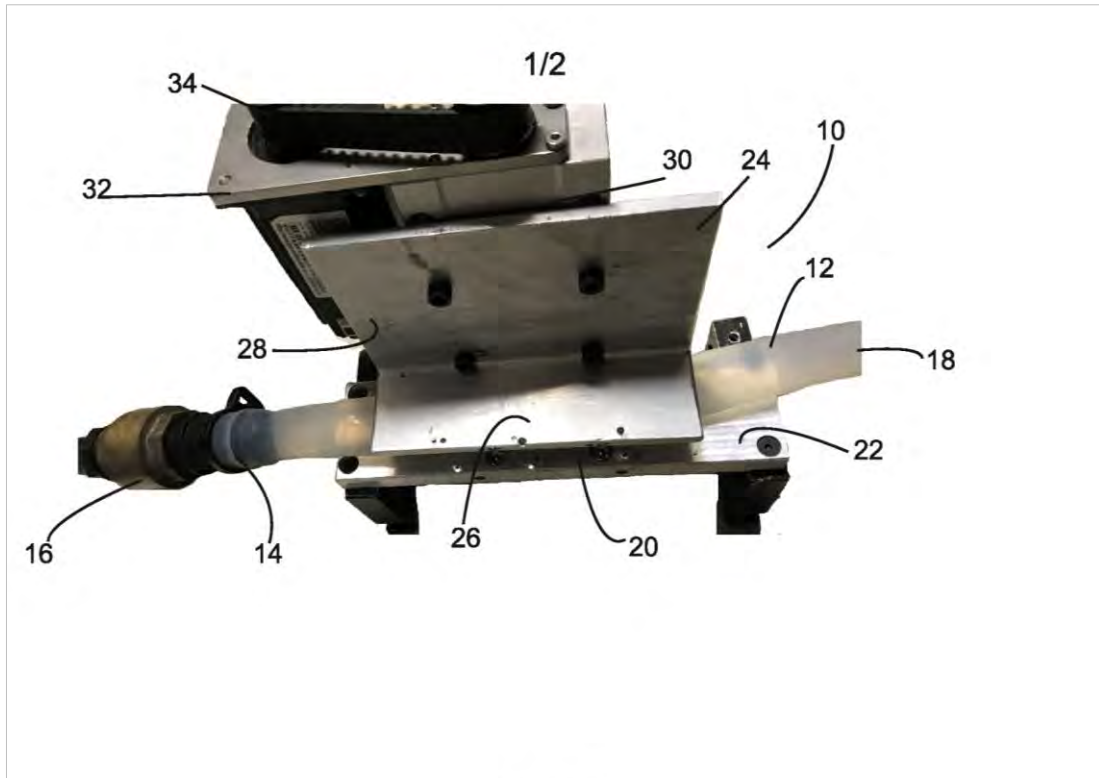


Fig. 1

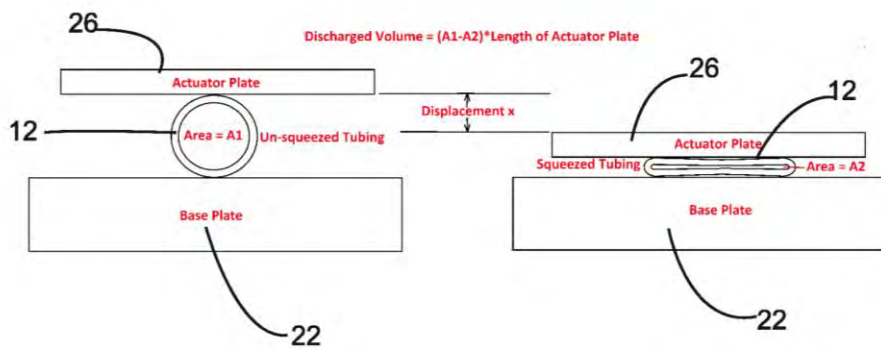


Fig. 2

2/2

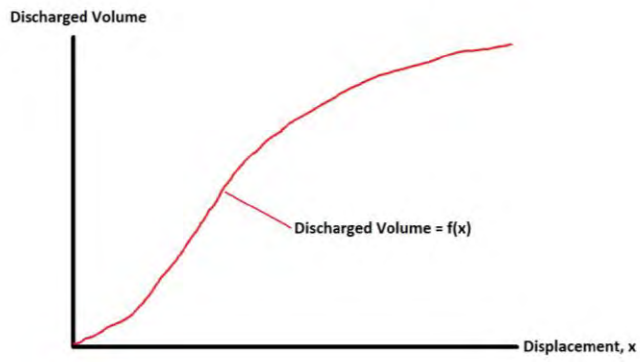


Fig. 3

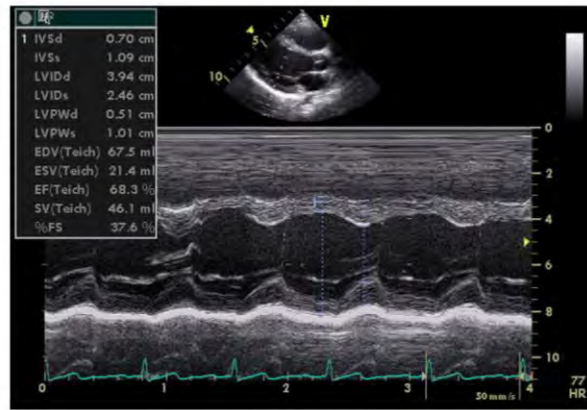


Fig. 4

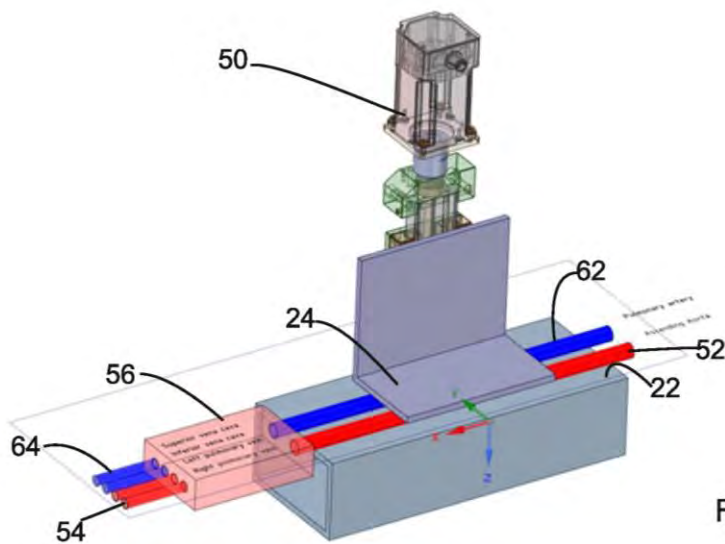


Fig. 5

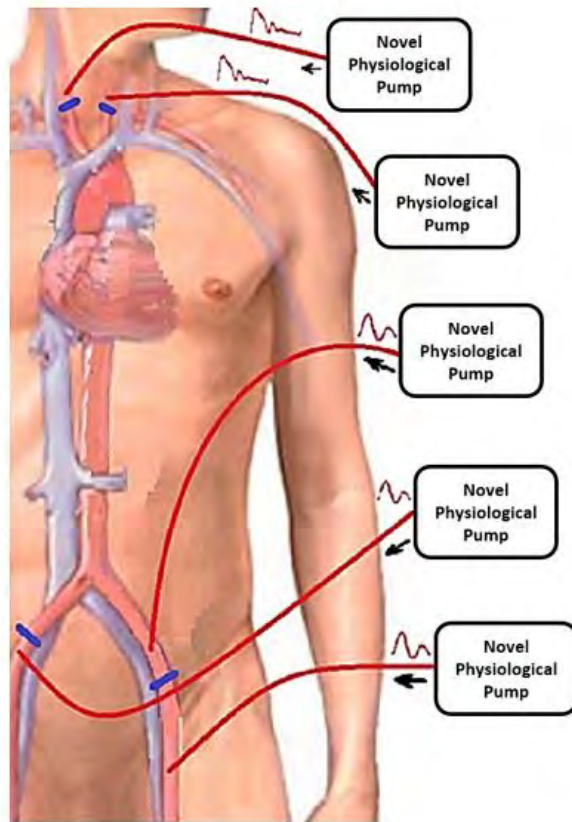


Fig. 6

## Appendix H Conference Proceedings

The 9th Congress of Asian Society of Cardiovascular Imaging conference at the Le Meridien, Kuala Lumpur, Malaysia, 11 – 13 June 2015

### COMPUTATIONAL FLUID DYNAMIC ANALYSIS OF BLOOD FLOW PATTERN AT AORTOILIAC BIFURCATION WITH ATHEROSCLEROTIC PLAQUE TREATED WITH KISSING STENTS

Yoon Song Chong<sup>1</sup> Zhonghua Sun<sup>1</sup> Julien Cisonni<sup>2</sup> Shirley Jansen<sup>3,4</sup>

<sup>1</sup>Medical Radiation Sciences, Curtin University, Perth, Australia <sup>2</sup>Department of Mechanical Engineering, Curtin University, Perth, Australia

<sup>3</sup>Harry Perkins Institute of Medical Research, Perth, Australia <sup>4</sup>Sir Charles Gairdner Hospital, Perth, Australia

#### Background and Motivation

Atherosclerotic occlusive disease at the aortoiliac bifurcation is most commonly treated now with covered or bare stents. There are several configurations possible, some include relining the entire bifurcation with covered stents (CERAB) procedure. Ultrasound surveillance of recurrent disease in this stented segment is difficult and often conflicts with computed tomography (CT) findings. Further understanding of the changes in haemodynamics from this treatment are required to interpret follow-up imaging.



Fig.1 Occluded Common Iliac Artery

#### Objective

Routine post-operative follow up of blood flow velocity measurements using ultrasound can indicate higher than expected velocity in or distal to the stented segment. This usually indicates stenosis. We used computational fluid dynamics (CFD) methods to analyze blood flow velocity and pattern in order to explain these findings and to avoid unnecessary radiation exposure of invasive procedure such as angiography.

#### Material and Methods

Three-dimensional models of aortic arteries were generated by two methods. The first used a three dimensional computerized drafting software and the second method used patient data from multi-slice helical computed tomography scanning where the two dimensional images were transformed into three dimensional volume data using commercially available software. Three dimensional model of the patient specific vascular anatomy was then generated using segmentation techniques.



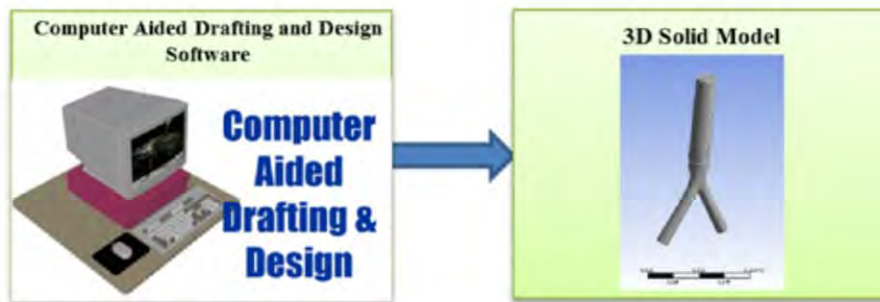


Fig.2 Creation of 3D Solid Model from Computer Aided Drafting &amp; Design Software



Fig.3 Creation of 3D Solid Model from Patient Specific CTA Data

Using commercially available CFD solver, cardiac blood flow was simulated based on the following realistic physiological conditions :

- . Realistic Aortoiliac geometry<sup>1</sup>
- . Blood density of 1060 kg/m<sup>3</sup>
- . Blood flow was considered to be laminar and incompressible
- . Blood was assumed to be a Non-Newtonian Fluid<sup>2</sup>, its viscosity was estimated using Carreau Model<sup>3</sup>

$$\mu = \mu_{\infty} + (\mu_0 - \mu_{\infty})[1 + (\lambda\dot{\gamma})^2]^{(n-1)/2},$$

$$\text{where } \lambda = 3.313s, n = 0.3568, \mu_0 = 0.56 \text{ P and } \mu_{\infty} = 0.0345 \text{ P}$$

- . Plaques were assumed to be rigid bodies
- . An aortic bifurcation angle of 40° were in the models<sup>4</sup>
- . Non-slip conditions were applied at the artery walls
- . Triphasic pulsatile waveform was applied at the inlet<sup>5</sup>
- . 100cm/s Peak Systolic Velocity (PSV) were applied at the inlet<sup>6</sup>
- . Courant Frederick Lewy (CFL) criteria were used to determine time-step

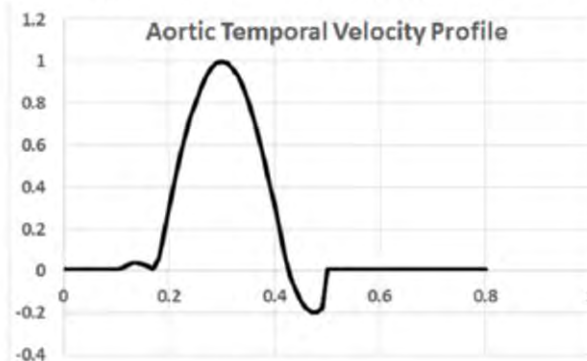


Fig.4 Triphasic waveform

**Results**

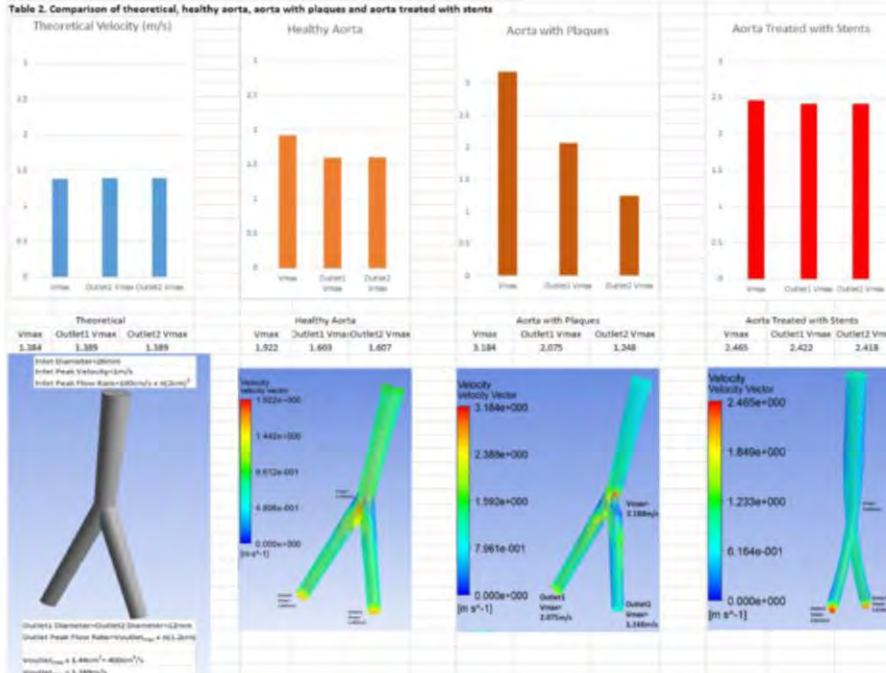
CFD Simulations were initially carried out for the idealized healthy aortoiliac bifurcation to establish grid independence where the parameter of interest, velocity converges. 80,321 elements were deemed to be optimum with acceptable simulation time of 2 hours and four minutes running on a Dell Precision Desktop computer.

**Table 1. CFD Simulation Results for Idealized Healthy Aortoiliac Bifurcation**

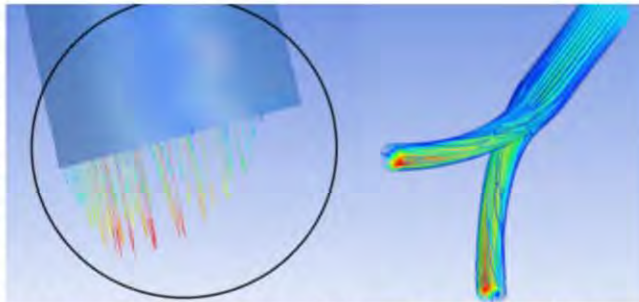
Quantity of Elements in Mesh	Orthogonality (Mean/Deviation)	Skewness (Mean/Deviation)	Vmax (M/s)	Outlet1 Vmax (M/s)	Outlet2 Vmax (M/s)	Simulation time (Hr)
18291	0.8376/0.1257	0.3077/0.1548	1.911	1.581	1.609	0:52
26883	0.8904/0.0962	0.2480/0.1228	1.914	1.59	1.604	0:54
54388	0.9153/0.0861	0.2021/0.1082	1.917	1.598	1.597	1:01
60991	0.9102/0.0870	0.2085/0.1122	1.918	1.599	1.588	1:31
80321	0.9112/0.0872	0.2002/0.1119	1.922	1.603	1.607	2:04
104827	0.9100/0.0877	0.1970/0.1120	1.924	1.601	1.61	2:39
156307	0.9067/0.0893	0.1975/0.1144	1.926	1.602	1.604	5:06

Subsequent simulation was carried out on a 70% occluded aortic bifurcation which showed high velocity distal to the stenoses before treatment which is caused by area reduction due to narrowing of the artery. Further simulation of a bifurcating artery treated with CERAB stents, indicated reduction in blood flow velocity in the stented section and distal to the stent. However the velocity reduction was less than the theoretically calculated value and the corresponding velocity in the healthy aorta as shown in the comparison charts in Table 2.

**Table 2. Comparison of theoretical, healthy aorta, aorta with plaques and aorta treated with stents**



The non-planar iliac branches of the CERAB stents are the main reasons for the higher than expected velocities. It was found that the fully developed parabolic velocity profiles at the two outlets are skewed to-



**Fig.5 Skewed Parabolic Velocity Profile**

**Fig.6 Rotational Flow**

ward one end of the artery wall and retrograde flow was observed in the opposing artery wall therefore higher peak velocity was observed at the outlet. In addition to the axial flow along the centre line of the artery, the simulation also showed a flow pattern which has a significant rotational flow component. The skewed parabolic profile and rotational flow provide explanations for the overall higher blood flow velocity after CERAB stents implant.

### Conclusions

CFD is proven to be a powerful and reliable tool for virtual analysis of blood flow pattern. Future studies using actual CT patient data are underway with the aim of validating the CFD findings. Furthermore, experimental benchtop models will be used to validate both simulation result and patient specific data. These studies will ultimately attempt to provide a means of calibrating a new baseline flow velocity profile immediately after stenting upon which, subsequent follow-up imaging can be compared, in the knowledge that the imaging findings are an accurate representation of the clinical situation.



**Fig. 7 Benchtop model using 3D printed aorta and pulsatile flow system under development**

### References:

1. O'Flynn P, O'Sullivan G, Pandit A. Geometric Variability of the Abdominal Aorta and Its Major Peripheral Branches. *Ann. Biomed. Eng.* 2010; 38(3):824-840. DOI:10.1007/s10439-010-9925-5
2. Rallison JM. Dynamics of Polymer Liquids. Vol. 1: Fluid Mechanics (2nd Edn.) By R. B. BIRD, R. C. ARMSTRONG and O. HASSAGER. 649 pp. 65
3. Johnston BM, Johnston P, Corney S, Kilpatrick D. Non-Newtonian blood flow in human right coronary arteries: steady state simulations. *J. Biomech.* 2004; 37(5):709-720. DOI:10.1016/j.jbiomech.2003.09.016
4. Shakeri AB, Shoja RS, Nosratinia MM, Tubbs H, Oakes WJ, Tubbs WJ. Aortic bifurcation angle as an independent risk factor for aortoiliac occlusive disease. *Folia Morphologica.* 2007; 66(3):181-184
5. Donnelly R. ABC of Arterial and Venous Disease. 2nd ed., ed. Hoboken: Hoboken: Wiley; 2009.
6. Mc Loughlin MJ, Mc Loughlin S. Diastolic Retrograde Arterial Flow and Biphasic Abdominal Aortic Doppler Wave Pattern: An Early Sign of Arterial Wall Deterioration? *Ultrasound in Medicine and Biology.* 2013; 39(4):592-596. DOI:10.1016/j.ultrasmedbio.2012.11.003.



## One Curtin International Conference (OCPC) 2017

Proceedings of One Curtin International Postgraduate Conference (OCPC) 2017 Miri, Sarawak, Malaysia, December 10 – 12, 2017

### **Development of a triphasic pulsatile flow phantom for experimental study of abdominal aortic blood flow**

Albert Chong, Zhonghua Sun  
Department of Medical Radiation Sciences, Curtin University  
Kent Street, Bentley, Perth, Western Australia 6102, Australia  
Telephone: +61 8 9266 3232  
Telephone: +61 8 9266 2377

*Corresponding Author:* Albert Chong, [yoon.s.chong@postgrad.curtin.edu.au](mailto:yoon.s.chong@postgrad.curtin.edu.au)

#### ***Introduction***

Experimental flow phantoms are indispensable tools for in vitro studies, especially in relation to the study of stenoses, aneurysms, stent design, vessel elasticity and related haemodynamic parameters of human arterial blood flow. These phantoms are important tools for studying and validating new treatment methods such as minimally invasive endovascular stent treatments [1, 2]. Phantoms are also used to help interpret clinical scanning, validate physical measurements used in clinical practice and research, characterize machines, help in the development of new medical imaging techniques and validate numerical methods such as finite element analysis (FEA) and computational fluid dynamics (CFD). [3-5]

The requirements of phantom to reproduce realistic arterial flow waveforms were reviewed extensively by Law et al [6], Holdsworth et al [7] and Hoskins et al [8] The basic requirement is that the flow phantom must be capable of reproducing pulsatile flow mimicking human arterial flow physiology and easy to program. These authors have also provided thorough reviews of previous works. Basically, previous devices can be classified according to the type of pump used in the phantom i.e. gear, piston or roller/peristaltic. Gear pumps have been used by Groot Jebbink et al [1], Boersen et al [2] and Hoskins [8] to generate pulsatile waveforms. However, the disadvantage of gear pump is that suspended particles are easily damaged and it is sensitive to cavitation due to the grinding action of the gears. Piston pumps have been used by Holdsworth et al [7], Rudenick et al [9] and Poot et al [10] to simulate peripheral arterial flow. This class of pumps shares the general disadvantage of difficulty in programming. Modified peristaltic pumps have been used by Law et al [6] and Douville et al [11] to generate physiological flow waveforms by mechanical manipulation of the backplate or computer control of the roller. This technique allows the generation of a limited number of waveforms. It is also difficult to program new waveforms, or produce reverse flow with this method. More recently Shkolnikov et al [12] and Neto et. al [13] developed roller-free peristaltic pump using actuators to produce pulsatile waveforms. However these pumps were developed for use in micro-fluidic applications and not suitable for blood flow investigation of carotid, abdominal and peripheral arteries. The main advantage of peristaltic pump is due to the fact that there is no contact between the pump driving components and the liquid. In addition, the pumping chamber i.e. the platinum cured silicone tubing is disposable [14], which ensures the sterility and avoids cross-contamination [15, 16]. The peristaltic pump is a technology which has been

Proceedings of One Curtin International Postgraduate Conference (OCPC) 2017 Miri, Sarawak, Malaysia, December 10 – 12, 2017

widely used in cardiopulmonary bypass (CPB) and extracorporeal membrane oxygenation (ECMO) procedures carried out over the past seven decades since its introduction in the 1950s. The main limitation of the standard peristaltic pump is that it generates approximately a sinusoidal waveform which does not conform to human blood flow physiology. The proposed triphasic cardiac pump is an improved version and it overcomes the limitation of the standard peristaltic pump by a unique mechanical design and combined with digital control technology, it has the capability to generate triphasic waveform and is programmable.

### ***Material and methods***

A fluid circulation system as shown in Figure 1 was developed based on an improved cardiac pump driven by a 8.5Nm NEMA34 stepper motor 86HBS85 and a closed loop hybrid servo drive HBS860H (Just Motion Control, Shenzhen, China). Arduino Uno microcontroller was used to control the stepper motor and generate the appropriate flow profile. Masterflex platinum-cured silicone tubing, L/S 36 and I/P82 (Cole-Parmer, Vernon Hills, Illinois, USA)

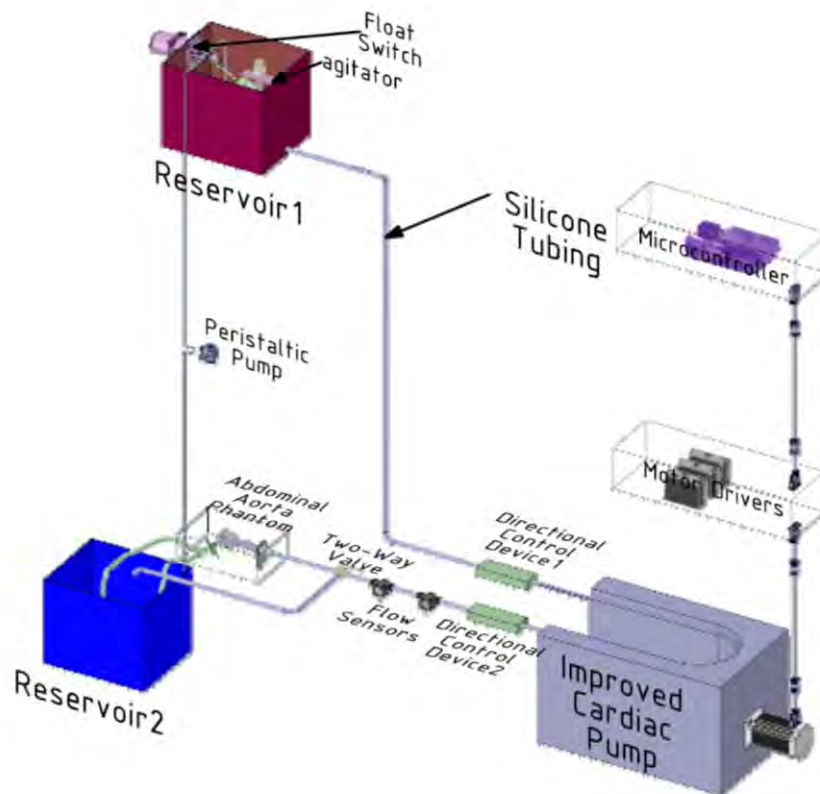


Figure 1 Fluid Circulation System

Proceedings of One Curtin International Postgraduate Conference (OCPC) 2017 Miri, Sarawak, Malaysia, December 10 – 12, 2017

with tubing internal diameters of 9.7mm and 12.5mm were used to circulate the blood mimic fluid (BMF) made of % by weight, pure water (85.41%), pure glycerol (10.25%), Sigma D4876 Dextran (3.43%) and surfactant (0.92%), density =  $1,037 \text{ Kg m}^{-3}$  and viscosity =  $4.1 \text{ (mPa s)}$  [17]. There are two reservoirs in the flow circuit where Reservoir 1 is located at a higher elevation than Reservoir 2. The difference in heights between Reservoir 1 and Reservoir 2 in millimeters (mm) is the gauge pressure in mmH<sub>2</sub>O. The height difference was set to 1088mm therefore a gauge pressure of 1088 mmH<sub>2</sub>O or 80 mmHg was produced at the inlet of cardiac pump and at the start of the cardiac cycle. A manually operated two-way valve located at the outlet of the cardiac pump allows the user to direct the flow either to the phantom or directly to Reservoir 2. When the cardiac pump is in operation, volume of BMF in Reservoir 1 will decrease where as volume of BMF in Reservoir 2 will increase. When the BMF level falls below a pre-determined level in Reservoir 1, the float-switch will activate the peristaltic pump to transfer BMF from Reservoir2 to Reservoir 1 thereby maintain the gauge pressure.

### **Flow Rate Measurements**

The average volumetric flow rates were measured by means of stop watch and the amount of BMF delivered by the cardiac pump directly into the calibrated Reservoir 2. The cardiac pump was programmed to generate 60 pulses per minute. The instantaneous flow rate generated by the cardiac pump is captured by the flow sensor located between the pump outlet and two-way valve. The output from flow sensors were displayed on a display monitor via serial communication link between the Arduino and a laptop computer (Lenovo, Morrisville, North Carolina, USA). To visualize the sensor outputs, Microsoft Excel spreadsheet is used to plot the graph of instantaneous volumetric flow rate (L/min) on the vertical axis and time (s) on the horizontal axis. To facilitate Doppler ultrasound measurements of the centerline velocity, 1200 Grit (15 micron) aluminium oxide powder was suspended in the BMF using an agitator located in Reservoir 1. Ultrasound gel is applied on the outer diameter of the silicone tubing distal to cardiac pump outlet and the probe from a portable ultrasound scanner BV-520T (Shenzhen Bestman Instrument Co. Ltd, Shenzhen, China) is then placed on the tubing with an incident angle of about 30 degree to capture the centerline velocity profile.



Proceedings of One Curtin International Postgraduate Conference (OCPC) 2017 Miri, Sarawak, Malaysia, December 10 – 12, 2017

## Results

Table 1 outlines the measurement results using Masterflex tubings LS36 and IP82 where average flow rates were 1.27L/min and 1.97 L/min respectively.

Table 1. Flowrate measurement results for Masterflex Tubing LS36 and IP82

Masterflex Tubing	Inner Diameter (mm)	Time taken to fill 5L (minutes)	Flow Rate (L/min)
LS36	9.7	3:56	1.27
IP82	12.5	2:32	1.97

Figure 2 shows a typical graph of instantaneous flow rate in L/min plotted against time in second. In this case, the mean flow rate generated from Masterflex Tubing LS36 with 9.7mm inner diameter is 1.2L/min with peak systolic flow rate of 8.25 L/min and a peak diastolic flow rate of 1.68L/min.

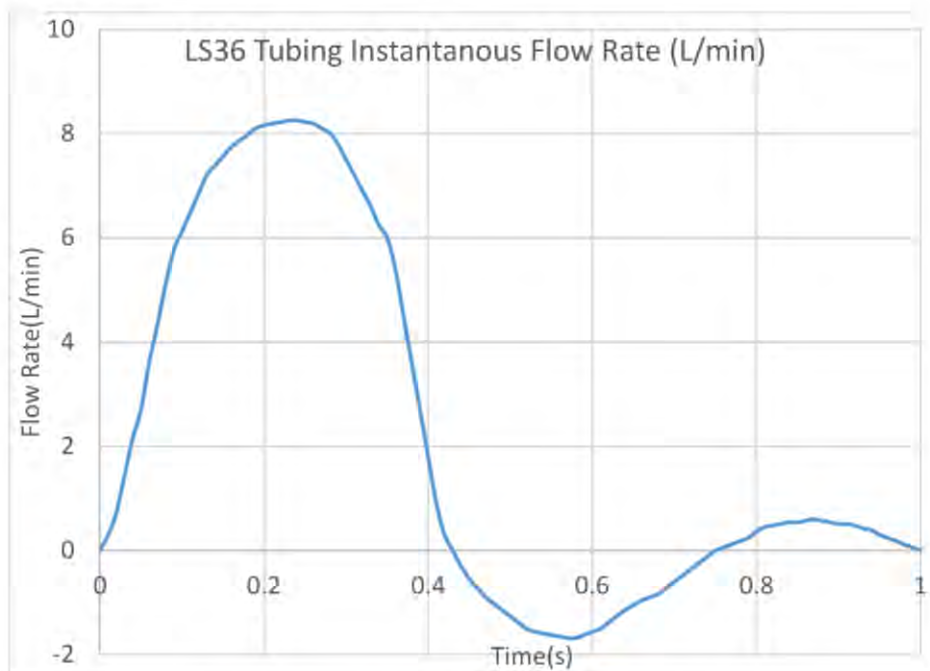


Figure 2. LS36 Tubing Instantaneous Flow Rate

Proceedings of One Curtin International Postgraduate Conference (OCPC) 2017 Miri, Sarawak, Malaysia, December 10 – 12, 2017

Figure 3 shows the centreline velocity profile from the portable Doppler Ultrasound scanner which indicates triphasic flow profile close to the physiology of human abdominal blood flow.

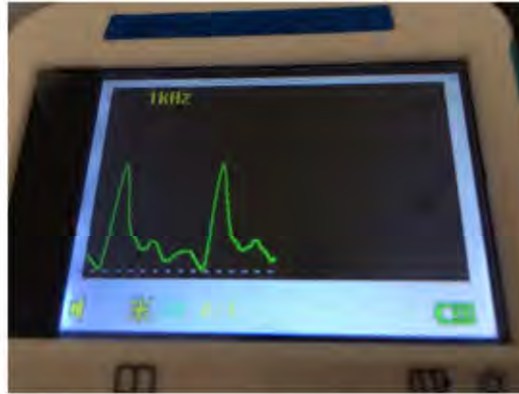


Figure 3 Display of centerline flow velocity profile from the Doppler Ultrasound Scanner

## Discussions

Since the mean abdominal aortic flow rate determined by Fraser et al [18] is 13.3mL/s or 0.798L/min therefore the mean flow rate of 1.27L/min generated by the improved cardiac pump using Masterflex LS36 tubing is more than sufficient for phantom studies of abdominal blood flow. In addition, the cardiac pump flow rate and pulsae rate can be programmed to match any patient specific physiology. Further studies of flow pressures is planned by adding transducers at inlet and outlet of the improved cardiac pump. At the time of writing this manuscript, a patent search has been completed which confirmed the novelty of the improved cardiac pump design. Intellectual Property (IP) filing is planned for this novel cardiac pump design and computer simulation is also planned to optimise the design.

## Conclusions

The newly developed cardiac pump is capable of generating triphasic waveform conforming to human physiology therefore suitable for use in experimental studies of abdominal blood flow.

## References:

- [1] E. Groot Jebbink, V. Mathai, J.T. Boersen, C. Sun, C.H. Slump, P.C.J.M. Goverde, M. Versluis, M.M.P.J. Reijnen, Hemodynamic comparison of stent configurations used for aortoiliac occlusive disease, *Journal of Vascular Surgery*, 66 (2017) 251-260.e251.
- [2] J.T. Boersen, E. Groot Jebbink, M. Versluis, C.H. Slump, D.N. Ku, J.-P.P.M. de Vries, M.M.P.J. Reijnen, Flow and wall shear stress characterization after endovascular aneurysm repair and endovascular aneurysm sealing in an infrarenal aneurysm model, *Journal of Vascular Surgery*, (2017).
- [3] M.D. Ford, H.N. Nikolov, J.S. Milner, S.P. Lownie, E.M. DeMont, W. Kalata, F. Loth, D.W. Holdsworth, D.A. Steinman, PIV-measured versus CFD-predicted flow dynamics in anatomically










Proceedings of One Curtin International Postgraduate Conference (OCPC) 2017 Miri, Sarawak, Malaysia, December 10 – 12, 2017

- realistic cerebral aneurysm models, *Journal of Biomechanical Engineering*, 130 (2008)
- &lt;xocs:firstpage xocslns:xocs=&#034;&#034;/&gt;.
- [4] E. Soudah, P. Rudenick, M. Bordone, B. Bijmens, D. García-Dorado, A. Evangelista, E. Oñate, Validation of numerical flow simulations against in vitro phantom measurements in different type B aortic dissection scenarios, *Computer Methods in Biomechanics and Biomedical Engineering*, (2013) 1-11.
- [5] P. Hariharan, M. Giarra, V. Reddy, S. Day, K. Manning, S. Deutsch, S. Stewart, M. Myers, M. Berman, G. Burgreen, E. Paterson, R. Malinauskas, Multilaboratory Particle Image Velocimetry Analysis of the FDA Benchmark Nozzle Model to Support Validation of Computational Fluid Dynamics Simulations, *J. Biomech. Eng.-Trans. ASME*, 133 (2011).
- [6] Y.F. Law, R.S.C. Cobbold, K.W. Johnston, P.A.J. Bascom, Computer-controlled pulsatile pump system for physiological flow simulation, *Med. Biol. Eng. Comput.*, 25 (1987) 590-595.
- [7] D. Holdsworth, D. Rickey, M. Drangova, D. Miller, A. Fenster, COMPUTER-CONTROLLED POSITIVE DISPLACEMENT PUMP FOR PHYSIOLOGICAL FLOW SIMULATION, *Med. Biol. Eng. Comput.*, 29 (1991) 565-570.
- [8] P.R. Hoskins, Simulation and Validation of Arterial Ultrasound Imaging and Blood Flow, *Ultrasound in Medicine & Biology*, 34 (2008) 693-717.
- [9] P.A. Rudenick, B.H. Bijmens, D. García-Dorado, A. Evangelista, An in vitro phantom study on the influence of tear size and configuration on the hemodynamics of the lumina in chronic type B aortic dissections, *Journal of Vascular Surgery*, 57 (2013) 464-474.e465.
- [10] K. Poots, R. Cobbold, K. Johnston, R. Appugliese, M. Kassam, P. Zuech, R. Hummel, A new pulsatile flow visualization method using a photochromic dye with application to Doppler ultrasound, *Ann Biomed Eng*, 14 (1986) 203-218.
- [11] Y. Douville, K.W. Johnston, M. Kassam, P. Zuech, R.S.C. Cobbold, A. Jares, An in vitro model and its application for the study of carotid doppler spectral broadening, *Ultrasound in Medicine & Biology*, 9 (1983) 347-356.
- [12] V. Shkolnikov, J. Ramunas, J.G. Santiago, A self-priming, roller-free, miniature, peristaltic pump operable with a single, reciprocating actuator, *Sensors and actuators. A, Physical*, 160 (2010) 141-146.
- [13] A.G.S.B. Neto, A.M.N. Lima, H. Neff, C.L. Gomes, C. Moreira, Linear peristaltic pump driven by three magnetic actuators: Simulation and experimental results, 2011, pp. 1-6.
- [14] N.J. Graf, M.T. Bowser, A soft-polymer piezoelectric bimorph cantilever-actuated peristaltic micropump, *Lab on a Chip*, 8 (2008) 1664-1670.
- [15] D.J. Laser, A review of micropumps, 2004, pp. R35-R64.
- [16] B. Iverson, S. Garimella, Recent advances in microscale pumping technologies: a review and evaluation, *Microfluidics and Nanofluidics*, 5 (2008) 145-174.
- [17] K.V. Ramnarine, D.K. Nassiri, P.R. Hoskins, J. Lubbers, Validation of a New Blood-Mimicking Fluid for Use in Doppler Flow Test Objects, *Ultrasound in Medicine & Biology*, 24 (1998) 451-459.
- [18] K.H. Fraser, S. Meagher, J.R. Blake, W.J. Easson, P.R. Hoskins, Characterization of an Abdominal Aortic Velocity Waveform in Patients with Abdominal Aortic Aneurysm, *Ultrasound in Medicine & Biology*, 34 (2008) 73-80.

# Appendix I Attribution Statements

**Journal:** Artificial Organs







**Paper Title:** A novel roller pump for physiological flow.

	Design and Conception	Acquisition of Data and Method	Data Conditioning and Manipulation	Analysis and Statistical Method	Interpretation and Discussion	Final Approval	Total % contribution
<b>Co-Author 1 (Albert Chong)</b>	75	85	90	90	30	16	64
Co Author 1 Acknowledgment: I acknowledge that these represent my contribution to the above research output  Signed: 							
<b>Co-Author 2 (Zhonghua Sun)</b>	5				10	14	5
Co Author 2 Acknowledgment: I acknowledge that these represent my contribution to the above research output  							
<b>Co-Author 3 (Lennart van de Veld)</b>	5	5		5	10	14	6
Co Author 3 Acknowledgment: I acknowledge that these represent my contribution to the above research output  							
<b>Co-Author 4 (Shirley Jansen)</b>	5				10	14	5
Co Author 4 Acknowledgment: I acknowledge that these represent my contribution to the above research output  							
<b>Co-Author 5 (Michel Verluis)</b>	5				10	14	4
Co Author 5 Acknowledgment: I acknowledge that these represent my contribution to the above research output  							
<b>Co-Author 6 (Michel Reijnen)</b>					10	14	4
Co Author 6 Acknowledgment: I acknowledge that these represent my contribution to the above research output  							
<b>Co-Author 7 (Erik Groot Jebbink)</b>	10	10	10	5	20	14	12
Co Author 7 Acknowledgment: I acknowledge that these represent my contribution to the above research output  							
<b>Total %</b>	100	100	100	100	100	100	100

Appendix I. Attribution Statements

**Journal:** Computers in Biology and Medicine

**Paper Title:** Blood Flow Velocity Prediction in Aortoiliac Stent Grafts using Computational Fluid Dynamics and Taguchi Method.


	Design and Conception	Acquisition of Data and Method	Data Conditioning and Manipulation	Analysis and Statistical Method	Interpretation and Discussion	Final Approval	Total % contribution
<b>Co-Author 1 (Albert Chong)</b>	80	80	100	100	30	25	69
Co Author 1 Acknowledgment: I acknowledge that these represent my contribution to the above research output  Signed:							
<b>Co-Author 2 (Barry Doyle)</b>	5	5			15	15	7
Co Author 2 Acknowledgment: I acknowledge that these represent my contribution to the above research output 							
<b>Co-Author 3 (Shirley Jansen)</b>	5	5			15	15	7
Co Author 3 Acknowledgment: I acknowledge that these represent my contribution to the above research output 							
<b>Co-Author 4 (Stefan Ponosh)</b>					10	15	4
Co Author 4 Acknowledgment: I acknowledge that these represent my contribution to the above research output 							
<b>Co-Author 5 (Julien Cissoni)</b>					10	15	4
Co Author 5 Acknowledgment: I acknowledge that these represent my contribution to the above research output 							
<b>Co-Author 6 (Zhonghua Sun)</b>	10	10			20	15	9
Co Author 6 Acknowledgment: I acknowledge that these represent my contribution to the above research output 							
<b>Total %</b>	100		100	100	100	100	100

	Design and Conception	Acquisition of Data and Method	Data Conditioning and Manipulation	Analysis and Statistical Method	Interpretation and Discussion	Final Approval	Total % contribution
<b>Co-Author 1 (Albert Chong)</b>	75	70	40	55	55	15	54
Co Author 1 Acknowledgment: I acknowledge that these represent my contribution to the above research output Signature Redacted							
<b>Co-Author 2 (Hadi Mirgolbabaee)</b>		10	35	30	5	10	15
Co Author 2 Acknowledgment: I acknowledge that these represent my contribution to the above research output Signature Redacted							
<b>Co-Author 3 (Zhonghua Sun)</b>	5				5	10	3
Co Author 3 Acknowledgment: I acknowledge that these represent my contribution to the above research output Signature Redacted							
<b>Co-Author 4 (Lennart van de Veld)</b>	5	10	5	5	5	10	6
Co Author 4 Acknowledgment: I acknowledge that these represent my contribution to the above research output Signature Redacted							
<b>Co-Author 5 (Shirley Jansen)</b>	5				5	10	3
Co Author 5 Acknowledgment: I acknowledge that these represent my contribution to the above research output Signature Redacted							
<b>Co-Author 6 (Barry Doyle)</b>	5				5	10	3
Co Author 6 Acknowledgment: I acknowledge that these represent my contribution to the above research output Signature Redacted							
<b>Co-Author 7 (Michel Verluis)</b>					5	10	3
Co Author 7 Acknowledgment: I acknowledge that these represent my contribution to the above research output Signature Redacted							
<b>Co-Author 8 (Michel Reijnen)</b>					5	10	3
Co Author 8 Acknowledgment: I acknowledge that these represent my contribution to the above research output Signature Redacted							
<b>Co-Author 9 (Erik Groot Jebbink)</b>	5	10	10	10	10	15	10
Co Author 9 Acknowledgment: I acknowledge that these represent my contribution to the above research output Signature Redacted							
<b>Total %</b>	100	100	100	100	100	100	100

# Appendix J Copyright Permissions

**Paper Title:** Training to Perform Ankle-Brachial Index: Systematic Review and Perspectives to Improve Teaching and Learning  
**Journal:** European journal of vascular and endovascular surgery  
**Rights Holder:** Elsevier Science & Technology Journals

7/13/2020 <https://marketplace.copyright.com/rs-ui-web/mp/license/8dae2b97-2c81-4cf0-b112-b838186ca8de/989147fd-9aeb-4233-acc9-69201...>



## Elsevier Science & Technology Journals - License Terms and Conditions

This is a License Agreement between Albert Yoonsong Chong ("You") and Elsevier Science & Technology Journals ("Publisher") provided by Copyright Clearance Center ("CCC"). The license consists of your order details, the terms and conditions provided by Elsevier Science & Technology Journals, and the CCC terms and conditions.

All payments must be made in full to CCC.

<b>Order Date</b>	13-Jul-2020	<b>Type of Use</b>	Republish in a thesis/dissertation
<b>Order license ID</b>	1048016-2	<b>Publisher Portion</b>	W.B./SAUNDERS CO. LTD. Image/photo/illustration
<b>ISSN</b>	1078-5884		

### LICENSED CONTENT

<b>Publication Title</b>	European journal of vascular and endovascular surgery : the official journal of the European Society for Vascular Surgery	<b>Rightsholder</b>	Elsevier Science & Technology Journals
		<b>Publication Type</b>	Journal
		<b>Start Page</b>	240
		<b>End Page</b>	247
<b>Article Title</b>	Training to Perform Ankle-Brachial Index: Systematic Review and Perspectives to Improve Teaching and Learning.	<b>Issue</b>	2
		<b>Volume</b>	51
<b>Author/Editor</b>	EUROPEAN SOCIETY FOR VASCULAR SURGERY.		
<b>Date</b>	01/01/1995		
<b>Language</b>	English		
<b>Country</b>	United Kingdom of Great Britain and Northern Ireland		

### REQUEST DETAILS

<b>Portion Type</b>	Image/photo/illustration	<b>Distribution</b>	Worldwide
<b>Number of images / photos / illustrations</b>	1	<b>Translation</b>	Original language of publication
<b>Format (select all that apply)</b>	Print, Electronic	<b>Copies for the disabled?</b>	No
<b>Who will republish the content?</b>	Academic institution	<b>Minor editing privileges?</b>	No
<b>Duration of Use</b>	Life of current edition	<b>Incidental promotional use?</b>	No
<b>Lifetime Unit Quantity</b>	Up to 499	<b>Currency</b>	AUD
<b>Rights Requested</b>	Main product		

### NEW WORK DETAILS

<b>Title</b>	Training to Perform Ankle-Brachial Index: Systematic Review and Perspectives to Improve Teaching and Learning	<b>Institution name</b>	Curtin University
		<b>Expected presentation date</b>	2020-08-17

<https://marketplace.copyright.com/rs-ui-web/mp/license/8dae2b97-2c81-4cf0-b112-b838186ca8de/989147fd-9aeb-4233-acc9-69201cda1803> 1/4

## Appendix J. Copyright Permissions

7/13/2020 <https://marketplace.copyright.com/rs-ui-web/mp/license/8dae2b97-2c81-4cf0-b112-b838186ca8de/989147fd-9aeb-4233-acc9-69201...>

Instructor name Professor Zhonghua Sun

### ADDITIONAL DETAILS

Order reference number	N/A	The requesting person / organization to appear on the license	Albert Yoonsong Chong
------------------------	-----	---	-----------------------

### REUSE CONTENT DETAILS

Title, description or numeric reference of the portion(s)	Figure 1	Title of the article/chapter the portion is from	Training to Perform Ankle-Brachial Index: Systematic Review and Perspectives to Improve Teaching and Learning.
Editor of portion(s)	Chaudru, S.; de Müllenheim, P.-Y.; Le Faucheur, A.; Kaladji, A.; Jaquinandi, V.; Mahé, G.	Author of portion(s)	Chaudru, S.; de Müllenheim, P.-Y.; Le Faucheur, A.; Kaladji, A.; Jaquinandi, V.; Mahé, G.
Volume of serial or monograph	51	Issue, if republishing an article from a serial	2
Page or page range of portion	240-247	Publication date of portion	2016-02-01

### PUBLISHER TERMS AND CONDITIONS

Elsevier publishes Open Access articles in both its Open Access journals and via its Open Access articles option in subscription journals, for which an author selects a user license permitting certain types of reuse without permission. Before proceeding please check if the article is Open Access on <http://www.sciencedirect.com> and refer to the user license for the individual article. Any reuse not included in the user license terms will require permission. You must always fully and appropriately credit the author and source. If any part of the material to be used (for example, figures) has appeared in the Elsevier publication for which you are seeking permission, with credit or acknowledgement to another source it is the responsibility of the user to ensure their reuse complies with the terms and conditions determined by the rights holder. Please contact [permissions@elsevier.com](mailto:permissions@elsevier.com) with any queries.

### CCC Reproduction Terms and Conditions

1. Description of Service; Defined Terms. This Reproduction License enables the User to obtain licenses for reproduction of one or more copyrighted works as described in detail on the relevant Order Confirmation (the "Work(s)"). Copyright Clearance Center, Inc. ("CCC") grants licenses through the Service on behalf of the rightsholder identified on the Order Confirmation (the "Rightsholder"). "Reproduction", as used herein, generally means the inclusion of a Work, in whole or in part, in a new work or works, also as described on the Order Confirmation. "User", as used herein, means the person or entity making such reproduction.
2. The terms set forth in the relevant Order Confirmation, and any terms set by the Rightsholder with respect to a particular Work, govern the terms of use of Works in connection with the Service. By using the Service, the person transacting for a reproduction license on behalf of the User represents and warrants that he/she/it (a) has been duly authorized by the User to accept, and hereby does accept, all such terms and conditions on behalf of User, and (b) shall inform User of all such terms and conditions. In the event such person is a "freelancer" or other third party independent of User and CCC, such party shall be deemed jointly a "User" for purposes of these terms and conditions. In any event, User shall be deemed to have accepted and agreed to all such terms and conditions if User reproduces the Work in any fashion.
3. Scope of License; Limitations and Obligations.
  - 3.1. All Works and all rights therein, including copyright rights, remain the sole and exclusive property of the Rightsholder. The license created by the exchange of an Order Confirmation (and/or any invoice) and payment by User of the full amount set forth on that document includes only those rights expressly set forth in the Order Confirmation and in these terms and conditions, and conveys no other rights in the Work(s) to User. All rights not expressly granted are hereby reserved.

<https://marketplace.copyright.com/rs-ui-web/mp/license/8dae2b97-2c81-4cf0-b112-b838186ca8de/989147fd-9aeb-4233-acc9-69201cda1803>

2/4



## Appendix J. Copyright Permissions

7/13/2020 <https://marketplace.copyright.com/rs-ui-web/mp/license/8dae2b97-2c81-4cf0-b112-b838186ca8de/989147fd-9aeb-4233-acc9-69201...>

- 3.2. General Payment Terms: You may pay by credit card or through an account with us payable at the end of the month. If you and we agree that you may establish a standing account with CCC, then the following terms apply: Remit Payment to: Copyright Clearance Center, 29118 Network Place, Chicago, IL 60673-1291. Payments Due: Invoices are payable upon their delivery to you (or upon our notice to you that they are available to you for downloading). After 30 days, outstanding amounts will be subject to a service charge of 1-1/2% per month or, if less, the maximum rate allowed by applicable law. Unless otherwise specifically set forth in the Order Confirmation or in a separate written agreement signed by CCC, invoices are due and payable on "net 30" terms. While User may exercise the rights licensed immediately upon issuance of the Order Confirmation, the license is automatically revoked and is null and void, as if it had never been issued, if complete payment for the license is not received on a timely basis either from User directly or through a payment agent, such as a credit card company.
- 3.3. Unless otherwise provided in the Order Confirmation, any grant of rights to User (i) is "one-time" (including the editions and product family specified in the license), (ii) is non-exclusive and non-transferable and (iii) is subject to any and all limitations and restrictions (such as, but not limited to, limitations on duration of use or circulation) included in the Order Confirmation or invoice and/or in these terms and conditions. Upon completion of the licensed use, User shall either secure a new permission for further use of the Work(s) or immediately cease any new use of the Work(s) and shall render inaccessible (such as by deleting or by removing or severing links or other locators) any further copies of the Work (except for copies printed on paper in accordance with this license and still in User's stock at the end of such period).
- 3.4. In the event that the material for which a republication license is sought includes third party materials (such as photographs, illustrations, graphs, inserts and similar materials) which are identified in such material as having been used by permission, User is responsible for identifying, and seeking separate licenses (under this Service or otherwise) for, any of such third party materials; without a separate license, such third party materials may not be used.
- 3.5. Use of proper copyright notice for a Work is required as a condition of any license granted under the Service. Unless otherwise provided in the Order Confirmation, a proper copyright notice will read substantially as follows: "Republished with permission of [Rightsholder's name], from [Work's title, author, volume, edition number and year of copyright]; permission conveyed through Copyright Clearance Center, Inc. " Such notice must be provided in a reasonably legible font size and must be placed either immediately adjacent to the Work as used (for example, as part of a by-line or footnote but not as a separate electronic link) or in the place where substantially all other credits or notices for the new work containing the republished Work are located. Failure to include the required notice results in loss to the Rightsholder and CCC, and the User shall be liable to pay liquidated damages for each such failure equal to twice the use fee specified in the Order Confirmation, in addition to the use fee itself and any other fees and charges specified.
- 3.6. User may only make alterations to the Work if and as expressly set forth in the Order Confirmation. No Work may be used in any way that is defamatory, violates the rights of third parties (including such third parties' rights of copyright, privacy, publicity, or other tangible or intangible property), or is otherwise illegal, sexually explicit or obscene. In addition, User may not conjoin a Work with any other material that may result in damage to the reputation of the Rightsholder. User agrees to inform CCC if it becomes aware of any infringement of any rights in a Work and to cooperate with any reasonable request of CCC or the Rightsholder in connection therewith.
4. Indemnity. User hereby indemnifies and agrees to defend the Rightsholder and CCC, and their respective employees and directors, against all claims, liability, damages, costs and expenses, including legal fees and expenses, arising out of any use of a Work beyond the scope of the rights granted herein, or any use of a Work which has been altered in any unauthorized way by User, including claims of defamation or infringement of rights of copyright, publicity, privacy or other tangible or intangible property.
5. Limitation of Liability. UNDER NO CIRCUMSTANCES WILL CCC OR THE RIGHTSHOLDER BE LIABLE FOR ANY DIRECT, INDIRECT, CONSEQUENTIAL OR INCIDENTAL DAMAGES (INCLUDING WITHOUT LIMITATION DAMAGES FOR LOSS OF BUSINESS PROFITS OR INFORMATION, OR FOR BUSINESS INTERRUPTION) ARISING OUT OF THE USE OR INABILITY TO USE A WORK, EVEN IF ONE OF THEM HAS BEEN ADVISED OF THE POSSIBILITY OF SUCH DAMAGES. In any event, the total liability of the Rightsholder and CCC (including their respective employees and directors) shall not exceed the total amount actually paid by User for this license. User assumes full liability for the actions and omissions of its principals, employees, agents, affiliates, successors and assigns.
- 6.

<https://marketplace.copyright.com/rs-ui-web/mp/license/8dae2b97-2c81-4cf0-b112-b838186ca8de/989147fd-9aeb-4233-acc9-69201cda1803>

3/4

## Appendix J. Copyright Permissions

7/13/2020 <https://marketplace.copyright.com/rs-ui-web/mp/license/8dae2b97-2c81-4cf0-b112-b838186ca8de/989147fd-9aeb-4233-acc9-69201...>

Limited Warranties. THE WORK(S) AND RIGHT(S) ARE PROVIDED "AS IS". CCC HAS THE RIGHT TO GRANT TO USER THE RIGHTS GRANTED IN THE ORDER CONFIRMATION DOCUMENT. CCC AND THE RIGHTSHOLDER DISCLAIM ALL OTHER WARRANTIES RELATING TO THE WORK(S) AND RIGHT(S), EITHER EXPRESS OR IMPLIED, INCLUDING WITHOUT LIMITATION IMPLIED WARRANTIES OF MERCHANTABILITY OR FITNESS FOR A PARTICULAR PURPOSE. ADDITIONAL RIGHTS MAY BE REQUIRED TO USE ILLUSTRATIONS, GRAPHS, PHOTOGRAPHS, ABSTRACTS, INSERTS OR OTHER PORTIONS OF THE WORK (AS OPPOSED TO THE ENTIRE WORK) IN A MANNER CONTEMPLATED BY USER; USER UNDERSTANDS AND AGREES THAT NEITHER CCC NOR THE RIGHTSHOLDER MAY HAVE SUCH ADDITIONAL RIGHTS TO GRANT.

7. Effect of Breach. Any failure by User to pay any amount when due, or any use by User of a Work beyond the scope of the license set forth in the Order Confirmation and/or these terms and conditions, shall be a material breach of the license created by the Order Confirmation and these terms and conditions. Any breach not cured within 30 days of written notice thereof shall result in immediate termination of such license without further notice. Any unauthorized (but licensable) use of a Work that is terminated immediately upon notice thereof may be liquidated by payment of the Rightsholder's ordinary license price therefor; any unauthorized (and unlicensable) use that is not terminated immediately for any reason (including, for example, because materials containing the Work cannot reasonably be recalled) will be subject to all remedies available at law or in equity, but in no event to a payment of less than three times the Rightsholder's ordinary license price for the most closely analogous licensable use plus Rightsholder's and/or CCC's costs and expenses incurred in collecting such payment.

8. Miscellaneous.

8.1. User acknowledges that CCC may, from time to time, make changes or additions to the Service or to these terms and conditions, and CCC reserves the right to send notice to the User by electronic mail or otherwise for the purposes of notifying User of such changes or additions; provided that any such changes or additions shall not apply to permissions already secured and paid for.

8.2. Use of User-related information collected through the Service is governed by CCC's privacy policy, available online here: <https://marketplace.copyright.com/rs-ui-web/mp/privacy-policy>

8.3. The licensing transaction described in the Order Confirmation is personal to User. Therefore, User may not assign or transfer to any other person (whether a natural person or an organization of any kind) the license created by the Order Confirmation and these terms and conditions or any rights granted hereunder; provided, however, that User may assign such license in its entirety on written notice to CCC in the event of a transfer of all or substantially all of User's rights in the new material which includes the Work(s) licensed under this Service.

8.4. No amendment or waiver of any terms is binding unless set forth in writing and signed by the parties. The Rightsholder and CCC hereby object to any terms contained in any writing prepared by the User or its principals, employees, agents or affiliates and purporting to govern or otherwise relate to the licensing transaction described in the Order Confirmation, which terms are in any way inconsistent with any terms set forth in the Order Confirmation and/or in these terms and conditions or CCC's standard operating procedures, whether such writing is prepared prior to, simultaneously with or subsequent to the Order Confirmation, and whether such writing appears on a copy of the Order Confirmation or in a separate instrument.

8.5. The licensing transaction described in the Order Confirmation document shall be governed by and construed under the law of the State of New York, USA, without regard to the principles thereof of conflicts of law. Any case, controversy, suit, action, or proceeding arising out of, in connection with, or related to such licensing transaction shall be brought, at CCC's sole discretion, in any federal or state court located in the County of New York, State of New York, USA, or in any federal or state court whose geographical jurisdiction covers the location of the Rightsholder set forth in the Order Confirmation. The parties expressly submit to the personal jurisdiction and venue of each such federal or state court. If you have any comments or questions about the Service or Copyright Clearance Center, please contact us at 978-750-8400 or send an e-mail to [support@copyright.com](mailto:support@copyright.com).

v 1.1


<https://marketplace.copyright.com/rs-ui-web/mp/license/8dae2b97-2c81-4cf0-b112-b838186ca8de/989147fd-9aeb-4233-acc9-69201cda1803>

4/4



**Paper Title:** Blood Flow Velocity Prediction in Aortoiliac Stent Grafts using Computational Fluid Dynamics and Taguchi Method  
**Journal:** Computers in biology and medicine  
**Rights Holder:** Elsevier Science & Technology Journals

7/13/2020 [Manage Account](#)

 **Marketplace™**

---

**Order Number:** 1047960  
**Order Date:** 13 Jul 2020

**Payment Information**

Albert Chong yoon.s.chong@postgrad.curtin.edu.au	<b>Billing Address:</b> Mr. Albert Chong 40 Clevedon place Kallaroo, Western Australia 6025 Australia  +61 (4)28537287 yoon.s.chong@postgrad.curtin.edu.au	<b>Customer Location:</b> Mr. Albert Chong Level 1 22 Stirling Highway Nedlands, Western Australia 6009 Australia
<b>Payment method:</b> Credit Card		

**Order Details**

1. Computers in biology and medicine **Billing Status:**  
Open

Article: Blood flow velocity prediction in aorto-iliac stent grafts using computational fluid dynamics and Taguchi method.

Order license ID	1047960-1
Order detail status	Completed
ISSN	0010-4825
Type of use	Republish in a thesis/dissertation
Publisher	PERGAMON
Portion	Chapter/article

**0.00 AUD**  
Republishing Permission

**LICENSED CONTENT**

<b>Publication Title</b>	Computers in biology and medicine	<b>Rights holder</b>	Elsevier Science & Technology Journals
<b>Article Title</b>	Blood flow velocity prediction in aorto-iliac stent grafts using computational fluid dynamics and Taguchi method.	<b>Publication Type</b>	Journal
		<b>Start Page</b>	235
		<b>End Page</b>	246
		<b>Volume</b>	84
<b>Date</b>	01/01/1970		
<b>Language</b>	English		
<b>Country</b>	United Kingdom of Great Britain and Northern Ireland		

**REQUEST DETAILS**

<b>Portion Type</b>	Chapter/article	<b>Rights Requested</b>	Main product
<b>Page range(s)</b>	235-246	<b>Distribution</b>	Worldwide
<b>Total number of pages</b>	12		

[https://marketplace.copyright.com/rs-ui-web/manage\\_account/orders/view-search/1047960](https://marketplace.copyright.com/rs-ui-web/manage_account/orders/view-search/1047960) 1/8

7/13/2020

Manage Account

<b>Format (select all that apply)</b>	Print,Electronic	<b>Translation</b>	Original language of publication
<b>Who will republish the content?</b>	Academic institution	<b>Copies for the disabled?</b>	No
<b>Duration of Use</b>	Life of current edition	<b>Minor editing privileges?</b>	Yes
<b>Lifetime Unit Quantity</b>	Up to 499	<b>Incidental promotional use?</b>	No
		<b>Currency</b>	AUD

**NEW WORK DETAILS**

<b>Title</b>	In Vitro and Computational Analyses of Blood Flow at Aortoiliac Bifurcation for Patients with Atherosclerotic Plaque Treated with Endovascular Procedures	<b>Institution name</b>	Curtin University
		<b>Expected presentation date</b>	2020-08-17
<b>Instructor name</b>	Professor Zhonghua sun		

**ADDITIONAL DETAILS**

<b>The requesting person / organization to appear on the license</b>	Albert Yoonsong Chong
--	-----------------------

**REUSE CONTENT DETAILS**

<b>Title, description or numeric reference of the portion(s)</b>	In Vitro and Computational Analyses of Blood Flow at Aortoiliac Bifurcation for Patients with Atherosclerotic Plaque Treated with Endovascular Procedures	<b>Title of the article/chapter the portion is from</b>	Blood flow velocity prediction in aorto-iliac stent grafts using computational fluid dynamics and Taguchi method.
<b>Editor of portion(s)</b>	Chong, Albert Y.; Doyle, Barry J.; Jansen, Shirley; Ponosh, Stefan; Cisonni, Julien; Sun, Zhonghua	<b>Author of portion(s)</b>	Chong, Albert Y.; Doyle, Barry J.; Jansen, Shirley; Ponosh, Stefan; Cisonni, Julien; Sun, Zhonghua
<b>Volume of serial or monograph</b>	84	<b>Publication date of portion</b>	2017-05-01
<b>Page or page range of portion</b>	235-246		

**Elsevier Science & Technology Journals Terms and Conditions**

Elsevier publishes Open Access articles in both its Open Access journals and via its Open Access articles option in subscription journals, for which an author selects a user license permitting certain types of reuse without permission. Before proceeding please check if the article is Open Access on <http://www.sciencedirect.com> and refer to the user license for the individual article. Any reuse not included in the user license terms will require permission. You must always fully and appropriately credit the author and source. If any part of the material to be used (for example, figures) has appeared in the Elsevier publication for which you are seeking permission, with credit or acknowledgement to another source it is the responsibility of the user to ensure their reuse complies with the terms and conditions determined by the rights holder. Please contact [permissions@elsevier.com](mailto:permissions@elsevier.com) with any queries.

[https://marketplace.elsevier.com/rs-ui-web/manage\\_account/orders/view-search/1047960](https://marketplace.elsevier.com/rs-ui-web/manage_account/orders/view-search/1047960)

2/8

7/13/2020	Manage Account		
<b>2. Quantitative imaging in medicine and surgery</b>			<b>Billing Status:</b> Open
Article: CT angiography in the diagnosis of cardiovascular disease: a transformation in cardiovascular CT practice.			
Order license ID	1047960-2		
Order detail status	Completed		
ISSN	2223-4306		
Type of use	Republish in a thesis/dissertation		
Publisher	AME Publishing Company		
Portion	Image/photo/illustration		
			<b>0.00 AUD</b>
			Republishing Permission
<b>LICENSED CONTENT</b>			
Publication Title	Quantitative imaging in medicine and surgery	Publication Type	Journal
Article Title	CT angiography in the diagnosis of cardiovascular disease: a transformation in cardiovascular CT practice.	Start Page	376
		End Page	396
		Issue	5
		Volume	4
		URL	http://www.amepc.org/qims
Date	01/01/2011		
Language	English		
Country	China		
Rightholder	Nancy International Ltd Subsidiary AME Publishing Company		
<b>REQUEST DETAILS</b>			
Portion Type	Image/photo/illustration	Distribution	Worldwide
Number of images / photos / illustrations	1	Translation	Original language of publication
Format (select all that apply)	Print,Electronic	Copies for the disabled?	No
Who will republish the content?	Academic institution	Minor editing privileges?	No
Duration of Use	Life of current edition	Incidental promotional use?	No
Lifetime Unit Quantity	Up to 499	Currency	AUD
Rights Requested	Main product		
<b>NEW WORK DETAILS</b>			
Title	In Vitro and Computational Analyses of Blood Flow at Aortoiliac Bifurcation for Patients with Atherosclerotic Plaque Treated with Endovascular Procedures	Institution name	Curtin University
		Expected presentation date	2020-08-17
<a href="https://marketplace.copyright.com/rs-ui-web/manage_account/orders/view-search/1047960">https://marketplace.copyright.com/rs-ui-web/manage_account/orders/view-search/1047960</a>			
			3/8

7/13/2020
Manage Account

---

**Instructor name** Professor Zhonghau Sun

**ADDITIONAL DETAILS**

**The requesting person / organization to appear on the license** Albert Yoonsong Chong

**REUSE CONTENT DETAILS**

<b>Title, description or numeric reference of the portion(s)</b>	In Vitro and Computational Analyses of Blood Flow at Aortoiliac Bifurcation for Patients with Atherosclerotic Plaque Treated with Endovascular Procedures	<b>Title of the article/chapter the portion is from</b>	CT angiography in the diagnosis of cardiovascular disease: a transformation in cardiovascular CT practice.
<b>Editor of portion(s)</b>	Sun, Zhonghua; Al Moudi, Mansour; Cao, Yan	<b>Author of portion(s)</b>	Sun, Zhonghua; Al Moudi, Mansour; Cao, Yan
<b>Volume of serial or monograph</b>	4	<b>Issue, if republishing an article from a serial</b>	5
<b>Page or page range of portion</b>	376-396	<b>Publication date of portion</b>	2014-10-01

**Nancy International Ltd Subsidiary AME Publishing Company Terms and Conditions**

It is the responsibility of the users' to identify the copyright holder of any materials. If the user has any doubts, please contact the publisher at [permissions@amegroups.com](mailto:permissions@amegroups.com). For illustrations owned by Ms. Croce, please contact [beth@bioperspective.com](mailto:beth@bioperspective.com).

---

**3. Journal of vascular and interventional radiology : JVIR** **Billing Status:**  
Open

**Article:** Aortic bifurcation stenosis: treatment with intravascular stents.

<b>Order license ID</b>	1047960-3
<b>Order detail status</b>	Completed
<b>ISSN</b>	1051-0443
<b>Type of use</b>	Republish in a thesis/dissertation
<b>Publisher</b>	LIPPINCOTT WILLIAMS & WILKINS
<b>Portion</b>	Image/photo/illustration

**0.00 AUD**  
Republication Permission

**LICENSED CONTENT**

<b>Publication Title</b>	Journal of vascular and interventional radiology : JVIR	<b>Rightsholder</b>	Elsevier Science & Technology Journals
<b>Article Title</b>	Aortic bifurcation stenosis: treatment with intravascular stents.	<b>Publication Type</b>	Journal
		<b>Start Page</b>	319
		<b>End Page</b>	323
		<b>Issue</b>	3
		<b>Volume</b>	2

[https://marketplace.copyright.com/rs-ui-web/manage\\_account/orders/view-search/1047960](https://marketplace.copyright.com/rs-ui-web/manage_account/orders/view-search/1047960)
4/8

7/13/2020	Manage Account
-----------	----------------

<b>Author/Editor</b>	SOCIETY OF CARDIOVASCULAR AND INTERVENTIONAL RADIO		
<b>Date</b>	01/01/1996		
<b>Language</b>	English		
<b>Country</b>	United States of America		

**REQUEST DETAILS** -----

<b>Portion Type</b>	Image/photo/illustration	<b>Distribution</b>	Worldwide
<b>Number of images / photos / illustrations</b>	1	<b>Translation</b>	Original language of publication
<b>Format (select all that apply)</b>	Print,Electronic	<b>Copies for the disabled?</b>	No
<b>Who will republish the content?</b>	Academic institution	<b>Minor editing privileges?</b>	No
<b>Duration of Use</b>	Life of current edition	<b>Incidental promotional use?</b>	No
<b>Lifetime Unit Quantity</b>	Up to 499	<b>Currency</b>	AUD
<b>Rights Requested</b>	Main product		

**NEW WORK DETAILS** -----

<b>Title</b>	In Vitro and Computational Analyses of Blood Flow at Aortoiliac Bifurcation for Patients with Atherosclerotic Plaque Treated with Endovascular Procedures	<b>Institution name</b>	Curtin University
<b>Instructor name</b>	Professor Zhonghua Sun	<b>Expected presentation date</b>	2020-08-17

**ADDITIONAL DETAILS** -----

<b>The requesting person / organization to appear on the license</b>	Albert Yoonsong Chong
--	-----------------------

**REUSE CONTENT DETAILS** -----

<b>Title, description or numeric reference of the portion(s)</b>	Aortic bifurcation stenosis: treatment with intravascular stents.	<b>Title of the article/chapter the portion is from</b>	Aortic bifurcation stenosis: treatment with intravascular stents.
<b>Editor of portion(s)</b>	Palmaz, Julio C., MD; Encarnacion, Carlos E., MD; Garcia, Oscar J., MD; Schatz, Richard A., MD; Rivera, Frank J., MD; Laborde, Jean Claude, MD; Dougherty, Sarsfield P., MD	<b>Author of portion(s)</b>	Palmaz, Julio C., MD; Encarnacion, Carlos E., MD; Garcia, Oscar J., MD; Schatz, Richard A., MD; Rivera, Frank J., MD; Laborde, Jean Claude, MD; Dougherty, Sarsfield P., MD
<b>Volume of serial or monograph</b>	2	<b>Issue, if republishing an article from a serial</b>	3

<a href="https://marketplace.copyright.com/rs-ui-web/manage_account/orders/view-search/1047960">https://marketplace.copyright.com/rs-ui-web/manage_account/orders/view-search/1047960</a>	5/8
---	-----

7/13/2020

Manage Account

Page or page range of portion 319-323 Publication date of portion 1991-01-01

### Elsevier Science & Technology Journals Terms and Conditions

Elsevier publishes Open Access articles in both its Open Access journals and via its Open Access articles option in subscription journals, for which an author selects a user license permitting certain types of reuse without permission. Before proceeding please check if the article is Open Access on <http://www.sciencedirect.com> and refer to the user license for the individual article. Any reuse not included in the user license terms will require permission. You must always fully and appropriately credit the author and source. If any part of the material to be used (for example, figures) has appeared in the Elsevier publication for which you are seeking permission, with credit or acknowledgement to another source it is the responsibility of the user to ensure their reuse complies with the terms and conditions determined by the rights holder. Please contact [permissions@elsevier.com](mailto:permissions@elsevier.com) with any queries.

#### 4. VASA : Zeitschrift für Gefäßkrankheiten. Journal for vascular diseases

Billing Status:  
Open

Article: Percutaneous implantation of a unibody endograft to treat non-aneurysmal aortoiliac disease.

Order license ID	1047960-4
ISSN	0301-1526
Publisher	VERLAG/HANS HUBER AG
Order detail status	Completed
Type of Use	Distribute via commercial document delivery

26.55 AUD  
Print Permission

#### LICENSED CONTENT

Publication Title	VASA : Zeitschrift für Gefäßkrankheiten. Journal for vascular diseases	Rights holder	ProLitteris
		Publication Type	Journal
		Start Page	138
Article Title	Percutaneous implantation of a unibody endograft to treat non-aneurysmal aortoiliac disease.	End Page	141
		Issue	2
		Volume	46



7/13/2020
Manage Account

---

**Author/Editor** SCHWEIZERISCHE  
GESELLSCHAFT FUR  
ANGIOLOGIE.,SCHWEIZ  
ERISCHE  
GESELLSCHAFT FUR  
PHLEBOLOGIE.,DEUTSC  
HE GESELLSCHAFT FUR  
ANGIOLOGIE.,OSTERREI  
CHISCHE  
GESELLSCHAFT FUR  
ANGIOLOGIE.,OSTERREI  
CHISCHE  
GESELLSCHAFT FUR  
GEFASSCHIRURGI,OSTE  
RREICHISCHE  
ARBEITSGEMEINSCHAF  
T FUR  
MORPHOLO.,NIEDERLA  
NDISCHE  
GESELLSCHAFT FUR  
GEFASSCHIRURGI,SOCI  
ETAS PHLEBOLOGICA  
SCANDINAVICA.

**Date** 01/01/1972

**Language** English, German,  
German

**Country** Switzerland

---

**REQUEST DETAILS**

<b>Publication year of title being used</b>	2020	<b>Number of copies</b>	1
<b>Total number of pages</b>	130	<b>Currency</b>	AUD

---

**ADDITIONAL DETAILS**

<b>Article/Chapter</b>	Figure 2	<b>Your reference</b>	Figure 1-9
------------------------	----------	-----------------------	------------

---

**5. Inhalation toxicology** **Billing Status:**  
Open

Article: Screening tests: a review with examples.

<b>Order license ID</b>	1047960-5
<b>ISSN</b>	0895-8378
<b>Publisher</b>	TAYLOR & FRANCIS INC.
<b>Order detail status</b>	Completed
<b>Type of Use</b>	Distribute via commercial document delivery

**91.85 AUD**  
Print Permission

---

**LICENSED CONTENT**

<b>Publication Title</b>	Inhalation toxicology	<b>Publication Type</b>	Journal
<b>Article Title</b>	Screening tests: a review with examples.	<b>Start Page</b>	811
		<b>End Page</b>	828
<b>Date</b>	01/01/1988	<b>Issue</b>	13
<b>Language</b>	English	<b>Volume</b>	26

---

[https://marketplace.copyright.com/rs-ui-web/manage\\_account/orders/view-search/1047960](https://marketplace.copyright.com/rs-ui-web/manage_account/orders/view-search/1047960) 7/8

7/13/2020
Manage Account

<b>Country</b>	United States of America		
<b>Rightholder</b>	Taylor & Francis Informa UK Ltd - Journals		

**REQUEST DETAILS** .....

Publication year of title being used	2020	Number of copies	1
Total number of pages	130	Currency	AUD

**ADDITIONAL DETAILS** .....

Article/Chapter	Figure 1	Your reference	Figure 5-5
-----------------	----------	----------------	------------

**Taylor & Francis Informa UK Ltd - Journals Terms and Conditions**  
 This journal title may publish some Open Access articles, which provide specific user rights for reuse. Please refer to the article copyright line to determine whether the content you wish to use is Open Access. For Open Access content, permission to reuse is granted subject to the terms of the License under which the work was published. Please check the License conditions for the work which you wish to reuse. Full and appropriate attribution must be given. This permission does not cover any third party copyrighted material which may appear in the work requested. For queries, please email: OASpermissionrequests@tandf.co.uk

---

<b>Total Items: 5</b>	Subtotal:	118.40 AUD
	<b>Order Total:</b>	<b>118.40 AUD</b>

[https://marketplace.copyright.com/rs-ui-web/manage\\_account/orders/view-search/1047960](https://marketplace.copyright.com/rs-ui-web/manage_account/orders/view-search/1047960)
8/8



**Paper Title:** An Update on Methods for Revascularization and Expansion of the TASC Lesion Classification to Include Below-the-Knee Arteries ...  
**Journal:** Annals of Vascular Diseases  
**Rights Holder:** Editorial Committee of the Annals of Vascular Diseases

## Annals of Vascular Diseases

### Reprint Permission

The materials with permission granted by the Editorial Committee of the Annals of Vascular Diseases (AVD) should have copyright credit provided below.

Copyright by the Editorial Committee of the Annals of Vascular Diseases. All rights reserved.

To apply for reprint permission, please complete the "Reprint Request Form" below and send it to AVD Editorial Office avd-edit[at]bunken.co.jp by Email.

Please note that the permission will be applicable only to the book / journal / electronic publication / institutional repository. There is no cost for the material to be reprinted for scholarly use.

If you have further questions about our permission policies, please contact AVD Editorial Office. Email: avd-edit[at]bunken.co.jp; Tel: +81-3-5389-6492; Fax: +81-3-3368-2830.

### Reprint Request Form

#### 1) Requester's Information

First Name	Albert
Last Name	Chong
Name of Company or Organization	Curtin University
Postal Address (City, State/Province, Zip/Postal Code, Country)	4 Clevedon Place Kallaroo, WA 6025 Australia
TEL	+61-428-537-287
FAX	+61-8-9266-3232
Email	yoon.s.chong@postgrad.curtin.edu.au
Email (Reprise)	yoon.s.chong@postgrad.curtin.edu.au

## Annals of Vascular Diseases

### 2) Materials for Reprint

Title of article	An Update on Methods for Revascularization and Expansion of the TASC Lesion Classification to Include Below-the-Knee Arteries: A Supplement to the Inter-Society Consensus for the Management of Peripheral Arterial Disease (TASC II): The TASC Steering Committee(.)
Author(s)	Jaff, Michael R. White, Christopher J. Hiatt, William R. Fowkes, Gerry R. Dormandy, John Razavi, Mahmood Reekers, Jim Norgren, Lars
Volume	8
Issue	4
Year	2015
Page(s) (start page to end page)	343-357
Parts to be used (Specific range of text, figure(s), table(s) which you wish to reproduce)	Figure 1
You are the author of the requested material. (yes / no)	No

## Annals of Vascular Diseases

### 3) The Information how / where the article will be used

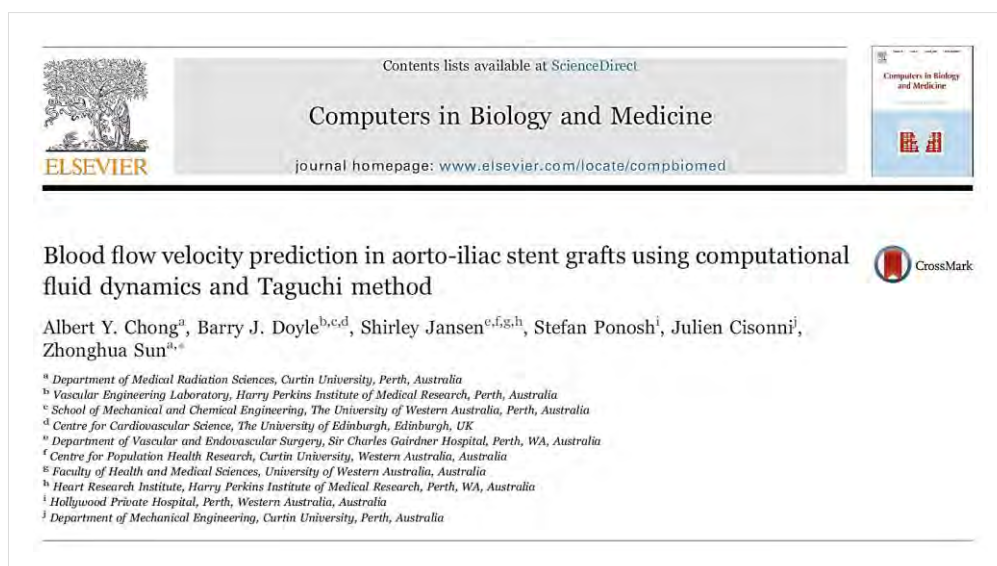
<Select either "not-for profit" or "to be included in for-profit", then provide details of publisher, title of journal, issue language, use (CD / Print / Web / Intranet)>

<input type="checkbox"/> For not-for-profit use in	
presentation materials	
journal article	
thesis	In Vitro and Computational Analyses of Blood Flow at Aortoiliac Bifurcation for Patients with Atherosclerotic Plaque Treated with Endovascular Procedures
other	
<input type="checkbox"/> To be included in for-profit materials (please give details of use)	

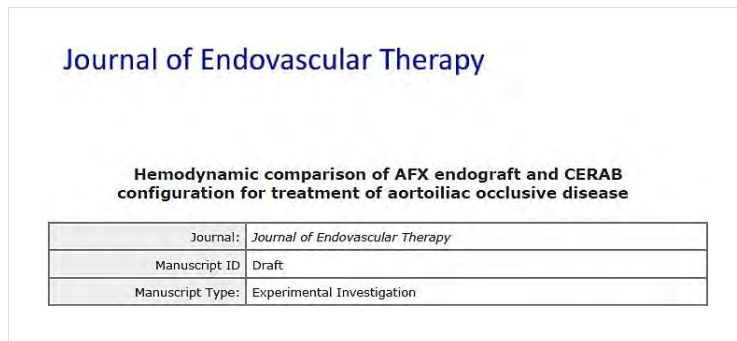
# Appendix K Published Manuscript Details

## Paper 1 (Chapter 2)

### BLOOD FLOW VELOCITY PREDICTION IN AORTO-ILIAC STENT GRAFTS USING COMPUTATIONAL FLUID DYNAMICS AND TAGUCHI METHOD





<b>Title:</b>	Blood flow velocity prediction in aorto-iliac stent grafts using computational fluid dynamics and Taguchi method
<b>Authors:</b>	Chong AY, Doyle BJ, Jansen S, Ponosh S, Cisonni J, Sun Z
<b>Candidate Contribution:</b>	69%
<b>Status:</b>	Accepted for publication
<b>Reference:</b>	Chong AY, Doyle BJ, Jansen S, Ponosh S, Cisonni J, Sun Z. Blood flow velocity prediction in aorto-iliac stent grafts using computational fluid dynamics and Taguchi method. <i>Computers. Biology and Medicine.</i> 2017; 84:235-246.
<b>Keywords:</b>	Analysis of variance, Aortoiliac stenting, Computational fluid dynamics, Multiple linear regressions, Orthogonal array, Peak Systolic Velocity, Taguchi method

**Paper 2 (Chapter 6)****HEMODYNAMIC COMPARISON OF AFX STENT-GRAFT AND CERAB CONFIGURATIONS FOR TREATMENT OF AORTOILIAC OCCLUSIVE DISEASE**

<b>Title:</b>	Hemodynamic comparison of AFX stent-graft and CERAB configuration for treatment of aortoiliac occlusive disease
<b>Authors:</b>	Chong AY <sup>1</sup> , Mirgolbabaee H <sup>2</sup> , Sun Z <sup>1</sup> , van de Velde L <sup>2,3,4</sup> , Jansen S <sup>5,6,7,8</sup> , Doyle B <sup>9,10,11</sup> , Verluis M <sup>4</sup> , Reijnen M <sup>2,3</sup> , Groot Jebbink E <sup>2,3</sup> <sup>1</sup> Department of Medical Radiation Sciences, Curtin University, Perth, WA, Australia <sup>2</sup> Multi-Modality Medical Imaging (M3I) Group, Technical Medical Centre, University of Twente, Enschede, The Netherlands <sup>3</sup> Department of Surgery, Rijnstate, Arnhem, The Netherlands <sup>4</sup> Physics of Fluids Group, TechMed Center and MESA+ Institute for Nanotechnology, University of Twente, Enschede, The Netherlands <sup>5</sup> Department of Vascular and Endovascular Surgery, Sir Charles Gairdner Hospital, Perth, WA, Australia <sup>6</sup> Medical School, Curtin University, Perth, WA, Australia <sup>7</sup> Faculty of Health and Medical Sciences, University of Western Australia, Perth, WA, Australia <sup>8</sup> Heart and Vascular Research Institute, Harry Perkins Institute of Medical Research, Perth, WA, Australia <sup>9</sup> Vascular Engineering Laboratory, Harry Perkins Institute of Medical Research, Perth, Australia <sup>10</sup> School of Engineering, The University of Western Australia, Perth, Australia <sup>11</sup> BHF Centre for Cardiovascular Science, The University of Edinburgh, Edinburgh, UK
<b>Candidate Contribution:</b>	54%
<b>Status:</b>	Under review
<b>Reference:</b>	Chong AY, Mirgolbabaee H, Sun Z, van de Velde L, Jansen S, Doyle B, Verluis M, Reijnen M, Groot Jebbink E. Hemodynamic comparison of AFX stent-graft and CERAB configurations for treatment of aortoiliac occlusive disease. <i>Journal of Endovascular Therapy</i> .
<b>Keywords:</b>	Stent-graft, Covered Endovascular Reconstruction of Aortic Bifurcation, Particle Image Velocimetry, hemodynamic, Wall Shear Stress, Oscillatory Shear Index, Relative Residence Time, Atherosclerosis, Time Averaged Wall Shear Stress

## Paper 3 (Chapter 7)

## A NOVEL ROLLER PUMP FOR PHYSIOLOGICAL FLOW

Received: 1 December 2019	Revised: 28 January 2020	Accepted: 10 February 2020
DOI: 10.1111/aor.13670		
<b>MAIN TEXT ARTICLE</b>		 <b>WILEY</b>
<b>A novel roller pump for physiological flow</b>		
Albert Chong <sup>1</sup>    Zhonghua Sun <sup>1</sup>   Lennart van de Velde <sup>2,3,4</sup>   Shirley Jansen <sup>5,6,7,8</sup>   Michel Versluis <sup>2,4</sup>   Michel M. P. J. Reijnen <sup>2,3</sup>   Erik Groot Jebbink <sup>2,3</sup>		
<sup>1</sup> Department of Medical Radiation Sciences, Curtin University, Perth, WA, Australia <sup>2</sup> Multi-Modality Medical Imaging (M3I) Group, Technical Medical Centre, University of Twente, Enschede, The Netherlands <sup>3</sup> Department of Surgery, Instate, Arnhem, The Netherlands <sup>4</sup> Physics of Fluids Group, TechMed Center and MESA+ Institute for Nanotechnology, University of Twente, Enschede, The Netherlands <sup>5</sup> Department of Vascular and Endovascular Surgery, Sir Charles Gairdner Hospital, Perth, WA, Australia <sup>6</sup> Department of Vascular Surgery, Curtin University, Perth, WA, Australia <sup>7</sup> Faculty of Health and Medical Sciences, University of Western Australia, Perth, WA, Australia <sup>8</sup> Heart and Vascular Research Institute, Harry Perkins Institute of Medical Research, Perth, WA, Australia		

<b>Title:</b>	A novel roller pump for physiological flow
<b>Authors:</b>	Chong A, Sun Z, van de Velde L, Jansen S, Versluis M, Reijnen, M M.P.J., Groot Jebbink E.
<b>Candidate Contribution:</b>	64%
<b>Status:</b>	Accepted for publication
<b>Reference:</b>	Chong A, Sun Z, van de Velde L, Jansen S, Versluis M, Reijnen, M M.P.J., Groot Jebbink E. A novel roller pump for physiological flow. <i>Artificial Organs</i> , 2020
<b>Keywords:</b>	blood pump, cardiopulmonary bypass, experimental study, extracorporeal membrane oxygenation, flow phantom, in vivo, physiological flow, pulsatile flow, roller pump, triphasic flow